Coordination Complexes with Redox-Active Macrocyclic Ligands as Redox-Responsive ^{1}H and ^{19}F MRI Contrast Agent Sensors and Catalysts for the Degradation of Hydrogen Peroxide

by

Sana Karbalaei

A dissertation submitted to the Graduate Faculty of
Auburn University
in partial fulfillment of the
requirements for the Degree of
Doctor of Philosophy

Auburn, Alabama
May 6, 2023

Keywords: Reactive oxygen species, MRI contrast agents, Macrocyclic ligands, Catalase mimics, Superoxide dismutase mimics

Approved by

Christian R. Goldsmith, Chair, Professor, Dept. of Chemistry and Biochemistry
Eduardus Duin, Professor, Dept. of Chemistry and Biochemistry
Bryon H. Farnum, Associate Professor, Dept. of Chemistry and Biochemistry
Rashad R. Karimov, Associate Professor, Dept. of Chemistry and Biochemistry
Dean D. Schwartz, Associate Professor, Dept. of Anatomy, Physiology, and Pharmacology

Abstract

Reactive oxygen species (ROS), including hydroxyl radicals ($^{\cdot}OH$), superoxide anions (O_2^{-}), and hydrogen peroxide (H_2O_2), play vital roles in cell signaling and cellular signal transduction; however, the overproduction of ROS has been associated with inflammatory, cardiovascular, and neurological diseases. To better understand the connections between ROS and diseases, we need to develop non-invasive and reliable sensors that can monitor the overproduction and traffic of ROS within biological systems. Magnetic resonance imaging (MRI) is particularly useful for non-invasive whole-body imaging due to its superior visualization depth, and MRI contrast agents are commonly used to change the T_1-weighted relaxivity (r_1) of protons and improve image contrast. To this end, I have reported a series of macrocyclic redox-responsive manganese- and iron-based MRI contrast agents that respond to H_2O_2, the most abundant ROS in biology.

Upon reaction with H_2O_2, metal oxidation results in an increase in the relaxivity of the iron-containing sensor; with the manganese complex, conversely, the enhanced relaxivity results from the oxidation of the organic ligand. Furthermore, it has been demonstrated that the inclusion of the macrocycle into the ligand structure improves the thermodynamic and kinetic stabilities of the MRI contrast agent sensors while amplifying the response to H_2O_2. To resolve the problem of false positives for ^1H MR imaging due to the background signal of water molecules, a fluorinated quinol-containing compound and its Fe(II) complex were developed as a dual-mode MRI contrast agent. Before oxidation, the sensor has a strong ^{19}F MRI signal but does not provide adequate T_1-weighted ^1H MRI contrast. Upon reaction with H_2O_2, the ^{19}F MRI signal disappears as the r_1 for ^1H MRI intensifies.

High concentrations of ROS can overwhelm the body's defenses against oxidative stress; these defenses include superoxide dismutases (SODs), which catalyze the conversion of $O_2^{\cdot -}$ to O_2 and H_2O_2, and catalases (CATs), which promote the dismutation of H_2O_2 to O_2 and H_2O. The development of

small molecules capable of replicating this catalysis represents a therapeutic strategy to combat disorders affiliated with oxidative stress. In this dissertation, I synthesized a series of quinol-containing compounds consisting of redox-active and redox-inactive metal ions to act as potent antioxidants that mimic either SOD and/or CAT. Further investigation revealed that the mechanistic pathway of hydrogen peroxide degradation can proceed using either metal- or ligand-centered redox partners for the ROS.

Acknowledgments

I would like to express my gratitude to all those who have helped and supported me throughout my research journey. First and foremost, I am deeply thankful to my advisor, Professor Christian R. Goldsmith, for his exceptional guidance, encouragement, and support throughout my Ph.D. program. His expertise, knowledge, and dedication have been invaluable to my research projects. More than that, he has been a constant source of motivation and energy, inspiring me to pursue excellence in every aspect of my work. I have learned so much from him, not only in terms of scientific knowledge but also in terms of how to handle difficult situations and stay patient under pressure.

I would also like to extend my heartfelt appreciation to my committee members, Professor Eduardus Duin, Dr. Bryon H. Farnum, and Dr. Rashad R. Karimov, for their insightful feedback, constructive criticism, and unwavering support throughout my research. Their contributions have been instrumental in shaping the direction and scope of my work. In addition, I would like to thank my collaborators Prof. Dr. Ivana Ivanović-Burmazović (Department of Chemistry of Ludwig-Maximilians-Universität München), Dr. Ronald J. Beyers (MRI Research Center of Auburn University), and Dr. Dean D. Schwartz (Department of Anatomy, Physiology, and Pharmacology of Auburn University), for their assistance and expertise in facilitating sophisticated measurements. Their support and guidance have been invaluable in helping me to overcome technical challenges and achieve meaningful results.

Lastly, I would like to express my gratitude to my family, my husband, and my friends for their unwavering love, support, and encouragement throughout my academic journey. Their belief in me has been a constant source of strength and inspiration, and I could not have done this without them.

Thank you all for your invaluable contributions, guidance, and support. I am deeply grateful for everything you have done for me, and I can’t wait to see what our future holds.

Table of Contents

Abstract ii

Acknowledgment iv

List of Tables viii

List of Figures ix

List of Schemes xviii

List of Abbreviations xviiii

Chapter 1 Introduction to Responsive MRI Contrast Agents Capable of Detecting Reactive Oxygen Species 1

1.1 Reactive Oxygen Species (ROS) in Biology 2

1.2 H_2O_2 Detection – General Considerations for Sensor Design 2

1.3 Why MRI? 5

1.4 Fundamental MRI theory 5

1.4.1 T_1-weighted relaxation 6

1.4.2 ^{19}F MRI 8

1.4.3 Chemical Exchange Saturation Transfer (CEST) 10

1.5 Recently Reported MRI Contrast Agent Sensors for ROS 11

1.5.1 T_1-Weighted MRI Contrast Agent Sensors 11

1.5.1.1. Sensors that rely on a change to the oxidation sate of the metal ion 11

1.5.1.2 Sensors that rely on a change to the oxidation state of the organic ligand 20

1.5.2 ^{19}F MRI contrast agent sensors 29

1.5.3 CEST-based MRI Contrast Agent Sensors 32

1.5.3.1 Sensors that rely on a change to the oxidation state of the metal ion 32

1.5.3.2 Sensors that rely on a change to the oxidation state of the organic ligand 36

1.6 Conclusions and Outlook 38

References 40

Chapter 2 A Macrocyclic Ligand Framework That Improves Both the Stability and T_1-Weighted MRI Response of Quinol-Containing H_2O_2 Sensors 48

2.1 Introduction 49

2.2 Experimental Section 51

2.3 Results 56

2.4 Discussion 68

2.5 Conclusions 74

Appendix A 75

References 92
Chapter 3 A Highly Water- and Air-Stable Iron-Containing MRI Contrast Agent Sensor for H_2O_2 95
3.1 Introduction 96
3.2 Experimental Section 98
3.3 Results and Discussion 104
3.4 Conclusions 117
Appendix B 118
References 141
Chapter 4 An Fe(II) Complex Acts as a Bimodal Sensor for Hydrogen Peroxide with ^{1}H and ^{19}F Magnetic Resonance Imaging Responses 144
4.1 Introduction 145
4.2 Experimental Section 147
4.3 Results and Discussion 154
4.4 Conclusions 163
Appendix C 164
References 178
Chapter 5 A Macrocyclic Quinol-Containing Ligand Enables High Catalase Mimicry even with a Redox-Inactive Metal at the Expense of the Ability to Mimic Superoxide Dismutase 181
5.1 Introduction 182
5.2 Experimental Section 184
5.3 Results 188
5.4 Discussion 197
5.5 Conclusions 204
Appendix D 205
References 222

List of Tables

Table 1.1 Relaxivities of T_1-weighted MRI contrast agents that respond to ROS through changes in the oxidation state of the metal ion 16

Table 1.2 Relaxivities of T_1-weighted MRI contrast agents that respond to ROS through changes in the oxidation state of the organic ligand 29

Table 2.1 Selected crystallographic data for $[H_6qp4](OTf)_2$ and $[Mn^{III}(H_2qp4)]^+$ 60

Table 2.2 pMn, log K_{ML}, and pK_a Values Determined by Potentiometric Titration of H_4qp4 and **1** ... 62

Table 2.3 Water exchange activation parameters obtained for Mn(II) complexes of H_4qp4, H_2qp1, and H_4qp2 62

Table A1. Parameters for the Hyperquad model for **1** 81

Table 3.1 pFe, log K_{ML}, and pK_a Values Determined by Potentiometric Titration of H_4qp4 and **1** 106

Table B1. Parameters for the Hyperquad model used for **1** 123

Table B2. Parameters for the Hyperquad model used for **3** 136

Table B3. Fit of the data to the Michaelis-Menten equation. 140

Table 4.1 pFe, log K_{ML}, and pK_a Values Determined for **1** 157

Table C1. Parameters for the Hyperquad model used for F_2H_4qp4 and **1** 173

Table C2. Selected crystallographic data for 2,5-dimethoxy-4-fluorobenzaldehyde and 2,5-dihydroxy-4-fluorobenzaldehyde 177

Table 5.1 Catalytic rate constants, k_{cat} (M^{-1} s^{-1}), measured by stopped-flow kinetics for the direct reactions of **1**, **2**, and **3** with superoxide 192

Table 5.2 Michaelis-Menten rate constants, k_2 rate constants, and turnover numbers (TON) calculated from oxygraphic data 192

Table D1. Selected crystallographic data for $[Zn^{II}(H_3qp4)](OTf)$ (**3**) 208

Table D2. Parameters for the Hyperquad model for the potentiometric pH titration data of **3** 210

Table D3. Parameters for the Michaelis-Menten models that were fit to the oxygraphy data displayed in Figure 5.3 211

Table D4. Parameters for the Michaelis-Menten models that were fit to the UV/vis data displayed in Figure D9 213

List of Figures

Figure 1.1 Structure of the 5,10,15,20-tetrakis-(*p*-sulfonatophenyl)porphinate ($TPPS^{8-}$) ligand.....12

Figure 1.2 Structure of 5,10,15,20-(4-PEG500–2,3,5,6-fluorophenyl) porphyrin 12

Figure 1.3 Structures of ligands for the manganese complexes.....14

Figure 1.4 Structure of the iron-binding ligand $PyC3A^{3-}$ 18

Figure 1.5 Structures of the cobalt-binding ligands.....19

Figure 1.6 Organic ligands for the Gd(III)-containing MRI contrast agent sensors.....21

Figure 1.7 Oxidative coupling of Gd(III)-phenol complexes to other phenol-containing molecules .21

Figure 1.8 Full structure of the DO3A derivative.....24

Figure 1.9 Proposed mechanism for the r_1 turn-off observed for the Gd(III)-containing probe 25

Figure 1.10 Ligands for the manganese-containing complexes.....25

Figure 1.11 Depiction of the formation of the binuclear Mn(II) complex.....26

Figure 1.12 Illustration of the oxidation of the Mn(II)-quinolate to a Mn(II)-aqua species.....27

Figure 1.13 Fluorinated ligands used for the ^{19}F MRI contrast agent sensors for ROS 31

Figure 1.14 Structure of the ligand used in the CEST-based cobalt-containing sensor 33

Figure 1.15 Ligands used in the preparation of the air-responsive Eu(II) complexes.....34

Figure 1.16 The europium-containing sensor 35

Figure 1.17 Ligands for the diiron complex 36

Figure 1.18 Yb(III)-containing sensor for NO/O_2 mixtures 37

Figure 1.19 Eu(III)-containing sensor for singlet oxygen 37

Figure 2.1 ORTEP representations of $[H_6qp4]^{2+}$ and $[Mn^{III}(H_2qp4)]^{+}$ 58

Figure 2.2 Predicted speciation as a function of pH for H_4qp4 and **1** 61

Figure 2.3 Plots of $r_2°$ as a function of temperature for **1** before and after oxidation by H_2O_2.....63

Figure 2.4 Response of **1** to H_2O_2..... 67

Figure A1. ^{1}H NMR spectrum of H_4qp4 in DMSO-*d6* 75

Figure A2. ^{13}C NMR spectrum of H_4qp4 in DMSO-*d6*.....75

Figure A3. MS (ESI+) of H_4qp4 in MeCN.....76

Figure A4. MS (ESI+) of $[Mn^{II}(H_3qp4)](OTf)$ (**1**) in MeCN 76

Figure A5. IR spectrum of **1**.....77

Figure A6. UV/vis spectra depicting the stability of a 0.10 mM solution of **1** in MeCN to air 77

Figure A7. Raw potentiometric pH titration data for 1.0 mM H_4qp4 and 1.0 mM **1** 78

Figure A8. Hyperquad model overlaid on the experimental data from the potentiometrictitration of H_4qp4 79

Figure A9. Hyperquad model overlaid on the experimental data from the potentiometrictitration of **1** 80

Figure A10. LC trace for the free H_4qp4 ligand.....82

Figure A11. LC trace for $[Mn^{II}(H_3qp4)]^+$.....82

Figure A12. UV/vis spectra of 0.10 mM solutions of H_4qp4 and 1 in aqueous solutions.....83

Figure A13. UV/vis spectroscopic titration of a 0.05 mM solution of **1** in water 83

Figure A14. Cyclic voltammetry of 1.0 mM **1** in 0.10 M phosphate buffer.....84

Figure A15. Spectrophotometric analysis of the reaction between 0.1 mM $Fe^{II}(ClO_4)_2$ and 0.1 mM **1** in A) MeCN B) 50 mM HEPES buffer pH=7.0 at 298 K.....85

Figure A16. A) Reaction between 20 mM $Zn(ClO_4)_2$ and 10 mM **1** in CD_3CN B) ^1H NMR spectrum of the product of thereaction between 10 mM $Zn(ClO_4)_2$ and 10 mM metal-free H4qp4 C) Same A in D_2O D) Same B in D_2O 86

Figure A17. MS (ESI+) of the product of the reaction between **1** and 2,3-dichloro-5,6-dicyano- 1,4-benzoquinone (DDQ) in MeCN....88

Figure A18. IR spectrum of the product of the reaction between **1** and DDQ 88

Figure A19. UV/vis spectra of a 0.10 mM solutions of **1** in MeCN before and after the addition of 1 equiv. of DDQ....89

Figure A20. Mass spectrometry (ESI) of a mixture of **1** in acetonitrile and 10 equiv. of H_2O_2. 89

Figure A21. Mass spectrometry (ESI) a sample of **1** that was sequentially oxidized by H_2O_2 and reduced by sodium dithionite ($Na_2S_2O_4$)....90

Figure A22. Plot of R_1 ($1/T_1$) versus pH for a 0.50 mM solution of **1** in unbuffered water....90

Figure A23. Representative kinetic traces for the reaction between 100 nM **1** and 10 mM H_2O_2 91

Figure 3.1 Predicted speciation as a function of pH for 1.0 mM **1** in an aqueous solution 107

Figure 3.2 ORTEP representation of $[Fe^{III}(H_2qp4)]^+$ (**2**) 108

Figure 3.3 X-band EPR spectra depicting the reaction of 1.0 mM **1** with 10 mM H_2O_2....109

Figure 3.4 Plots of $1/T_1$ versus iron concentration for **1** in the presence and absence of 10 mM H_2O_2.. 111

Figure 3.5 Water exchange at the Fe(II) center in **1** in an aqueous solution containing 0.06 M MOPS buffered to pH 7.4 followed by ^{17}O NMR 112

Figure 3.6 Cytotoxicity of $[Fe^{II}(H_3qp4)](OTf)$ and $[Mn^{II}(H_3qp4)](OTf)$ complexes toward H9c2 cells 116

Figure B1. Mass spectrometry (ESI) of **1** in MeCN.... 118

Figure B2. IR spectrum of **1** (KBr)....118

Figure B3. ^1H NMR spectrum of a 1 mM solution of 1 in CD_3CN....119

Figure B4. LC trace for **1** 119

Figure B5. Comparative UV/vis spectra of 0.10 mM solutions of H_4qp4 and **1** in aqueous solutions 120

Figure B6. Potentiometric pH titration data for 1.0 mM H4qp4 and 1.0 mM **1** 120

Figure B7. UV/vis spectroscopic titration of a 0.05 mM solution of **1** in water 121

Figure B8. Hyperquad model overlaid on the experimental potentiometric pH titration data collected for **1** 122

Figure B9. Cyclic voltammetry of 1.0 mM **1** in 0.10 M phosphate buffer 124

Figure B10. UV/vis spectra depicting the stability of a 0.10 mM solution of **1** in MeCN to air..... 124

Figure B11. UV/vis spectra depicting the stability of a 0.10 mM solution of **1** in buffered water to air.. 125

Figure B12. A) UV/vis spectra showing the reaction between 0.10 mM **1** and 10 mM H_2O_2 B) Expansion of the 400-700 nm region. C) The change in the absorbance at 297 nm 126

Figure B13. IR spectrum of the crude product from the reaction between 1.0 mM **1** and 10 mM H_2O_2 127

Figure B14. Mass spectrometry (ESI) of a sample of **1** that was oxidized by H_2O_2 and subsequently reduced by cysteine 128

Figure B15. Mass spectrometry (ESI) of a sample of **1** that was sequentially oxidized by H_2O_2 and reduced by sodium dithionite 129

Figure B16. Plot of R_1 ($1/T_1$) versus pH for a 0.50 mM solution of **1** in unbuffered water..... 130

Figure B17. ^{17}O NMR signals of the bulk solvent in the absence (black line, reference) and presence of a 1:10 mixture of **1** and H_2O_2 at various temperatures.. 131

Figure B18. Mass spectrometry (ESI) of **3** in MeCN 132

Figure B19. IR spectrum of $[Fe^{III}(H_3qp4)](OTf)_2$ (**3**) 132

Figure B20. UV/vis spectrum of a 0.10 mM solution of **3** in an aqueous solution B) Spectrophotometric pH titration of **3** 133

Figure B21. X-band EPR spectrum for a 1.0 mM solution of **3** in an aqueous solution 133

Figure B22. LC trace for **3** 134

Figure B23. Hyperquad model overlaid on the experimental potentiometric pH titration data collected for **3** 134

Figure B24. Predicted speciation as a function of pH for 1.0 mM **3** 135

Figure B25. A) Reaction between 20 mM $Zn(ClO_4)_2$ and 10 mM **3** in D_2O. B) ^1H NMR spectrum of the product of the reaction between 10 mM $Zn(ClO_4)_2$ and 10 mM metal-free H_4qp4 in D_2O.....137

Figure B26. Plot of $1/T_1$ versus iron concentration for **3** 138

Figure B27. A) UV/vis spectra for the reaction between 0.10 mM **1** and 0.60 mM H_2O_2 B) Plot of the absorbance at 297 nm as a function of time.....138

Figure B28. Representative kinetic traces for the reaction between 100 nM **1** and 10 mM H_2O_2 139

Figure B29. Activity of **1** with increasing concentrations of H_2O_2 140

Figure 4.1 Predicted speciation as a function of pH for 1.0 mM F_2H_4qp4 and 1.0 mM **1** 157

Figure 4.2 A) UV/vis spectra showing the reaction between 0.13 mM **1** and 10 mM H_2O_2 in 50 mM HEPES solution buffered to pH 7.00. B) X-band EPR spectra depicting the reaction of 1.0 mM **1** with 10 mM H_2O_2 C) ^{19}F NMR spectra of 0.1 mM **1** in 50 mM HEPES buffer 160

Figure 4.3 A) Plots of $1/T_1$ versus iron concentration for **1** in the presence and absence of 10 mM H_2O_2 B) Phantom images of solutions containing 0.1–1.0 mM **1** in the absence and presence of 10 mM H_2O_2 161

Figure 4.4 A) ^{19}F and T_1-weighted ^1H MRI phantom images of 10.0 mM **1** before and after reaction with 10.0 mM H_2O_2 B) A histogram of signal-to-noise ratios (SNRs) corresponding to ^{19}F MRI phantom images 162

Figure C1. ^1H NMR spectrum of 2,5-dimethoxy-4-fluorobenzaldehyde in DMSO-*d6*.....164

Figure C2. ^{19}F NMR spectrum of 2,5-dimethoxy-4-fluorobenzaldehyde in CD_3OD.....164

Figure C3. ^{13}C NMR spectrum of 2,5-dimethoxy-4-fluorobenzaldehyde in CD_3CN.....165

Figure C4. ORTEP representation of 2,5-dimethoxy-4-fluorobenzaldehyde.....165

Figure C5. ^{1}H NMR spectrum of 2,5-dihydroxy-4-fluorobenzaldehyde in DMSO-*d6* 166

Figure C6. ^{19}F NMR spectrum of 2,5-dihydroxy-4-fluorobenzaldehyde in CD_3OD 166

Figure C7. ^{13}C NMR spectrum of 2,5-dihydroxy-4-fluorobenzaldehyde in CD_3CN 167

Figure C8. ORTEP representation of 2,5-dihydroxy-4-fluorobenzaldehyde..... 167

Figure C9. ^{1}H NMR spectrum of F_2H_4qp4 in CD_3OD..... 168

Figure C10. ^{19}F NMR spectrum of F_2H_4qp4 in CD_3OD 168

Figure C11. ^{13}C NMR spectrum of F_2H_4qp4 in CD_3OD 169

Figure C12. MS (ESI+) of F_2H_4qp4 in MeOH 169

Figure C13. IR spectrum of F_2H_4qp4..... 170

Figure C14. IR spectrum of [Fe^{II}(F_2H_3qp4)](OTf) (**1**)..... 170

Figure C15. ^{1}H NMR spectrum of a 1 mM solution of [Fe^{II}(F_2H_3qp4)](OTf) (**1**) in $CDCl_3$ 171

Figure C16. UV/vis spectra of 0.10 mM solutions of F_2H_4qp4 and [Fe^{II}(F_2H_3qp4)](OTf) (**1**) 171

Figure C17. Hyperquad model overlaid on the experimental data from the potentiometric titration of F_2H_4qp4..... 172

Figure C18. Hyperquad model overlaid on the experimental data from the potentiometric titration of 1.0 mM **1**..... 172

Figure C19. UV/vis spectroscopic titration of a 0.05 mM solution of **1** in water 174

Figure C20. LC trace for the free F_2H_4qp4 ligand run under Method **1** 174

Figure C21. LC trace for 1 run under Method **1** 175

Figure C22. IR spectrum of the product from the reaction between 1.0 mM **1** and 10 mM H_2O_2 175

Figure C23. Cyclic voltammetry of 1.0 mM F_2H_4qp4 in 0.10 M phosphate buffer 176

Figure C24.A. Cyclic voltammetry of 1.0 mM [$Fe^{II}(F_2H_3qp4)$](Otf) **(1)** in 0.10 M phosphate buffer B. Expansion of -0.5 V to +0.1 V 176

Figure 5.1 ORTEP representation of the structure of $[Zn^{II}(H_3qp4)]^+$ 189

Figure 5.2 Superoxide scavenging effects of A) **1**, B) **2**, and C) **3** 191

Figure 5.3 Plots of v_o/[M] *vs.* the concentration of H_2O_2, A) Data for **1**. B) Data for **2**. C) Data for **3** 193

Figure 5.4 Determination of k_2 from plots of the initial rates (v_o) vs. concentration of catalyst 194

Figure 5.5 UV/vis spectra of reactions between **3** and H_2O_2. A) Data for the reaction between 0.1 mM 3 and 10 mM H_2O_2. B) Data for the reaction between 0.1 mM **3** and 0.60 mM H_2O_2 196

Figure D1. Mass spectrometry (ESI) of **3** in MeOH 205

Figure D2. IR spectrum of **3** 205

Figure D3. ^1H NMR spectrum of a crystalline sample of **3** dissolved in CD_3OD 206

Figure D4. ^{13}C NMR spectrum of crystalline **3** in CD_3OD 206

Figure D5. UV/vis data for a 0.10 mM solution of **3** in 294 K water 207

Figure D6. Cyclic voltammogram of 1.0 mM **3** 207

Figure D7. A) Hyperquad model overlaid on the experimental potentiometric pH titration data collected for **3**. B) Spectrophotometric pH titration of a 0.05 mM solution of **3** in water 209

Figure D8. Kinetic traces of superoxide decomposition at 250 nm by **1** in three different aqueous solutions. A) 60 mM MOPS buffer, pH 7.4, B) 50 mM phosphate buffer, C) 60 mM MOPS buffer 211

Figure D9. Kinetic traces of oxygen production upon reaction between 0.1 μM of each H_4qp4 catalyst and 10.0 mM H_2O_2 in 50 mM Tris buffered to pH 7.2 and 0.1 M EDTA to scavenge adventitious metal ions. A) Data for **1**. B) Data for **2**. C) Data for **3**. 212

Figure D10. Plots of v_o/[**M**] *vs.* the concentration of H_2O_2, where [**M**] is the concentration of the tested H_4qp4 complex. A) Data for **1**. B) Data for **2**. C) Data for **3** 213

Figure D11. Plots of v_o/[M] *vs*. the concentration of H_2O_2, where [M] is the concentration of the tested complex of A) **1**, B) **2**. Determination of k_3 from plots of the initial rates (v_o) *vs*. concentration of ABTS for A) **1**, B) **2**.....214

Figure D12. X-band EPR spectra of 1.0 mM solutions of **1**, **2**, and **3** in MeCN in the absence and presence of 10 mM H_2O_2.....215

Figure D13. Mass spectrometry (ESI) of the reaction between 10 mM H_2O_2 and **1** in MeCN at RT. The sample was analyzed 30 s after the beginning of the reaction.....216

Figure D14. Mass spectrometry (ESI) of the reaction between 10 mM H_2O_2 and **2** in MeCN at RT. The sample was analyzed 30 s after the beginning of the reaction.....217

Figure D15. Mass spectrometry (ESI) of the reaction between 10 mM H_2O_2 and **3** in MeCN at RT. The sample was analyzed 30 s after the beginning of the reaction.....218

Figure D16. Expansion of the data in Figure D15, showing the new feature with m/z = 539.1395, which is consistent with the addition of two O atoms to $[Zn(H_3qp4)]^+$.. 219

Figure D17. Mass spectrometry (ESI) of the reaction between 10 mM H_2O_2 and **3** in MeCN at RT. The data were acquired 60 s after the beginning of the reaction 220

Figure D18. X-band EPR data for the reaction between 1 mM **3** and 20 equiv. KO_2 in 50 mM HEPES buffered to pH 7.0.....221

Figure D19. UV/vis data for the reaction between 0.1 mM **3** and 20 equiv. KO_2 in water.....221

List of Schemes

Scheme 2.1 Molecular structures of the quinol-containing polydentate ligands and the compositions of coordination complexes 50

Scheme 2.2 Synthesis of H_4qp4 57

Scheme 2.3 Oxidized forms of the H_4qp4 ligand 64

Scheme 2.4 Other Mn(II)-binding ligands used in MRI contrast agents 70

Scheme 2.5 Proposed competing catalase and quinol oxidation pathways 73

Scheme 3.1 Oxidation of an Fe(II)-quinol to a more aquated Fe(III)-*para*-quinone 97

Scheme 3.2 Structure of H_4qp4 and compositions of isolated and solution-state iron complexes 104

Scheme 4.1 Structures of quinol-containing polydentate ligands and formulae for their coordination complexes.....147

Scheme 4.2 Synthesis of F_2H_4qp4. 156

Scheme 4.3 A Bimodal sensor with ^{1}H T_1-weighted and ^{19}F MRI responses to H_2O_2.....163

Scheme 5.1 Linear polydentate quinol-containing ligands 182

Scheme 5.2 Structure of H_4qp4 ligand and formulations of the discussed coordination complexes. 183

Scheme 5.3 Proposed mechanism for catalase activity that avoids metal-centered redox 202

Scheme 5.4 Proposed mechanism for catalase activity with metal-centered redox 204

List of Abbreviations

CAT	Catalase
CEST	Chemical Exchange Saturation Transfer
CV	Cyclic Voltammetry
DCM	Dichloromethane (CH_2Cl_2)
DMSO	Dimethyl Sulfoxide
DPPH	2,2-Diphenyl-1-picryl-hydrazyl hydrate
EDTA	Ethylenediaminetetraacetic Acid
EPR	Electron Paramagnetic Resonance
ESI	Electrospray Ionization
Ether	Diethyl Ether
EtOAc	Ethyl Acetate
Eq.	Equation
Equiv.	Equivalent
F_2H_4qp4	1,8-Bis(2,5-dihydroxy-4-fluorobenzyl)-1,4,8,11-tetraazacyclotetradecane
Fe	Iron
FTIR	Fourier-Transform Infrared Spectroscopy
H_2O_2	Hydrogen Peroxide
H_2qp1	*N*-(2,5-dihydroxybenzyl)-*N,N',N'*-tris(2-pyridinylmethyl)-1,2-ethanediamine
H_4qp2	*N,N'*-(2,5-dihydroxybenzyl)-*N,N'*-bis(2-pyridinylmethyl)-1,2-ethanediamine
H_4qp4	(1,8-Bis(2,5-dihydroxybenzyl)-1,4,8,11-tetraazacyclotetradecane
HEPES	4-(2- Hydroxyethyl)-1-piperazineethanesulfonic Acid
HCl	Hydrochloric Acid

HO_2	High Performance Liquid Chromatography
Hptp1	*N*-(2-Hydroxy-5-methyl-benzyl)-*N,N',N'*-tris(2-pyridinylmethyl)-1,2-ethanediamine
HR-MS	High Resolution Mass Spectrometry
KBr	Potassium Bromide
KCl	Potassium Chloride
KO_2	Potassium Superoxide
KOH	Potassium Hydroxide
MeCN	Acetonitrile
MeOH	Methanol
Mn	Manganese
MOPS	3-(*N*- Morpholino)propane Sulfonic Acid
MRI	Magnetic Resonance Imaging
MS	Mass Spectrometry
MTT	3-(4,5- Dimethylthiazol-2-yl)-2,5-diphenyltetrazolium Bromide
NHE	Normal Hydrogen Electrode
NMR	Nuclear Magnetic Resonance
$O_2^{\cdot-}$	Superoxide anion
OTf_3	Triflate
p*K*	Dissociation Constant
q	Aquation Number
r_1	Longitudinal Relaxivity
r_2	Transverse Relaxivity
ROs	Reactive Oxygen Species

SOD	Superoxide Dismutase
SODm	Superoxide Dismutase Mimetic
T_1	Longitudinal Relaxation Time
T_2	Transverse Relaxation Time
UV/vis	Ultraviolet Visible Spectrometry
V	Volt
XOD	Xanthine Oxidase
Zn	Zinc

Chapter 1

Introduction to Responsive MRI Contrast Agents Capable of Detecting Reactive Oxygen Species*

* This chapter is a modified version of a published paper: Sana Karbalaei, Christian R. Goldsmith, *Journal of Inorganic Biochemistry* **2022**, 230, 111763, and has been reproduced here with the permission of the copyright holder.

1.1 Reactive Oxygen Species (ROS) in Biology

Reactive oxygen species (ROS), including hydrogen peroxide (H_2O_2), superoxide anion radical ($O_2^{\cdot-}$), and hydroxyl radical ($^{\cdot}OH$), are produced in small quantities during many physiological processes. In eukaryotic cells, it is estimated that over 90% of ROS are generated by the mitochondria when electrons inadvertently escape from the mitochondrial electron-transport chain.[1–3] The cell uses a variety of antioxidants, such as superoxide dismutase and catalase enzymes, in order to regulate ROS levels.[4–7]

Although ROS have been demonstrated to serve essential and beneficial roles in several biological processes, such as cellular signaling[8–11] and the modulation of neuron and cardiomyocyte excitability,[12–17] high concentrations of these oxidants are harmful and lead to organ-damaging oxidative stress through the degradation of biomolecules such as proteins and lipids. The overproduction of ROS has been linked to many and diverse health conditions that include a variety of inflammatory,[18,19] cardiovascular,[20–24] and neurological disorders.[25–29] The roles of ROS in disease progression, however, have not been fully resolved and require further elucidation. Methods that can monitor ROS concentrations in biological environments have the potential to directly address this issue. Appropriate sensors for ROS could enable the earlier diagnoses of these health conditions by linking spatiotemporal patterns of oxidative stress to specific disorders. Further, probes capable of detecting ROS could also direct researchers to more effective treatments for these conditions by providing more information about their underlying physiological bases.

1.2 H_2O_2 Detection – General Considerations for Sensor Design

Although there are many sorts of ROS, this chapter will focus on sensors that can detect H_2O_2. ROS are intrinsically highly reactive,[30,31] and the cell produces a variety of antioxidants designed to lower their numbers even further. Consequently, each of these species accumulates at relatively low levels. Although such numbers have not yet been firmly defined, the steady-state *in vivo* concentrations

of H_2O_2 and $O_2^{\cdot-}$ in a typical cell are estimated to be 0.1 μM and 0.1 nM, respectively.[32] $^{\cdot}OH$ and $^{\cdot}OOH$ radicals are too reactive to be reliably intercepted by an antioxidant or sensor, and their steady-state levels would be even lower. Of the ROS listed in this paragraph, H_2O_2 is arguably the easiest analyte to pursue due to its higher abundance.

In designing a practical sensor, one must worry about the selectivity of its response. Different analytes may react with a probe to yield similar species with similar or even identical spectroscopic signatures; in such circumstances, one cannot distinguish these analytes. Ideally, a ROS sensor will be able to differentiate one ROS from another. In practice, this is difficult to achieve since different oxidants, including O_2, can enable the same chemical transformation that produces the signal. Possible reactivity with O_2 is arguably the greater concern since a probe that non-discriminately reacts with ROS nonetheless detects oxidative stress of some sort. Ideally, the redox potential of the sensor is such that it can be oxidized by one or more ROS, but not by O_2. Many of the sensors described in this chapter will react with O_2; some are included in the discussion since this side reactivity is often either slight enough to ignore over a short period of time or occurs much more slowly than the reaction with H_2O_2. In other cases, we discuss O_2-responsive contrast agents that do not have a documented response to H_2O_2 in order to introduce a strategy that could be applied to H_2O_2 sensing.

Even in situations where the sensor is not sensitive to O_2 and reacts specifically with one ROS, it can be difficult to attribute a probe's response to just a single ROS since these species can chemically transform into each other under physiological conditions. Whenever it is in a protic environment, $O_2^{\cdot-}$, for instance, reacts with itself to yield O_2 and H_2O_2. A compound that is activated by H_2O_2 in water can therefore also be activated either directly or indirectly by $O_2^{\cdot-}$. H_2O_2 reacts with transition metals to form $^{\cdot}OH$ and $^{\cdot}OOH$, which are both extremely potent oxidants that will certainly activate sensors designed to react with either O_2^- or H_2O_2.[33,34]

Magnetic resonance imaging (MRI)-based sensors are typically administered above 10 μM in order to provide signal-to-noise ratios that are high enough to unambiguously detect their analytes.[35–47] With T_1-weighted MRI contrast agents, this 10 μM value is very much a lower limit. These are frequently formulated at concentrations closer to 0.5 M and administered to provide 10 s or 100 s of μmol of contrast agent per kg of body weight. The sensor concentrations are therefore much higher than physiological ROS levels. ROS sensors need to be activated by small but continually replenishing pools of oxidants. The reactions that activate the redox-sensitive compounds described in this chapter consume the ROS but can sometimes be reversed by reductants, including many that are physiologically produced. Consequently, some of the described sensors can potentially revert to their pre-activated states upon the alleviation of oxidative stress. Given the low steady-state concentrations of ROS, it may take a prolonged period of time for a MRI-based sensor to reach equilibrium.

Generally, sensors can be classified into two major categories: turn-on and turn-off. In the former case, the signal increases upon activation. A turn-on fluorescent compound, for instance, may become brighter or emit light at a new wavelength. In a turn-off sensor, the signal decreases or disappears entirely upon reaction with the analyte; the system more closely resembles what would be observed in the absence of the sensor. With T_1-weighted contrast agents, a turn-off response will reduce the relaxivity and lessen its ability to sharpen image contrast. Turn-on sensors tend to be more practical since a diminished signal can result from a variety of different scenarios, including decomposition of the probe or its diffusion out of the area of study. Ratiometric probes provide distinct signals in their pre-activated and activated states; these are attractive in that they can more readily allow researchers to determine the extent of sensor activation in a specific region. Many of the contrast agent ROS probes with ^{19}F MRI outputs described in this chapter are ratiometric sensors as are the compounds with multiple modalities.

1.3 Why MRI?

MRI has been used extensively for the non-invasive visualization of soft tissues within whole-body subjects. In addition to identifying and outlining morphological features, MRI can potentially provide insight into biochemical processes within these tissues through the use of a chemically responsive contrast agent.[37,48] A chemical probe that produces a change to the MR image upon oxidation by an ROS could be used to non-invasively monitor biological redox environments using clinically approved MRI scanners.

This chapter is heavily indebted to a number of other reviews of redox-responsive MRI contrast agents.[48–54] The focus of this chapter will be on coordination complex probes that have been documented to react with H_2O_2. Compounds that react with reductants or have only had their response with O_2 characterized will generally not be discussed at length unless they illustrate concepts that have been or could readily be applied to the detection of H_2O_2. As will be detailed in the final section of this chapter, H_2O_2 probes will need to traverse a complicated path to the clinic. An excellent *in vitro* response to H_2O_2 does not necessarily lead to an adequate *in vivo* response, and the pharmacological properties of the sensor (*e.g.* toxicity, clearance from the body) need to be thoroughly assessed before one can even consider using these probes for clinical diagnoses. This chapter will primarily focus on the preclinical development of these sensors but will nonetheless highlight instances where complexes have been used to image oxidative activity in biological samples.

1.4 Fundamental MRI theory

MRI instruments apply a static magnetic field and specific radiofrequency (RF) pulses. Under the magnetic field, the nuclei with non-zero spin precess at the Larmor frequency (ω), determined by the field strength (B0) and the gyro-magnetic ratio (γ) of the nucleus under investigation (Eq. 1).

$$\omega = \gamma B0 \quad (1)$$

The RF pulses, matched to the Larmor frequency, cause the nuclei spins to rotate or 'tip' out of alignment from the static magnetic field by angle (α) determined by RF pulse strength (B1) and pulse duration (τ).

$$\alpha = \tau B1 \quad (2)$$

After the pulse, the tipped spins continue to precess and radiate a secondary echo RF signal. The MRI scanner detects the echo signals released by the relaxing nuclei over time as the spins revert to their original magnetization equilibrium and converts these data into an image. Most frequently, ^{1}H nuclei are visualized, but other nuclei, such as ^{19}F, have also been explored as reporters.[49] Since water is the major source of ^{1}H nuclei within the body, ^{1}H-based MRI usually differentiates soft tissues from each other based on their water content, with the more water-rich regions being more readily visualized.

Both the relaxation times of magnetically resonant nuclei and their concentrations impact the contrast of the MR image. Endogenous contrast is not always sufficient to delineate abnormalities and differentiate nearby tissues with similar water contents, but this problem can sometimes be resolved by the administration of contrast agents, which most frequently work by shortening the relaxation time of the visualized nuclei.[49,55–57] There are two relaxation pathways: longitudinal relaxation T_1 (spin-lattice relaxation) and transverse relaxation T_2 (spin-spin relaxation). T_1 and T_2 are both time constants; the corresponding rates of nuclear relaxation are associated with the rate constants $1/T_1$ and $1/T_2$.

All of the ROS-responsive MRI contrast agents described in this chapter rely on one or two of three fundamental physical processes to alter the MR image: T_1-weighted ^{1}H relaxation, ^{19}F relaxation, and chemical exchange saturation transfer (CEST).

1.4.1 T_1-weighted relaxation

The most widely employed MRI contrast agents use highly paramagnetic metal ions to hasten the rate of T_1-associated relaxation for the ^{1}H nuclei of nearby water molecules. This improves the T_1-

weighted (T_{1w}) contrast of the signal. Although a wide array of mononuclear Gd(III), Fe(III), and Mn(II) complexes have been demonstrated to act as MRI contrast agents,[35–40,55,58,59,61–69] only a handful of Gd(III) complexes are currently approved for clinical use.[49]

The longitudinal proton relaxivity (r_1) of a compound is the primary measure of its effectiveness as a T_1 relaxation agent. Higher values of r_1 result in stronger contrast. The r_1 is related to the observed T_1 ($T_{1,obs}$) through the following relationship:

$$\frac{1}{T_{1,obs}} = \frac{1}{T_{1,dia}} + r_1 \mathrm{C} \qquad (3)$$

In Eq. 3, $T_{1,dia}$ is the longitudinal relaxation time in the absence of the contrast agent, and C is the concentration of the contrast agent.

The r_1 value is determined by the nature of the interactions between the contrast agent and molecules from the bulk water. The inner-sphere component (r_{1IS}) originates from the interactions between the electron spin of the paramagnetic metal center and the nuclear spins from protons of water molecules that are directly coordinated to the metal ion. The outer-sphere component of the relaxivity (r_{1OS}) results from interactions with nearby non-coordinated water molecules. The second-sphere component (r_{1SS}) results from the electron spin of the metal ion interacting with water molecules that are hydrogen bonding to the metal complex. Of the three contributors to r_1, the r_{1IS} is the most straightforward to manipulate through synthetic modifications to the contrast agent. The inner-sphere relaxation is dependent on the aquation number of metal center (q), the relaxation time (T_{1m}), and the mean residency time (τ_m) of the coordinated water molecules (Eq. 4).[55] The magnitude of inner-sphere relaxation can be modified by changing the structure of ligand. A less highly coordinating polydentate ligand, for instance, will leave more open coordination sites for water, increasing q. One must be cautious in making such modifications, however, since the polydentate ligand needs to coordinate tightly enough to the metal ion to keep the contrast agent intact in water. Altering the charge of the

donor atoms will impact the rate of the water exchange and thereby τ_m. The metal ion strongly influences T_{1m}, with more paramagnetic ions leading to shorter values and higher r_{1IS}.

$$r_{1IS} = \frac{q/[\mathrm{H2O}]}{T_{1m} + \tau_m} \quad (4)$$

The relaxation time of the water molecules coordinated to the metal center (T_{1m}) can also be modified by altering the correlation time (τ_c), which is defined as the time needed for 1 rad rotation perpendicular to the applied field. τ_c depends on three dynamic processes (Eq. 5): the residency time (τ_m), the field-dependent electronic longitudinal relaxation time (T_{1e}), and the rotational correlation time of the metal compound (τ_R).[70] The fastest dynamic process contributes the most to τ_c. For most Gd(III) and Mn(II) complexes, T_{1e} and τ_m are on the ns timescale, whereas τ_R is on the ps time scale. Consequently, τ_c is approximately equal to τ_R for these complexes.

$$\frac{1}{\tau_c} = \frac{1}{\tau_R} + \frac{1}{\tau_m} + \frac{1}{T_{1e}} \quad (5)$$

The rotational correlation time can be slowed by binding the contrast agent to a biomacromolecule through either a non-covalent or covalent linkage. The impact of tethering the contrast agent to a larger structure on the r_1 is highly dependent on the magnetic field strength. Larger gains in the r_1 are generally seen with weaker fields.[71,72]

1.4.2 ^{19}F MRI

The physical basis of ^{19}F MRI is similar to that of ^{1}H MRI, and the two nuclei can be imaged with mostly the same instrumentation.[73–75] ^{19}F MRI data can be acquired on a traditional ^{1}H MRI scanner equipped with a specialized radiofrequency coil. The primary difference between these two forms of MRI is that the longitudinal (R_1) and transverse (R_2) rates of relaxation for ^{19}F are more similar to each other, and one cannot effectively weight the measurements towards one process as is frequently done with ^{1}H MRI. The signal intensity (I) is approximated by Eq. 6, where N(F) is the

density of ^{19}F nuclei and T_R and T_E are the repetition and echo times of the pulse sequence. The strongest signals will result when T_1 and T_2 are approximately equal.

$$I = N(F) \exp(-T_E/T_2)[1 - 2 \exp(-(T_R - T_E/2)/T_1) + \exp(-T_E/T_1)] \quad (6)$$

^{19}F MRI has two significant advantages over T_1-weighted ^{1}H MRI. First, there is essentially no background signal since the small amount of fluorine that is present in the body is embedded in the solid matrices of the teeth and bones. The inability of these matrices to tumble increases R_2, leading to extreme line broadening and the effective loss of the ^{19}F MRI signal. Second, the chemical shifts of ^{19}F nuclei are spread over a 300 ppm range, facilitating the differentiation of fluorine-containing species. Consequently, if the ^{19}F signals of the pre-activated and activated forms of a sensor have sufficiently different energies, the fluorine-containing probe could provide a ratiometric response, even without a secondary spectroscopic output.

The chief disadvantage of ^{19}F MRI is that successful imaging often requires lengthy acquisition times and/or high loadings of the contrast agent. The low sensitivity results from two factors. First, there are few imageable ^{19}F nuclei in a typical experiment, and the visualizable ^{19}F comes almost exclusively from an added contrast agent. With T_1- weighted ^{1}H MRI, conversely, the signal originates from the bulk water molecules. The low numbers of ^{19}F nuclei typically lead to poor signal-to-noise ratios. The signal quality can be improved by installing multiple chemically equivalent F atoms onto the imaging agent. Unfortunately, this can introduce another problem: heavily fluorinated molecules tend to be poorly soluble in water.[76] Second, the T_1 relaxation times of ^{19}F nuclei tend to be long; a typical value for a diamagnetic molecule is about 0.5–3 s. The T_1 can be shortened by using a paramagnetic molecule as the fluorine source. As with ^{1}H MRI, more paramagnetic species tend to shorten T_1 to greater extents. However, these ions can also shorten T_2, which leads to line broadening.[75] Mn(II), which is effective in increasing the contrast of T_{1w} ^{1}H MRI, severely attenuates ^{19}F MRI signals due to its tendency to decrease T_2.[75,77]

1.4.3 Chemical Exchange Saturation Transfer (CEST)

MRI-visualizable nuclei can potentially exchange between multiple chemical species, with the nucleus having a discrete resonance frequency for each chemical environment. Saturating one of these frequencies with the appropriate radiation will decrease the intensity of the signals associated with the other chemical environments. This phenomenon is referred to as Chemical Exchange Saturation Transfer (CEST).[78] Compounds with N–H or O–H bonds, for instance, can exchange ^{1}H protons with those from water molecules. Irradiating at the resonance frequencies of the N–H or O–H protons will weaken the signal arising from the water nuclei.[79] Reducing the intensity of the total water signal results in decreased contrast for the MR image.[52,79] As such, CEST is intrinsically a turn-off phenomenon, but a turn-on sensor could be created if one were to start with a CEST-active compound that converts to a CEST-inactive species upon reaction with an analyte.

CEST is more efficient when the ^{1}H nuclei exchange between chemical environments with greatly different resonance frequencies.[52,79] With diamagnetic CEST agents, there tends to be strong overlap between the contrast agent's resonance frequencies and that of the bulk water. Although only certain paramagnetic metal ions, such as Gd(III) and Mn(II), relax hydrogen nuclei quickly enough to allow T_1-weighted MRI contrast enhancement, most paramagnetic metal ions shift the hyperfine resonance energies of nearby nuclei to extents that dwarf those attainable with diamagnetic species.[52] CEST with paramagnetic agents is often referred to as PARACEST. Traditional MRI contrast agents rely upon rapid water molecule exchange into the coordination sphere of the paramagnetic ion to enhance the MRI contrast.[55] Such rapid water molecule exchange essentially nullifies CEST by coalescing the frequencies associated with the different chemical environments associated with the nuclei into a single signal.

One disadvantage to using CEST for ROS sensing is that the CEST effect is highly sensitive to pH and temperature; it can therefore be difficult to attribute a change in the local CEST signal to

just a change in the redox environment. The local pH and temperature impact both the resonance frequencies of the exchanging nuclei and the rate of exchange. Another significant disadvantage is that the RF pulses needed for CEST are much longer (~ 1 s) than those used for other forms of MRI (~ 10 ms).[80] These longer pulses transfer more power to the sample, potentially heating it to hazardous levels. Variations of CEST that use a series of short pulses instead of one long RF pulse are currently being explored.

1.5 Recently Reported MRI Contrast Agent Sensors for ROS

1.5.1 T_1-Weighted MRI Contrast Agent Sensors

1.5.1.1. Sensors that rely on a change to the oxidation sate of the metal ion

Although the complex in question was not explicitly demonstrated to react with H_2O_2, a sensor reported by Aime et al. in 2000 deserves mention for using a Mn(III/II) couple to detect O_2.[35] The authors' early use of a metal-based redox couple to detect an oxidant in conjunction with MRI has unquestionably influenced the other work in this section. Nuclear magnetic resonance dispersion data indicated that the r_1 values of the Mn(II) and Mn(III) complexes with the porphyrinic ligand $TPPS^{8-}$ (Figure 1.1) were too similar above ~3 MHz to distinguish by MRI. Aime et al., however, were able to better separate the relaxivities of these compounds at higher fields by encapsulating them into cyclodextrin (CD) hosts. This strategy works since the r_1 of the Mn(II) species is more strongly impacted by the rotational motion and τ_R; the relaxivity of the Mn(III) complex, conversely, is more dependent on the electronic relaxation time.[81,82] With a 20 MHz field, the macromolecular adducts of the Mn(II) and Mn(III) complexes with a poly-β-CD had r_1 values of 40.8 mM^{-1} s^{-1} and 15.2 mM^{-1} s^{-1}, respectively.[35] Upon reaction with 40 Torr of O_2, the Mn(II) complex completely converts to the Mn(III) in under 5 min. Although the addition of H_2O_2 would likely result in a similar, if not identical, turn-off in r_1, the speed of the O_2 oxidation would prevent the Mn(II)-$TPPS^{8-}$ complex from differentiating between the two oxidants.

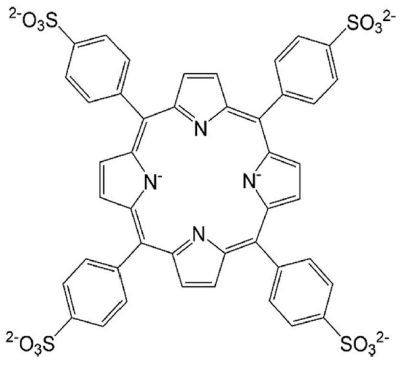

Figure 1.1 Structure of the 5,10,15,20-tetrakis-(*p*-sulfonatophenyl)porphinate ($TPPS^{8-}$) ligand used in reference 35.

Manganese complexes with porphyrinic ligands could potentially be used to detect H_2O_2 if the O_2 reactivity was significantly slowed. Pinto et al. reported a manganese-containing O_2 sensor with a porphyrin ligand covalently modified with polyethylene glycol (PEG) groups (Figure 1.2).[83] Much like the aforementioned $TPPS^{8-}$/CD system, the Mn(II) complex displays a much higher r_1 than the Mn(III), but without the necessity of including a second component to make a macromolecular adduct. The Mn(III) can be rapidly reduced to the Mn(II) using ascorbic acid or β-mercaptoethanol. Notably, the authors describe the oxidation of the Mn(II) form by O_2, as being "quite slow but… fully achieved after 24 h."[83] Although the complex could potentially react with H_2O_2 quickly enough to selectively detect it over O_2, the oxidation of the Mn(II) form by H_2O_2 was not described.

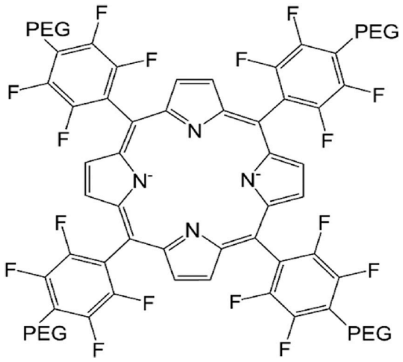

Figure 1.2 Structure of 5,10,15,20-(4-PEG500–2,3,5,6-fluorophenyl)porphyrin, the PEG-derivatized ligand used in reference 83.

The research groups led by Caravan and Gale have developed a series of responsive MRI contrast agents that rely on M(III/II) redox processes to detect biologically relevant reductants and oxidants, including H_2O_2.[84–87] Much of the T_1 response results from the change to the paramagnetism of the metal center, with the more paramagnetic species in the redox couple having a shorter T_{1m}. The aquation number, q, also impacts the r_1, but this can only be reliably measured for Mn(II).[88] q would be anticipated to decrease upon oxidation due to the smaller size of the oxidized metal ion; this would reduce r_1 as a consequence. Most of the contrast agents reported by Caravan, Gale, and co-workers contain manganese and display analogous turn-off responses to H_2O_2,[84–86] but a more recent sensor contains iron and converts to a species with a higher relaxivity upon exposure to H_2O_2.[87]

In the manganese-containing contrast agents initially reported by Loving et al., the metal ions are coordinated to derivatives of ethylenediaminetetraacetate ($EDTA^{4-}$, Figure 1.3).[84] $[Mn^{II}(EDTA)(H_2O)]^{2-}$ itself is difficult to oxidize. The Mn(II) complex with $EDTA^{4-}$ is straightforward to isolate and characterize, does not react with air in water,[89–91] and has an irreversible oxidation feature with a Mn(III/II) reduction potential of 633 mV *vs.* NHE.[84] Replacing the carboxylate groups of the $EDTA^{4-}$ with phenolates yields ligands that stabilize Mn(III) to a greater extent. Although the diphenolate ligand $HBED^{4-}$ does not form a stable Mn(II) complex,[92] the derivative with just a single phenolate group ($HBET^{4-}$) adequately stabilizes both the +2 and +3 oxidation states.[84]

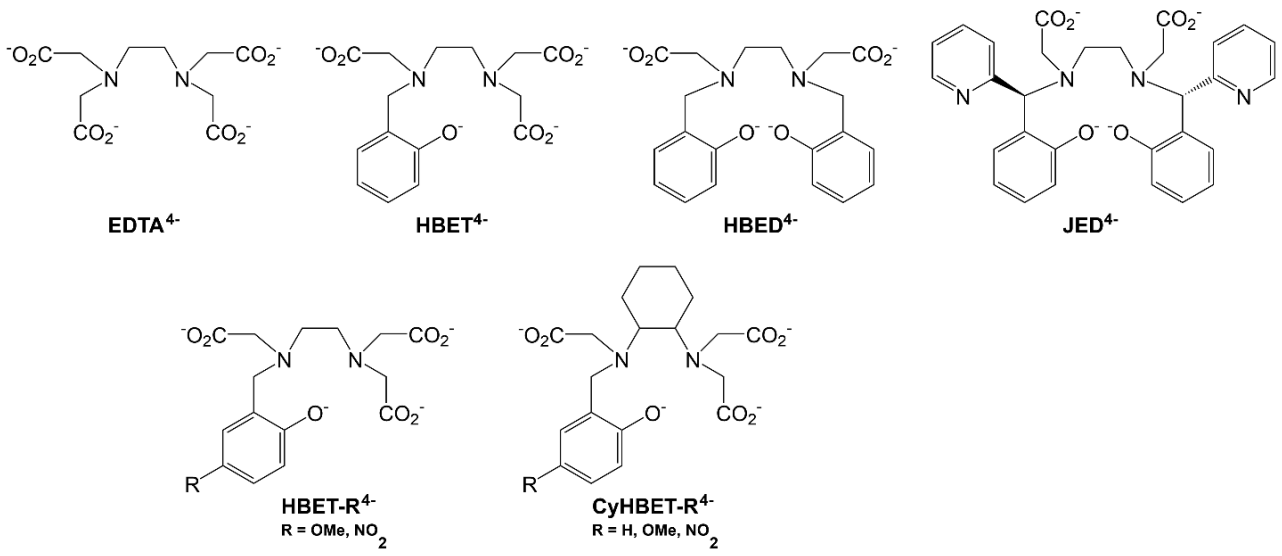

Figure 1.3 Structures of ligands for the manganese complexes discussed in references 84–86. $EDTA^{4-}$ = ethylenediamine-*N,N*′-tetraacetate; $HBET^{4-}$ = *N*-(phenolate)ethylenediamine-*N,N*′-triacetate; $HBED^{4-}$ = *N,N*′-bis(2-phenolate)ethylenediamine-*N,N*′-diacetate; JED^{4-} = (+/–) (R,R/S,S) *N,N*′-bis((pyridin-2-ylmethylene)phenolate)ethylenediamine-*N,N*′-diacetate; $CyHBET^{4-}$ = *N*-(2-phenolate)-*trans*-1,2-cyclohexylenediamine-*N,N′,N*′-triacetate.

The Mn(II) and Mn(III) complexes with HBET can therefore react with oxidants and reductants, respectively.[84] Glutathione (GSH) reduces the Mn(III) compound to Mn(II), with a concomitant increase in r_1 (Table 1.1). When the Mn(III) is reduced by 1 mM GSH, a concentration that represents the lower limit for cellular glutathione,[93] the half-life of the reaction is approximately 30 min. The Mn(II) form of the contrast agent can be oxidized back to the Mn(III) with H_2O_2 with a turn-off response in r_1. With 1 mM H_2O_2, 70% of the Mn(II) gets re-oxidized to Mn(III) in 4 min. The authors were concerned about the *in vivo* stability of the probe, noting that $EDTA^{4-}$ readily removes the manganese.[84]

With manganese complexes, water stability is a major concern. Coordination complexes with Mn(II) tend to be less stable than analogous species with other transition metal ions.[94] Physiologically relevant metal chelators further complicate the issue *in vivo* as they can potentially remove metal ions from contrast agents that are ostensibly water-stable. Consequently, one major initiative within this sub-field is to stabilize the sensors to as great an extent as possible.

Gale et al. subsequently modified the $HBET^{4-}$ framework by replacing the ethylene linkage between the amines with a cyclohexane to yield the $CyHBET^{4-}$ series of ligands and by introducing different substituents (R = H, OMe, NO_2) onto the 5-position of the phenolate group (Figure 1.3).[85] Mn(II) and Mn(III) complexes were prepared for most of the ligands; the Mn(III) complexes with the two methoxy-derivatized ligands appear to spontaneously decompose over the course of minutes and were not successfully isolated and characterized.

The manganese compounds with the other ligands act as redox-responsive MRI contrast agents. The introduction of the cyclohexane ring modestly improves the water stabilities of the Mn(II) complexes and boosts the r_1 response observed upon reduction from 2.6-fold ($HBET^{4-}$) to 8.25-fold ($CyHBET^{4-}$) when R = H. This benefit does not extend to the NO_2-derivatized Mn(III) complexes, which display identical within error 4.6-fold r_1 enhancements upon reduction (Table 1.1). The addition of the nitro group decreases the r_1 of the Mn(II) complexes at pH 7.4 but does not do so consistently with the Mn(III) species – a noticeable drop is seen for the $HBET^{4-}$ framework but not the $CyHBET^{4-}$ (Table 1.1). T_2-weighted relaxivities (r_2) were also measured and found to likewise increase upon reduction of the metal center.

The electronically modified complexes were analyzed using cyclic voltammetry. The Mn(III/II) reduction potentials fall within a narrow range, with $E_{1/2}$ varying from 0.45 to 0.57 V *vs.* NHE.[85] As anticipated, the reduction potentials are highest when R = NO_2. Consequently, all of the isolated Mn(III) complexes can be reduced by L-cysteine. The nitrosylated ligands accelerate this reactivity by approximately one order of magnitude over the Mn(III) complexes with the two R = H ligands. The oxidation of the Mn(II) complexes was not studied in the 2014 report.[85] The Mn(III) complexes with the HBET-derived ligands would be anticipated to rapidly reduce to Mn(II) species in blood plasma, limiting their practical use.

Table 1.1 Relaxivities of T_1-weighted MRI contrast agents that respond to ROS through changes in the oxidation state of the metal ion.

Contrast Agent	$r_1(M^{2+})$ (mM^{-1} s^{-1})	$r_1(M^{3+})$ (mM^{-1} s^{-1})	$r_1(M^{3+})/r_1(M^{2+})$	Reference
$[Mn^{II/III}(HBET)]^{2-/-}$	2.76	1.05	0.38	[84]
$[Mn^{II/III}(HBET\text{-}OMe)]^{2-/-}$	3.1	N.A.	N.A.	[85]
$[Mn^{II/III}(HBET\text{-}NO_2)]^{2-/-}$	2.3	0.5	0.22	[85]
$[Mn^{II/III}(CyHBET)]^{2-/-}$	3.3	0.4	0.12	[85]
$[Mn^{II/III}(CyHBET\text{-}OMe)]^{2-/-}$	3.3	N.A.	N.A.	[85]
$[Mn^{II/III}(CyHBET\text{-}NO_2)]^{2-/-}$	2.3	0.5	0.22	[85]
$[Mn^{II/III}(JED)]^{2-/-}$	3.3	0.5	0.15	[86]
$[Fe^{II/III}(PyC3A)]^{-/0}$	0.18	1.8	10	[87]
$[Mn^{II/III}(HTFBED)]^{2-/1\ a}$	2.7	0.7	0.26	[95]

All measurements taken in pH 7.4 Tris buffer at 37 °C with a 1.4 T field unless stated otherwise. [a]Measurements taken in pH 7.4 4-(2-hydroxyethyl)-1-piperazineethanesulfonic acid (HEPES) buffer with a 0.5 T field.

Gale et al. subsequently prepared the "Janus chelator" JED^{4-} (Figure 1.3), which was designed to provide differing coordination modes for Mn(II) and Mn(III) in order to improve the aqueous stabilities of both forms.[86] With this ligand, the pyridine rings were anticipated to bind to Mn(II), but not Mn(III). The phenolates, conversely, are expected to ligate Mn(III), but not Mn(II). Spectrophotometric pH titrations were used to investigate the coordination of the phenolates and confirmed that they bind to Mn(III) but not Mn(II). The JED^{4-} ligand successfully stabilizes both the Mn(II) and Mn(III) complexes, with high-performance liquid chromatography traces demonstrating that more than 95% of the Mn(II) and Mn(III) compounds remain intact after 24 h in plasma. There was "little interconversion" between the two oxidation states, suggesting negligible O_2 reactivity and/or disproportionation of Mn(III).

As with the $HBET^{4-}$ complex, the manganese complex with JED^{4-} can interconvert between Mn(II) and Mn(III) forms. The Mn(III) species can be reduced to Mn(II) by L-cysteine. In buffered water, this reduction is associated with a 6.6-fold enhancement in r_1 (Table 1.1). In plasma, the sensor performs more effectively, with the relaxivity increasing by a factor of 8.5. When the contrast agent is exposed to 5 equiv. of the thiol, the Mn(III) is reduced within seconds. The oxidation of $[Mn^{II}(HBET)]^{2-}$, conversely, does not occur as readily. H_2O_2 by itself will not oxidize the Mn(II) form, but incubating the Mn(II) complex with both H_2O_2 and peroxidase rapidly oxidizes it to the Mn(III) form with the anticipated decrease in r_1.

Most recently, Wang et al. reported a T_1-weighted MRI contrast agent sensor that uses iron rather than manganese as the paramagnetic reporter.[87] The selection of the Fe(III/II) couple significantly impacts the r_1 response since it is the higher oxidation state that is more paramagnetic. Further and more importantly, high-spin Fe(II) complexes undergo much faster electron spin relaxation than Fe(III); this substantially decreases τ_c (Eq. 5) and thereby $1/T_1$.[96] Even when high-spin, Fe(II) complexes are inefficient T_1-weighted MRI contrast agents. The key advantage to this design is that the pre-activated sensor has a negligible impact on the MR image; any contrast enhancement can be largely attributed to the oxidation of the Fe(II) complex rather than the accumulation of a large amount of the pre-activated ferrous probe in an area of interest.

Although the $PyC3A^{3-}$ ligand (Figure 1.4) was found to stabilize complexes with both Fe(II) and Fe(III), the ferrous species oxidizes upon hours-long exposure to air.[87] Ascorbic acid was added to stock solutions of the Fe(II) complex to prevent premature oxidation. Based on variable pH relaxivity measurements and ^{17}O NMR measurements with ^{17}O-labeled water, Wang et al. concluded that the Fe(III) complex is aquated, and the NMR data indicate a fast enough rate of water exchange to support the efficient T_1 relaxation of bulk water. As with the previous Mn(III) complexes from the Caravan and Gale groups, the Fe(III) complex with $PyC3A^{3-}$ is rapidly reduced by L-cysteine to the

nearly MRI-silent Fe(II) species. Conversely, the ferrous form is readily oxidized by H_2O_2 to the higher relaxivity ferric compound. The iron system thereby displays a strong turn-on response to H_2O_2. Upon oxidation, the r_1 improves by a factor of 10 with a 1.4 T field (Table 1.1), and even larger percentile gains to the relaxivity are observed at 4.7 T (13.3-fold) and 11.7 T (14.5-fold). The key drawback is that the 1.8 mM^{-1} s^{-1} r_1 of the Fe(III) form is low relative to the 3–4 mM^{-1} s^{-1} values observed for typical Mn(II)- and Gd(III)-containing MRI contrast agents; this may necessitate the administration of a higher dose of the sensor for many biological imaging applications.

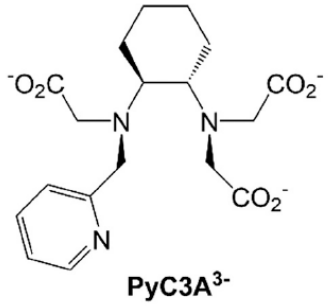

Figure 1.4 Structure of the iron-binding ligand *N*-picolyl-*N*,*N*′,*N*′-*trans*-1,2-cyclohexylenediaminetriacetate ($PyC3A^{3-}$) used in reference 87.

The utility of the $[Fe^{II}(PyC3A)]^-$ complex was demonstrated in an animal model of inflammation.[97] Wang et al. induced pancreatic inflammation in mice using intraperitoneal injections of caerulein and then imaged the animals before and after the administration of the contrast agent; the administered dose of the Fe(II) probe was 0.2 mmol/ kg.[87] The Fe(II) complex failed to activate in the control mice but enhanced the MR image of the pancreas of animals that had been dosed with caerulein. The 1.6 mM^{-1} s^{-1} difference in r_1 (measured in HEPES buffer) was sufficient to enable the complex to detect biologically relevant oxidative stress.

O'Neill et al. described a redox-responsive T_1-weighted MRI contrast agent that instead made use of a Co(III/II) couple.[98] The authors initially prepared a Co(III) complex with the TPA ligand (Figure 1.5), $[Co^{III}(TPA)(acac)]^{2+}$ ($acac^-$ = acetylacetonate), and determined that they were able to

reduce it to a discrete Co(II) species upon reduction by dithionite. The complex oxidizes back to the Co(III) form upon exposure to air over the course of a few hours. The oxidation of the Co(II) by H_2O_2 was not investigated. The Co(II) form was found to have a r_1 of approximately 0.06 mM^{-1} s^{-1} and a r_2 of approximately 0.24 mM^{-1} s^{-1} at 37 ◦C in pH 7.4 Tris buffer with a field strength of 9.4 T. The low r_1 value was attributed to the short electronic relaxation time of Co(II). The authors later installed carboxylate groups on the pyridine rings of TPA; the r_1 values of the resultant Co(II) complexes were approximately the same.[99] These complexes were used to successfully image the hypoxic regions of tumor spheroids, but the tumors needed to be incubated with 2 mM solutions of the Co(III) complexes for 24 h for enough of the compounds to enter the spheroids to make them visible.

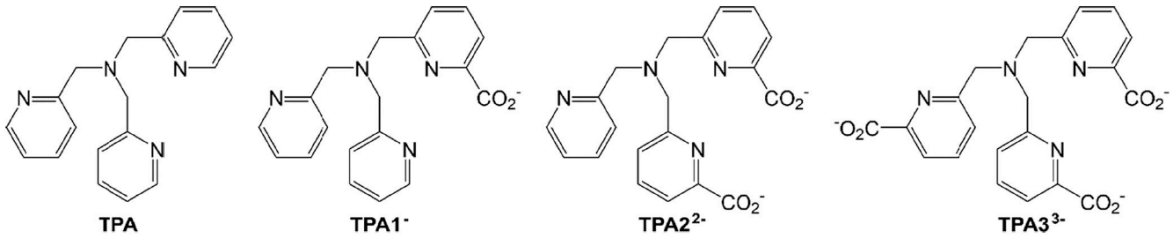

Figure 1.5 Structures of the cobalt-binding ligands used in references 98 and 99. TPA = tris(2-pyridylmethyl)amine.

Another redox-couple that has been explored for T_1-weighted MRI is Eu(III/II). Like Gd(III), Eu(II) has seven unpaired electrons in its ground state, and its complexes exhibit similarly high r_1 values.[100–105] The more oxidatively stable Eu(III) complexes, conversely, have little impact on T_1 but can be visualized using CEST, with a fluorinated derivative also displaying an oxidation-triggered ^{19}F MRI response.[101,102,105] Since these latter two modes provide a turn-on signal rather than the turn-off in r_1 accompanying the oxidation of Eu(II) to Eu(III), these complexes will be more fully described in the CEST portion of this chapter.

1.5.1.2 Sensors that rely on a change to the oxidation state of the organic ligand

Other T_1-weighted sensors for ROS display changes in r_1 that result from oxidation of the organic ligand, rather than the metal center. Early examples include a variety of Gd(III) compounds.[18,71,72,106,107] Since Gd(III) is almost completely redox-inactive,[108] the only way for a Gd(III) complex to undergo a chemical reaction with ROS is for the organic portion of the compound to be oxidized rather than the metal.

The Chen and Bogdanov groups prepared a series of Gd(III) complexes with ligands containing pendent phenol derivatives, such as 5-hydroxytryptamine (serotonin, Figure 1.6), that oligomerize upon reaction with H_2O_2 and peroxidase enzymes.[18,71,72,106,107] Unlike most of the H_2O_2 sensors described in this chapter, the Gd(III) complexes do not react with H_2O_2 directly; the MRI response strictly requires both the enzyme and H_2O_2. The peroxidase enzymes are needed to react with H_2O_2 and convert it to a more reactive ROS that is capable of directly activating the ligand. Myeloperoxidase (MPO), for instance, reacts with H_2O_2 and Cl^- to form HOCl.[71] The HOCl generated by MPO then abstracts a H atom from the phenolic portion of the ligand to generate a phenoxyl radical, which subsequently oxidatively couples to other phenolic species (Figure 1.7). In the absence of other phenol-containing biomolecules, such as proteins with exposed tyrosine residues, the sensor oligomerizes.[107] The larger size of the now polynuclear Gd(III) complex slows the rotation of the paramagnetic products, increasing τ_R and thereby r_1.

The r_1 of the first studied complex with the D-DOTA^{3-} ligand (Figure 1.6) increased 3-fold upon activation by 3.5 mM H_2O_2 and horseradish peroxidase, with a 500 ng/L loading of the enzyme

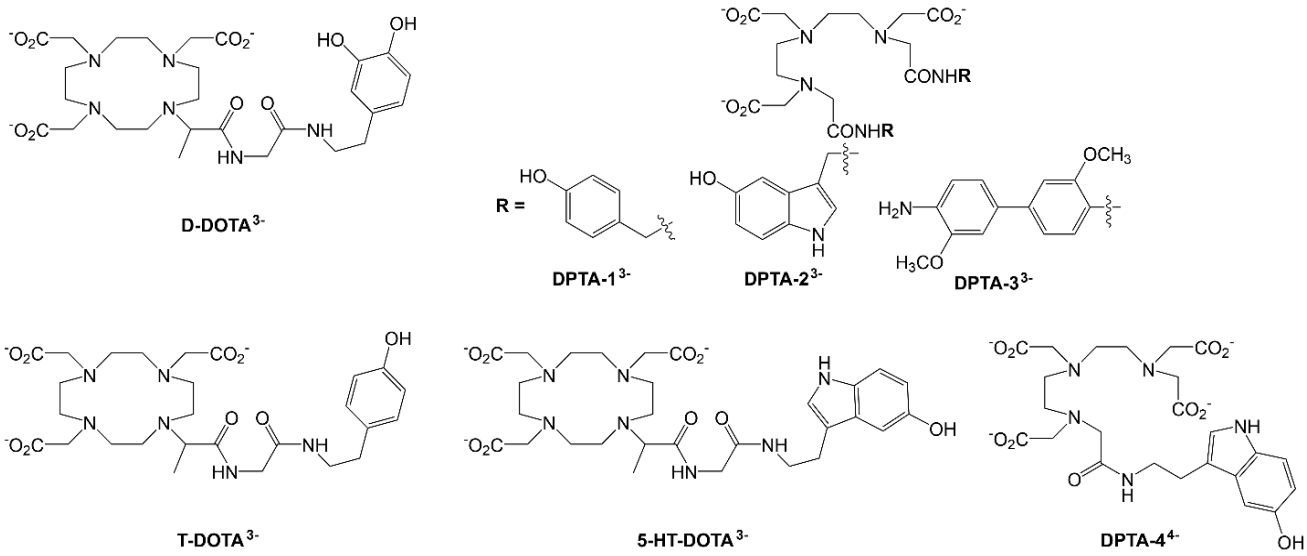

Figure 1.6 Organic ligands for the Gd(III)-containing MRI contrast agent sensors described in references 18,71,72,106, and 107. $DOTA^{4-}$ = 2,2′,2″,2‴-(1,4,7,10-tetraazacyclododecane-1,4,7,10-tetrayl)tetraacetate; $DPTA^{5-}$ = diethylenetriaminepentaacetate. The displayed ligands have other functional groups in place of one or more of the $DOTA^{4-}$ and $DPTA^{5-}$ acetates.

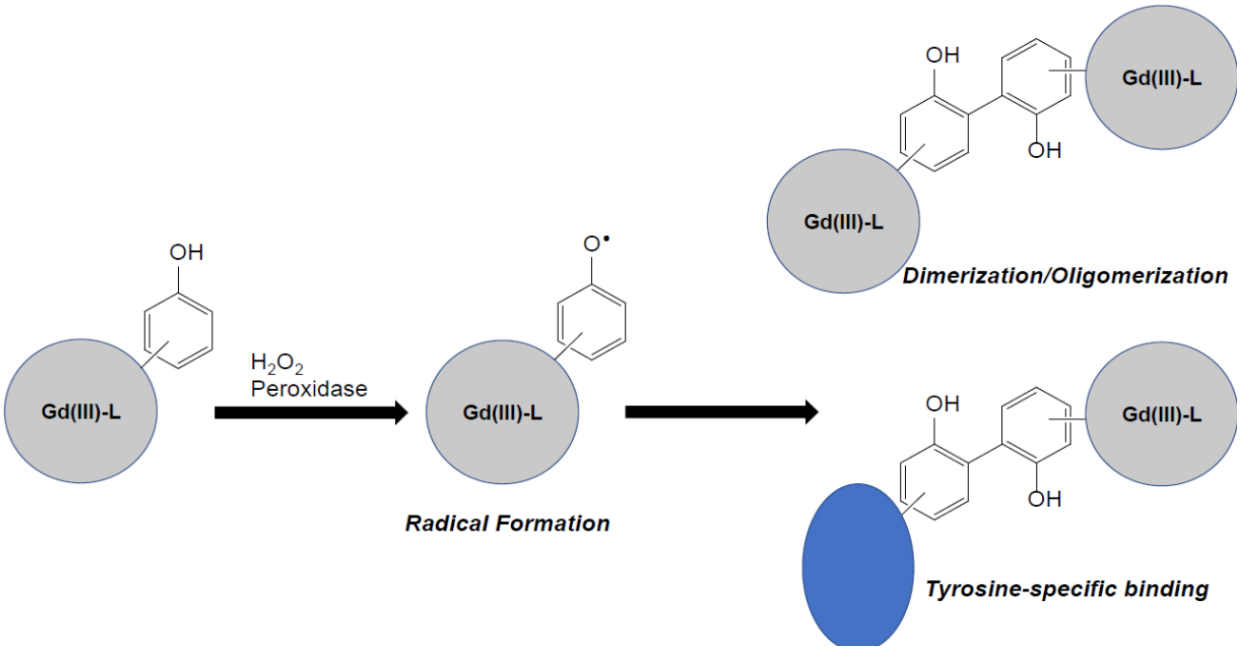

Figure 1.7 Oxidative coupling of Gd(III)-phenol complexes to other phenol-containing molecules and biomolecules.

fully oligomerizing the complex within 1 h (0.47 T, 40 ◦C).[107] The oligomerization raises r_1 from 3.75 to 11.50 mM^{-1} s^{-1}. The Gd(III) complexes with the non-macrocyclic ligands $DTPA\text{-}1^{3-}$ and $DTPA\text{-}2^{3-}$

behave similarly and exhibit 3.7- and 2.4-fold enhancements, respectively, under the same conditions.[72] As anticipated, the relaxivity response is field-dependent; the r_1 of the Gd(III) complex with DTPA-1^{3-} only increases 1.7-fold when measured in a stronger 1.5 T field. Mass spectrometry analysis of the oligomers isolated from the oxidation reactions suggests that, on average, they consist of either 7 or 8 monomeric units. The Gd(III) complex with the 5-hydroxytryptamide-containing DTPA-2^{3-} ligand was subsequently used to image MPO activity associated with ischemia-induced inflammation in mice brains.[18]

The speed and extent of activation for this class of sensor depend strongly on the choice of the enzyme catalyst. As an alternative to horseradish peroxidase, Chen et al. investigated the ability of MPO to activate the Gd(III) complexes with D-DOTA^{3-}, T-DOTA^{3-}, and 5-HT-DOTA^{3-} (Figure 1.6).[71] With this enzyme, the oxidation of the ligands occurs more slowly, and D-DOTA^{3-} did not react to a noticeable extent. The other two ligands were associated with r_1 increases ranging from 1.4- to 2-fold with 0.47 and 1.5 T fields, with the larger enhancements again being observed with the weaker 0.47 T field.

Rodríguez et al. later demonstrated that the Gd(III) complexes with the DTPA-1^{3-}, DTPA-2^{3-}, DTPA-3^{3-}, and DTPA-4^{4-} ligands (Figure 1.6) could potentially covalently tether to tyrosine-containing peptides.[106] MPO was primarily used as the enzyme catalyst; eosinophil peroxidase was also tested but did not promote any oligomerization. Upon reaction with H_2O_2, MPO, and a cysteine-containing polypeptide, the r_1 values of the complexes with DTPA-2^{3-}, DTPA-3^{3-}, and DTPA-4^{4-} increase by 22–59%, with larger gains seen for the latter two ligands. The authors identified a competition between oligomerization and protein cross-linking. The lower response of the DTPA-2^{3-} complex to the peptide was attributed to its preference for oligomerization. In the same publication, Rodríguez et al. demonstrated that these reagents could detect regions with high MPO activity in mouse thighs. In these experiments, the authors embedded MPO within the animals using Matrigel

and administered a 0.3 mmol/kg dose of the studied Gd(III) complex. The authors also investigated the cytotoxicity of their probes, finding that NIH-3T3 cells could tolerate concentrations of up to 5 mM for the DPTA-3^{3-} and DPTA-4^{4-} complexes. In parallel experiments with RAW 264.7 macrophages, which can secrete MPO upon chemical stimulation, the authors found no difference in the viability of activated *versus* non-activated cells, suggesting that the oxidized forms of the sensors were similarly non-toxic.

Tu et al. prepared a Gd(III) complex with a ligand consisting of a spironaphthaoxazine group tethered to 1,4,7,10-tetraazacyclododecane-1,4,7-triacetic acid (DO3A) that acts as a turn-on MRI contrast agent sensor for the reduced form of nicotinamide adenine dinucleotide (NADH).[109] The coordination of the spironaphthoxazine portion to the Gd(III) is modulated by the redox environment (Figure 1.8). When the Gd(III) complex reacts with NADH, the ligand cyclizes upon reduction, removing the phenol as a potential ligand. This opens a coordination site on the metal center for an additional water molecule. q increases from 1.3 to 2.0 as r_1 improves from 5.58 to 8.60 mM^{-1} s^{-1} (60 MHz, 37 ◦C, pH 7.0 deionized water). The subsequent addition of H_2O_2 in a 3-fold excess relative to the initially added amount of NADH reverses the reaction, both opening the heterocycle and oxidizing the ligand back to the spironaphthaoxazine form. The relaxivity decreases during the H_2O_2 reaction; the compound thereby acts as a turn-off sensor.

Harris et al. synthesized and characterized a Gd(III) complex with a macrocyclic ligand with a redox-active nicotinamide arm (Figure 1.9).[110] The reduced form of the complex has a q of 1.9, leading to a relatively high r_1 of 6.9 mM^{-1} s^{-1} (60 MHz, 37 ◦C, pH 7.0). Upon oxidation of 2 mM of the complex

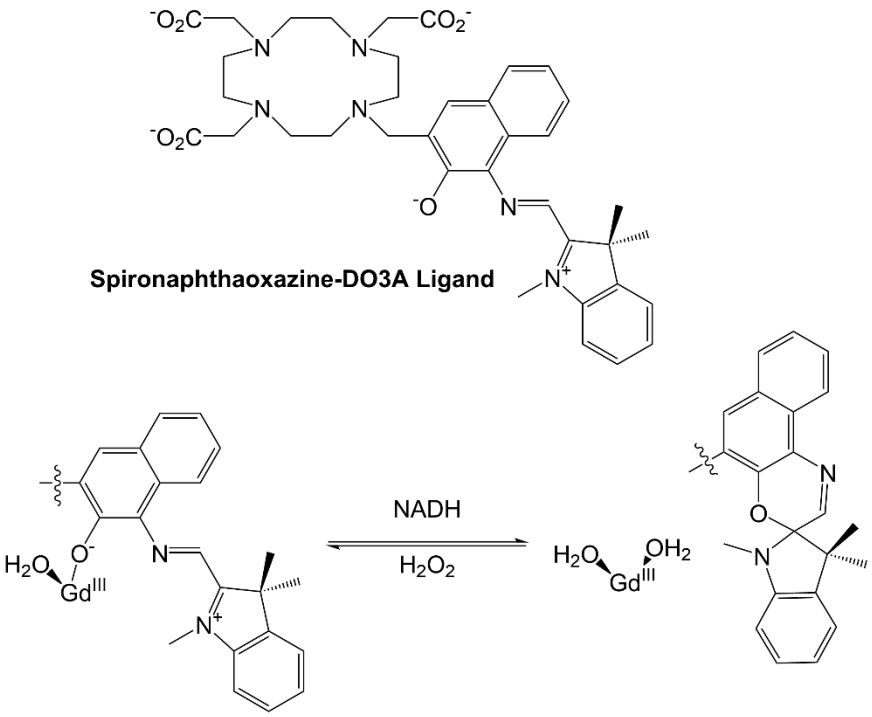

Figure 1.8 Full structure of the DO3A derivative used as the ligand in the redox-active MRI contrast agent reported in reference 109 and its proposed mode of activation, with a focus on the aquation number of the Gd(III) and the redox-sensitive portion of the ligand. $DO3A^{3-}$ = 1,4,7,10-tetraazacyclododecane-1,4,7-triacetate.

by 20 mM of H_2O_2, *q* drops to 0.3 and r_1 decreases to 3.7 mM^{-1} s^{-1}. Harris et al. determined that the presence of bicarbonate was essential for the response; *q* remains equal within error to the 1.9 value (2.1) when the oxidized sample is instead prepared in solutions that have been rigorously degassed with Ar. The authors speculate that the positive charge of the nicotinimidum in the oxidized form renders the coordination of bicarbonate more favorable by giving the Gd(III) complex an overall charge of +1. The Gd(III) complex with the reduced form of the ligand, conversely, is neutral. The positive charge of the oxidized species is proposed to enable bicarbonate to act as a more competitive inhibitor for water coordination. The oxidation of the ligand can be reversed by dithionite. The results are surprising in that the bicarbonate would be anticipated to bind strongly to the reduced form of the Gd(III) complex despite its lower overall charge.

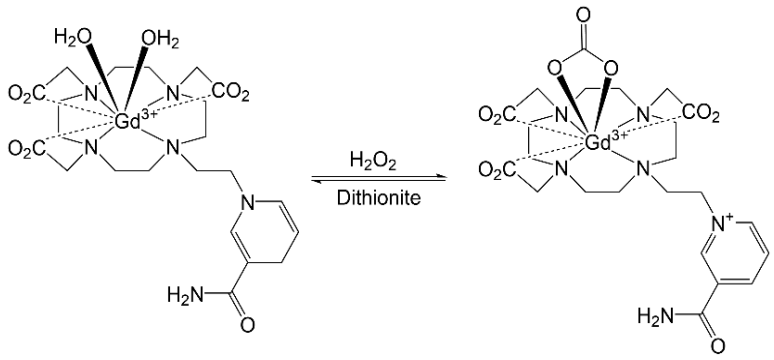

Figure 1.9 Proposed mechanism for the r_1 turn-off observed for the Gd(III)-containing probe described in reference 110.

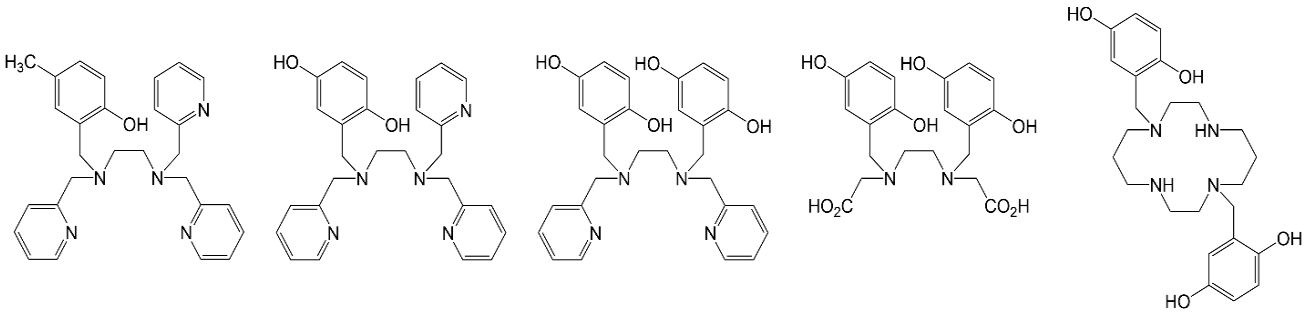

Figure 1.10 Ligands for the manganese-containing complexes discussed in references 111-117. Hptp1 = *N*-(2-hydroxy-5-methyl-benzyl)-*N,N′,N′*-tris(2-pyridinylmethyl)-1,2-ethanediamine; H_2qp1 = *N*-(2,5-dihydroxybenzyl)-*N,N′,N′*-tris(2-pyridinylmethyl)-1,2-ethanediamine; H_4qp2 = *N,N′*-bis(2,5-dihydroxybenzyl)-*N*, *N′*-bis(2-pyridinylmethyl)-1,2-ethanediamine; H_6qc1 = *N,N′*-bis(2,5-dihydroxybenzyl)ethanediamine-*N,N′*-diacetic acid; H_4qp4 = 1,8-bis(2,5 dihydroxybenzyl)- 1,4,8,11-tetraazacyclotetradecane.

Work from our own laboratory has focused on preparing manganese-containing MRI contrast agents with redox-active ligands (Figure 1.10).[111-117] Upon reaction with ROS, the metal ion may be oxidized transiently, but the observed changes in the T_1-weighted relaxivity are instead correlated to oxidation-triggered changes in the ligand structure. One benefit to this approach is that one does not need to provide a coordination environment that can accommodate two different metal oxidation states. Further, it can enable turn-on r_1 responses with Mn(II) ions.

The Hptp1 ligand features a redox-active *para*-methylphenol group that will coordinate to Mn(II) as a phenolate at physiological pH.[111,112] In water, the Mn(II) ion ligates a water molecule to

form $[Mn^{II}(ptp1)(H_2O)]^+$.[112] The complex with deprotonated Hptp1 ($ptp1^-$) rapidly reacts with H_2O_2; during this reaction, the phenolate groups from two separate molecules oxidatively couple together through the carbon atoms *ortho* to the hydroxides to yield a binuclear Mn(II) species (Figure 1.11).[111] The r_1 per metal center decreases due to the lesser overall paramagnetism of the binuclear cage complex (Table 1.2). The compound, therefore, acts as a turn-off sensor for H_2O_2. The $ptp1^-$ complex also behaves as a mimic of superoxide dismutase.[112] During the reactivity with $O_2^{\cdot-}$, the same binuclear Mn(II) product is observed as an end-product. The MRI response to $O_2^{\cdot-}$, however, was not thoroughly analyzed, largely due to the difficulty in deconvoluting the responses of the complex to $O_2^{\cdot-}$ and H_2O_2, the latter of which is a product of the catalyzed superoxide degradation.

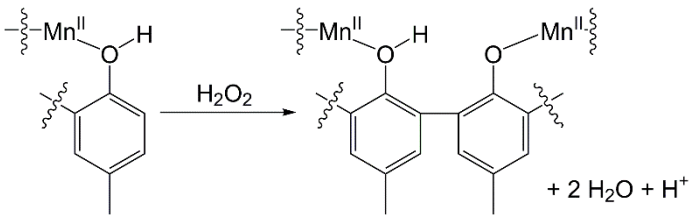

Figure 1.11 Depiction of the formation of the binuclear Mn(II) complex from two equiv. of $[Mn^{II}(Hptp1)]^{2+}$. This figure also appeared in reference 111.

Other work from our laboratory has used 1,4-hydroquinones, or quinols, as the redox-active group (Figure 1.10).[113–117] Although this appears at first glance to be a modest change from the *para*-methylphenol used in Hptp1, the switch from a methyl to a second hydroxy group fundamentally changes the sort of oxidation reaction that preferentially occurs. Instead of coupling two quinols together, the quinols are converted to *para*-quinones (Figure 1.12). Due to their inability to deprotonate to anionic forms, the *para*-quinones cannot bind to metal centers as avidly and are more readily displaced by water molecules. This increases q and thereby improves r_1.

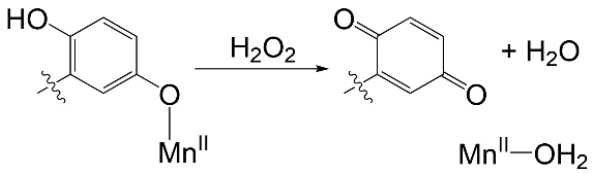

Figure 1.12 Illustration of the oxidation of the Mn(II)-quinolate to a Mn(II)-aqua species with a detached *para*-quinone.

The Mn(II) complexes with the H_2qp1, H_4qp2, and H_4qp4 ligands all react with H_2O_2 to yield Mn(II) species with *para*-quinone-containing ligands.[113,115,117] The oxidation of the ligand does not go to completion even when a large excess of H_2O_2 is provided, with only 70% of the quinols converting to quinones. The complex with H_4qp4 has displayed catalase activity,[117] and we currently believe that the oxidized complexes can oxidize H_2O_2 and revert to the pre-activated state. With an excess of ROS, the ability to cycle between oxidized and reduced forms leads to an equilibrium mixture of quinol and *para*-quinone species. As with most of the Mn(II) complexes described in this chapter, these compounds are mostly air-stable, with only ~5% oxidation observed at 18 h, which is much longer than the typical retention time of a MRI contrast agent within the body.

The ligand structure greatly impacts the water stability of the Mn(II) complexes and the magnitude of the relaxivity response. The r_1 of the complex with the monoquinol ligand, $[Mn^{II}(H_2qp1)]^{2+}$, increases by only 10% upon oxidation by H_2O_2 (Table 1.2).[113] The H_2qp1 complex is somewhat stable in water, existing mostly as $[Mn^{II}(Hqp1)(H_2O)]^{+}$ above pH 7.00, but its oxidized form readily exchanges its Mn(II) for Zn (II).[113,114] It is highly likely that physiologically relevant chelators would be able to remove the metal from the sensor in either its pre-activated or activated states. The Mn(II) complex with the diquinol ligand H_4qp2 displays a larger 30% increase in r_1 upon oxidation.[115] The substitution of the second quinol for one of the pyridine rings, however, greatly destabilizes both the reduced and oxidized Mn(II) complexes in water. The oxidation of the H_4qp2 ligand almost certainly leads to dissociation of the Mn(II) from the coordination complex, rendering

the sensor impractical for many *in vivo* applications. Installing carboxylate groups in place of the remaining pyridines yields the H_6qc1 ligand, which coordinates to metal ions as a mixture of the much more anionic H_3qc1^{3-} and H_2qc1^{4-}.[116] Although the $[Mn^{II}(H_6qc1)]^{2+}$ is much more stable in an aqueous solution, the added negative charge renders the metal center more susceptible to oxidation. The reaction with H_2O_2 oxidizes both the ligand and metal. The oxidation of the metal to the less paramagnetic Mn(III) counteracts any benefit that the oxidation of the ligand would provide; the H_6qc1 complex, consequently, displays essentially no r_1 response to H_2O_2.

The inclusion of a macrocycle into the ligand framework markedly improves the stability and unexpectedly enhances the r_1 response to H_2O_2 as well. The speciation of $[Mn^{II}(H_4qp4)]^{2+}$ strongly resembles that of $[Mn^{II}(H_4qp2)]^{2+}$ in that it exists as a mixture of $[Mn^{II}(H_3qp4)(H_2O)]^{+}$ and $[Mn^{II}(H_2qp4)(H_2O)]$ at pH 7.0.[117] Potentiometric pH titration data for the pre-activated sensor demonstrate that both of these species are extremely stable in water. The kinetic stability of the complex is also excellent. Unlike the H_2qp1 and H_4qp2 complexes with Mn(II), the H_4qp4 species do not readily exchange metal ions with added Fe(II) or Zn(II) in either the pre-activated or oxidized form. The reaction between a large 10 mM excess of H_2O_2 and $[Mn^{II}(H_4qp4)]^{2+}$ differs from those of the H_2qp1 and H_4qp2 systems in that it exhibits an induction period and requires 90 min to reach equilibrium. The induction period has been attributed to competing catalase activity; when a lower amount of H_2O_2 is added, the ligand oxidizes much more quickly. During the reaction, both the measured q and r_1 increase, demonstrating that the ligand oxidation, aquation number, and T_1-weighted relaxivity are indeed connected to each other. The relaxivity improves by 130% (Table 1.2).

Table 1.2 Relaxivities of T_1-weighted MRI contrast agents that respond to ROS through changes in the oxidation state of the organic ligand.

Contrast Agent	r_1(-H_2O_2) (mM^{-1} s^{-1})	r_1(+H_2O_2) (mM^{-1} s^{-1})	r_1(+H_2O_2)/r_1(-H_2O_2)	Reference
$[Mn^{II}(Hptp1)]^{2+}$	4.39	3.59[a]	0.82	[111]
$[Mn^{II}(H_2qp1)]^{2+}$	4.73	5.30	1.12	[113]
$[Mn^{II}(H_4qp2)]^{2+}$	5.46	7.17	1.31	[115]
$[Mn^{II}(H_6qc1)]^{2+}$	3.48[b]	3.46[b]	0.99	[116]
$[Mn^{II}(H_4qp4)]^{2+}$	3.16	7.35[c]	2.32	[117]

All measurements taken in pH 7.0 HEPES buffer at 25 °C with a 3T field. All of the oxidized samples were treated with 10 mM H_2O_2 and measured 30 min after the beginning of the reaction unless otherwise stated. [a]This value is per Mn(II) ion. [b]Measurements taken in pH 7.0 50 mM phosphate buffer. [c]Measurement taken 90 min after the reaction with 10 mM H_2O_2.

The major drawback to these probes is that the pre-activated sensors have high background relaxivities. Although the changes in r_1 for the pre-activated and activated forms are large enough to clearly differentiate the two forms of each of these sensors in *in vitro* samples, it would be difficult to assess *in vivo* whether an enhancement in contrast results from the activation of the probe or the accretion of the reduced form of the compound in a particular region.

1.5.2 ^{19}F MRI contrast agent sensors

Recently, there have been many efforts towards preparing sensors with ^{19}F MRI outputs, some of which are responsive to analytes.[73,77,118–121] The installation of the fluorinated groups needed to provide the MRI signal tends to complicate the syntheses of the organic components. As stated previously, having more F atoms will improve the signal-to-noise ratio, but installing too many F atoms can render the compounds insufficiently soluble in water to use for MRI analysis.[76] As of this writing, all of the redox-responsive sensors with ^{19}F MRI outputs rely on changes to the oxidation state of the metal ion to provide their spectroscopic response.

With respect to redox-responsive contrast agents that do not react with ROS, Que's group has recently synthesized a series of copper-containing probes that detect thiols.[122–124] These generally feature less highly paramagnetic metal ions that would be poorly suited for T_1-weighted ^{1}H MRI. The key design considerations are the impacts of the metal ions on T_1 and T_2 and the distance between the ^{19}F atoms and the metal. Optimal paramagnetic enhancement of the ^{19}F signal seems to occur when the F atoms are 5–7 Å away from the metal center.[75]

Chen et al. recently reported a bimodal MRI contrast agent with ^{1}H and ^{19}F outputs that consists of manganese bound to *N,N*′-bis(2-hydroxy-4-trifluoromethylbenzyl)-ethylenediamine-*N,N*′-diaceticacid (HTFBED, Figure 1.13).[95] The coordination of Mn(III) with the ligand results in an 8-fold intensification of its ^{19}F NMR signal. Coordinating Mn(II) to the ligand, conversely, essentially eliminates the ^{19}F signal. As with the manganese-containing redox-responsive MRI contrast agents reported by the Gale and Caravan groups,[84–86] the r_1 associated with the ^{1}H MRI signal decreases to 26% of its original value upon oxidation of the metal center from Mn(II) to Mn(III) (Table 1.1). A ^{19}F MRI signal, conversely, appears as the Mn(II) compound is oxidized by H_2O_2. Chen et al. used their Mn(II) complex to successfully detect pyocyanin-induced ROS production in HepG2 cells.

Yu et al. reported a series of Co(II) complexes with fluorinated derivatives of 1,4,7-triazacyclononane (TACN) that produce a strong ^{19}F MRI signal upon oxidation by H_2O_2.[125,126] The pre-activated Co(II) species are high-spin; much like high-spin Mn(II), these metal ions can shorten the T_2 relaxation time and attenuate the ^{19}F MRI signal. The reaction with H_2O_2 oxidizes the metal center to diamagnetic low-spin Co (III); this eliminates the paramagnetic relaxation enhancement, lengthens T_2, and produces a strong ^{19}F MRI signal.

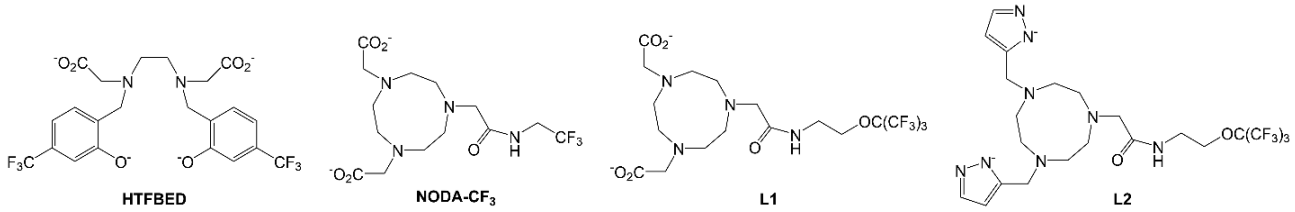

Figure 1.13 Fluorinated ligands used for the ^{19}F MRI contrast agent sensors for ROS described in references 95,125, and 126. HTFBED^{4-} = *N,N*′-bis(4-trifluoromethylphenolate)ethylenediamine-*N,N*′-diacetate; NODA-CF_3 = 4,7-bis(acetate)-1,4,7-triazacyclononane-1-*N*-(2,2,2-trifluoroethylacetamide; L1 = 2,2′-(7-(2- ((2-((1,1,1,3,3,3-hexafluoro-2-(trifluoromethyl)propan-2-yl)oxy)ethyl)amino)-2-oxoethyl)-1,4,7-triazonane-1,4-diyl)diacetate; L2 = 2-(4,7-bis((1H-pyrazol-3-yl)methyl)-1,4,7-triazonan-1-yl)-*N*-(2-((1,1,1,3,3,3-hexafluoro-2-(trifluoromethyl)propan-2-yl)oxy)ethyl)acetamide.

The TACN framework endows the Co(II) and Co(III) compounds with great measures of thermodynamic and kinetic stability.[125,126] The Co(II) complex with 1,4,7-triazacyclononanetriacetic acid is air-sensitive,[127] necessitating that the authors carefully modify the TACN ring in order to avoid O_2 reactivity (Figure 1.13).[125,126] The initially explored complex, [Co^{II}(NODA-CF_3)], reacts relatively slowly with H_2O_2, and 30 min are required for 4 equiv. of the oxidant to fully activate the sensor.[125] Upon oxidation to Co(III), the ^{19}F MRI signal intensifies over 2-fold. The T_1 and T_2 values for the Co(II) form are 18.0 and 6.6 ms, respectively; these values are different enough to flatten the ^{19}F NMR peak and weaken the MRI signal. Yu et al. surveyed a number of oxidants and found that $O_2^{\cdot-}$ and $ONOO^-$, but not ClO^- and *tert*-butyl hydroperoxide, could also trigger the response. The reactions involving the former two oxidants, however, proceeded more slowly than those with H_2O_2.

The L1 and L2 ligands (Figure 1.13) contain more F atoms and should thereby give rise to stronger ^{19}F MRI signals.[126] Despite the two ligands sharing some structural features with NODA-CF_3, the Co(II) complexes with L1 and L2 behave quite differently with respect to their ^{19}F NMR and MRI behavior in that their T_1 and T_2 values are approximately equal to each other. Consequently, strong ^{19}F MRI signals are seen for the pre-activated sensors. When the L1 and L2 complexes are oxidized by excess H_2O_2, the frequencies of the ^{19}F NMR peaks shift by almost 10 ppm. The large magnitude of the shift was attributed to the trigonal prismatic geometries of the compounds which provide greater

magnetic anisotropies than the more commonly seen octahedral coordination environments; this phenomenon has been documented for other Co(II) complexes.[128-130] Yu et al. confirmed the hypothesized anisotropy of their complexes using variable temperature magnetic susceptibility measurements.[126] The sensor can thereby ratiometrically detect ROS by using different excitation pulses to separately visualize the Co(II) and Co(III) forms of the sensor. The authors also found that the complex with L2, but not L1, could successfully detect the low steady-state levels of H_2O_2 generated from the reaction between glucose oxidase and glucose.

1.5.3 CEST-based MRI Contrast Agent Sensors

Several redox-active MRI contrast agents have been developed that rely on CEST for their response. Sherry's group, for instance, reported two Eu(III)-containing complexes that react with reductants.[131,132] The coordination compounds described in this section can respond to oxidants through changes to the oxidation states of either their metal ions or their organic ligands.

1.5.3.1 Sensors that rely on a change to the oxidation state of the metal ion

The Co(III/II) redox couple would be ideal for a ROS sensor that relies on PARACEST. Co(II) in either its high-spin or low-spin forms is paramagnetic, whereas octahedral Co(III) complexes have a strong tendency to be low-spin and diamagnetic.[108] Oxidizing a CEST-active probe containing Co(II) to a Co(III) species would be anticipated to eliminate the paramagnetically shifted resonance peaks required for PARACEST and result in an enhancement of the water signal – a turn-on response.[54] The Co(III/II) reduction potential can be tuned to enable Co(II) compounds to be oxidized by a variety of oxidants. Although this has not yet been applied towards the development of a sensor that is selective for H_2O_2 over O_2, it should be feasible.

The Morrow group prepared a Co(II)-containing sensor that loses its ability to participate in PARACEST upon its oxidation to a Co(III) complex by O_2.[133] Tsitovich et al. synthesized a high-spin Co(II) complex with the TPT ligand (Figure 1.14). Proton exchange between the pyrazole groups on

the ligand and the bulk water is proposed to enable CEST. The chemical shift of the pyrazole protons is temperature-dependent, decreasing from 149 ppm at 25 °C to a value of 140 ppm at 37 °C. At 37 °C, the optimal frequency offset is 135 ppm. The frequency offset is not impacted by pH, but the magnitude of the CEST effect is, being most prominent at pH 6.9. Upon oxidation by air, the NMR features associated with the Co(II) complex vanish, and CEST no longer occurs with the 135 ppm pre-saturation pulse. The reaction with O_2 occurs moderately quickly, with a second-order rate constant of 0.32 M^{-1} s^{-1}. The authors estimate that the Co(II)-TPT complex would have a half-life of 2.6 h in arterial blood, approximating the concentration of O_2 as 0.17 mM under these conditions. The Co(III) form of the sensor can be reduced back to Co(II) with dithionite, but the oxidation of Co(II) by H_2O_2 was not investigated.

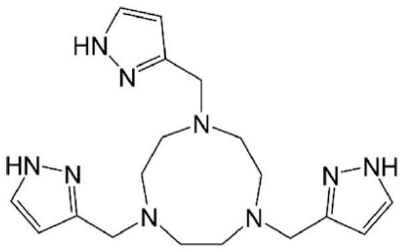

TPT

Figure 1.14 Structure of the ligand used in the CEST-based cobalt-containing sensor described in reference 133. TPT = 1,4,7-tris(pyrazol-3-ylmethyl)-1,4,7-triazacyclononane.

The Allen group has explored a series of redox-responsive MRI contrast agents that rely on Eu(III/II) redox couples.[101–105] Eu(II) is isoelectronic to Gd(III) and likewise can endow coordination complexes with high r_1 values that are suitable for T_1-weighted MRI. Although it is still relatively paramagnetic, Eu(III) has a slow water exchange rate and does not significantly impact T_1; instead, this ion greatly shifts the NMR signals of nearby protons, including those from bound ligands that can exchange with those from the bulk water. Eu(III) is therefore highly suitable for PARACEST. The use of a fluorinated ligand (Figure 1.15) can also enable redox-responsive ^{19}F MRI. Eu(III) complexes

with such ligands can give rise to strong ^{19}F MRI signals whereas Eu(II) species are ^{19}F MRI silent.[105] The ability to facilely support multimodal imaging makes the Eu(III/II) couple highly attractive for redox-responsive probes. The key challenge with these sensors is that the Eu(II) oxidation state tends to be highly unstable. Even when they can be sufficiently stabilized under anaerobic environments, most Eu(II) complexes react quickly with air[101–105] and only persist under hypoxic conditions, such as the necrotic interiors of tumors.[103]

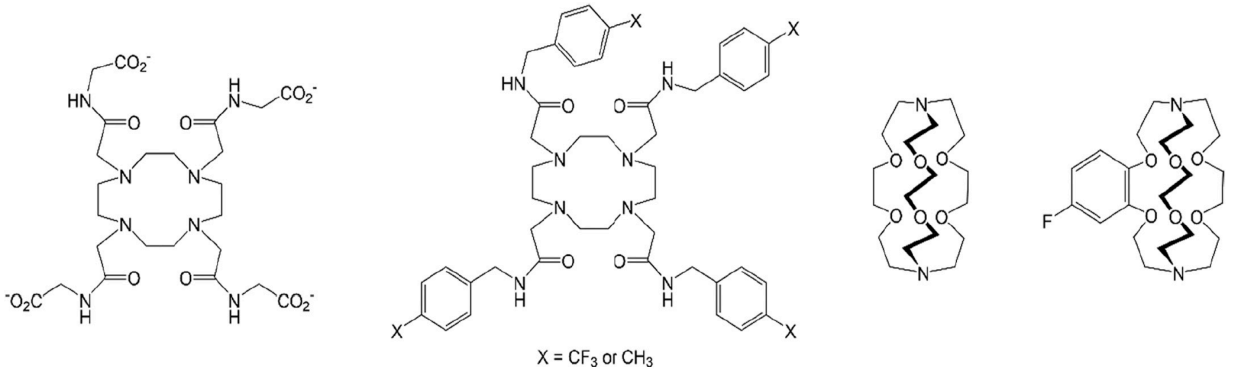

Figure 1.15 Ligands used in the preparation of the air-responsive Eu(II) complexes described in references 101–105.

Funk et al. prepared a Eu(II) complex with DOTA(gly)$_4^{4-}$ that oxidizes to a Eu(III) species upon reaction with H_2O_2 over the course of 1 h (Figure 1.16).[134] Most Eu(II) complexes are highly reactive,[108] and the amide groups of the DOTA(gly)$_4^{4-}$ ligand were installed to improve the redox stability of the Eu(II) form. Indeed, the Eu(III/II) reduction potential was measured to be -226 mV *vs.* Ag/AgCl as opposed to -585 mV for the Eu(II) aqua ion. The amide groups also provide protons that can exchange with the bulk water; the frequency offset for the ligand protons is +54 ppm. The Eu(II) complex has a r_1 of 3.2 mM^{-1} s^{-1} (1T, pH 7.0). During its oxidation by H_2O_2, the T_1-weighted signal from the Eu(II) fades while the CEST-based effect from the Eu(III) manifests. The maximum CEST effect for a 10 mM sample of the Eu(III) complex results in a 27% decrease of the water signal. The

Eu(II) complex displays a similar, but slower, response to O_2. Eliminating the side reactivity with O_2 remains a significant barrier in using Eu(III/II) couples as the basis for H_2O_2-selective sensors.

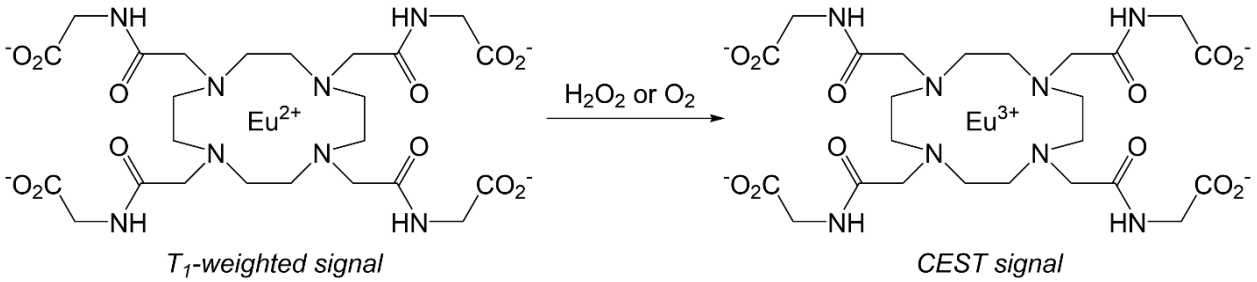

Figure 1.16 The europium-containing sensor that responds to oxidation with changes to both its T_1-weighted and CEST signals described in reference 134.

Du et al. reported a binuclear Fe(II) complex with a tetra(carboxamide) ligand (Figure 1.17) and etidronate.[135] The metal ions in $[Fe_2(L)(etidronate)]^-$ can be oxidized, yielding either Fe(II)Fe(III) or $Fe(III)_2$ species. The carboxamide groups on the polydentate ligand can exchange protons with water, allowing the $Fe(II)_2$ and Fe(II)Fe(III) complexes to engage in CEST. At 37 °C and pH 7.4, the diferrous complex has CEST peaks at +29, +40, and +68 ppm; excitation at these frequencies reduces the water signal by approximately 9%, 10%, and 5%, respectively. The Fe(II)Fe(III) complex is more effective as a PARACEST reagent, and the water signal decreases in intensity by approximately 20% when peaks at either +74 or +83 ppm are irradiated. Selective irradiation can therefore distinguish the $Fe(II)_2$ and Fe(II)Fe(III) species. As with other PARACEST agents, the intensities and the frequency offsets of the CEST peaks are influenced by pH and temperature. With respect to the impact of temperature, a 2 °C change was found to shift the 83 ppm CEST peak of the Fe(II)Fe(III) complex by 1 ppm.

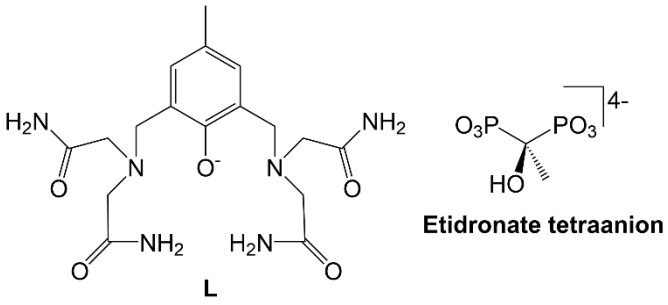

Figure 1.17 Ligands for the diiron complex described in reference 135.

Oxidation of 4 mM of $[Fe^{II}_2(L)(etidronate)]^-$ by a substoichiometric amount (1 mM) of KO_2 in pH 7.4 buffer partly oxidizes the complex to the Fe(II)Fe(III) species. The reaction occurs quickly, reaching equilibrium in under 10 min. With proper ligand modifications, such a diiron system could be tuned towards the selective detection of H_2O_2.

1.5.3.2 Sensors that rely on a change to the oxidation state of the organic ligand

Thus far, there are no known examples of CEST-based sensors that detect H_2O_2 through changes to their organic portions. Nonetheless, this is one avenue that could be explored further as the following two cases demonstrate.

Liu et al. prepared a Yb(III) complex with the redox-active macrocyclic ligand DO3A-oAA (Figure 1.18).[136] The compound exhibits two CEST peaks at -11 ppm and +8 ppm that are attributed to the amide and amine groups, respectively. The CEST effect from the amine protons can decrease the water signal by as much as 30%, with the maximum impact observed at pH 5. The amide protons can decrease the water intensity by as much as 20%, with the optimal effect observed at pH 7. Upon reaction with a mixture of NO and O_2, the aniline groups of two equiv. of the Yb(III) complex irreversibly combine into a triazene bridge (Figure 1.18). After the ligand oxidation, neither the -11 ppm nor the +8 ppm CEST effects are observed. The loss of the amine protons accounts for the elimination of the +8 ppm signal, but the disappearance of the amide-based signal was unanticipated. The authors speculate that the ligand oxidation triggers a conformational change that moves the amides

far enough away from the Yb(III) ions to eliminate the paramagnetic shift needed for efficient PARACEST.

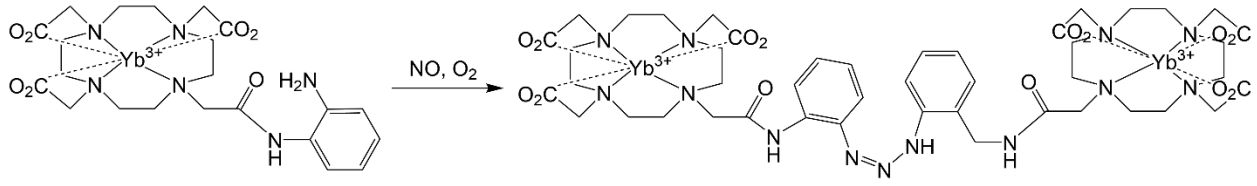

Figure 1.18 Yb(III)-containing sensor for NO/O_2 mixtures from reference 136. DO3A-oAA = 1,4,7,10-tetraazacyclododecane-1,4,7-triacetic acid)-orthoaminoanilide.

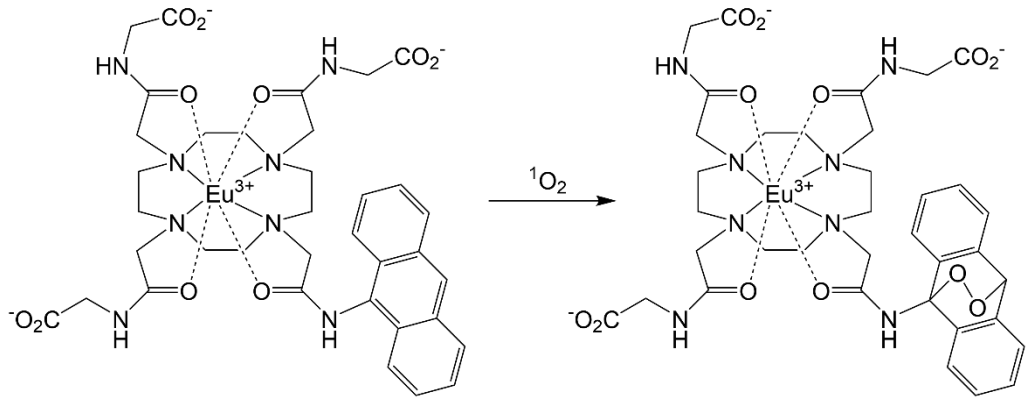

Figure 1.19 Eu(III)-containing sensor for singlet oxygen described in reference 137.

Song et al. synthesized a Eu(III)-containing sensor with a redox-active anthracene that exhibits a response that is selective for singlet oxygen (Figure 1.19).[137] In the reduced form, the Eu(III) complex exhibits a CEST signal at +50 ppm that attenuates the water intensity by approximately 8%. Reaction with chemically generated $^1O_2$ converts the anthracene into a peroxide and shifts the frequency of the nearby amide proton to +53 ppm. The CEST effect for the oxidized complex is stronger, with approximately a 12% decrease in the intensity of the water signal. Song et al. investigated other ROS but did not observe any change to the CEST properties with either $ONOO^-$, H_2O_2, OH, or $O_2^{\cdot -}$. The authors were able to use the ratio of the CEST effects at +54 and +47 ppm to monitor the production of singlet oxygen in phantom samples and cell lysates from HeLa cells.

1.6 Conclusions and Outlook

Small molecule MRI contrast agent sensors for ROS, such as H_2O_2, continue to be developed at a rapid pace. Recent progress in this field has benefitted from the exploration of new modes of MRI, specifically ^{19}F and CEST. The sensors described here are incredibly diverse with respect to the metal ions and ligand structures employed. Some of the organic components include redox-active functional groups that can be oxidized to either couple the sensor to another molecule, effect changes in the coordination sphere of the metal ion, or alter the resonance frequencies of protons participating in CEST.

This said, there remain several challenges that need to be overcome before any of these probes can enter clinical use and possibly diagnose health conditions from patterns of abnormal oxidative activity. Some of these challenges are general and apply to all potential sensors. How toxic are the probes in both their pre-activated and activated states? Where do they accumulate in the body and how quickly do they clear these areas? Can they encounter enough H_2O_2, react with it quickly enough, and provide a sufficiently large change in the signal to clearly differentiate a region experiencing oxidative stress? The timescale of the reaction is particularly important if the probes are freely circulating through the body.

These general challenges may be more acute for certain classes of probes. Coordination complexes with redox-active metal ions that can participate in Fenton-like chemistry, such as manganese and iron, would be anticipated to be more toxic than those with redox-inactive metals. Complexes with weak stability constants would have a stronger tendency to release free metal ions, which would also worsen the toxicity. The probes that are capable of tethering to biomolecules could potentially target tissues of interest but may clear the body less avidly. Those that oligomerize risk becoming insoluble. Most of the complexes described here are not likely to be lipophilic enough to enter cells; indeed, this is perhaps for the better since high lipophilicity would be expected to impede

the clearance of the contrast agent from the body. MRI contrast agent sensors will instead likely react with the H_2O_2 that diffuses into extracellular spaces. Fortunately, the successful use of some of these sensors in biological imaging suggests that enough ROS do make it to these spaces to enable MRI to detect aberrant oxidative activity.

Other challenges are specific to individual spectroscopic techniques. With T_1-weighted MRI, it is difficult to differentiate sensor activation from an accumulation of the lower-relaxivity form of the probe. These probes can be used to detect oxidative stress, but only after their performance has been carefully and systematically calibrated in populations of physiologically healthy and unhealthy tissues. The same issue applies to arguably a lesser extent with ^{19}F MRI-based sensors, but with these, a much higher loading of the contrast agent is generally needed, exacerbating concerns about toxicity. Given the solubility difficulties that arise upon further fluorinating small molecules, the need for a high dose of a ^{19}F MRI contrast agent may be a rarely surmounted obstacle. With CEST, the more intense irradiation needed to acquire an unambiguous signal represents a substantial technical challenge, but it may be overcome through making changes to how the irradiation is provided. With respect to using CEST as the basis for redox-responsive MRI, the temperature- and pH-dependencies of the CEST effect will further complicate calibration and the determination of what an observed change in the signal may actually mean.

The necessary calibration may be much simpler for multimodal sensors. With multiple spectroscopic signatures that can separately visualize the pre-activated and activated states, one can readily assess sensor distribution and the extent to which the probes have been activated. Ultimately, such probes may have a slightly easier path to being applied fruitfully in the clinic.

References

1. Stefanova, N.A.; Muraleva, N.A.; Skulachev, V.P.; Kolosova, N.G. *J. Alzheimers Dis.* **2014**, 38, 681-694.

2. Skulachev, V.P.; *J. Alzheimers Dis.* **2012**, 28, 283-289.

3. Lushchak, V.I. *Chem. Biol. Interact.* **2014**, 224, 164-175.

4. Abreu, I.A.; Cabelli, D.E. *Biochim. Biophys. Acta* **2010**, 1804, 263-274.

5. Wieghardt, K. *Angew. Chem. Int. Ed.* **1989**, 28, 1153-1172.

6. Mukhopadhyay, S.; Mandal, S.K.; Bhaduri, S.; Armstrong, W.H. *Chem. Rev.* **2004**, 104, 3981-4026.

7. Holm, R.H.; Kennepohl, P.; Solomon, E.I. *Chem. Rev.* **1996**, 96, 2239-2314.

8. van Rossum, G.S.A.T.; Drummen, G.P.C.; Verkleij, A.J.; Post, J.A.; Boonstra, J. *Biochim. Biophys. Acta* **2004**, 1636, 183-195.

9. Vaarmann, A.; Gandhi, S.; Abramov, A.Y. *J. Biol. Chem.* **2010**, 285, 25018-25023.

10. Sundaresan, M.; Yu, Z.-X.; Ferrans, V.J.; Irani, K.; Finkel, T. *Science* **1995**, 270, 296-299.

11. Woo, H.A.; Yim, S.H.; Shin, D.H.; Kang, D.; Yu, D.-Y.; Rhee, S.G. *Cell* **2010**, 140, 517-528.

12. Angelova, P.R.; Müller, W.S.; *Eur. J. Neurosci.* **2009**, 29, 1943-1950.

13. Angelova, P.; Müller, W. *Eur. J. Neurosci.* **2006**, 23, 2375-2384.

14. Hool, L.C.; Corry, B.; *Antioxid. Redox Signal.* **2007**, 9, 409-435.

15. Forman, H.J.; Fukuto, J.M.; Torres, M. *Am. J. Phys. Cell Phys.* **2004**, 287, C246-C256.

16. Forman, H.J.; Maiorino, M.; Ursini, F.*; Biochemistry* **2010**, 49, 835-842.

17. Lyle, A.N.; Griendling, K.K. *Physiology* **2006**, 21 269-280.

18. Breckwoldt, M.O.; Chen, J.W.; Stangenberg, L.; Aikawa, E.; Rodriguez, E.; Qiu, S.; Moskowitz, M. A.; Weissleder, R. *Proc. Nat. Acad. Sci., U. S. A.* **2008**, 105, 18584-18589.

19. Kinnula, V.L. *Curr. Drug Targets. Inflamm. Allergy* **2005**, 4, 465-470.

20. Ahmed, M.I.; Gladden, J.D.; Litovsky, S.H.; Lloyd, S.G.; Gupta, H.; Inusah, S.; Denney Jr., P.; Powell, T.; McGiffin, D.C.; Dell'Italia, L.J. *J. Am. Coll. Cardiol.* **2010**, 55, 671-679.

21. Gladden, J.D.; Ahmed, M.I.; Litovsky, S.H.; Schiros, C.G.; Lloyd, S.G.; Gupta, H.; Denney Jr., T. S.; Darley-Usmar, V.; McGiffin, D.C.; Dell'Italia, L.J. *Am. J. Med. Sci.* **2011**, 342, 114-119.

22. Gaddam, K.; Corros, C.; Pimenta, E.; Ahmed, M.; Denney, T.; Aban, I.; Inusah, S.; Gupta, H.; Lloyd, S.G.; Oparil, S.; Husain, A.; Dell'Italia, L.J.; Calhoun, D.A. *Hypertension* **2010**, 55, 1137-1142.

23. Viappiani, S.; Schulz, R. *Am. J. Physiol. Heart Circ. Physiol*. **2006**, 290, H2167-H2168.

24. Fearon, I.M.; Faux, S.P. *J. Mol. Cell. Cardiol*. **2009**, 47, 372-381.

25. van Horssen, J.; Witte, M.E.; Schreibelt, G.; de Vries, H.E. *Biochim. Biophys. Acta* **2011,** 1812, 141-150.

26. Wang, J.-Y.; Wen, L.-L.; Huang, Y.-N.; Chen, Y.-T.; Ku, M.-C. *Curr. Pharm. Des*. **2006**, 12, 3521- 3533.

27. Tretter, L.; Sipos, I.; Adam-Vizi, V.; *Neurochem. Res*. **2004**, 29, 569-577.

28. Mosley, R.L.; Benner, E.J.; Kadiu, I.; Thomas, M.; Boska, M.D.; Hasan, K.; Laurie, C.; Gendelman, H.E. *Clin. Neurosci. Res.* **2006**, 6, 261-281.

29. Aksenov, M.Y.; Aksenova, M.V.; Butterfield, D.A.; Geddes, J.W.; Markesbery, W.R; *Neuroscience* **2001**, 103, 373-383.

30. Riley, D.P.; Rivers, W.J.; Weiss, R.H.; *Anal. Biochem*. **1991**, 196, 344-349.

31. Fridovich, I.; *J. Biol. Chem.* **1997**, 272, 18515-18517.

32. Giorgio, M.; Trinei, M.; Migliaccio, E.; Pelicci, P.G. *Nat. Rev. Mol. Cell Biol.* **2007**, 8, 722-728.

33. Haber, F.; Weiss, J.; Naturwissenschaften **1932**, 20, 948-950.

34. Fenton, H.J.H. *J. Chem. Soc. Trans*. **1894**, 65, 899-910.

35. Aime, S.; Botta, M.; Gianolio, E.; Terreno, E. *Angew. Chem., Int. Ed. Engl.* **2000**, 39, 747-750.

36. Rojas-Quijano, F.A.; Benyó, E.T.; Tircsó, G.; Kálmán, F.K.; Baranyai, Z.; Aime. S.; Sherry, A.D.; Kovács, Z. *Chemistry* **2009**, 15, 13188-200.

37. Major, J.L.; Meade, T.J. *Acc. Chem. Res.* **2009**, 42, 893-903.

38. Lee, J.; Zylka, M.J.; Anderson, D.J.; Burdette, J.E.; Woodruff, T.K.; Meade, T.J. *J. Am. Chem. Soc.* **2005**, 127, 13164-13166.

39. Major, J.L.; Parigi, G.; Luchinat, C.; Meade, T.J. *Proc. Natl. Acad. Sci. U.S.A.* **2007**, 104, 13881-13886.

40. Zhang, X.A.; Lovejoy, K.S.; Jasanoff, A.; Lippard, S. *J. Proc. Natl. Acad. Sci. U. S. A.* **2007**, 104, 10780-10785.

41. Kawabata, E.; Kikuchi, K.; Urano, Y.; Kojima, H.; Odani, A.; Nagano, T. *J. Am. Chem. Soc.* **2005**, 127, 818-819.

42. Hirano, T.; Kikuchi, K.; Urano, Y.; Higuchi, T.; Nagano, T. *J. Am. Chem. Soc.* **2000**, 122, 12399-12400.

43. Maruyama, S.; Kikuchi, K.; Hirano, T.; Urano, Y.; Nagano, T. *J. Am. Chem. Soc*. **2002**, 124, 10650-10651.

44. Divya, K. P.; Sreejith, S.; Ashokkumar, P.; Yuzhan, K.; Peng, Q.; Maji, S. K.; Tong, Y.; Yu, H.; Zhao, Y.; Ramamurthy, P.; Ajayaghosh, A. *Chem. Sci*. **2014**, 5, 3469-3474.

45. Torrado, A.; Walkup, G. K.; Imperiali, B. *J. Am. Chem. Soc.* **1998**, 120, 609-610.

46. Zhang, J.; Campbell, R. E.; Ting, A.Y.; Tsien, R.Y. *Nat. Rev. Mol. Cell Biol.* **2002**, 3, 906-918.

47. Griffin, B.A.; Adams, S.R.; Tsien, R.Y. *Science* **1998**, 281, 269-272.

48. De Leon-Rodriguez, L. M.; Lubag, A. J. M.; Malloy, C. R.; Martinez, G. V.; Gillies, R. J.; Sherry, A. D. *Acc. Chem. Res.* **2009**, 42, 948-957.

49. Wahsner, J.; Gale, E.M.; Rodríguez-Rodríguez, A.; Caravan, P. *Chem. Rev.* **2019**, 119, 957-1057.

50. Pinto, S.M.; Tome, V.; Calvete, M. J. F.; Castro, M. M. C. A.; Toth, E.; Geraldes, C. F. G. C. *Coord. Chem. Rev.* **2019**, 390, 1-31.

51. Do, Q. N.; Ratnakar, J. S.; Kovács, Z.; Sherry, A.D. *Chem. Med. Chem.* **2014**, 9, 1116-1129.

52. Zhang, S.; Merritt, M.; Woessner, D. E.; Lenkinski, R. E.; Sherry, A. D. *Acc. Chem. Res.* **2003**, 36, 783-790.

53. Tsitovich, P. B.; Burns, P. J.; McKay, A. M.; Morrow, J. R. J. *Inorg. Biochem*. **2014**, 133, 143-154.

54. Renfrew, A. K.; O'Neill, E. S.; Hambley, T. W.; New, E. J. *Coord. Chem. Rev*. **2018**, 375, 221-233.

55. Caravan, P.; Ellison, J. J.; McMurry, T. J.; Lauffer, R. B. *Chem Rev.* **1999**, 99, 2293-2352.

56. Toth, E.; Helm, L.; Merbach, A. E. *Top. Curr. Chem.* **2002**, 221, 61-101

57. Draho˘s, B.; Luke˘s, I.; T´oth, ´E. *Eur. J. Inorg. Chem*. **2012**, 2012, 1975-1986.

58. Gale, E. M.; Atanasova, I. P.; Blasi, F.; Ay, I.; Caravan, P. *J. Am. Chem. Soc.* **2015**, 137, 15548-15557.

59. Troughton, J.S.; Greenfield, M. T.; Greenwood, J. M.; Dumas, S.; Wiethoff, A. J.; Wang, J.; Spiller, M.; McCurry, T. J.; Caravan, P. *Inorg. Chem*. **2004**, 43, 6313-6323.

61. Rocklage, S. M.; Cacheris, W. P.; Quay S. C.; Hahn, F. E.; Raymond K. N. *Inorg. Chem*. **1989**, 28, 477-485.

62. Aime, S.; Baroni, S.; Delli Castelli, D.; Brucher, E.; Fabian, I.; Serra, S. C.; Fringuello Mingo, A.; Napolitano, R.; Lattuada, L.; Tedoldi, F.; Baranyai, Z. *Inorg. Chem.* **2018**, 57, 5567-5574.

63. Duimstra, J. A.; Femia, F. J.; Meade, T. J. *J. Am. Chem. Soc.* **2005**, 127, 12847-12855.

64. Schwert, D. D.; Davies, J. A.; Richardson, N. *Top. Curr. Chem.* **2002**, 221, 165-199

65. Snyder, E. M.; Asik, D.; Abozeid, S. M.; Burgio, A.; Bateman, G.; Turowski, S. G.; Spernyak, J. A.; Morrow, J. R., *Angew. Chem. Int. Ed.* **2020,** 59, 2414-2419.

66. Hoener, B. A.; Engelstad, B. L.; Ramos, E. C.; Macapinlac, H. A.; Price, D. C.; Johnson, T. R.; White, D. L. **1991**, 1, 357-362.

67. Regueiro-Figueroa, M.; Rolla, G.A.; Esteban-Gómez, D.; de Blas, A.; Rodríguez-Blas, T.; Botta, M.; Platas-Iglesias, C. *Chem. Eur. J.* **2014**, 20,17300-17305.

68. Jacques, V.; Dumas, S.; Sun, W. C.; Troughton, J. S.; Greenfield, M.T.; Caravan, P. *Invest. Radiol.* **2010**, 45, 613-624.

69. Zhang, Q.; Gorden, J. D.; Beyers, R. J.; Goldsmith, C. R. *Inorg Chem.* **2011**, 50, 9365-9373.

70. Gupta, A.; Caravan, P.; Price, W. S. Platas-Iglesias, C.; Gale, E. M. *Inorg Chem*. **2020**, 59, 6648-6678.

71. Chen, J. W.; Pham, W.; Weissleder, R.; Bogdanov, A. *Jr. Magn. Reson. Med.* **2004**, 52, 1021-1028.

72. Querol, M.; Chen, J.W.; Weissleder, R.; Bogdanov, A. Jr. *Org Lett.* **2005**, 7,1719-1722.

73. Xie, D.; Yu. M.; Kadakia, R. T.; Que, E.L. *Acc. Chem. Res.* **2020**, 53, 2-10

74. Tirotta, I.; Dichiarante, V.; Pigliacelli, C.; Cavallo, G.; Terraneo, G.; Bombelli, F. B.; Metrangolo, P.; Resnati, G. *Chem. Rev.* **2015**, 115, 1106-1129.

75. Peterson, K.L.; Srivastava, K.; Pierre, V.C. *Front Chem.* **2018**, 6, 160.

76. Díaz-L´opez, R.; Tsapis, N.; Fattal, E.; *Pharm. Res.* **2010**, 27, 1-16.

77. Sarkar, A.; Biton, I. E.; Neeman, M.; Datta, A. *Inorg. Chem. Commun.* **2017**, 78, 21-24.

78. van Zijl, P. C.; Yadav, N. N.; *Magn. Reson. Med*. **2011**, 65, 927-948.

79. Ward, K. M.; Aletras, A. H.; Balaban, R. S. *J. Magn. Reson.* **2000**, 143, 79-87.

80. Wu, B.; Warnock, G.; Zaiss, M.; Lin, C.; Chen, M.; Zhou, Z.; Mu, L.; Nanz, D.; Tuura, R.; Delso, G. *EJNMMI Phys.* **2016**, 3, 19.

81. Bryant, L.H.; Hodges, M.W.; Bryant, R.G.; *Inorg. Chem.* **1999**, 38, 1002-1005.

82. Hernandez, G.; Bryant, R. G. *Bioconjug. Chem.* **1991**, 2, 394-397.

83. Pinto, S. M. A.; Calvete M.J.F.; Ghica, M. E.; Soler, S.; Gallardo, I.; Pallier, A.; Laranjo, M.B.; Cardoso, A.M.S.; Castro, M.M.C.A.; Brett, C.M.A.; Pereira, M.M.; T´oth,´E.; Geraldes, C. F. G. C.; *Dalton Trans.* **2019**, 48, 3249-3262.

84. Loving, G.S.; Mukherjee, S.; Caravan, P. *J. Am. Chem. Soc.* **2013**, 135, 4620-4623.

85. Gale, E. M.; Mukherjee, S.; Liu, C.; Loving, G. S.; Caravan, P. *Inorg. Chem.* **2014**, 53, 10748-10761.

86. Gale, E. M.; Jones, C.M.; Ramsay, I.; Farrar, C.T.; Caravan, P. *J. Am. Chem. Soc*. **2016**, 138, 15861-15864.

87. Wang, H.; Jordan, V. C.; Ramsay, I. A.; Sojoodi, M.; Fuchs, B.C.; Tanabe, K. K.; Caravan, P.; Gale, E. *J. Am. Chem. Soc.* **2019**, 141, 5916-5925.

88. Gale, E. M.; Zhu, J.; Caravan, P. *J. Am. Chem. Soc.* **2013**, 135, 18600-18608.

89. Oakes, J.; Smith, E. G.; *J. Chem. Soc., Faraday Trans. 2* **1981**, 77, 299-308.

90. Richards, S.; Pedersen, B.; Silverton, J. V.; Hoard, J. L. *Inorg. Chem.* **1964**, 3, 27-33.

91. Zetter, M. S.; Grant, M. W.; Wood, E. J.; Dodgen, H. W.; Hunt, J. P. *Inorg. Chem.* **1972**, 11, 2701-2706.

92. Frost, A.E.; Freedman, H. H.; Westerback, S. J.; Martell, A. E. *J. Am. Chem. Soc.* **1958**, 80, 530-536.

93. Banerjee, R. *J. Biol. Chem.* **2012**, 287, 4397-4402.

94. Martell, A.E. Critical Stability Constants, Plenum Press, New York, NY, **1974**.

95. Chen, H.; Tang, X.; Gong, X.; Chen, D.; Li, A.; Sun, C.; Lin, H.; Gao, J. *Chem. Commun*. **2020**, 56, 4106-4109.

96. Gore, J. C.; Kang, Y. S. *Phys. Med. Biol.* **1984**, 29, 1189-1197.

97. Ding, S. -P.; Li, J. -C.; Jin, C. *World J. Gastroenterol.* **2003**, 9, 584-589.

98. O'Neill, E. S.; Kolanowski, J. L.; Yin, G. H.; Broadhouse, K. M.; Grieve, S. M.; Renfrew, A. K.; Bonnitcha, P. D.; New, E. J. *RSC Adv.* **2016**, 6, 30021-30027.

99. O'Neill, E. S.; Kaur, A.; Bishop, D. P.; Shishmarev, D.; Kuchel, P. W.; Grieve, S. M.; Figtree, G. A.; Renfrew, A. K.; Bonnitcha, P. D.; New, E. J.; *Inorg. Chem.* **2017**, 56, 9860-9868.

100. Caravan, P.; T´oth, ´E.; Rockenbauer, A.; Merbach, A. E. *J. Am. Chem. Soc.* **1999**, 121, 10403-10409.

101. Ekanger, L. A.; Mills, D. R.; Ali, M. M.; Polin, L. A.; Shen, Y.; Haacke, E. M.; Allen, M. J. *Inorg. Chem.* **2016**, 55, 9981-9988.

102. Ekanger, L. A.; Ali, M. M.; Allen, M. J. *Chem. Commun.* **2014**, 50, 14835-14838.

103. Ekanger, L. A.; Polin, L. A.; Shen, Y.; Haacke, E. M.; Martin, P. D.; Allen, M. J. *Angew. Chem. Int. Ed.* **2015**, 54, 14398-14401.

104. Basal, L. A.; Yan, Y.; Shen, Y.; Haacke, E. M.; Mehrmohammadi, M.; Allen, M. J. *ACS Omega* **2017**, 2, 800-805.

105. Basal, L. A.; Bailey, M. D.; Romero, J.; Ali, M. M.; Kurenbekova, L.; Yustein, J.; Pautler, R.G.; Allen, M. J. *Chem. Sci.* **2017**, 8 8345-8350.

106. Rodríguez, E.; Nilges, M.; Weissleder, R.; Chen, J. W. *J. Am. Chem. Soc.* **2010**, 132, 168-177.

107. Bogdanov, A.; Matuszewski, L.; Bremer, C.; Petrovsky, A.; Weissleder, R.; *Mol. Imaging* **2002**, 1, 16-23.

108. Cotton, F.A.; G. Wilkinson, Advanced Inorganic Chemistry, 5 ed., John Wiley & Sons, New York, **1988**.

109. Tu, C.; Nagao, R.; Louie, A. Y. *Angew. Chem. Int. Ed.* **2009**, 48, 6547-6551.

110. Harris, M.; Kolanowski, J. L.; O'Neill, E. S.; Henoumont, C.; Laurent, S.; ParacVogt, T. N.; New, E. J. *Chem. Commun*. **2018**, 54,12986-12989.

111. Yu, M.; Beyers, R. J.; Gorden, J. D.; Cross, J. N.; Goldsmith, C. R. *Inorg. Chem.* **2012**, 51, 9153-9155.

112. Kenkel, I.; Franke, A.; Dürr, M.; Zahl, A.; Dücker-Benfer, C.; Langer, J.; Filipovi´c, M. R.; Yu, M.; Puchta, R.; Fiedler, S. R.; Shores, M. P.; Goldsmith, C. R.; Ivanovi´c-Burmazovi´c, I. *J. Am. Chem. Soc.* **2017**, 139, 1472-1484.

113. Yu, M.; Ambrose, S. L.; Whaley, Z. L.; Fan, S.; Gorden, J. D.; Beyers, R. J.; Schwartz, D. D.; Goldsmith, C. R. *J. Am. Chem. Soc*. **2014**, 136, 12836-12839.

114. Senft, L.; Moore, J. L.; Franke, A.; Fisher, K. R.; Scheitler, A.; Zahl, A.; Puchta, R.; Fehn, D.; Ison, S.; Sader, S.; Ivanović-Burmazović, I.; Goldsmith, C. R. *Chem. Sci*. **2021**, 12, 10483-10500.

115. Yu, M.; Ward, M. B.; Franke, A.; Ambrose, S. L.; Whaley, Z. L.; Bradford, T. M.; Gorden, J. D.; Beyers, R. J.; Cattley, R. C.; Ivanovi´c-Burmazovi´c, I.; Schwartz, D. D.; Goldsmith, C. R. *Inorg. Chem.* **2017**, 56, 2812-2826.

116. Hutchinson, T. E.; Bashir, A.; Yu, M.; Beyers, R. J.; Goldsmith, C. R. *Inorg. Chim. Acta* **2019,** 496, 119045.

117. Karbalaei, S.; Knecht, E.; Franke, Zahl, A.; Saunders, A. C.; Pokkuluri, P. R.; Beyers, R. J.; Ivanovi´c-Burmazovi´c, I.; Goldsmith, C. R. *Inorg. Chem.* **2021**, 60, 8368-8379.

118. Srivastava, K.; Weitz, E.A.; Peterson, K. L.; Marja´nska, M.; Pierre, V. C. *Inorg. Chem.* **2017**, 56, 1546-1557.

119. Srivastava, K.; Ferrauto, G.; Young, V. G.; Aime, S.; Pierre, V. C. *Inorg. Chem.* **2017**, 56, 12206-12213.

120. Fox, M. S.; Gaudet, J. M.; Foster, P. J. *Magn. Reson. Insights* **2016**, 8, 53-67.

121. Blahut, J., Benda, L., Kotek, J., Pintacuda, G., Hermann, P. *Inorg. Chem*. **2020,** 59, 10071-10082.

122. Kadakia, R. T.; Xie, D.; Guo, H.; Bouley, B.; Yu, M.; Que, E. L. *Dalton Trans.* **2020**, 49, 16419-16424.

123. Kadakia, R. T.; Xie, D.; Martinez, D.; Yu, M.; Que, E. L. *Chem. Commun.* **2019**, 55, 8860-8863.

124. Enriquez, J. S.; Yu, M.; Bouley, B. S.; Xie, D.; Que, E. L. *Dalton Trans.* **2018**, 47, 15024-15030.

125. Yu, M.; Xie, D.; Phan, K. P.; Enriquez, J. S.; Luci, J. J.; Que, E. L. *Chem. Commun.* **2016**, 52, 13885-13888.

126. Yu, M.; Bouley, B. S.; Xie, D.; Enriquez, J. S.; Que, E.L. *J. Am. Chem. Soc*. **2018**, 140, 10546-10552.

127. Wieghardt, K.; Bossek, U.; Chaudhuri, P.; Herrmann, W.; Menke, B. C.; Weiss, J. *Inorg. Chem.* **1982**, 21, 4308-4314.

128. Novikov, V. V.; Pavlov, A. A.; Nelyubina, Y. V.; Boulon, M. -E.; Varzatskii, O. A.; Voloshin, Y. Z.; Winpenny, R. E. P. *J. Am. Chem. Soc*. **2015**, 137, 9792-9795.

129. Gomez-Coca, S.; Cremades, E.; Aliaga-Alcalde, N.; Ruiz, E. *J. Am. Chem. Soc.* **2013**, 135, 7010-7018.

130. Tsitovich, P. B.; Cox, J. M.; Benedict, J. B.; Morrow, J. R. *Inorg. Chem.* **2016**, 55, 700-716.

131. Ratnakar, S. J.; Viswanathan, S.; Kovacs, Z.; Jindal, A. K.; Green, K. N.; Sherry, A. D. *J. Am. Chem. Soc.* **2012**, 134, 5798-5800.

132. Ratnakar, S. J.; Soesbe, T. C.; Lumata, L. L.; Do, Q. N.; Viswanathan, S.; Lin, C. -Y.; Sherry, A. D.; Kovacs, Z. *J. Am. Chem. Soc.* **2013**, 135, 14904-14907.

133. Tsitovich, P. B.; Spernyak, J. A.; Morrow, J. R. *Angew. Chem. Int. Ed.* **2013**, 52, 13997-14000.

134. Funk, A.M.; Clavijo Jordan, V.; Sherry, A. D.; Ratnakar, S. J.; Kovacs, Z. *Angew. Chem. Int. Ed.* **2016**, 55, 5024-5027.

135. Du, K.; Waters, E. A.; Harris, T. D. *Chem. Sci.* **2017**, 8, 4424-4430.

136. Liu, G.; Li, Y.; Pagel, M. D. *Magn. Reson. Med.* **2007**, 58, 1249-1256.

137. Song, B.; Wu, Y.; Yu, M.; Zhao, P.; Zhou, C.; Kiefer, G. E.; Sherry, A. D. *Dalton Trans.* **2013**, 42, 8066-8069.

Chapter 2

A Macrocyclic Ligand Framework That Improves Both the Stability and T_1-Weighted MRI Response of Quinol-Containing H_2O_2 Sensors[*]

[*] This chapter is a modified version of a published paper: Sana Karbalaei, Erik Knecht, Alicja Franke, Achim Zahl, Alexander C. Saunders, P. Raj Pokkuluri, Ronald J. Beyers, Ivana Ivanović-Burmazović, and Christian R. Goldsmith, *Inorganic Chemistry* **2021**, 60, 8368−8379. Reprint with permission.

2.1 Introduction

The over-production of reactive oxygen species (ROS), such as H_2O_2 and O_2^-, has been implicated in a wide array of pathologies, including a host of neurological and cardiovascular health conditions.[1-5] Given the possible roles of ROS in disease, our research group has strived to develop molecular probes that can be used to non-invasively monitor ROS concentrations in physiological environments. Such sensors could potentially distinguish pathologies with similar clinical symptoms and better inform preventative and ameliorative therapies. To this end, our laboratory has reported a series of complexes that respond to H_2O_2 with changes in their T_1-weighted relaxivity (r_1).[6-9]

Recent sensors from our laboratory have consisted of Mn(II) ions complexed to quinol-containing polydentate ligands (Scheme 2.1).[7–9] Positive r_1 responses to H_2O_2 are observed with N_4O_2 or N_5O coordination spheres, where the nitrogen donors come from either neutral pyridine or amine groups.[7-8] With a weakly anionic coordination sphere, the Mn(III/II) reduction potential is high enough to discourage oxidation of the metal to the less paramagnetic 3+ oxidation state. Terminal oxidants, such as H_2O_2, instead preferentially oxidize the ligand, differentiating our sensors from redox-responsive magnetic resonance imaging (MRI) contrast agents reported by Gale, Caravan, and others.[10–12] Oxidation of the quinol portions of the ligands to *para*-quinones is accompanied by an increase in r_1. Water molecules are proposed to displace *para*-quinones from the metal center, enhancing r_1 through better aquation of Mn(II).[8] Having a second quinol in the coordination sphere generally improves the r_1 response to H_2O_2. The relaxivities of $[Mn^{II}(H_2qp1)(MeCN)]^{2+}$ (MeCN = acetonitrile) and $[Mn^{II}(H_4qp2)Br_2]$ (**3**) increase by 10% and 30%, respectively, upon oxidation by excess H_2O_2.[7-8]

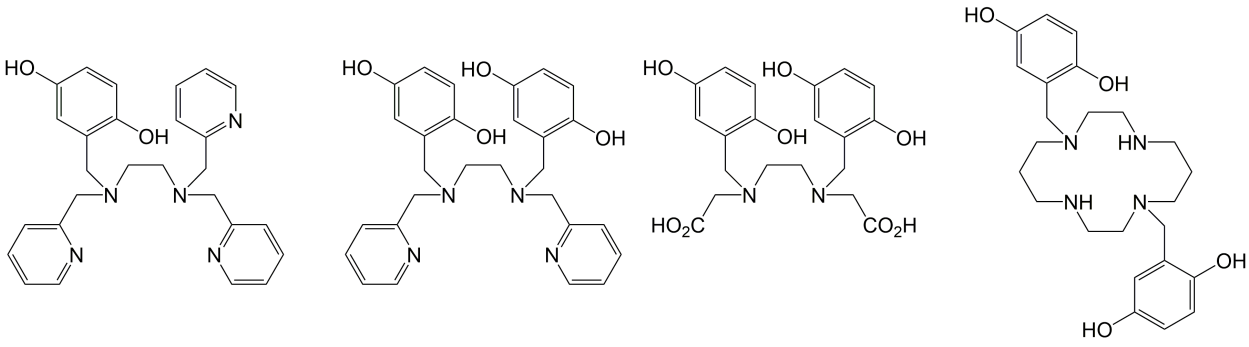

H_2qp1 **H_4qp2** **H_6qc1** **H_4qp4**

$[Mn^{II}(H_3qp4)](OTf)$ - **1**
$[Mn^{II}(H_2qp1)(MeCN)](OTf)_2$ - **2**
$[Mn^{II}(H_4qp2)Br_2]$ - **3**
$[Mn^{III}(H_2qp4)](OTf)$ - **4**

Scheme 2.1 Molecular structures of the quinol-containing polydentate ligands and the compositions of coordination complexes mentioned in this chapter.

This strategy necessarily relies on weakening of the ligand's affinity for Mn(II), and in the case of **3,** a substantial portion of the metal ion is likely released upon oxidation by H_2O_2.[8] Anionic groups and macrocycles are frequently used to stabilize Gd(III)- and Mn(II)-containing MRI contrast agents.[13-14] We had previously replaced the H_4qp2 pyridines with carboxylic acids in order to stabilize the Mn(II) complexes; the carboxylic acids entirely deprotonate to carboxylates at pH 7. Although the more anionic H_3qc1^{3-} and H_2qc1^{4-} forms of the H_6qc1 ligand do indeed allow it to coordinate more tightly to the dicationic metal center, the additional negative charges in the coordination sphere render the manganese more susceptible to oxidation. Oxidation of the metal center to the less paramagnetic Mn(III) eliminates the r_1 response of this complex to H_2O_2.[9] A Mn(II) complex with a fluorinated tetradentate ligand with nearly identical chelating groups likewise gets readily oxidized to a lower-relaxivity Mn(III) species upon reaction with excess H_2O_2.[15]

The other strategy to discourage metal release would be to incorporate a macrocycle into the ligand framework to stabilize the resultant transition-metal complexes both thermodynamically and kinetically.[16] Here, we synthesize a new macrocyclic ligand, 1,8-bis(2,5-dihydroxybenzyl)-1,4,8,11-tetraazacyclotetradecane (H_4qp4), and its complex with Mn(II). We find that the redox reactivity of the Mn(II) compound is similar to those of Mn(II) complexes with H_2qp1 and H_4qp2 in that 1) the reactivity with air is slight and 2) the reactivity with H_2O_2 primarily oxidizes the ligand rather than the metal ion. In addition to the anticipated stabilization of the Mn(II) complexes with the quinol- and *para*-quinone forms of the ligand, the inclusion of the macrocycle improves the maximal MRI response, with r_1 increasing by 130% upon oxidation by H_2O_2.

2.2 Experimental Section

Materials

All chemicals and solvents were purchased from Sigma-Aldrich and used as received unless otherwise noted. All deuterated solvents were bought from Cambridge Isotopes. Diethyl ether (ether) and methanol (MeOH) were bought from Fisher. Methylene chloride (CH_2Cl_2) was purchased from Mallinckrodt Baker.

Instrumentation

All ^{1}H and ^{13}C NMR spectra were recorded on either a 400 MHz or a 600 MHz AV Bruker NMR spectrometer. All reported NMR resonance peak frequencies were referenced to internal standards. ^{17}O NMR data were collected on a Bruker AVANCE DRX 400WB spectrometer with a superconducting wide-bore magnet operating at a 54.24 MHz resonance frequency and a 9.4T magnetic induction. A Varian Cary 50 spectrophotometer was used to collect optical data, which were then processed using software from the WinUV Analysis Suite. Electron paramagnetic resonance (EPR) spectra were collected using a Bruker EMX-6/1 X-band EPR spectrometer operated in the perpendicular mode and subsequently analyzed with the program EasySpin. All EPR samples were

run as frozen solutions in quartz tubes. We used a Johnson Matthey magnetic susceptibility balance (model MK I#7967) to measure the magnetic moments of solid samples of the metal complexes and estimated the diamagnetic component of the susceptibility using Pascal's constants.[17] Cyclic voltammetry (CV) was performed under N_2 at 294 K with an Epsilon electrochemistry workstation (Bioanalytical System, Inc.). The working, auxiliary, and reference electrodes were gold, platinum wire, and silver/silver(I) chloride, respectively. High-resolution mass spectrometry (HR-MS) data were collected at the Mass Spectrometer Center at Auburn University on a Bruker Microflex LT MALDI-TOF mass spectrometer via direct probe analysis operated in the positive ion mode. Solid samples of the Mn(II) complex were dried, stored under N_2, and sent to Atlantic Microlabs (Norcross, GA) for elemental analysis.

X-Ray Crystallography

Crystallographic data for $[H_6qp4](OTf)_2$ and the oxidized product $[Mn^{III}(H_2qp4)](OTf)$ were collected using a Bruker D8 VENTURE κ-geometry diffractometer system equipped with a Incoatec IμS 3.0 microfocus sealed tube and a multilayer mirror monochromator (Mo Kα, λ = 0.71073 Å). Diffraction data were integrated with the Bruker SAINT software package using a narrow-frame algorithm. Data were corrected for absorption effects using the Multi-Scan method (SADABS). The structure was solved and refined using the Bruker SHELXTL Software Package. Selected crystallographic data is presented in Table 2.1.

Potentiometric Titrations

The aqueous speciations of H_4qp4 and its Mn(II) complex were assessed using a METROHM 765 Dosimat with a jacketed, airtight glass titration vessel. A Fisher Scientific Accumet Research AR15 pH meter was used to monitor the pH of the sample solutions during the titrations. The electrode was calibrated before each titration using commercially available standard solutions buffered to pH 4.0, 7.0, and 10.0. All samples were purged with argon prior to analysis and subsequently analyzed

under an argon atmosphere at 25 °C to prevent carbonate contamination. All solution samples were prepared in solutions of 100 mM KCl in deionized Millipore water. The titrations investigating metal-ligand speciation were run with solutions that contained a 1:1 molar mixture of the ligand and $Mn^{II}(OTF)_2$. Carbonate-free solutions of 0.10 M KOH and 0.10 M HCl were prepared using argon-saturated deionized Millipore water. The titration data were analyzed and fitted to speciation models using the Hyperquad2006 program.[18]

High-Pressure Liquid Chromatography (HPLC)

HPLC was performed with UV detection at 254 nm using an Agilent 1100 series apparatus and an Agilent Zorbax SB-C18 column (4.6 × 150 mm, 5 μm pore size). The following eluents were used: A) 99.9 % water with 0.1% trifluoroacetic acid (TFA) and B) 99.9% MeCN with 0.1% TFA. The following method was used (Method 1): Gradient 90% A and 10% B to 100% B over 20 min. Flow rate = 0.20 mL/min, injection volume = 25.0 μL, column temperature = 37.0 °C. Before each run, the HPLC instrument was flushed with eluent 100 % A to 100% B over 16 min with a flow rate of 0.49 mL/min and an injection volume of 25.0 μL.

Measurement of Aquation Numbers (q)

Aquation numbers (q) were calculated from the maximum ^{17}O transverse relaxivity, r_{2max}^{o}, and the equation: $q = r_{2max}^{o}/510$; Gale, Zhu, and Caravan previously used this relationship to estimate the inner-sphere hydration state of Mn(II) in coordination complexes.[19] Relaxation rates were measured both for aqueous solutions containing Mn(II) complexes and for metal-free solutions buffered to pH 7.4. The linewidths at half-height of the signal were determined by a deconvolution procedure on the real part of the Fourier transformed spectra with a Lorentzian shape function in the data analysis module of Bruker Topspin *1.3* software. The measurements were performed with a commercial 5 mm Bruker broadband probe thermostated with a Bruker B-VT 3000 variable temperature unit. Samples were prepared by adding a solution of solid dissolved in a minimal amount of MeCN to an aqueous

solution containing either 60 mM HEPES or 60 mM MOPS buffered to pH 7.4. 10% (v/v) of ^{17}O-labeled water (10%, D-Chem Ltd. Tel Aviv, Israel) was added to these solutions resulting in a total enrichment of 1% ^{17}O in the studied samples. The resultant mixtures contained either 6.0 mM or 2.5 mM of the Mn(II) complex. The 2.5 mM sample was oxidized by 15 equiv. of H_2O_2 for 15 min prior to data acquisition. The temperature-dependence of ^{17}O-line broadening was studied from 274.2 to 338.2 K.

Magnetic Resonance Imaging (MRI)

All MRI data were collected at the Auburn University MRI Research Center on a Siemens Verio open-bore 3T MRI clinical scanner. A 15-channel knee coil was used to simultaneously image 12-15 samples. The imaging procedure was identical to those used for similar studies from our laboratory.[6-9, 20] An inversion recovery (IR) sequence was used that featured a non-selective adiabatic inversion pulse followed by a slice-selective gradient recalled echo (GRE) readout after a delay period corresponding to the inversion time (TI).[21-22] The GRE was a saturation readout, such that only one line of *k*-space was acquired per repetition time (TR), in order to maximize both signal strength and the accuracy of the T_1 estimates. The specific imaging parameters were as follows: TR was set to 10 s, TI was varied from 10 to 2600 ms over 20 steps, the echo time (TE) was set to 2.75 ms, the flip angle equaled 90°, averages = 1, slice thickness = 10 mm, field of view = 64 × 64 mm, matrix = 64 × 64, resulting in a pixel size of 1.0 × 1.0 × 10.0 mm. All samples were run in 50 mM solutions of HEPES in water, buffered to pH 7.0 and kept at 22 °C. The manganese content was systematically varied from 0.10 to 1.00 mM. The inverses of the T_1 values from two separate batches of contrast agent were plotted versus the concentration of Mn(II) to obtain r_1 values.

MRI Data Analysis

Image analysis was performed using custom MATLAB programs (Mathworks, Natick, MA). The initial TI = 4.8 ms image was used as a baseline to determine circular region of interest (ROI) boundaries for each sample; from these, the mean pixel magnitudes for each ROI were calculated. For each of the 36 subsequent TI images, the same ROI boundaries were applied, and the mean pixel magnitude calculations were repeated. This gave consistent ROI spatial definitions and a corresponding time course of magnitudes for each of the samples over all the TI time points. Each sample's complex phase was used to correct the magnitude polarity to produce a complete exponential T_1 inversion recovery curve. The Nelder-Mead simplex algorithm[23] was applied to each sample's exponential curve to estimate its corresponding T_1 value.

Preliminary Analysis of Catalase Activity

In order to assess the ability of the Mn(II) complex to catalyze the degradation of H_2O_2, we reacted 100 nM **1** with 10 mM H_2O_2 in 200 mM phosphate solution buffered to pH 7.0 and monitored the absorbance at 240 nm over time. H_2O_2 has a molar extinction coefficient of 39.4 M^{-1} cm^{-1} at this wavelength.[24] The consumption of H_2O_2 was evaluated using a UV-1601 Shimadzu spectrophotometer.

Synthesis

1,8-Bis(2,5-dihydroxybenzyl)-1,4,8,11-tetraazacyclotetradecane (H_4qp4)

1,4,8,11-tetraazacyclotetradecane (cyclam) (1.00 g, 4.99 mmol) and 2,5-dihydroxybenzaldehyde (1.37 g, 9.91 mmol) were combined in 15 mL of dry MeOH. The mixture was heated at reflux for 4 h under N_2. The reaction mixture was then cooled to 0 °C with an ice bath. Once the temperature reached 0 °C, 20 mL of additional dry MeOH and $NaBH_4$-Al_2O_3 (wt. 10 %, 0.83 g, ~ 0.02 mol) were gradually added to the solution. The resultant solution was heated at reflux for 6 h under N_2 and then cooled to 0 °C. The residual reductant was titrated with 1 M HCl until the solution

reached pH 8, depositing the crude product as a solid which was collected via filtration. The solid was dissolved in acetone and filtered. The acetone was rotavapped to yield the product as a yellow powder (842 mg, 38% yield). Typical yields range from 38 to 42%. ^{1}H NMR (400 MHz, DMSO-*d6*, 297 K): δ 8.55 (s, 2H), 6.97 (s, 2H), 6.50 – 6.56 (m, 4H), 6.45 (s, 2H), 3.16 (s, 4H), 2.45 – 2.59 (m, overlap with solvent peak), 2.28 (s, 4H), 1.69 (s, 4H), 1.14 (s, 2H). ^{13}C NMR (100 MHz, DMSO-*d6*, 297 K): δ 149.98, 149.17, 124.98, 118.02, 117.10, 115.48, 53.80, 53.11, 50.50, 49.26, 46.38, 24.71. MS (ESI): calcd for MH^+: *m/z* 445.2815; found, *m/z* 445.2821.

(1,8-Bis(2,5-dihydroxybenzyl)-1,4,8,11-tetraazacyclotetradecane)manganese(II) triflate ([Mn^{II}(H$_3$qp4)](OTf), 1)

H_4qp4 (500 mg, 1.12 mmol) and $Mn^{II}(OTf)_2$ (397 mg, 1.12 mmol) were dissolved in 5 mL of dried 1:1 MeCN-THF under N_2. The mixture was stirred at 60 °C for 48 h; over this time, a green solid precipitated from the solution. The crude product was collected via filtration and washed with cold MeCN to yield the product as a green powder (577 mg, 76% yield). Typical yields range from 70 to 75%. MS (ESI): calcd for $[Mn(H_2qp4)]^+$: *m/z* 497.1961; found, *m/z* 497.1931 and calcd for $[Mn(H_2qp4)(OTf)]^+$: *m/z* 646.1481; found, *m/z* 646.1470. Solid-state magnetic susceptibility (294 K): $\mu_{eff} = 5.6\ \mu_B$. Optical spectroscopy (MeCN, 294 K): 300 nm (6800 $M^{-1}\ cm^{-1}$), 388 nm (3500 $M^{-1}\ cm^{-1}$). IR (cm^{-1}): 3282 (m), 3069 (w), 2852 (w), 1611 (w), 1511 (m), 1483 (m), 1361 (m), 1279 (s), 1238 (s), 1212 (s), 1180 (s), 1150 (s), 1090 (m), 1060 (m), 1026 (s), 992 (m), 916 (m), 896 (w), 868 (m), 815 (s), 775 (w), 751 (m), 631 (s), 572 (m), 510 (m). Elemental analysis (powder) calcd for $C_{25}H_{35}N_4O_7F_3S_1Mn \cdot 1.5\ H_2O$: C, 44.51 %; H, 5.67 %; N, 8.30 %. Found: C, 44.27%; H, 5.14%; N, 8.09%.

2.3 Results

Synthesis and Non-Aqueous Characterization

The H_4qp4 ligand is synthesized in one step from cyclam, two equiv. of 2,5-

dihydroxybenzaldehyde, and excess $NaBH_4$-Al_2O_3 (Scheme 2.2). The synthesis was inspired by that used to prepare 1,8-bis(2-hydroxybenzyl)-1,4,8,11-tetraazacyclotetradecane (H_2bcyclamb), which features phenols in place of the quinol groups.[25] The preparation of H_4qp4 is complicated by the sensitivity of the bisaminal intermediate to air, necessitating that the addition of the quinols be done in a one-pot reaction rather than over two discrete steps. The one-pot reaction has the unexpected benefit of modestly improving the yield of H_4qp4 (38%); the overall yield of H_2bcyclamb was 28%. The purity and identity of H_4qp4 were confirmed by NMR and HR-MS. We also crystallized the triflic acid salt of the ligand, $[H_6qp4](OTf)_2$, from MeOH (Figure 2.1).

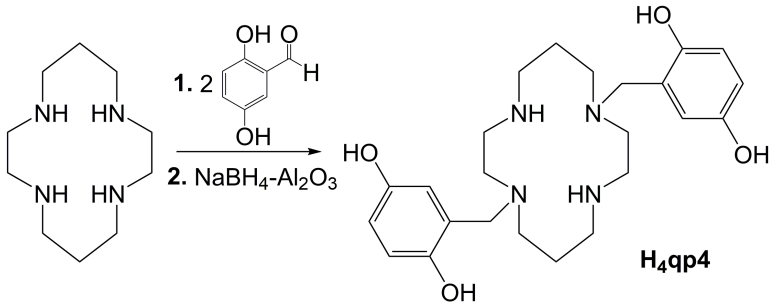

Scheme 2.2 Synthesis of H_4qp4.

A Mn(II) complex with H_4qp4, $[Mn^{II}(H_3qp4)](OTf)$ (**1**), can be prepared by refluxing the ligand and $Mn^{II}(OTf)_2$ in 1:1 MeCN/THF for 2 d. The complexation reaction requires a much higher temperature and a much longer reaction time than the syntheses of $[Mn^{II}(H_2qp1)(MeCN)](OTf)_2$ (**2**) and $[Mn^{II}(H_4qp2)Br_2]$ (**3**).[7-8] The incorporation of metal ions into macrocycles often requires such measures. Complex **1** differs from previously isolated Mn(II) complexes with polydentate quinol-containing ligands in that it features a deprotonated quinol. Elemental analysis of powdered samples of **1** indicates that there is a single triflate per manganese. The EPR and the magnetic susceptibility measurements both indicate that the metal ion is high-spin Mn(II). Since there is only one counteranion, this thereby necessitates a -1 charge on the polydentate ligand (H_3qp4^-). The presence of a quinolate is further supported by the presence of two bands in the UV/vis spectrum of the isolated

product in MeCN (Figure A6). The feature at 304 nm is consistent with a neutral quinol; bands at similar energies are the sole UV/vis features observed above 250 nm for both **2** and **3** in MeCN.[7-8] The additional band at 388 nm has an energy that is more consistent with a quinolate group; these have been observed for the H_2qp1 and H_4qp2 complexes in water.

Complex **1** is stable to air in the solid and solution states for prolonged periods of times. Samples of **1** in MeCN display negligible changes to their UV/vis features over a 12 h exposure to air (Figure A6). If solutions of **1** in either aqueous or organic solvents are kept under air for 1-2 weeks, the compound does eventually oxidize to $[Mn^{III}(H_2qp4)](OTf)$ (**4**), where H_2qp4^{2-} is the doubly deprotonated form of the ligand.

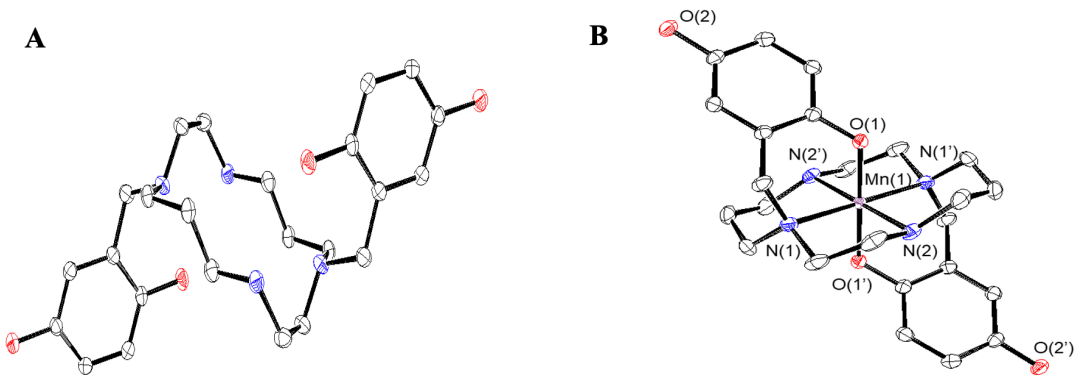

Figure 2.1 ORTEP representations of (A) $[H_6qp4]^{2+}$ and (B) $[Mn^{III}(H_2qp4)]^{+}$ (**4**). All hydrogen atoms, solvent molecules, and counteranions have been removed for clarity. All ellipsoids depict 50% probability.

*Structures of $[H_6qp4](OTf)_2$ and **4***

The crystal structure of the doubly protonated H_4qp4 ligand is shown in Figure 2.1A. The protonation state of the ligand was deduced from the 1:2 ligand/triflate ratio of the solid. Each additional proton bridges the two N atoms from a 1,2-ethanediamine portion of the macrocycle. One of the O atoms from the nearest quinol is centered over each 1,2-ethanediamine moiety, with nearly equal distances between the O atom and each N (2.94 and 2.95 Å).

Attempts to crystallize **1** have thus far been unsuccessful, but we crystallized **4** by slowly diffusing CH_2Cl_2 into a saturated solution of **1** in MeCN under air over 2 weeks (Figure 2.1B). The reddish color of the crystals suggests that the manganese has been oxidized to either the +3 or +4 oxidation state. Single crystal x-ray diffraction data unambiguously assign the metal center as Mn(III). The Mn-N and Mn-O bonds for **4** average 2.16 Å and 1.89 Å, respectively. Typical bonds between Mn(II) and neutral N-donors are longer, ranging from 2.2-2.3 Å; whereas bonds between Mn(II) and even anionic O-donors usually exceed 2.0 Å.[6-8, 20, 26-28] The Mn-N and Mn-O bond distances observed for **4** are instead more consistent with a Mn(III) ion bound to neutral N-donors and anionic O-donors.[26] Additionally, the coordination complex displays a rhombic [2+2+2] Jahn-Teller distortion, with pairs of short (Mn-O(1), Mn-O(1')), intermediate (Mn-N(2), Mn-N(2')) and long (Mn-N(1), Mn-N(1')) metal-ligand bonds.[26,29] Such distortions would be anticipated for a high-spin d^4 electronic configuration but not for a d^3 metal ion. The metal center is therefore more likely to be Mn(III) than Mn(IV).

*Stability and Speciation of **1** in Water*

The speciation of the free H_4qp4 ligand was investigated from pH 3 to 9 (Figure A7). The best-fitting model to the potentiometric pH titration data is comprised of four ionization events corresponding to pK_a values of 3.5, 7.7, 8.8, and 10.0 (Figure A8, Table A1, Table 2.2). Cyclam by itself is quadruply protonated under extremely acidic conditions, with two of the protons being retained from pH 2 to pH 10.[30] The H_4qp4 ligand appears to behave similarly, and the species at pH 3 is assigned as H_6qp4^{2+}. The ligand exists primarily as H_5qp4^{+} at pH 7.0, with a considerable amount of H_4qp4 (Figure 2.2A). Traces of doubly deprotonated H_2qp4^{2-}, which would feature two quinolates, are seen at the basic end point of the titration.

Table 2.1 Selected crystallographic data for $[H_6qp4](OTf)_2$ and **4**.

Parameter	$[H_6qp4](OTf)_2$	$[Mn^{III}(H_2qp4)](OTf)\cdot CH_2Cl_2$ (**4**)
Formula	$C_{26}H_{38}F_6N_4O_{10}S_2$	$C_{26}H_{35}Cl_2F_3MnN_4O_7S$
MW	744.72	730.48
Crystal system	Triclinic	Monoclinic
Space group	*P -1*	P 1 2_1/m 1
a (Å)	9.2212(3)	8.3460(2)
b (Å)	10.0950(4)	19.4089(5)
c (Å)	10.4689(3)	9.9382(3)
α (°)	107.310(1)	90
β (°)	111.234(1)	108.9230(10)
γ (°)	104.783(1)	90
V ($Å^3$)	791.83(5)	1522.85(7)
Z	1	2
Crystal color	Colorless	Pale red
T (K)	110	110
Reflns collected	63351	36113
Unique reflns	5270	3586
R1 (F, I > 2σ(I))[a]	0.0492	0.0259
wR2 (F^2, all data)[a]	0.1415	0.0837

[a] $R1 = \Sigma \left| |F_o| - |F_c| \right| / \Sigma |F_o|$; $wR2 = [\Sigma w(F_o^2-F_c^2)^2/\Sigma w(F_o^2)^2]^{1/2}$.

The inclusion of a macrocycle into the ligand framework greatly stabilizes **1** in water relative to previously prepared contrast agents from our laboratory. The stability and speciation of **1** were assessed using potentiometric pH titration data acquired from pH 3 to pH 9. Our best-fitting model for the data suggests that there is negligible Mn(II) release from the ligand even at pH 3 (Figure A9, Figure 2.2B). The pMn at pH 7.4 with 1.0 mM of Mn(II) and ligand is calculated to be 9.81. Two ionization events are observed between pH 3.0 and pH 9.0. The associated pK_a values of 5.09 and 7.39 are consistent with the sequential deprotonation of two Mn(II)-bound quinols as the solution is made more basic.[8,12,31] The calculated log K_{ML} values for Mn(II) bound to H_4qp4, H_3qp4^-, and H_2qp4^{2-} all exceed 14, with the binding affinity becoming stronger as the ligand deprotonates to more anionic forms.

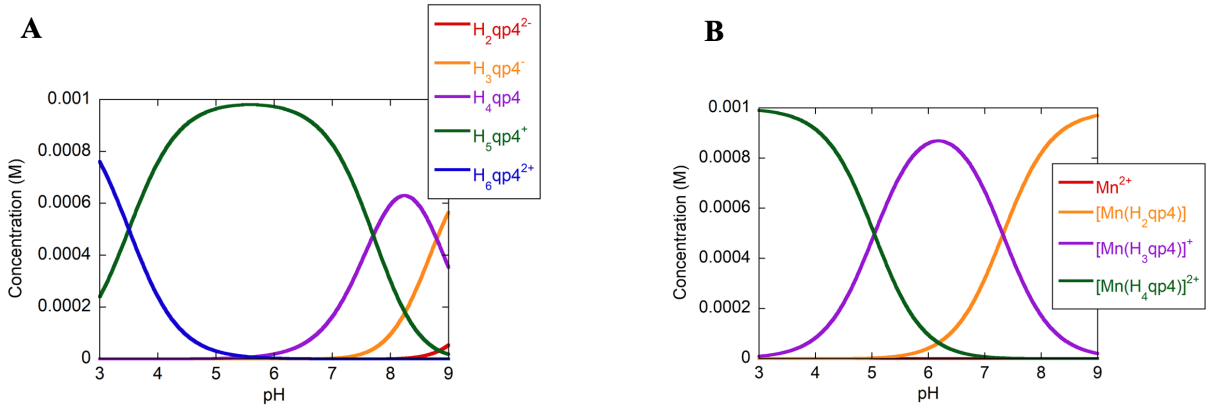

Figure 2.2 Predicted speciation as a function of pH for A) 1.0 mM H_4qp4 and B) 1.0 mM **1** in 100 mM KCl solution.

The stability of the Mn(II)-H_4qp4 complex in water is confirmed by HPLC (Figures A10 and A11). The H_4qp4 ligand and **1** each give rise to single LC peaks with distinct retention times. Partial deprotonation of the metal-bound quinols in **1** at pH 7.00 is supported by UV/vis measurements. The spectrum of **1** in 50 mM HEPES solution buffered to pH 7.00 displays an intense band at 388 nm that is absent in the spectrum for metal-free H_4qp4 under the same conditions (Figure A12). The energy of this new band is consistent with a phenolate or quinolate group.[8] The assignment of the 5.09 and 7.39 pK_a values to the deprotonation of the metal-bound quinols is also supported by a parallel spectrophotometric pH titration (Figure A13). The UV/vis spectrum of **1** changes markedly and continually as the pH rises from 4 to 9. Since Mn(II) does not generally support charge transfer or d-d bands, these changes can be assigned to the sequential deprotonation of the ligand's two quinols.

Complex **1** was electrochemically characterized by cyclic voltammetry (CV) in an aqueous 50 mM phosphate solution buffered to pH 7.2. An irreversible feature with E_{pa} = 1.25 V *vs.* Ag/AgCl was observed and assigned to the oxidation of the metal to Mn(III). In addition, we also detected a redox feature with $E_{1/2}$ of 100 mV *vs.* Ag/AgCl (295 mV *vs.* NHE, Figure A14). The separation between the anodic and cathodic peaks (ΔE) is approximately 260 mV. Since redox processes with similar $E_{1/2}$ values were found for manganese and zinc complexes with polydentate quinol-containing ligands, we

tentatively assign the 100 mV *vs.* Ag/AgCl feature to the oxidation and reduction of the ligand, rather than the manganese.[7,8,32] The ΔE for the 100 mV redox event is larger than the 230 mV value measured for **3**; we attribute the poor reversibility of both features to the more extensive acid/base chemistry associated with having two, rather than one, quinol/quinolate groups in these coordination complexes.

Table 2.2 pMn, log K_{ML}, and pK_a Values Determined by Potentiometric Titration at 25 °C.

pK_{L1}[a]	3.50 (±0.05)	log K_{ML} ($Mn^{II}(H_2qp4)$)[c]	20.85
pK_{L2}[a]	7.70 (±0.05)	log K_{ML} ($Mn^{II}(H_3qp4)$)$^{+}$ [c]	18.22
pK_{L3}[a]	8.80 (±0.05)	log K_{ML} ($Mn^{II}(H_4qp4)$)$^{2+}$ [c]	14.52
pK_{L4}[a]	10.02 (±0.05)	pMn(pH 7.4)[d]	9.81
pK_a($Mn^{II}(H_4qp4)^{2+}$)[b]	5.09 (±0.05)		
pK_a($Mn^{II}(H_3qp4)^{+}$)[b]	7.39 (±0.05)		

[a]Ligand pK_a values: $K_{L1} = [H_5qp4^{+}][H^{+}]/[H_6qp4^{2+}]$;
$K_{L2} = [H_4qp4][H^{+}]/[H_5qp4^{+}]$;
$K_{L3} = [H_3qp4^{-}][H^{+}]/[H_4qp4]$;
$K_{L4} = [H_2qp4^{2-}][H^{+}]/[H_3qp4^{-}]$

[b]Metal complex pK_a values: $K_a(Mn^{II}(H_4qp4)^{2+}) = [Mn^{II}(H_3qp4)^{+}][H^{+}]/[Mn^{II}(H_4qp4)^{2+}]$;
$K_a(Mn^{II}(H_3qp4)^{+}) = [Mn^{II}(H_2qp4)][H^{+}]/[Mn^{II}(H_3qp4)^{+}]$

[c]Metal complex K_{ML} values: $K_{ML}\,(Mn^{II}(H_2qp4)) = [Mn^{II}(H_2qp4)]/([Mn(II)][H_2qp4^{2-}])$;
$K_{ML}\,(Mn^{II}(H_3qp4))^{+} = [Mn^{II}(H_3qp4)^{+}]/([Mn(II)][H_3qp4^{-}])$;
$K_{ML}\,(Mn^{II}(H_4qp4))^{2+} = [Mn^{II}(H_4qp4)^{2+}]/([Mn(II)][H_4qp4])$

[d]pMn = $-\log[Mn(II)]_{free}$ calculated for [Mn(II)] = 1.0 mM, $[H_4qp4]$ = 1.0 mM, 298 K, pH 7.4.

Table 2.3 Water exchange activation parameters obtained for quinol-containing Mn(II) complexes **1**, **2**, and **3**.

Parameter	**1** (pH 7.4)	**1** (pH 7.4) after oxidation	**2** (pH 7.4)[a]	**3** (pH 7.0)[b]
q	1.2 (±0.2)	2.2 (±0.3)	0.7 (±0.2)	0.9 (±0.2)
k_{ex}^{298} (s^{-1})	1.7 (±0.1) × 10^7	1.6 (±0.4) × 10^7	6.9 (±0.6) × 10^7	4.9 (±1.4) × 10^6
$\Delta H^{‡}$ (kJ mol^{-1})	45 (±2)	50 (±9)	24.2 (±1.0)	22.0 (±1.7)
$\Delta S^{‡}$ (J K^{-1} mol^{-1})	43 (±6)	62 (±11)	-13.1 (±3.4)	-41 (±2)

[a]From reference 33. [b]From reference 8.

The ability of **1** to interact with water was studied using variable temperature ^{17}O NMR using the methodology pioneered by Gale et al. (Figure 2.3).[19] The results at pH 7.4 are consistent with q = 1.2 (Table 2.3). When **1** is dissolved in pH 7.4 water, the predominant species is therefore

$[Mn^{II}(H_3qp4)(H_2O)]^+$, with next most prevalent species being $[Mn^{II}(H_2qp4)(H_2O)]$. The calculated rate constant for water exchange at 298 K is 1.7×10^7 s^{-1}, which is at the slower end of the range typically seen for Mn(II) complexes.[8,19,34-40] The $\Delta S^{\ddagger}$ is highly positive, consistent with a dissociate mechanism for water exchange at the metal center.

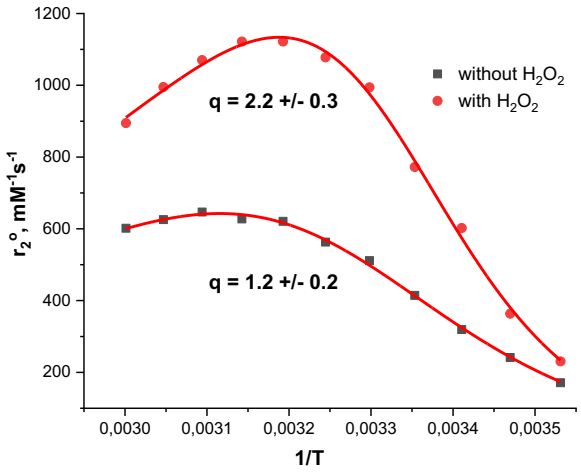

Figure 2.3 Plots of $r_2°$ as a function of temperature for **1** before and after oxidation by H_2O_2. Experimental conditions for pre-activated sensor (black squares): [**1**] = 6.0 mM in 60 mM HEPES buffered to pH 7.4 and 10% (v/v) of 10% $^{17}OH_2$, B = 9.4 T. Experimental conditions for activated sensor (red circles): [**1**] = 2.5 mM in 60 mM MOPS buffered to pH 7.4 with 15 equiv. H_2O_2 and 10% (v/v) of 10% $^{17}OH_2$, B = 9.4 T. We began to acquire NMR data 15 min after the start of the oxidation reaction.

*Stability of **1** to Air and Adventitious Metal Ions*

Complex **1** does not display any noticeable short-term reactivity to air. The UV/vis spectrum of **1** in MeCN does not appreciably change over the course of a 12 h exposure to air (Figure A6). Both **2** and **3**, conversely, appear to oxidize slightly (5-10%) to Mn(II) *para*-quinone complexes under the same conditions. O_2 does eventually oxidize **1**, with the Mn(III)-containing **4** depositing over 1-2 weeks (Figure 2.1B).

Complex **1** differs from **2** and **3** in that it strongly resists metal ion exchange. The reaction between 0.1 mM $Fe^{II}(ClO_4)_2$ and 0.1 mM **1** in MeCN does not yield UV/vis-detectable quantities of $[Fe^{II}(H_3qp4)]^+$, even at 18 h (Figure A15). The changes to the UV/vis spectrum of **1** over this time are

negligible. Complex **2**, conversely, slowly exchanges Fe(II) for Mn(II) in MeCN, with approximately 10% of the Mn(II) being displaced by an equimolar amount of Fe(II) by 15 h.[7] Complex **3** is the most susceptible of the three Mn(II)-quinol complexes to metal ion displacement, and 80% of its Mn(II) is displaced by an equimolar amount of Fe(II) by 3 h.[8] Both the H_2qp1 and H_4qp2 complexes with Mn(II) react readily with Zn(II), with the strong diamagnetic ^{1}H NMR features of the Zn(II)-H_2qp1 and Zn(II)-H_4qp2 complexes appearing within 2 h.[7-8] The reaction between 20 mM $Zn(ClO_4)_2$ and 10 mM **1** in CD_3CN or D_2O, however, fails to dislodge the Mn(II) from the ligand, as assessed by ^{1}H NMR (Figure A16). The ^{1}H NMR spectrum of the reaction is featureless aside from solvent peaks even 24 h after the introduction of the Zn(II). When 20 mM H_2O_2 is added to a mixture of 20 mM $Zn(ClO_4)_2$ and 10 mM **1**, the Mn(II) likewise remains in the oxidized forms of the ligand (H_2qp4 and qp4, Scheme 2.3) as assessed by ^{1}H NMR.

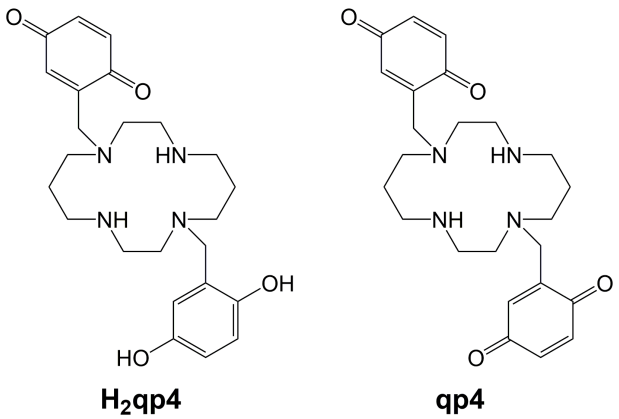

Scheme 2.3 Oxidized forms of the H_4qp4 ligand.

*Reactivity between **1** and H_2O_2*

Upon reaction with 2,3-dichloro-5,6-dicyano-1,4-benzoquinone (DDQ), the quinols in **1** appear to be partially oxidized to *para*-quinones as assessed by MS, UV/vis, and IR (Scheme 2.3, Figures A17-A19). A new IR feature at 1656 cm^{-1} provides strong evidence for the formation of the C=O bonds associated with the *para*-quinone.

When **1** reacts with a large 10 mM excess of H_2O_2, MS reveals similar *m/z* features to those seen for the oxidation of the Mn(II) complex by DDQ, suggesting that the quinols are likewise converted to *para*-quinones by this oxidant (Figure A20). Further investigation reveals that the speed of the reaction between **1** and excess H_2O_2 is significantly slower than analogous reactions with **2** and **3**.[7-8] Curiously, the changes to the optical spectra during the first 30 min are slight, consistent with an induction period (Figure 2.4A). The reaction then accelerates and finishes by 90 min. The most noticeable optical changes are the disappearance of the peaks at 293 and 388 nm; features with similar energies have been observed for **2** and **3** and assigned to intraligand transitions for quinol and quinolate moieties.[7-8] When a smaller amount of H_2O_2 (0.6 mM) is added to **1**, the quinol peak decreases immediately with the reaction completing in 20 min (Figure 2.4B), indicating that the induction period only occurs when H_2O_2 is present in a large excess.

When the reaction between 1.0 mM **1** and 10 mM H_2O_2 in pH 7.0 HEPES buffer is monitored by EPR, the spectrum taken before the oxidant was added looks nearly identical to those taken at 60 min and 90 min, suggesting that the manganese largely remains in the +2 oxidation state throughout the reaction (Figure 2.4C). As with prior quinol-containing H_2O_2 sensors from our laboratory, not all of the quinols are oxidized to *para*-quinones by excess H_2O_2.[7-8] The Mn(II) exists as a mixture of unreacted **1**, $[Mn^{II}(Hqp4)]^+$, and $[Mn^{II}(qp4)]^{2+}$, where $Hqp4^-$ and qp4 correspond to the mono-*para*-quinone/quinolate and di-*para*-quinone oxidized forms of the ligand. The oxidation of the quinols is potentially reversible. When **1** is oxidized by H_2O_2 in MeOH, we can regenerate the H_3qp4^- complex by subsequently adding sodium dithionite (Figure A21).

Upon oxidation by H_2O_2, the aquation number of the Mn(II) center in **1** increases by approximately one water molecule, resulting in an average of 2.2 water molecules binding to each metal center (Figure 2.3, Table 2.3). The rate of water exchange does not significantly change, with the rate constant being identical within error to that measured before oxidation. The $\Delta S^{\ddagger}$ for water

exchange remains highly positive after the reaction with H_2O_2, suggesting that this process still occurs through a dissociative pathway.

MRI Properties

The relaxivities of complex **1** before and during its reaction with H_2O_2 were assessed using a 3T MRI scanner (Figure 2.4D). T_1 values were measured for aqueous solutions containing 0-1.0 mM **1** and 50 mM HEPES buffered to pH 7.00. For each concentration of **1**, an oxidized sample was also prepared by adding 10 mM H_2O_2; the large excess of oxidant was used to ensure as full a turn-on as possible at the time points and to facilitate comparisons to manganese-containing MRI contrast agents that were previously prepared and characterized by our laboratory.[6-9, 20] The T_1 values for the H_2O_2-containing solutions were measured 1 h and 2 h after the reagents were initially mixed. Full series of data were collected for two independently prepared batches of **1** in order to confirm that the results were replicable.

Relaxivities (r_1) were obtained from the slopes of plots of $1/T_1$ versus manganese concentration. Prior to oxidation by excess H_2O_2, the r_1 is 3.16 mM^{-1} s^{-1}. The data taken for samples kept under air for 1 h and 2 h overlay well, suggesting that the short-term reactivity with air is slight. After oxidation by H_2O_2, the relaxivity rises, reaching 5.09 mM^{-1} s^{-1} by 1 h and peaking at 7.35 mM^{-1} s^{-1} as assessed by measurements taken at 2 h (Figure 2.4D). The pH-dependence of the relaxivity was investigated from pH 3 to pH 9 (Figure A22). R_1 values were measured for a 0.50 mM sample of **1**. The R_1 is highest at pH 3 and is lowest at pH 7. As the pH increases, the R_1 drops from pH 3 to pH 4, remains approximately constant from pH 4 to pH 6.5, decreases from pH 6.5 to pH 7, then rises slightly from pH 7 to pH 9.

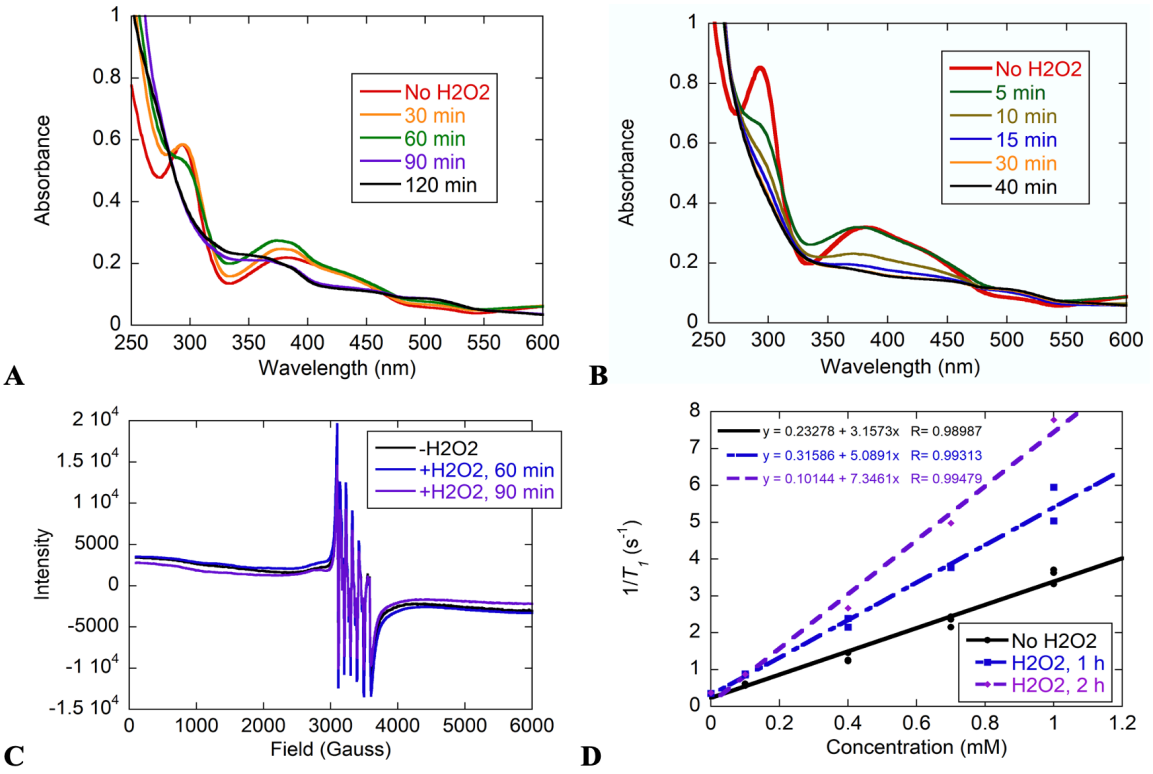

Figure 2.4 Response of **1** to H_2O_2. A) UV/vis spectra acquired during a reaction between 0.07 mM **1** and 10 mM H_2O_2 in 50 mM HEPES buffered to pH 7.00 at 298 K, B) UV/vis spectra acquired during a reaction between 0.10 mM **1** and 0.60 mM H_2O_2 in 50 mM HEPES buffered to pH 7.00 at 298 K, C) X-band EPR spectra of 1.0 mM solutions of **1** in 50 mM HEPES buffered to pH 7.00 in the absence and presence of 10 mM H_2O_2. The reaction between **1** and H_2O_2 proceeded for 60 min before the sample was frozen and analyzed at 77 K. D) Plots of $1/T_1$ versus Mn(II) concentration for **1** in the presence (blue, purple) and absence (black) of 10 mM H_2O_2. All samples were run in 298 K aqueous solutions containing 50 mM HEPES buffered to pH 7.00, using a 3T field provided by a clinical MRI scanner. All samples were prepared under air. The oxidized samples were prepared by directly adding H_2O_2 to solutions of **1** in aqueous solutions buffered to pH 7.0. Two sets of oxidation reactions were allowed to proceed for 60 min at 298 K before T_1 was measured (blue). A third set of oxidation reactions was allowed to proceed for 120 min before data acquisition. The data were fit to the indicated linear equations; the y-intercepts were within error of $1/T_1$ measurements associated with two control samples that contained no Mn(II): pure water (0.35 s^{-1}) and 50 mM HEPES buffer (0.34 s^{-1}).

2.4 Discussion

Both H_4qp4 and [$Mn^{II}(H_3qp4)$](OTf) (**1**) were prepared in straightforward manners using techniques slightly modified from previously successful procedures. The synthesis for a closely related cyclam derivative with two phenols appended to two of the amines was done in two distinct steps,[25] but the heightened air-sensitivity of the quinols under basic conditions led us to explore and eventually adopt a one-pot reaction. Once the ligand was prepared, the installation of the Mn(II) into the macrocycle proceeded cleanly using protocols commonly used for other macrocycle complexation reactions.[41-44] Unexpectedly, the Mn(II) is bound to the singly deprotonated ligand H_3qp4^- , rather than neutral H_4qp4, in the solid isolated from precipitation of the Mn(II) complex from organic solvents. Analogous complexes with H_2qp1 and H_4qp2 (Scheme 2.1), [$Mn^{II}(H_2qp1)$(MeCN)](OTf)$_2$ (**2**) and [$Mn^{II}(H_4qp2)Br_2$] (**3**), contain exclusively quinols rather than quinolates.[7-8] We speculate that residual metal-free H_4qp4 may serve as the base that deprotonates the metal-bound ligand. Although we have not isolated the protonated ligand byproduct(s), we feel that this is a likely explanation for the deprotonation of the Mn(II) complex due to the ligand's high affinity for protons and the ~75% yield of **1**, which would provide enough residual ligand to serve as a base.

As anticipated, **1** contains a high-spin Mn(II) metal center as evidenced by EPR, UV/vis, and solid-state magnetic susceptibility data. The UV/vis features correspond to intraligand transitions for the quinol and quinolate groups; these provide convenient spectroscopic signatures to follow the oxidation state of the ligand.[7-9]

Complex **1** is much more thermodynamically stable in water than the previously characterized **3**, which has a similar coordination sphere around the metal center in aqueous solution.[8] The pMn value measured at pH 7.4 with 1.0 mM concentrations of ligand and Mn(II) is 9.81, which represents over four orders of magnitude of improvement over the 5.36 value measured for **3**.[8] The gains in stability can be attributed largely to macrocyclic effects since H_4qp2 and H_4qp4 provide similar

coordination spheres: four neutral N-donors in addition to the two quinols/quinolates. Complex **1** is also more stable than **2**, which has a pMn of 7.25 under our standard conditions.[33]

The stability of **1** also exceeds those of most other reported mononuclear Mn(II)-containing MRI contrast agents. [9,14,37,39-40,45-48] The Gale and Caravan groups have recently reported a series of linear ligands with multiple carboxylate donors that coordinate tightly to Mn(II).[37,46] One representative example, PyC3A^{3-}, forms a Mn(II) complex with a log K_{ML} of 14.14 (Scheme 2.4).[37] The H_6qc1 ligand (Scheme 2.1) was inspired by this work, and the triply deprotonated H_3qc1^{3-} forms a Mn(II) complex with a log K_{ML} of 15.59.[9] The log K_{ML} values for the Mn(II) complexes with H_2qp4^{2-} and H_3qp4^{-} both exceed 18, demonstrating that the macrocycle can stabilize Mn(II) complexes more efficiently than more highly anionic linear ligands. The DOTA^{4-} ligand represents a combination of these strategies in that it is comprised of four carboxylates tethered to a cyclen framework (Scheme 2.4). The log K_{ML} value for its Mn(II) complex (19.89) is higher than the 18.22 value for H_3qp4^{-} but less than the 20.85 value measured for H_2qp4^{2-}.[47-48] The 19.01 log K_{ML} for the Mn(II) complex with the macrocyclic PC2A-EA^{2-} (Scheme 2.4) is also similar to that of **1**.[40]

The inclusion of the cyclam into the ligand also endows **1** with a high level of kinetic stability as assessed by metal competition experiments. Once in the macrocycle, the Mn(II) cannot be facilely displaced by either Fe(II) or Zn(II), two of the most common transition metal ions in biology. Complexes **2** and **3**, conversely, gradually react with equimolar amounts of free Fe(II) and quickly react with Zn(II). The inertness of **1** towards metal ion exchange compares well to those of other Mn(II)-containing MRI contrast agents with macrocyclic organic components.[14,40,44] The kinetic stability extends to Mn(II) complexes with oxidized forms of the H_4qp4 ligand. Oxidation by H_2O_2 yields a mixture of Mn(II) complexes with the monoquinol/monoquinone and diquinone ligands H_2qp4 and qp4 (Scheme 2.3). ^{1}H NMR analysis of the reaction between these oxidized complexes and Zn(II) reveals that the Zn(II) does not noticeably displace the Mn(II). The oxidized forms of complex **3**,

conversely, exchange Zn(II) for Mn(II) under these conditions, leading to intense diamagnetic peaks when visualized by NMR.[8]

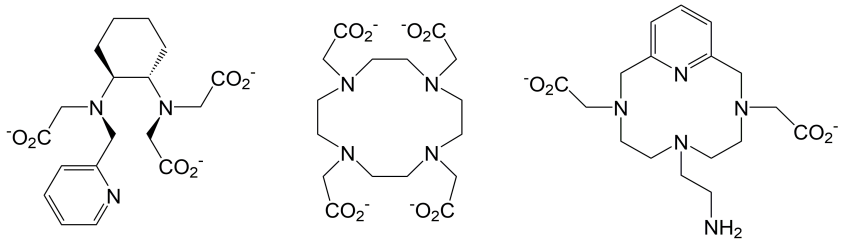

Scheme 2.4 Other Mn(II)-binding ligands used in MRI contrast agents.

Like **2** and **3**, **1** is a redox-active T_1-weighted MRI contrast agent. Curiously, the pre-oxidation relaxivity of **1** (3.15 mM^{-1} s^{-1}) is much lower than that of **3** (5.46 mM^{-1} s^{-1}), despite the two compounds having similar coordination spheres and acid/base behavior. Both r_1 values are the weighted averages of the relaxivities of the individual Mn(II) species present at pH 7.00: $[Mn^{II}(H_3qp4)(H_2O)]^+$ and $[Mn^{II}(H_2qp4)(H_2O)]$ in the case of **1**. The average aquation number measured for **1** is slightly higher than that of **3**, but this would be anticipated to raise rather than lower the T_1-weighted relaxivity, r_1. The pK_a values for the two Mn(II)-bound quinols in **1** and **3** are also similar: 5.82 and 7.14 for **3** versus 5.09 and 7.39 for **1**. The higher pK_a value in each pair would be anticipated to modulate the rate of proton transfer.[49] The slightly more basic quinolate in **1** could slow the rate of proton transfer between the Mn(II)-quinols and the bulk water enough to substantially reduce its contribution to the measured r_1, but further studies are needed to fully elucidate that possible relationship. The rate constants for water exchange at 298 K differ the most, with the k_{ex} value measured for **3** (4.9×10^6 s^{-1}) being approximately a third of that of **1** (1.7×10^7 s^{-1}).[8] Complex **1**, unlike **3**, appears to exchange water molecules through a dissociative mechanism, as evidenced by the highly positive entropy of activation (Table 2.3).

The relaxivity measured for non-oxidized **1**, like that of **3**, is higher under acidic conditions (Figure A22).[8] This may be consistent with water molecules displacing the quinol portions of the ligand from the metal. Alternatively, the protonation of the quinolate groups under more acidic conditions may increase the relaxivity by enabling more extensive exchange with the protons from the bulk water. As the pH becomes more basic, the metal-bound quinols deprotonate to anionic quinolates that can outcompete water for coordination sites on the metal center.

In addition to the higher stability, the inclusion of the cyclam into the ligand framework has the non-intuitive benefit of improving the relaxivity response to H_2O_2. The 130% increase in r_1 is approximately quadruple the percentile increase observed for **3**.[8] Complex **3** rapidly destabilizes as the pH drops below 7.0 due to the protonation of the Mn(II)-quinolates, and it is reasonable to assume that the oxidation of the quinols to *para*-quinones likewise weakens the binding affinity of the ligand enough to trigger release of the Mn(II). The H_2O_2-enhanced r_1 for **3**, however, cannot be attributed to the release of the metal. The T_1-weighted relaxivity of $[Mn^{II}(H_2O)_6]^{2+}$ was measured independently (5.26 mM^{-1} s^{-1}) and found to be approximately equal to that of the pre-activated form of **3** (5.46 mM^{-1} s^{-1}).[8, 20] Although one may expect $[Mn^{II}(H_2O)_6]^{2+}$ to have a higher r_1 due to its higher aquation number, this is not observed. Proton exchange between water molecules and the Mn(II)-bound quinols/quinolates would be anticipated to markedly increase the r_1 values of **1**, **2**, and **3** relative to q = 1 systems that lack metal-bound hydroxyl groups from their organic ligands.[49] Counter-intuitively, Mn(II) ion release from the oxidized forms of H_4qp2 may actually curtail the response of **3** to H_2O_2.

If **1** were to release free Mn(II) upon oxidation, we would anticipate an increase in r_1 due to the lower starting value, but this mechanism is not consistent with our data. Our NMR measurements indicate that the oxidation of **1** by H_2O_2 does not release significant amounts of Mn(II). Further, the maximum r_1 exceeds that of $[Mn^{II}(H_2O)_6]^{2+}$. We instead believe that the increase in relaxivity results from the formation of more highly aquated Mn(II) species with the oxidized forms of the ligand. Since

the H_2O_2 reaction does not make either $[Mn^{II}(Hqp4)(H_2O)_x]^+$ or $[Mn^{II}(qp4)(H_2O)_x]^{2+}$ cleanly, we, unfortunately, cannot measure the individual r_1 values of these two species and ascertain their contributions to the overall relaxivity. Oxidation by H_2O_2 does improve the aquation of the metal center, as evidenced by variable temperature ^{17}O NMR measurements (Table 2.3, Figure 2.3). On average, the metal centers coordinate one additional water molecule after oxidation.

Complex **1** differs substantially from **2** and **3** in that its response to H_2O_2 depends on the manner in which the oxidant is administered. When a large excess of H_2O_2 is added to **1** in a single portion, the oxidation of the quinols occurs after an induction period. The oxidation by 10 mM of H_2O_2 takes approximately 90 min to complete, as assessed by changes to both the relaxivity and the UV/vis spectrum. When a smaller portion of H_2O_2 is added, the quinols are oxidized more quickly and without a noticeable induction period. Based on these observations, we propose that the initial reaction between H_2O_2 and **1** generates an oxidant that can react either unimolecularly to oxidize one of the quinols to a *para*-quinone or bimolecularly with another equiv. of H_2O_2 to yield O_2 and regenerate **1** (Scheme 2.5). In high concentrations of H_2O_2, the second pathway dominates, and the manganese complex primarily acts as a catalase mimic. Complexes **2** and **3**, conversely, quickly react with excess H_2O_2 to yield Mn(II) *para*-quinone complexes, and these reactions do not feature induction periods. We speculate that efficient oxidation of quinols to *para*-quinones may require that the quinols be *cis* to the H_2O_2-derived ligand in a transient higher-valent intermediate, which we depict as a Mn(IV)-oxo complex in Scheme 2.5. If the macrocycle coordinates the manganese in a square planar fashion as it does to the Mn(III) in **4** (Figure 2.1B), an incoming H_2O_2 will likely displace a quinol/quinolate, forcing the H_2O_2-derived ligand to be *trans* to the remaining metal-bound quinol/quinolate. This would hinder intramolecular oxidation and enable bimolecular reactions with additional equiv. of H_2O_2 to proceed. A similar hindrance of intramolecular quinol oxidation may also explain the reaction between **1** and O_2. The product of this reaction is $[Mn^{III}(H_2qp4)](OTf)$ (**4**, Figure 2.1B) rather than a Mn(II) complex

with a *para*-quinone containing ligand; the latter of which might be anticipated to be more thermodynamically stable based on the electrochemistry (Figure A14).

Preliminary data suggest that **1** can indeed catalyze the degradation of H_2O_2. When reactions between 100 nM **1** and 10 mM H_2O_2 are followed spectrophotometrically, the absorbance of the H_2O_2 peak at 240 nm decreases quickly (Figure A23). From these data, the initial rate, $v_o/[\mathbf{1}]_T$, was estimated to be 6.6 (±2.3) × 10^3 s^{-1}.

Biological environments generally provide low but rapidly replenishing concentrations of H_2O_2 that are closer to 0.6 mM than 10 mM.[50-52] We, therefore, anticipate that **1** would provide a fast r_1 response to physiologically generated H_2O_2 that is more similar to the one displayed in Figure 2.4B than in Figure 2.4A. Even with this in mind, it is uncertain whether the sensor will respond quickly enough to oxidant to activate before circulating out of an area with elevated levels of H_2O_2. Other challenges exist in translating probes such as **1** to the clinic. The non-ratiometric response of **1**, for instance, makes it difficult to distinguish regions under oxidative stress from sites that merely accumulate more of the pre-activated sensor. Although **2** and **3** seem to be reasonably tolerated by cells,[7-8] the potential toxicity of **1** also needs to be considered and assessed.

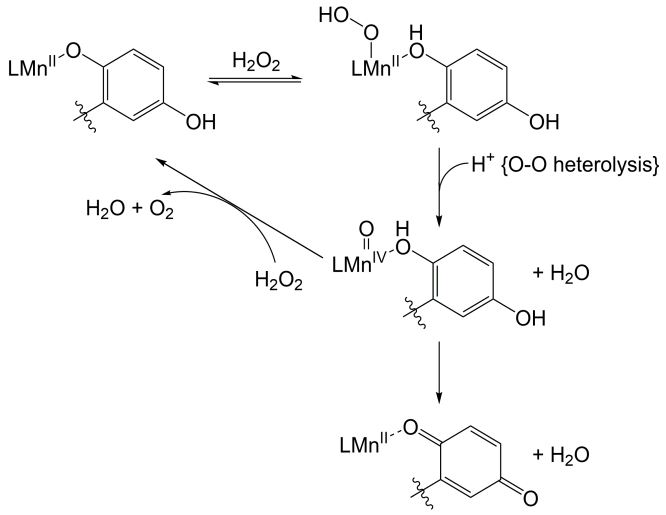

Scheme 2.5 Proposed competing catalase and quinol oxidation pathways.

2.5 Conclusions

A Mn(II) complex with a cyclam macrocycle derivatized with two quinols is a highly water-stable MRI contrast agent that displays a positive r_1 response to H_2O_2, one of the most prevalent reactive oxygen species in biology. The percentile relaxivity response is approximately four times that of a Mn(II) complex with a linear ligand that provides a similar set of donor atoms: two quinols/quinolates and four neutral N-donors. In addition to boosting the thermodynamic stability, the macrocycle also provides a kinetic barrier for metal ion dissociation, and the Mn(II) complex appears to retain the metal after the oxidation of the quinols to more poorly metal-binding *para*-quinones. The greater stability of the current complex addresses a key concern about other quinol-containing MRI contrast agent sensors that were previously prepared by our laboratory and should smooth the pathway towards using such complexes to monitor biologically relevant oxidative stress.

The reactivity with H_2O_2 appears to proceed through two competing pathways. With low H_2O_2 levels, intramolecular oxidation of the quinols to *para*-quinones occurs. This process appears to be slow relative to analogous reactions seen with manganese complexes with linear quinol-containing ligands. With high —and physiologically unrealistic— H_2O_2 concentrations, catalase activity is observed. Under such conditions, the quinol oxidation and the concomitant increase in r_1 only occur after much of the H_2O_2 has been consumed.

Appendix A

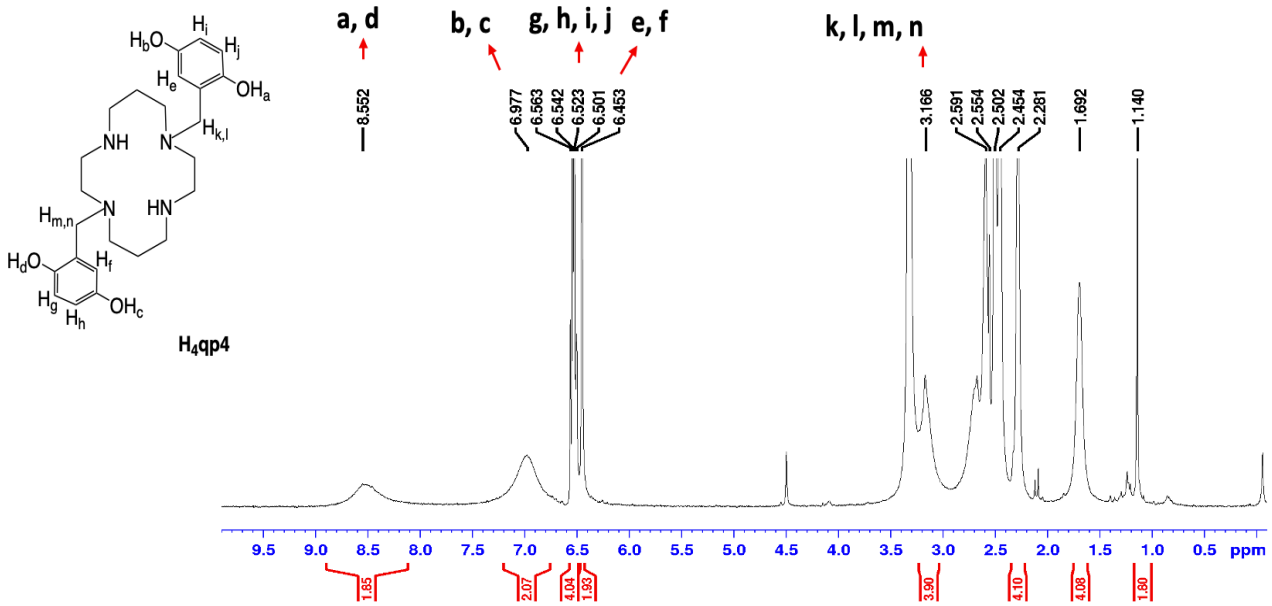

Figure A1. [1]H NMR spectrum of H_4qp4 in DMSO-*d6*. The peaks at ~6.6 ppm is assigned to the C-H protons on the quinol subunits. The peaks at ~6.97 and 8.55 ppm are assigned to the O-H protons on the quinol subunits.

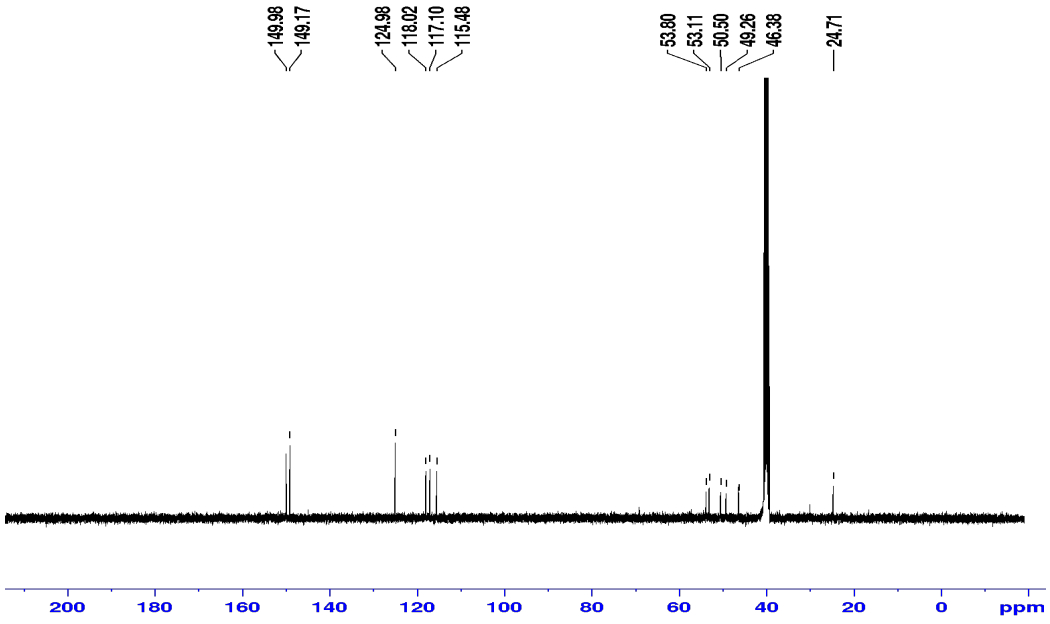

Figure A2. [13]C NMR spectrum of H_4qp4 in DMSO-*d6*.

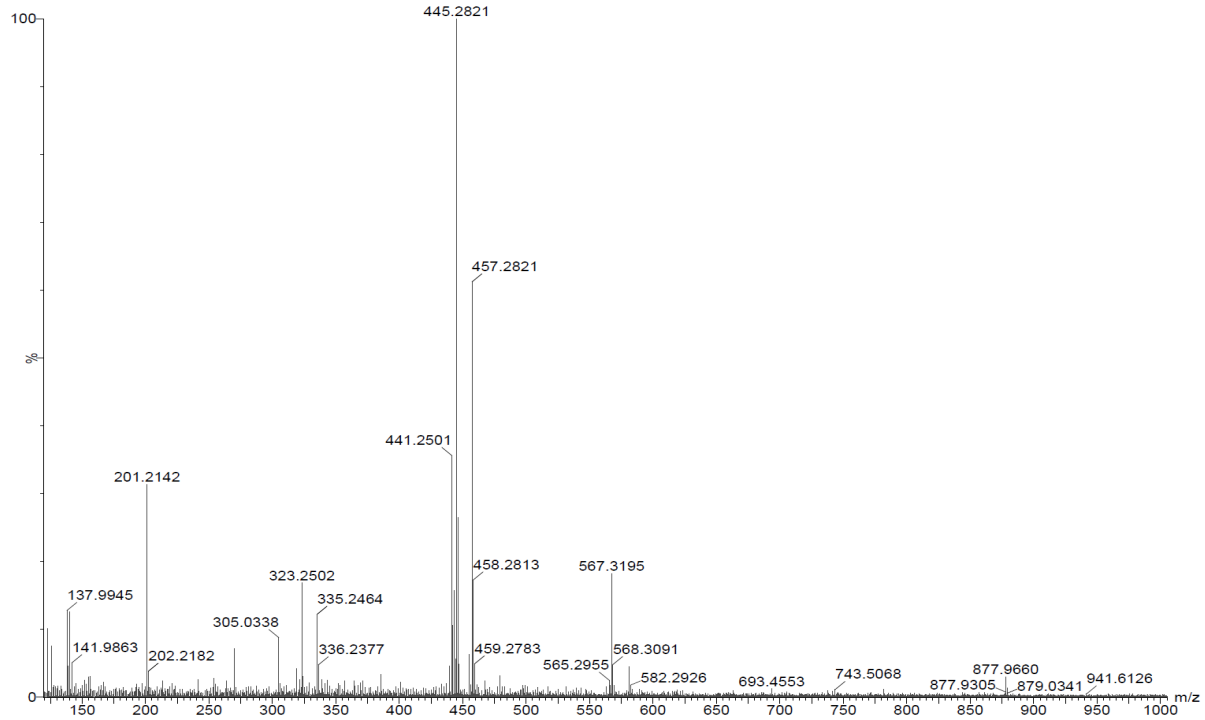

Figure A3. MS (ESI+) of H_4qp4 in MeCN. The 445.2821 *m/z* feature is assigned to the singly protonated ligand $(H_5qp4)^+$ (calculated *m/z* = 445.2815).

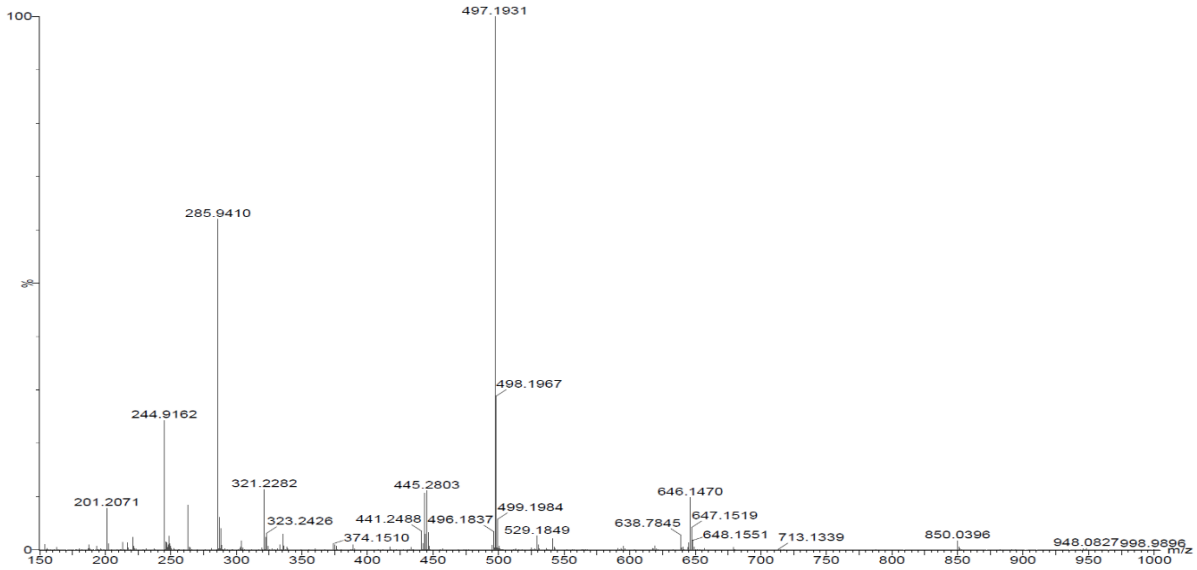

Figure A4. MS (ESI+) of $[Mn^{II}(H_3qp4)](OTf)$ (**1**) in MeCN. The 497.1931 *m/z* feature is assigned to a complex with the doubly deprotonated ligand, $[Mn(H_2qp4)]^+$ (calculated *m/z* = 497.1961). The 646.1470 *m/z* feature is assigned to $[Mn(H_2qp4)(OTf)]^+$ (calculated *m/z* = 646.1481).

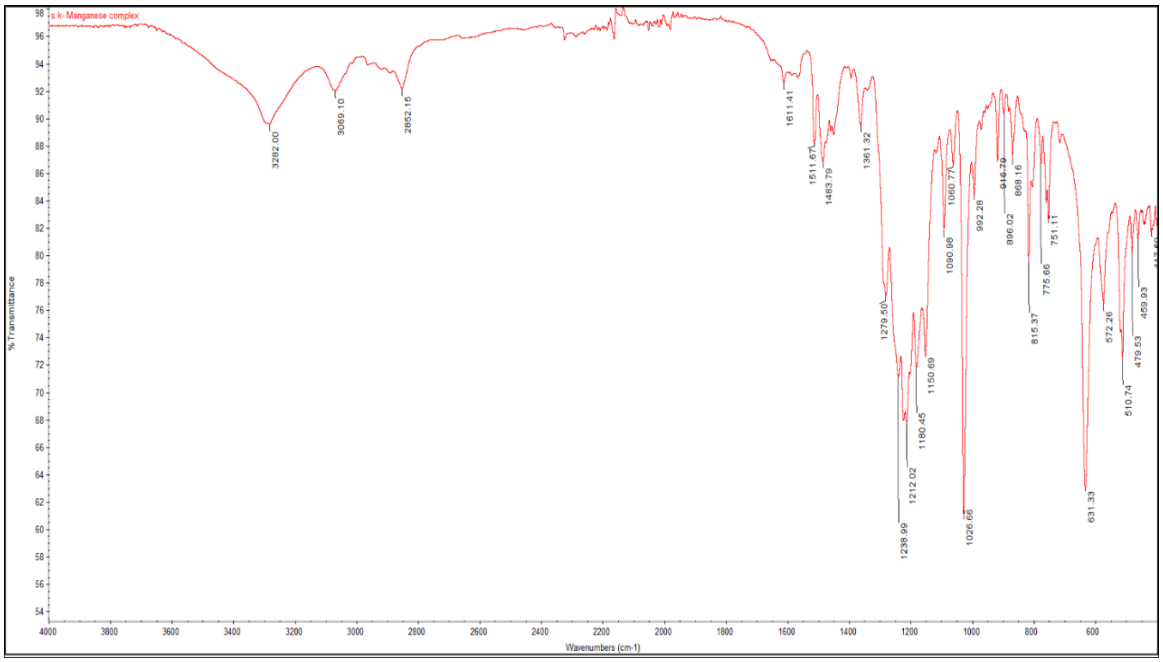

Figure A5. IR spectrum of **1**. The band at 3282 cm^{-1} is assigned to the O-H stretches for the quinol in the H_3qp4^- ligand.

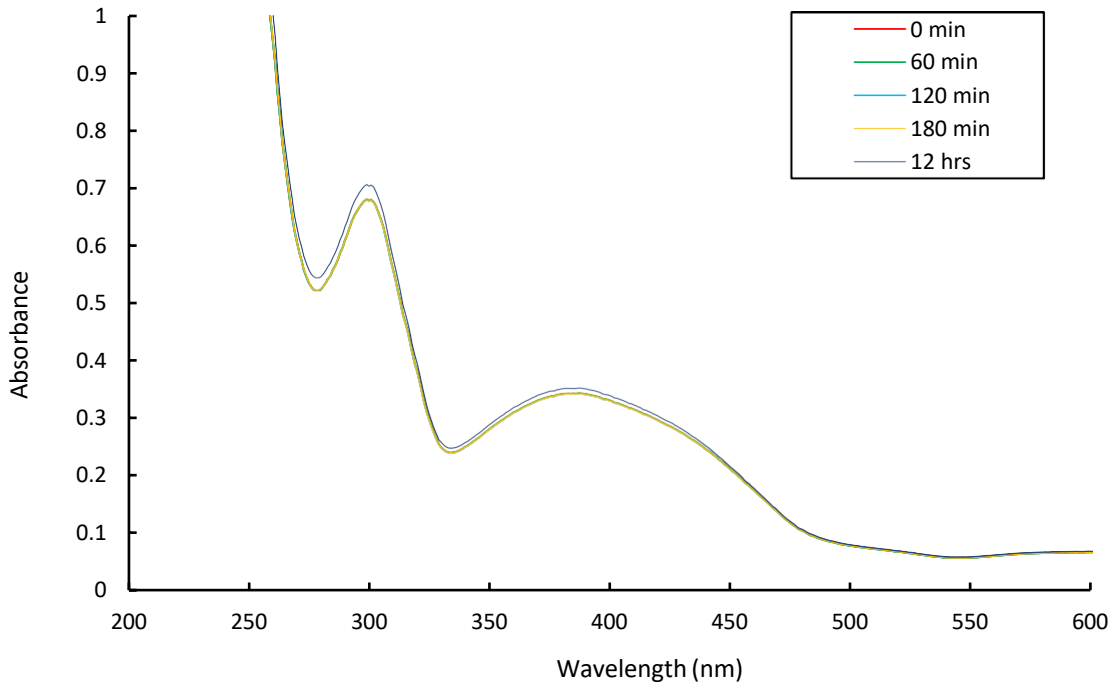

Figure A6. UV/vis spectra depicting the stability of a 0.10 mM solution of **1** in MeCN to air. The reaction was scanned at 0, 1, 2, 3, and 12 h. The band at 304 nm is characteristic of quinol functional groups, whereas the band at 388 nm is characteristic of a quinolate.

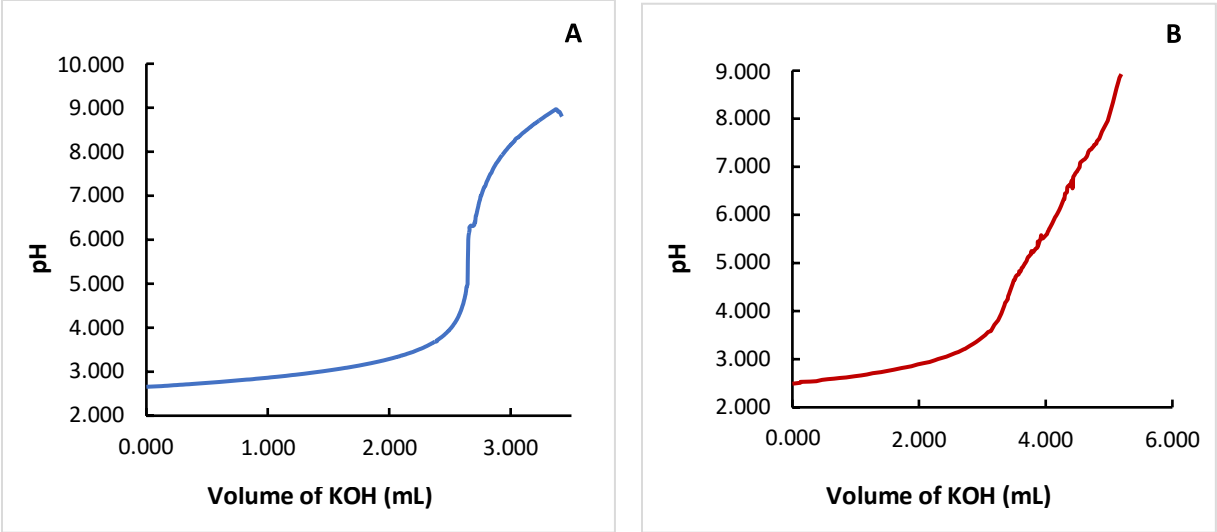

.

Figure A7. Raw potentiometric pH titration data for the addition of 0.08419 M KOH to acidic aqueous solutions containing 100 mM KCl and either A) 1.0 mM H_4qp4 or B) 1.0 mM **1**. Each titration was performed at 25 °C under an argon atmosphere

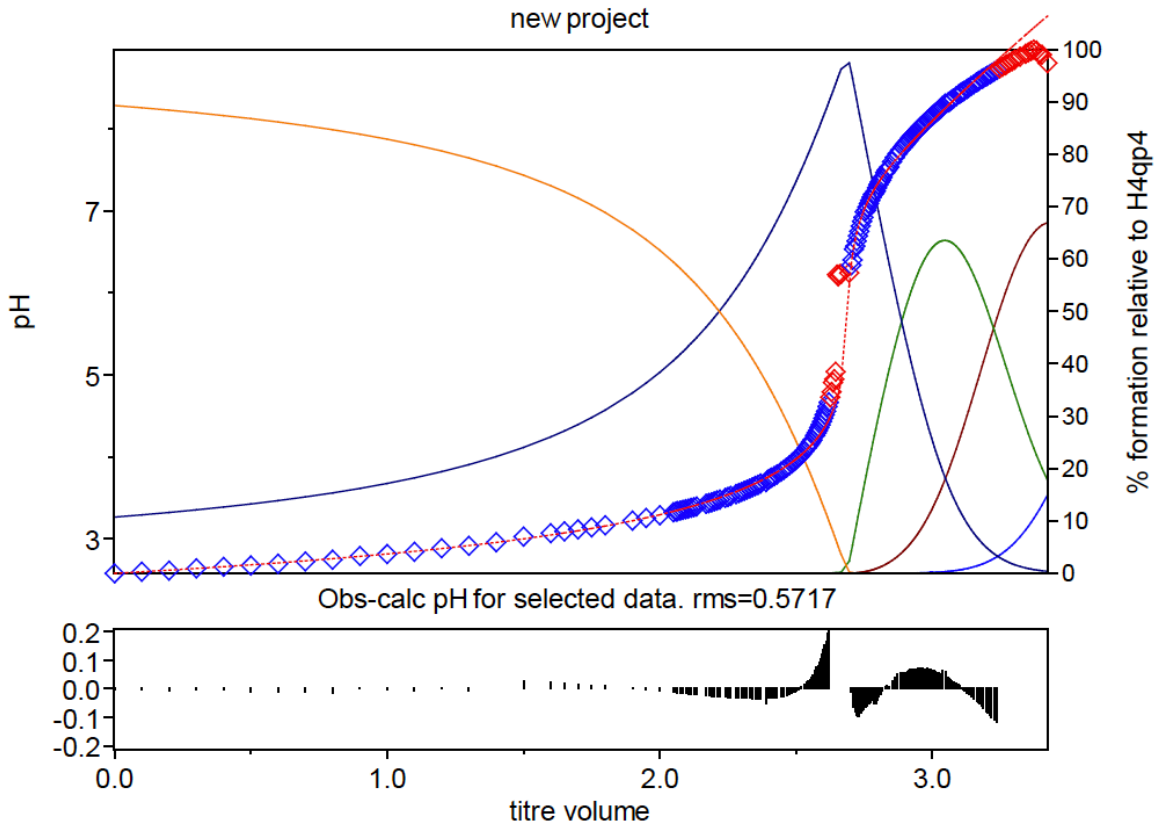

Figure A8. Hyperquad model (red line) overlaid on the experimental data from the potentiometric titration of H_4qp4 (blue). The data above pH 9.5 have been excluded from the calculations since precipitation was observed above this value. The parameters for the Hyperquad model are provided on Table A1. The residuals for the fit are provided below. The curves represent the formation of various species including H_2qp4^{2-} (blue), H_3qp4^{-} (brown), H_4qp4 (pine green), H_5qp4^{+} (indigo), and H_6qp4^{2+} (orange).

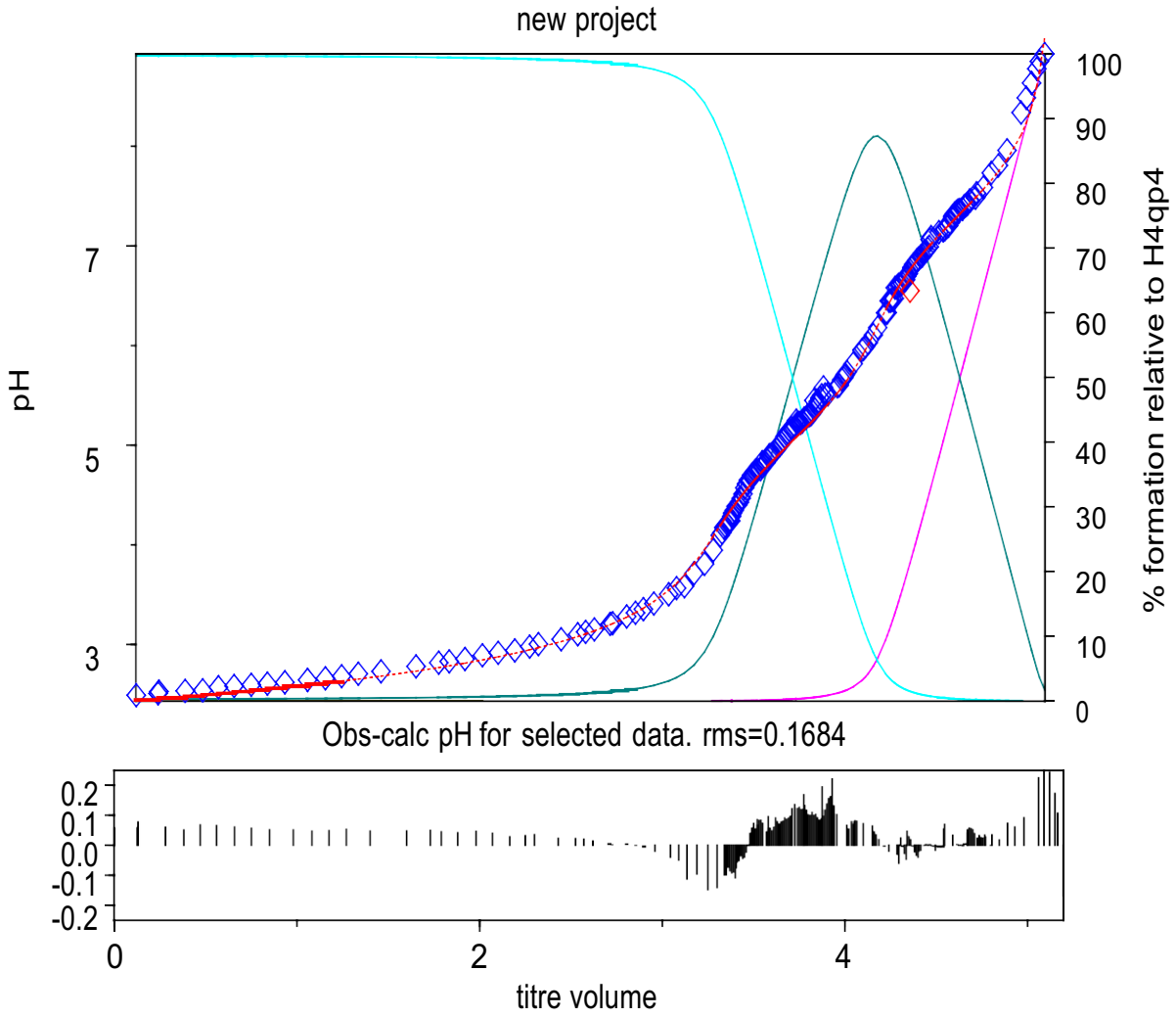

Figure A9. Hyperquad model (red line) overlaid on the experimental data from the potentiometric titration of **1** (blue). The data above pH 9 have been excluded from the calculations since precipitation was observed above this value. The parameters for the Hyperquad model are provided on Table A1. The fit assumes an initial total of 0.178 mmol H^+. The residuals for the fit are provided below. The curves represent the formation of various speciesincluding $[Mn^{II}(H_2qp4)]$ (purple), $[Mn^{II}(H_3qp4)]^+$ (pine green), and $[Mn^{II}(H_4qp4)]^{2+}$ (light blue).

Table A1. Parameters for the Hyperquad model used in Figure **A8** and **A9**.

Species	Mn(II)	H_4qp4	H^+	log(β)	Derived Values
$\mathbf{H_2}$qp4^{2-}	0	1	-2	12.480	
$\mathbf{H_3}$qp4^{-}	0	1	-1	22.504	pK_{L4} = 10.02 (±0.05)[a]
$\mathbf{H_4}$qp4	0	1	0	31.300	pK_{L3} = 8.80 (±0.05)[a]
$\mathbf{H_5}$qp4^{+}	0	1	1	39.005	pK_{L2} = 7.70 (±0.05)[a]
$\mathbf{H_6}$qp4^{2+}	0	1	2	42.506	pK_{L1} = 3.50 (±0.05)[a]
[Mn($\mathbf{H_2}$qp4)]	1	1	-2	33.330	log K_{ML} (Mn(H_2qp4)) = 20.85[c]
[Mn($\mathbf{H_3}$qp4)]$^{+}$	1	1	-1	40.721	pK_a(Mn(H_3qp4)$^{+}$) = 7.39 (±0.05)[b] log K_{ML} (Mn(H_3qp4))$^{+}$ = 18.22[c]
[Mn($\mathbf{H_4}$qp4)]$^{2+}$	1	1	0	45.816	pK_a(Mn(H_4qp4)$^{2+}$) = 5.10 (±0.05)[b] log K_{ML} (Mn(H_4qp4))$^{2+}$ = 14.52[c]

[a]Ligand pKa values:

K_{L1} = [H_5qp4^{+}][H^+]/[H_6qp4^{2+}], pK_{L1} = logβ_{012} – logβ_{011}
K_{L2} = [H_4qp4][H^+]/[H_5qp4^{+}], pK_{L2} = logβ_{011} – logβ_{010}
K_{L3} = [H_3qp4^{-}][H^+]/[H_4qp4], pK_{L3} = log$_{\beta 010}$ – log$\beta_{01(-1)}$
K_{L4} = [H_2qp4^{2-}][H^+]/[H_3qp4^{-}], pK_{L4} = log$\beta_{01(-1)}$ – log$\beta_{01(-2)}$

[b]Metal complex pK_a values:

K_a(Mn(H_4qp4)$^{2+}$) = [Mn(H_3qp4)$^{+}$][H^+]/[Mn(H_4qp4)$^{2+}$] {deprotonation of first quinol}
pK_a(Mn(H_4qp4)$^{2+}$) = log$_{\beta 110}$ – log$\beta_{11(-1)}$
K_a(Mn(H_3qp4)$^{+}$) = [Mn(H_2qp4)][H^+]/[Mn(H_3qp4)$^{+}$] {deprotonation of second quinol}
pK_a(Mn(H_3qp4)$^{+}$) = log$\beta_{11(-1)}$ – log$\beta_{11(-2)}$

[c]Metal complex K_{ML} values:

K_{ML} (Mn(H_2qp4)) = [Mn(H_2qp4)]/([Mn(II)][H_2qp4^{2-}])
log K_{ML} (Mn(H_2qp4)) = log$_{\beta 11(-2)}$ – log$_{\beta 01(-2)}$
K_{ML} (Mn(H_3qp4))$^{+}$ = [Mn(H_3qp4)$^{+}$]/([Mn(II)][H_3qp4^{-}])
log K_{ML} (Mn(H_3qp4))$^{+}$ = log$_{\beta 11(-1)}$ – log$_{\beta 01(-1)}$
K_{ML} (Mn(H_4qp4))$^{2+}$ = [Mn(H_4qp4)$^{2+}$]/([Mn(II)][H_4qp4])
log K_{ML} (Mn(H_4qp4))$^{2+}$ = logβ_{110} – logβ_{010}

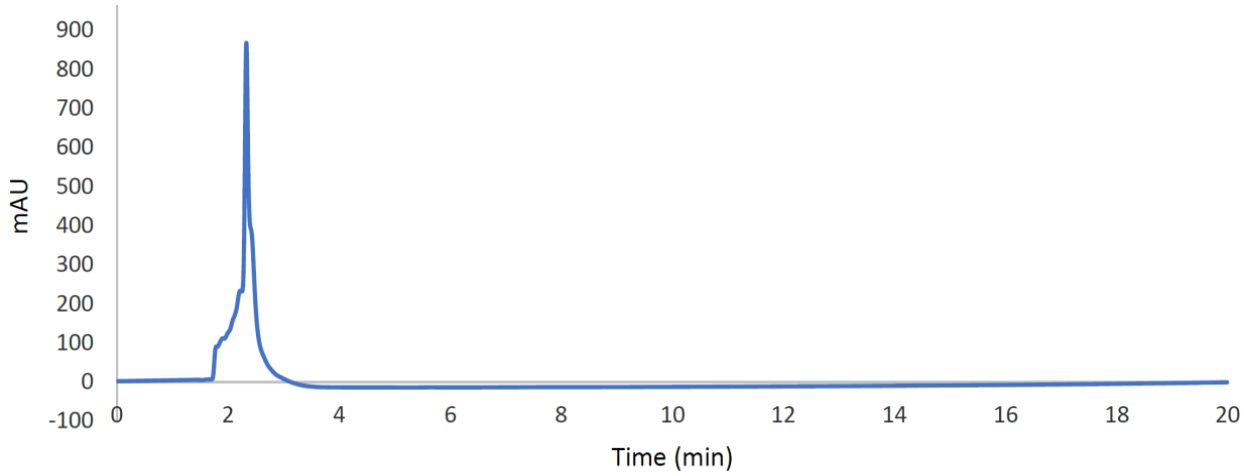

Figure A10. LC trace for the free H_4qp4 ligand run under Method **1**. The ligand elutes at 2.33 min.

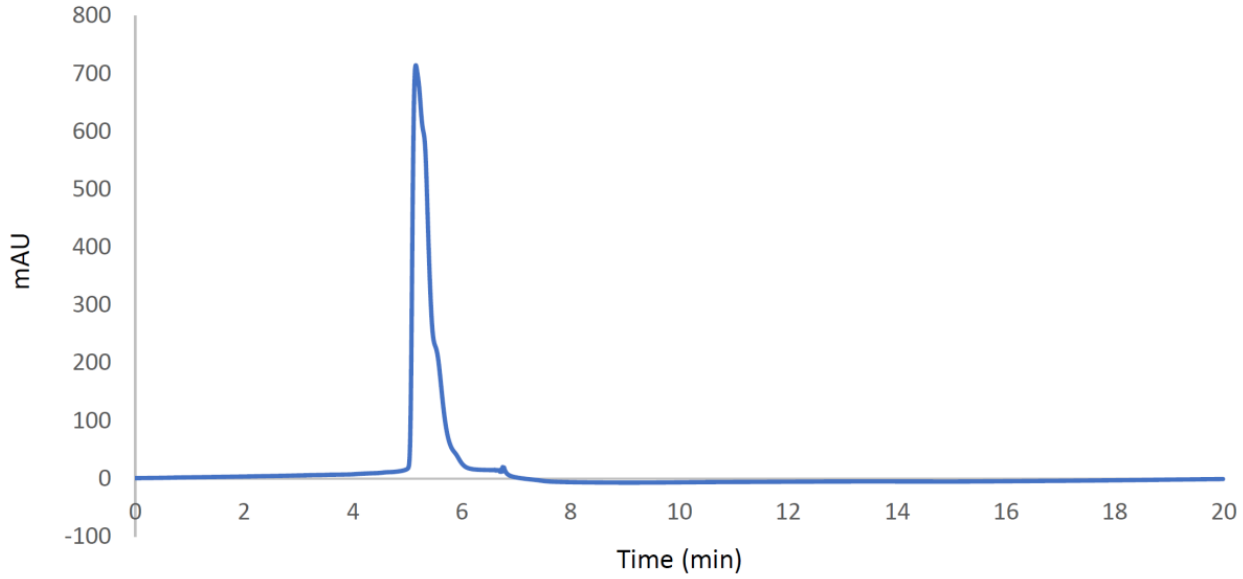

Figure A11. LC trace for $[Mn^{II}(H_3qp4)]^+$ run under Method **1**. The Mn(II) complex elutes at 5.22 min.

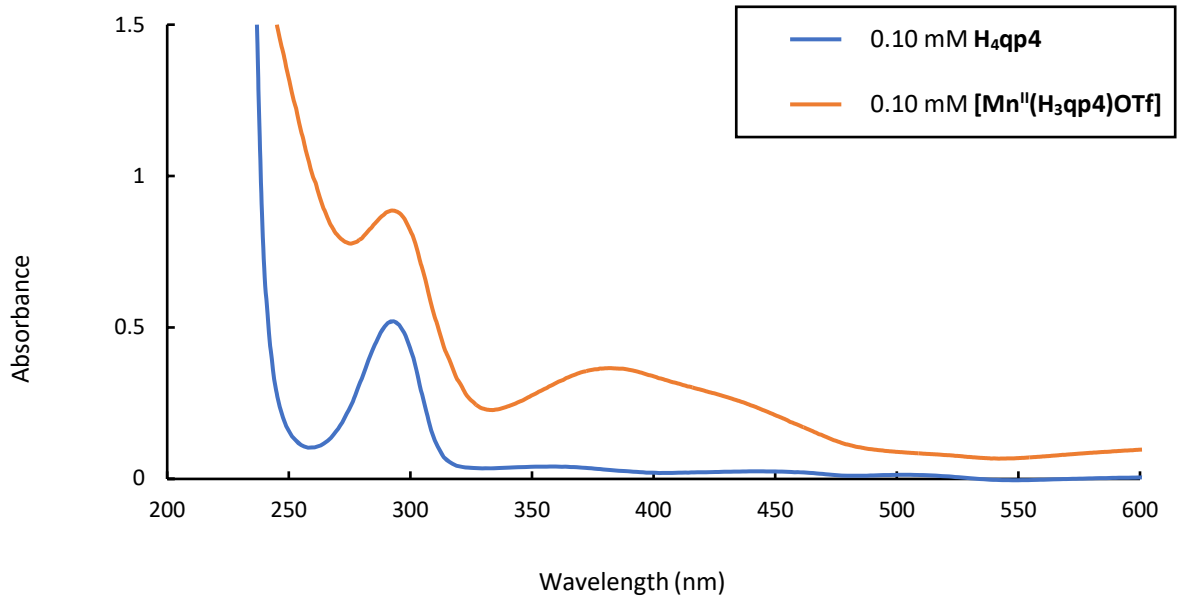

Figure A12. UV/vis spectra of 0.10 mM solutions of H_4qp4 and **1** in aqueous solutions containing 50 mM HEPES buffered to pH 7.00. The data indicate that the H_4qp4 ligand has been deprotonated to H_3qp4$^-$ in complex 1.

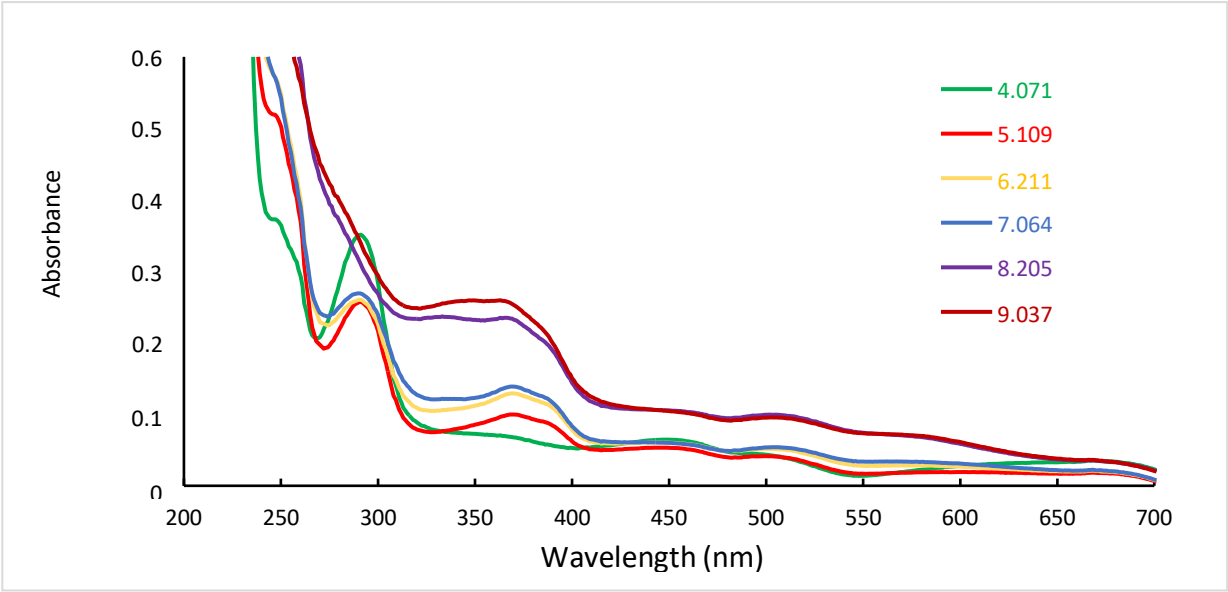

Figure A13. UV/vis spectra of a 0.05 mM solution of **1** in water adjusted to various pH values between 4 and 9 through the addition of either KOH or HCl. All spectra were obtained at 298 K under air using a 1.0 cm pathlength cuvette.

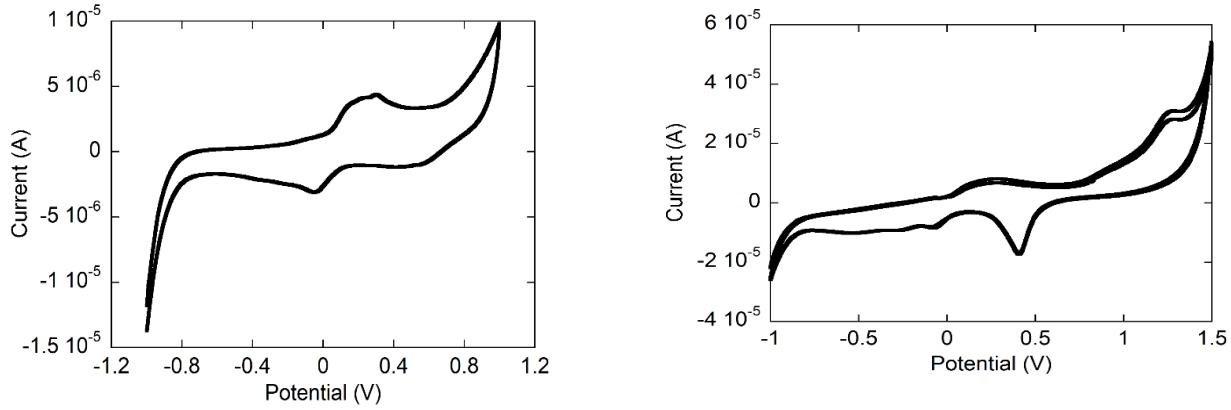

A **B**

Figure A14. Cyclic voltammetry of 1.0 mM **1** in 0.10 M phosphate buffer (NaH_2PO_4/Na_2HPO_4, pH = 7.2). The scan rate was 100 mV/s. For the redox event in panel A: $E_{1/2}$ = 100 mV *vs.* Ag/AgCl, ΔE = 260 mV. An irreversible feature with Ep_a = 1250 mV is also observed when the window is extended (B), but this appears to lead to the oxidation of the buffer as well; the additional feature at ~400 mV is also observed in the CV of a blank sample containing phosphate buffer.

A

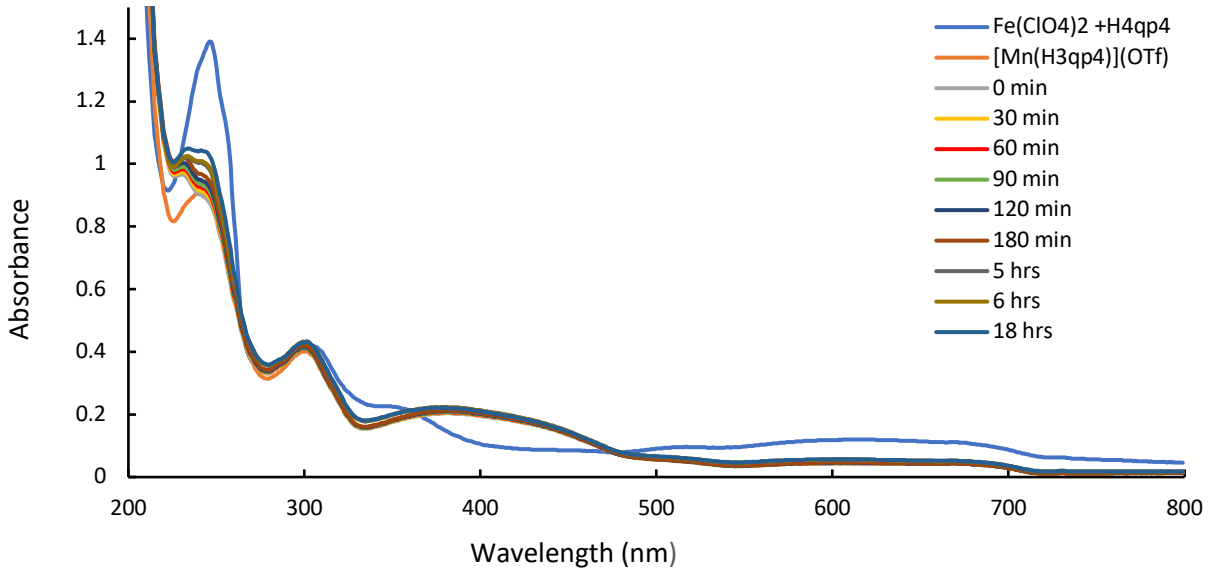

B

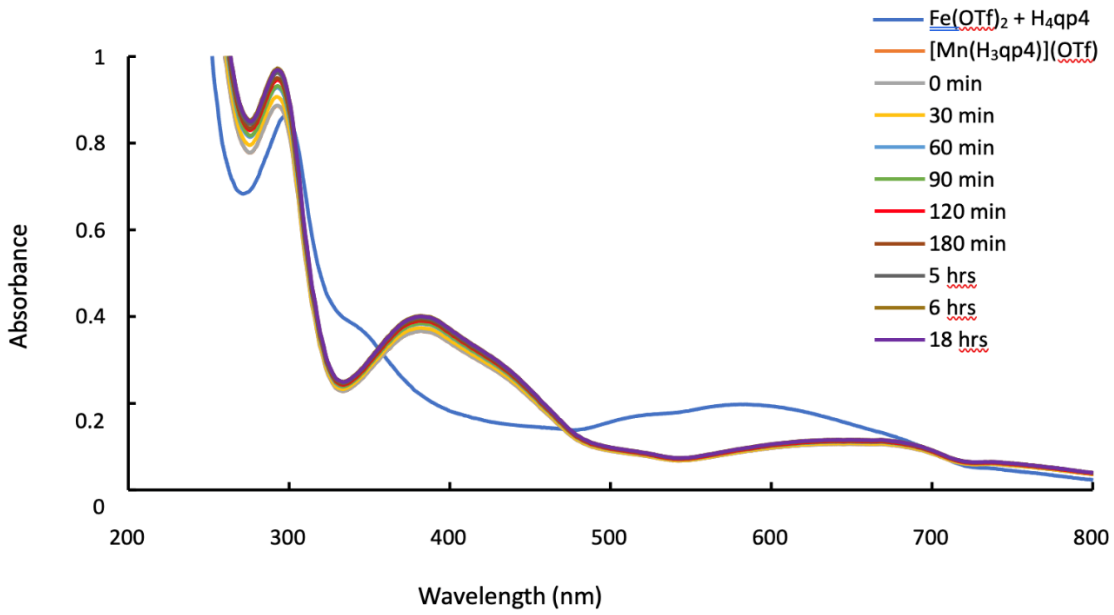

Figure A15. A) Spectrophotometric analysis of the reaction between 0.1 mM $Fe^{II}(ClO_4)_2$ and 0.1 mM **1** in MeCN at 298 K. The UV/vis spectra of the product formed from 0.1 mM $Fe^{II}(ClO_4)_2$ and 0.1 mM H_4qp4 (blue) and that corresponding to 0.1 mM **1** are provided for comparison. B) Spectrophotometric analysis of the reaction between 0.1 mM $Fe^{II}(OTf)_2$ and 0.1 mM **1** in aqueous solutions containing 50 mM HEPES buffered to pH 7.00 at 298 K. The UV/vis spectrum of the product formed from 0.1 mM $Fe^{II}(OTf)_2$ and 0.1 mM Hqp4 (blue) and that corresponding to 0.1 mM **1** are provided for comparison.

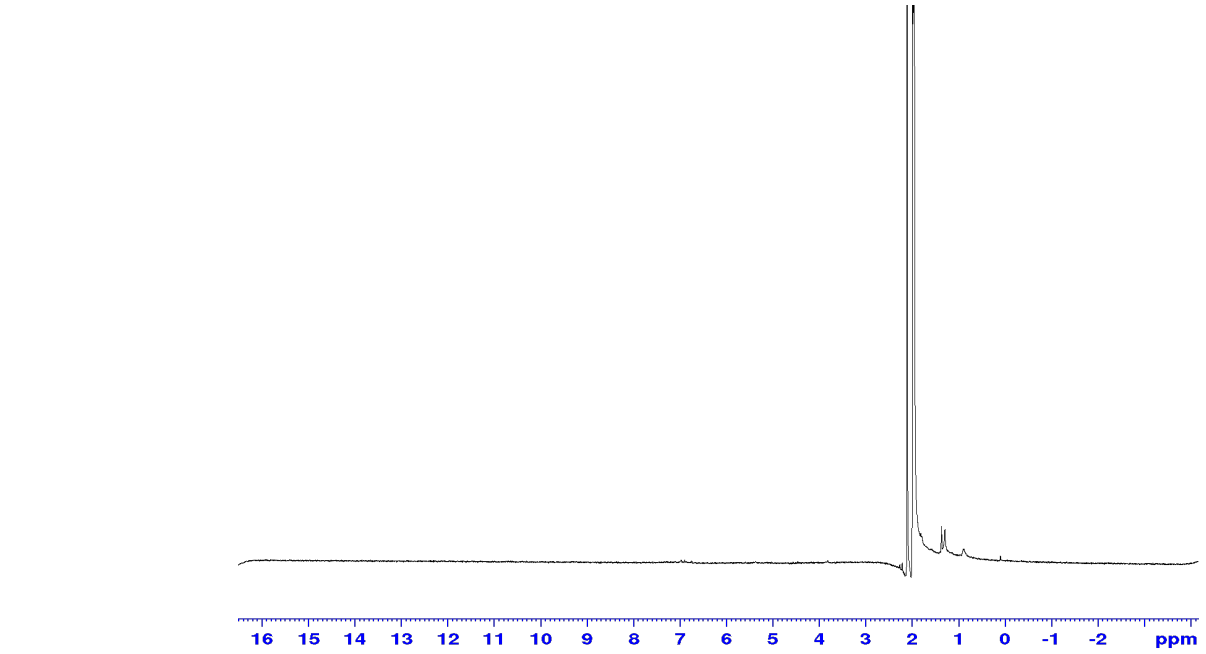

A

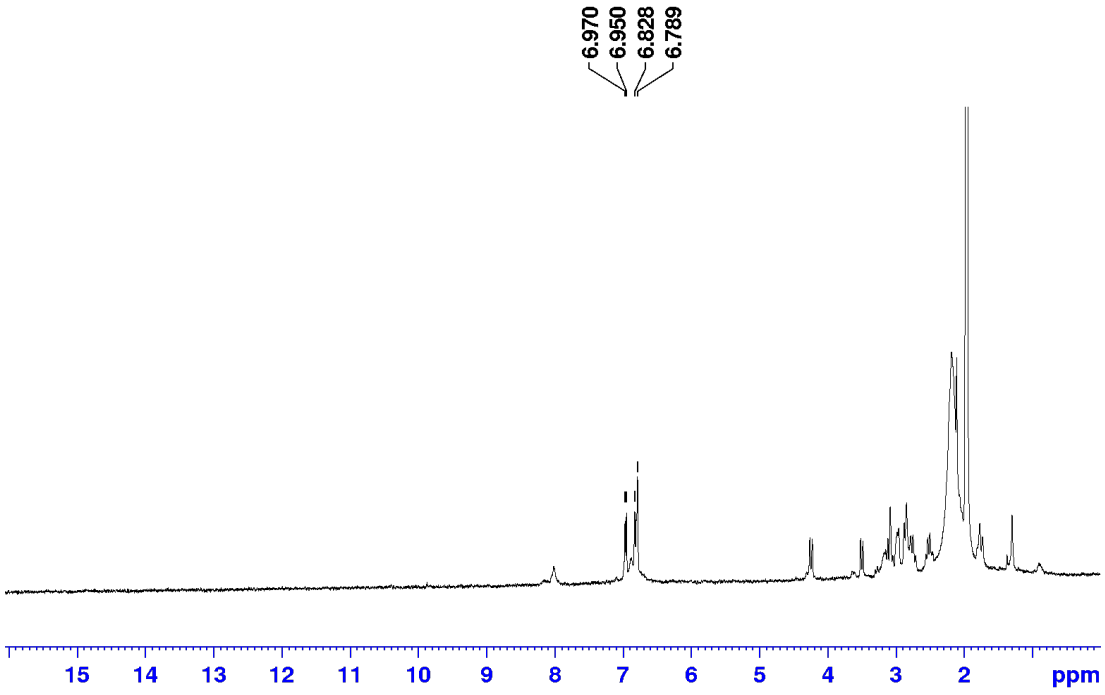

B

Figure A16. A) Reaction between 20 mM $Zn(ClO_4)_2$ and 10 mM **1** in CD_3CN. The reaction equilibrated at 295 K for 24 h prior to data acquisition. B) ^1H NMR spectrum of the product of the reaction between 10 mM $Zn(ClO_4)_2$ and 10 mM metal-free H4qp4.

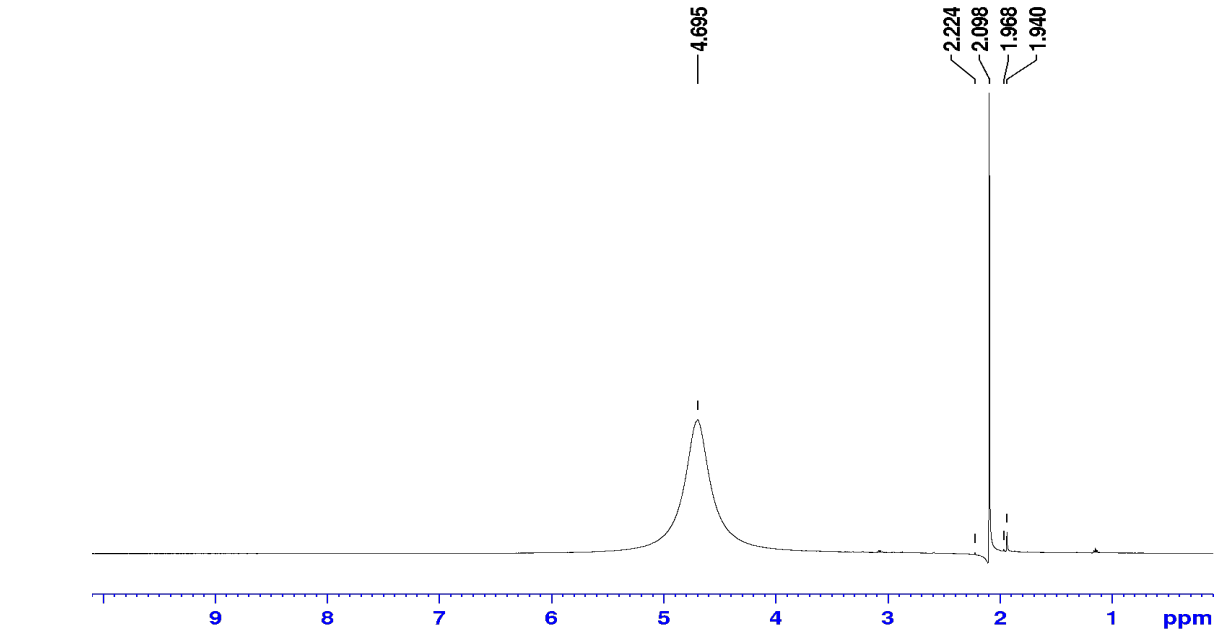

C

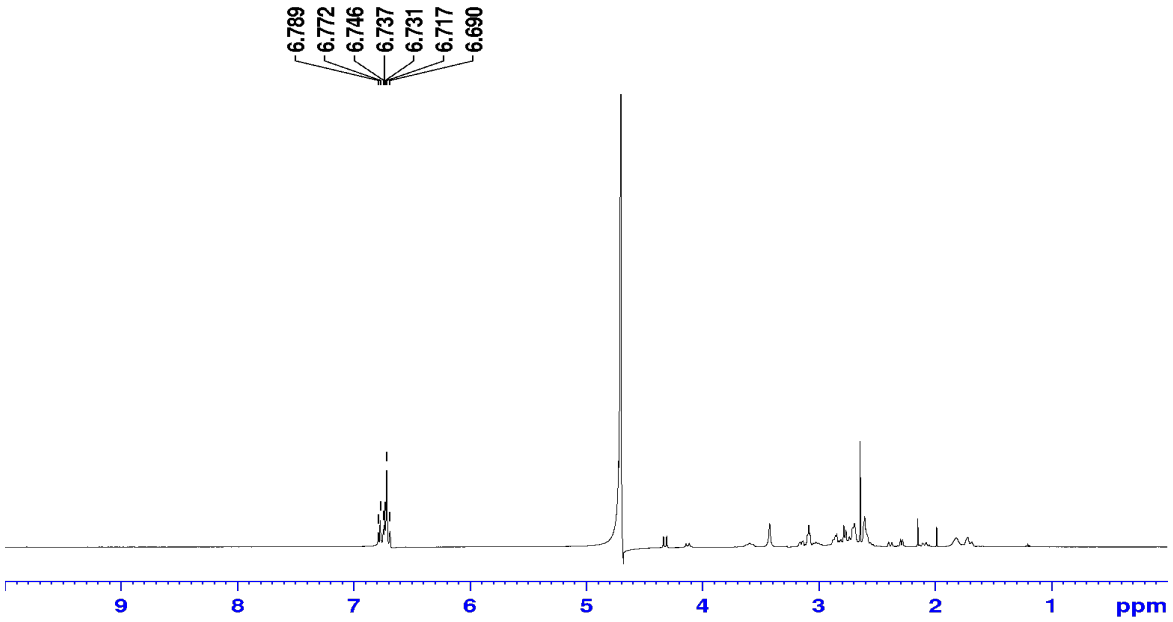

D

Figure A16 (continued). C) Reaction between 20 mM $Zn(ClO_4)_2$ and 10 mM **1** in D_2O. The reaction equilibrated at 295 K for 24 h prior to data acquisition. D) ^1H NMR spectrum of the product of the reaction between 10 mM $Zn(ClO_4)_2$ and 10 mM metal-free H_4qp4 in D_2O.

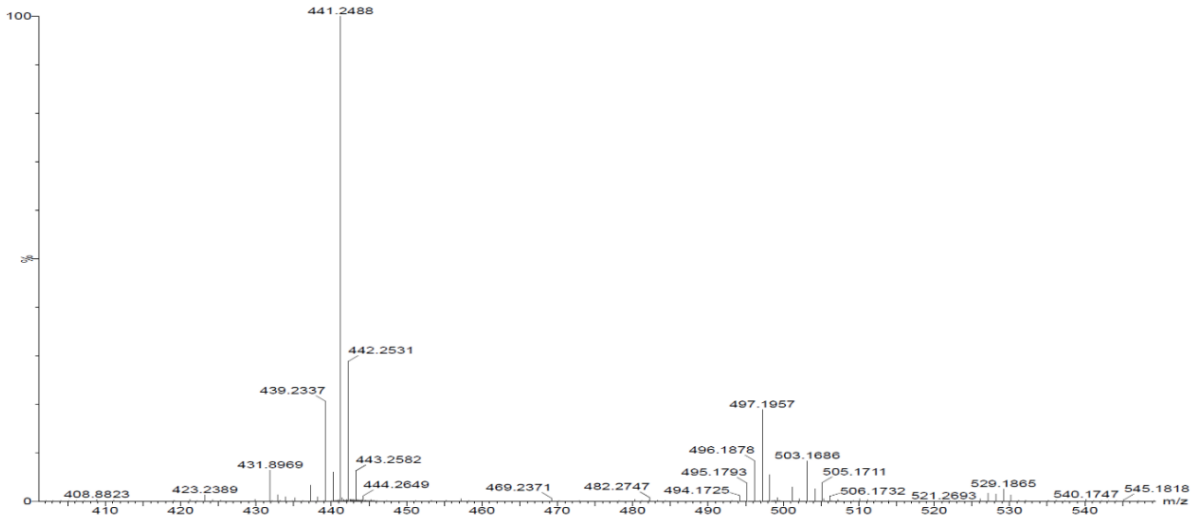

Figure A17. MS (ESI+) of the product of the reaction between **1** and 2,3-dichloro-5,6-dicyano-1,4-benzoquinone (DDQ) in MeCN. The *m/z* features at 495.1793, 496.1878, and 497.1957 are assigned to complexes with partially or fully oxidized ligands: $[Mn(qp4)]^+$ (calculated *m/z* = 495.1804), $[Mn(Hqp4)]^+$ (calculated *m/z* = 496.1883), and $[Mn(H_2qp4)]^+$ (calculated *m/z* =497.1961). The *m/z* feature at 441.2488 is assigned to the monoprotonated form of the fully oxidized ligand, $(Hqp4)^+$ (calculated *m/z* = 441.2502).

Figure A18. IR spectrum of the product of the reaction between **1** and DDQ. The 1656 cm^{-1} band is assigned to the C=O stretches of the *para*-quinone portions of the ligand.

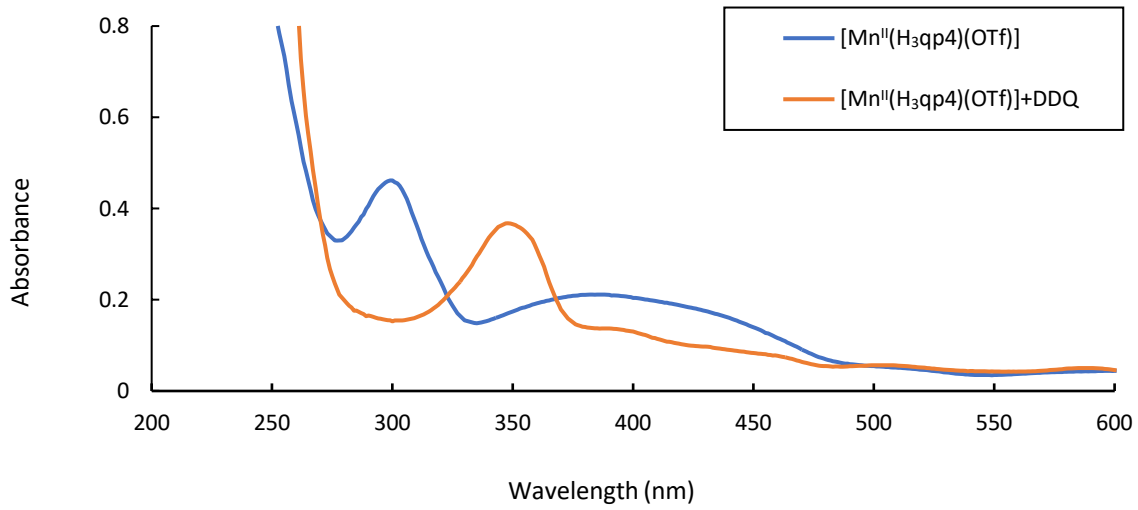

Figure A19. UV/vis spectra of a 0.10 mM solutions of **1** in MeCN before and after the addition of 1 equiv. of DDQ. The peak at 350 nm is from the reduced DDQ.

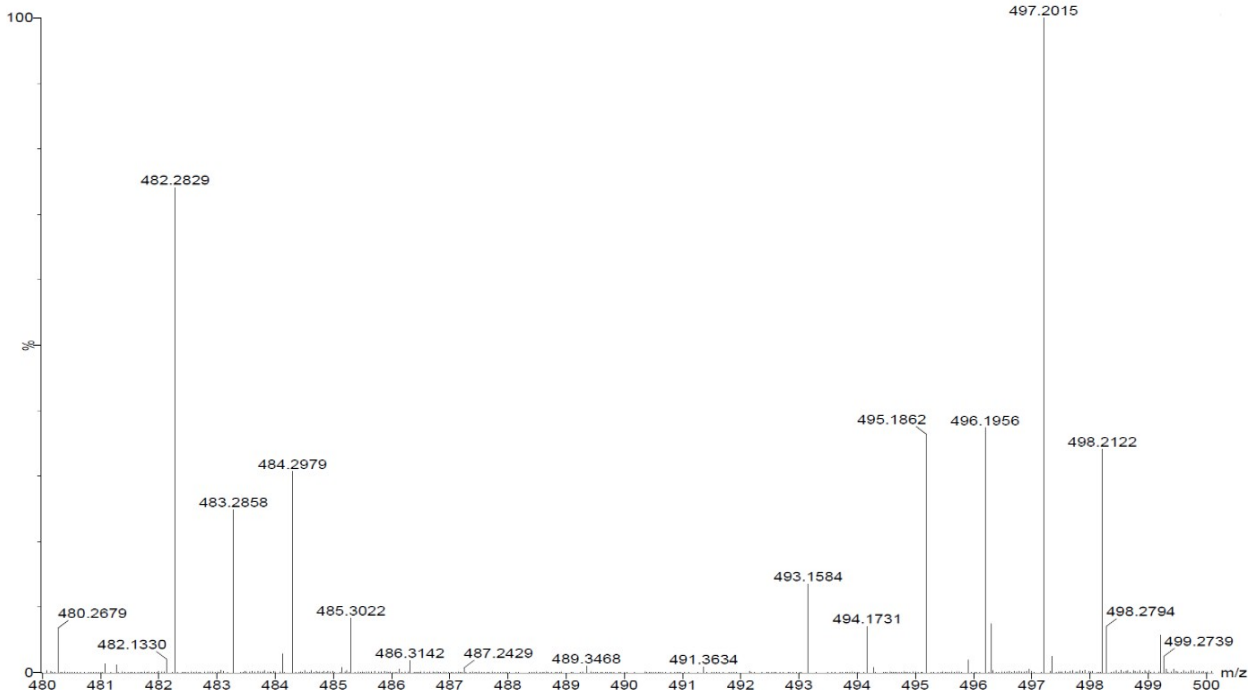

Figure A20. Mass spectrometry (ESI) of a mixture of **1** in MeCN and 10 equiv. of H_2O_2. The reaction was allowed to proceed for 10 min. The 495.1862 *m/z* feature is assigned to $[Mn(qp4)]^+$ (calculated *m/z* = 495.1804), the complex with the fully oxidized (diquinone) form of the ligand. The 496.1956 *m/z* feature is assigned to $[Mn(Hqp4)]^+$ (calculated *m/z* = 496.1883), the complex with the singly oxidized and singly deprotonated (monoquinone/quinolate) form of the ligand. The 497.2015 *m/z* feature is assigned to $[Mn(H_2qp4)]^+$ (calculated *m/z* = 497.1961), which could be either the complex with the singly oxidized but protonated form of the ligand (monoquinone/quinol) or the doubly deprotonated reduced form of the ligand (diquinolate).

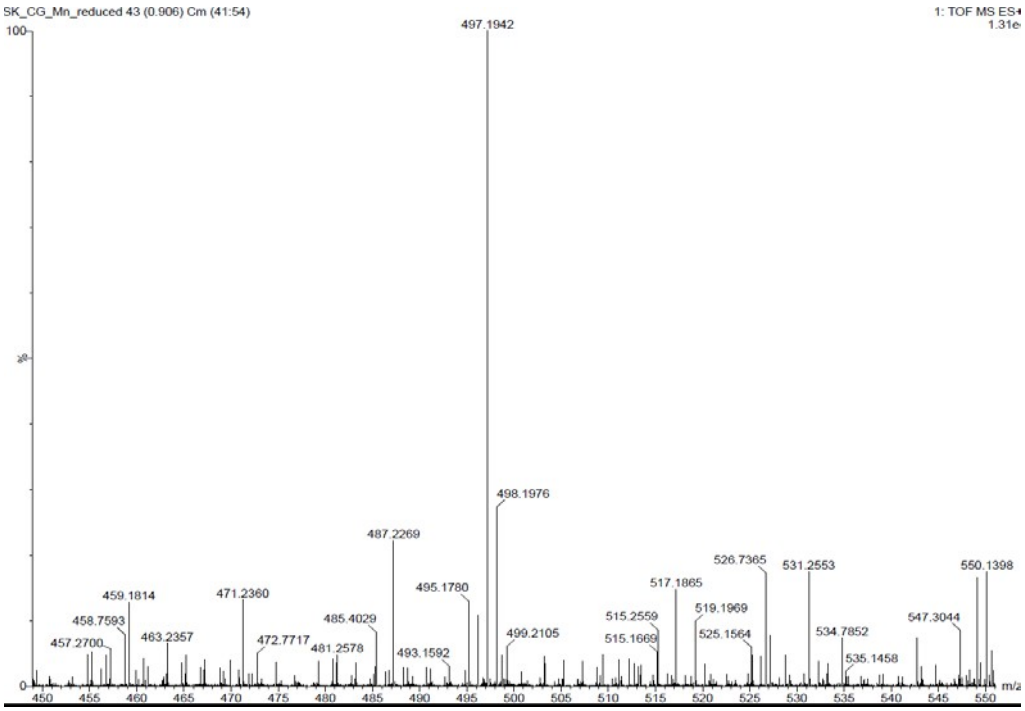

Figure A21. Mass spectrometry (ESI) a sample of **1** that was sequentially oxidized by H_2O_2 and reduced by sodium dithionite ($Na_2S_2O_4$). Complex **1** first reacted with 4 equiv. of H_2O_2 for 60 min at RT in MeOH. The solvent and excess H_2O_2 was removed, and the crude was allowed to react with 4 equiv. of $Na_2S_2O_4$ for an additional 60 min. The 497.1942 *m/z* feature is assigned to $[Mn(H_2qp4)]^+$ (calculated *m/z* =497.1961).

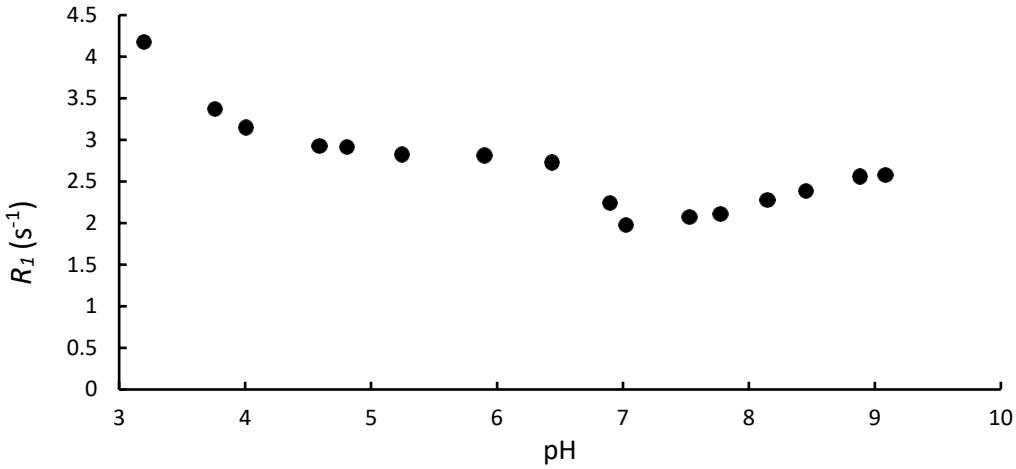

Figure A22. Plot of R_1 ($1/T_1$) versus pH for a 0.50 mM solution of **1** in unbuffered water. The pH was controlled via the addition of HCl and KOH. All samples were analyzed at 298 K using a 3T field provided by a clinical MRI scanner. Slight precipitation is observed above pH 8.5.

Start Time: 0 s, End Time: 1.271 s, Catalase Activity during this time : 1.530

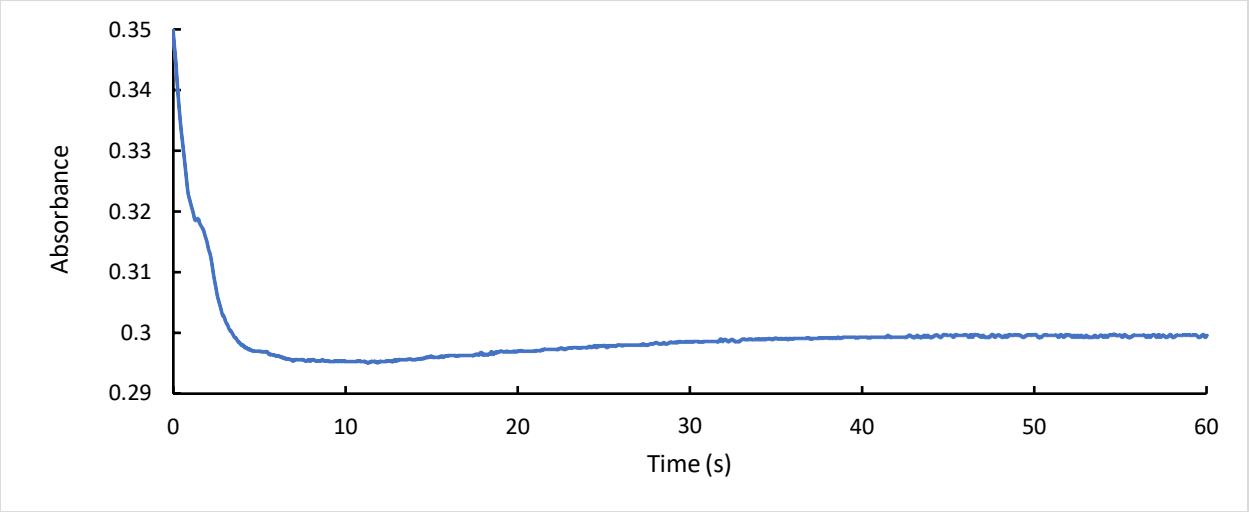

Start Time: 0 s, End Time: 3.001 s, Catalase Activity during this time : 1.540

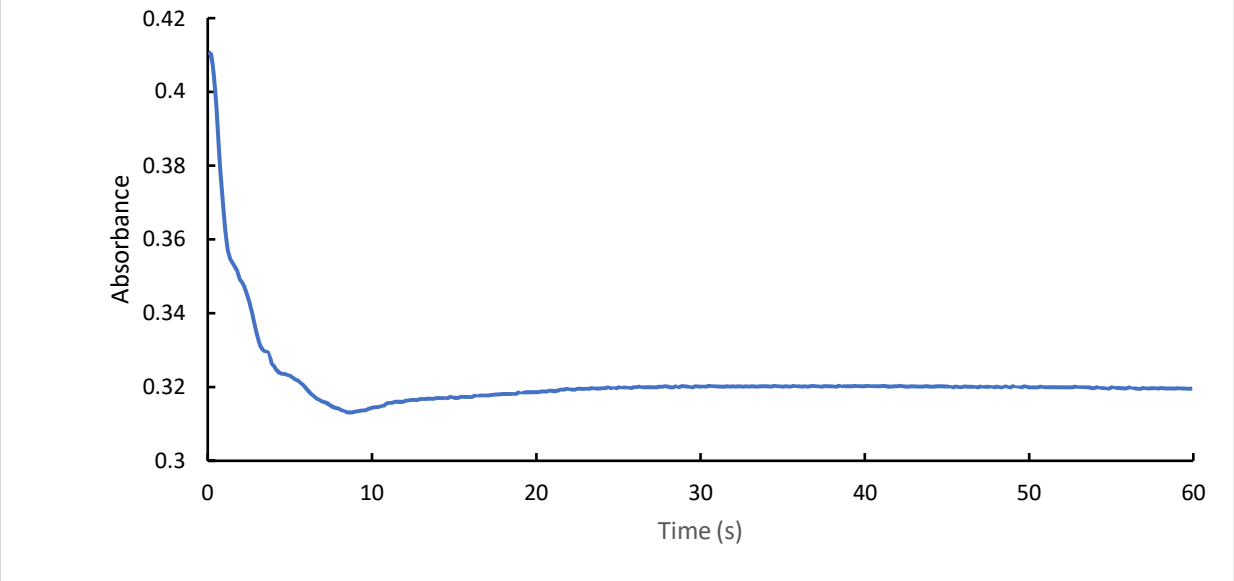

Figure A23. Representative kinetic traces for the reaction between 100 nM **1** and 10 mM H_2O_2 in 200 mM phosphate solution buffered to pH 7.0. The absorbance at 240 nm was monitored over time. Activity values were calculated using the UV-1601PC Kinetics program and converted to an initial rate (v_o/[**1**]$_T$) using the following equation:

v_o/[**1**]T = (activity)/[60 s × 0.1 μM × 0.0000394 μM^{-1} cm^{-1} × 1.0 cm]

References

1. Tretter, L.; Sipos, I.; Adam-Vizi, V. *Neurochem. Res.* **2004,** 29, 569-577.

2. Roberts, C. K.; Sindhu, K. K. *Life Sci.* **2009,** 84, 705-712.

3. Mosley, R. L.; Benner, E. J.; Kadiu, I.; Thomas, M.; Boska, M. D.; Hasan, K.; Laurie, C.; Gendelman, H. E. *Clin. Neurosci. Res.* **2006,** 6, 261-281.

4. Fearon, I. M.; Faux, S. P. *J. Mol. Cell. Cardiol.* **2009,** 47, 372-381.

5. Eskici, G.; Axelsen, P. H. *Biochemistry* **2012,** 51, 6289-6311.

6. Yu, M.; Beyers, R. J.; Gorden, J. D.; Cross, J. N.; Goldsmith, C. R. *Inorg. Chem.* **2012,** 51, 9153-9155.

7. Yu, M.; Ambrose, S. L.; Whaley, Z. L.; Fan, S.; Gorden, J. D.; Beyers, R. J.; Schwartz, D. D.; Goldsmith, C. R. *J. Am. Chem. Soc.* **2014,** 136, 12836-12839.

8. Yu, M.; Ward, M. B.; Franke, A.; Ambrose, S. L.; Whaley, Z. L.; Bradford, T. M.; Gorden, J. D.; Beyers, R. J.; Cattley, R. C.; Ivanović-Burmazović, I.; Schwartz, D. D.; Goldsmith, C. R. *Inorg. Chem.* **2017,** 56, 2812-2826.

9. Hutchinson, T. E.; Bashir, A.; Yu, M.; Beyers, R. J.; Goldsmith, C. R. *Inorg. Chim. Acta* **2019,** 496, 119045.

10. Wang, H.; Jordan, V. C.; Ramsay, I. A.; Sojoodi, M.; Fuchs, B. C.; Tanabe, K. K.; Caravan, P.; Gale, E. M. *J. Am. Chem. Soc.* **2019,** 141, 5916-5925.

11. Loving, G. S.; Mukherjee, S.; Caravan, P. *J. Am. Chem. Soc.* **2013,** 135, 4620-4623.

12. Gale, E. M.; Mukherjee, S.; Liu, C.; Loving, G. S.; Caravan, P. *Inorg. Chem.* **2014,** 53, 10748-10761.

13. Caravan, P.; Ellison, J. J.; McMurry, T. J.; Lauffer, R. B. *Chem. Rev.* **1999,** 99, 2293-2352.

14. Drahoš, B.; Lukeš, I.; Tóth, É. *Eur. J. Inorg. Chem.* **2012,** 2012, 1975-1986.

15. Chen, H.; Tang, X.; Gong, X.; Chen, D.; Li, A.; Sun, C.; Lin, H.; Gao, J. *Chem. Commun.* **2020,** 56, 4106-4109.

16. Hubin, T. J. *Coord. Chem. Rev.* **2003,** 241, 27-46.

17. Bain, G. A.; Berry, J. F. *J. Chem. Educ.* **2008,** 85, 532-536.

18. Gans, P.; Sabatini, A.; Vacca, A. *Talanta* **1996,** 43, 1739-1753.

19. Gale, E. M.; Zhu, J.; Caravan, P. *J. Am. Chem. Soc.* **2013,** 135, 18600-18608.

20. Zhang, Q.; Gorden, J. D.; Beyers, R. J.; Goldsmith, C. R. *Inorg. Chem.* **2011,** 50, 9365-9373.

21. Bernstein, M. A.; King, K. F.; Zhou, X. J. *Handbook of MRI Pulse Sequences*. Elsevier Academic Press: Amsterdam, **2004**.

22. Haacke, E. M.; Brown, R. W.; Thompson, M. R.; Venkatesan, R. *Magnetic Resonance Imaging: Physical Principles and Sequence Design*. John Wiley & Sons: New York, NY, **1999**.

23. Nelder, J. A.; Mead, R. *Comput. J.* **1965,** 7, 308-313.

24. Nelson, D. P.; Kiesow, L. A. *Anal. Biochem.* **1972,** 49, 474-478.

25. Luo, H.; Rogers, R.; Brechbiel, M. *Can. J. Chem.* **2001,** 79, 1105-1109.

26. Goldsmith, C. R.; Cole, A. P.; Stack, T. D. P. *J. Am. Chem. Soc.* **2005,** 127, 9904-9912.

27. Coates, C. M.; Nelson, A.-G. D.; Goldsmith, C. R. *Inorg. Chim. Acta* **2009,** 362, 4797-4803.

28. Klein Gebbink, R. J. M.; Jonas, R. T.; Goldsmith, C. R.; Stack, T. D. P. *Inorg. Chem.* **2002,** 41, 4633-4641.

29. Shongwe, M. S.; Mikuriya, M.; Ainscough, E. W.; Brodie, A. M. *J. Chem. Soc., Chem. Commun.* **1994**, 7, 887-888.

30. Motekaitis, R. J.; Rogers, B. E.; Reichert, D. E.; Martell, A. E.; Welch, M. J. *Inorg. Chem.* **1996,** 35, 3821-3827.

31. Sahoo, S. C.; Dubey, M.; Alam, M. A.; Ray, M. *Inorg. Chim. Acta* **2010,** 363, 3055-3060.

32. Ward, M. B.; Scheitler, A.; Yu, M.; Senft, L.; Zillmann, A. S.; Gorden, J. D.; Schwartz, D. D.; Ivanović-Burmazović, I.; Goldsmith, C. R. *Nature Chem.* **2018,** 10, 1207-1212.

33. Senft, L.; Moore, J. L.; Franke, A.; Scheitler, A.; Zahl, A.; Puchta, R.; Fehn, D.; Ison, S.; Sader, S.; Meyer, K.; Ivanović-Burmazović, I.; Goldsmith, C. R. *Chem Sci.* **2021**, 12, 10483-10500.

34. Dees, A.; Zahl, A.; Puchta, R.; van Eikema Hommes, N. J. R.; Heinemann, F. W.; Ivanović-Burmazović, I. *Inorg. Chem.* **2007,** 46, 2459-2470.

35. Kenkel, I.; Franke, A.; Dürr, M.; Zahl, A.; Dücker-Benfer, C.; Langer, J.; Filipović, M. R.; Yu, M.; Puchta, R.; Fiedler, S. R.; Shores, M. P.; Goldsmith, C. R.; Ivanović-Burmazović, I. *J. Am. Chem. Soc.* **2017,** 139, 1472-1484.

36. Lieb, D.; Friedel, F. C.; Yawer, M.; Zahl, A.; Khusniyarov, M. M.; Heinemann, F. W.; Ivanović-Burmazović, I. *Inorg. Chem.* **2013,** 52, 222-236.

37. Gale, E. M.; Atanasova, I. P.; Blasi, F.; Ay, I.; Caravan, P. *J. Am. Chem. Soc.* **2015,** 137, 15548-15557.

38. Troughton, J. S.; Greenfield, M. T.; Greenwood, J. M.; Dumas, S.; Wiethoff, A. J.; Wang, J.; Spiller, M.; McCurry, T. J.; Caravan, P. *Inorg. Chem.* **2004,** 43, 6313-6323.

39. Molnár, E.; Camus, N.; Patinec, V.; Rolla, G. A.; Botta, M.; Tircsó, G.; Kálmán, F. K.; Fodor, T.; Tripier, R.; Platas-Iglesias, C. *Inorg. Chem.* **2014,** 53, 5136-5149.

40. Botár, R.; Molnár, E.; Trencsényi, G.; Kiss, J.; Kálmán, F. K.; Tircsó, G. *J. Am. Chem. Soc.* **2020,** 142, 1662-1666.

41. McGowan, P. C.; Podesta, T. J.; Thornton-Pett, M. *Inorg. Chem.* **2001,** 40, 1445-1453.

42. Major, J. L.; Parigi, G.; Luchinat, C.; Meade, T. J. *Proc. Natl. Acad. Sci., U. S. A.* **2007,** 104, 13881-13886.

43. Regueiro-Figueroa, M.; Rolla, G. A.; Esteban-Gómez, D.; de Blas, A.; Rodríguez-Blas, T.; Botta, M.; Platas-Iglesias, C. *Chem. Eur. J.* **2014,** 20, 17300-17305.

44. Wang, S.; Westmoreland, T. D. *Inorg. Chem.* **2009,** 48, 719-727.

45. Phukan, B.; Mukherjee, C.; Goswami, U.; Sarmah, A.; Mukherjee, S.; Sahoo, S. K.; Moi, S. C. *Inorg. Chem.* **2018,** 57, 2631-2638.

46. Gale, E. M.; Jones, C. M.; Ramsay, I.; Farrar, C. T.; Caravan, P. *J. Am. Chem. Soc.* **2016,** *138*, 15861-15864.

47. Geraldes, C. F. G. C.; Sherry, A. D.; Brown III, R. D.; Koenig, S. H. *Magn. Reson. Med.* **1986,** 3, 242-250.

48. Chaves, S.; Delgado, R.; Da Silva, J. J. R. F. *Talanta* **1992,** 39, 249-254.

49. Aime, S.; Baroni, S.; Delli Castelli, D.; Brücher, E.; Fábián, I.; Serra, S. C.; Fringuello Mingo, A.; Napolitano, R.; Lattuada, L.; Tedoldi, F.; Baranyai, Z. *Inorg. Chem.* **2018,** 57, 5567-5574.

50. Kinnula, V. L.; Everitt, J. I.; Whorton, A. R.; Crapo, J. D. *Am. J. Physiol.* **1991,** 261, L84-91.

51. Lyublinskaya, O.; Antunes, F. *Redox Biol.* **2019,** 24, 101200.

52. Sies, H. *J. Biol. Chem.* **2014,** 289, 8735-8741.

Chapter 3

A Highly Water- and Air-Stable Iron-Containing MRI Contrast Agent Sensor for H_2O_2[*]

[*] This chapter is a modified version of a published paper: Sana Karbalaei, Alicja Franke, Aubree Jordan, Cayla Rose, P. Raj Pokkuluri, Ronald J. Beyers, Achim Zahl, Ivana Ivanović-Burmazović, and Christian R. Goldsmith, *Chemistry—A European Journal* **2022**, 28, e202201179. Reprint with permission.

3.1 Introduction

Although reactive oxygen species (ROS), such as H_2O_2 and O_2^-, have been found to serve beneficial roles in biology, the overaccumulation of these species is often observed in a wide array of pathologies, including several rightly feared cardiovascular and neurological disorders.[1] The involvement of ROS in disease has motivated other researchers and ourselves to develop methods to detect ROS in biological settings.[2-11] Our own approach has been to prepare redox-responsive contrast agents for magnetic resonance imaging (MRI) that activate upon reaction with H_2O_2.[12-15]

The probes prepared by our laboratory exhibit changes to their T_1-weighted relaxivity (r_1) upon oxidation by H_2O_2. The r_1 of a ^{1}H-based contrast agent is influenced by the nature and extent of its interactions with bulk water molecules and the electronic properties of the metal ion component. With respect to the interactions with water molecules, groups that can exchange protons with bulk water and sites for the direct coordination of water to the metal ion both improve the relaxivity. The number of water coordination sites on the metal is commonly referred to as the aquation number (q). The electronic structure of the metal ion is connected to two important parameters: the paramagnetism and the electron spin relaxation time. Highly paramagnetic metal ions with slow electron spin relaxation times, such as high-spin Mn(II) and Gd(III), enable high r_1 values. Conversely, metal ions with fast electron spin relaxation times, such as Fe(II), are associated with low r_1 values and have a nearly negligible impact on MRI contrast even when they are highly paramagnetic.

Most of the prior sensors from our group were air-stable Mn(II) complexes with polydentate quinol-containing ligands.[12-14] Upon reacting with H_2O_2, the quinols oxidize to *para*-quinones. Water molecules displace the *para*-quinone portions of the ligand, and the higher aquation thereby both increases the r_1 of the complex and improves MRI contrast. Although the

manganese may be transiently oxidized, it mostly reverts back to the +2 oxidation state.[12-14] The Mn(II) complexes can be modified to be exceptionally water-stable and can respond to H_2O_2 with a 130% increase in r_1,[12] but the high background relaxivities of the pre-activated sensors complicate analysis of biological redox environments. Enhanced contrast in a region could result from a combination of two factors: oxidation of the sensor to its higher relaxivity form and the mere accumulation of the sensor in its pre-activated and/or oxidized forms in the area of interest.

In order to decrease the background signal provided by the pre-activated form of the sensor, we replaced the Mn(II) in our most successful sensor, [Mn^{II}(H_3qp4)](OTf),[12] with Fe(II). Relative to Mn(II), Fe(II) complexes have a much lesser impact on the T_1 of water molecule ^{1}H nuclei due to their much faster electron spin relaxation.[11] Fe(II) also differs from Mn(II) in that it can be oxidized to the +3 oxidation state much more facilely.[16] When the metal centers are high-spin, the resultant Fe(III) complexes are more paramagnetic and exhibit slower electron spin relaxation; as such, they can interact with water molecules to substantially improve T_1-weighted MRI contrast.[17-18] Gale and Caravan recently designed a redox-responsive MRI contrast agent that relies on the oxidation of Fe(II) to Fe(III) to detect biologically relevant oxidants.[11] Although the percentile increase in r_1 is large and the pre-activated ferrous complex has little impact on the MR image, the activated form of the sensor has a relatively small r_1. The r_1 of our iron-containing sensor, conversely, could potentially be enhanced by both ligand and metal oxidation (Scheme 3.1).

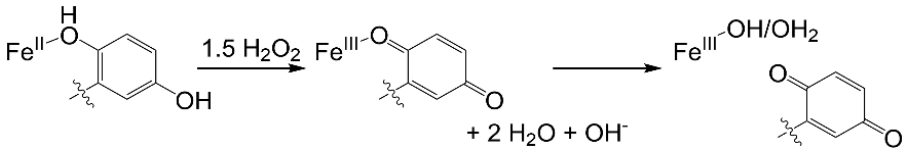

Scheme 3.1 Oxidation of an Fe(II)-quinol to a more highly aquated Fe(III)-*para*-quinone.

3.2 Experimental Section

Materials

Unless stated otherwise, all chemicals and solvents were purchased from Sigma-Aldrich and used as received. Deuterated solvents were bought from Cambridge Isotopes. Diethyl ether (ether) and methanol (MeOH) were bought from Fisher. Methylene chloride (CH_2Cl_2) was purchased from Mallinckrodt Baker. 1,8-Bis(2,5-dihydroxybenzyl)-1,4,8,11-tetraazacyclotetradecane (H_4qp4) was prepared through a previously described procedure.[12]

Instrumentation

All ^{1}H and ^{13}C NMR spectra were recorded on a 500 MHz AV Bruker NMR spectrometer. All reported NMR resonance peak frequencies were referenced to internal standards. A Varian Cary 50 spectrophotometer was used to collect optical data, which were then processed using software from the WinUV Analysis Suite. Electron paramagnetic resonance (EPR) spectra were collected using a Bruker EMX-6/1 X-band EPR spectrometer operated in the perpendicular mode and subsequently analyzed with the program Easy-Spin. All EPR samples were run as frozen solutions in quartz tubes. We used a Johnson Matthey magnetic susceptibility balance (model MK I#7967) to measure the magnetic moments of solid samples of the metal complexes and estimated the diamagnetic component of the susceptibility using Pascal's constants.[19] Solution-state magnetic moments were obtained using the Evans' method.[20-21] Cyclic voltammetry (CV) was performed under N_2 at 294 K with an Epsilon electrochemistry workstation (Bioanalytical System, Inc.). The working, auxiliary, and reference electrodes were gold, platinum wire, and silver/silver(I) chloride, respectively. High-resolution mass spectrometry (HR-MS) data were collected at the Mass Spectrometer Center at Auburn University on a Bruker Microflex LT MALDI-TOF mass spectrometer via direct probe analysis operated in the positive ion mode. Solid

samples of the isolated compounds were dried, stored under N_2, and sent to Atlantic Microlabs (Norcross, GA) for elemental analysis.

Potentiometric Titrations

The aqueous speciation of H_4qp4 was previously determined.[12] Those for its Fe(II) and Fe(III) complexes were assessed using a METROHM 765 Dosimat with a jacketed, airtight glass titration vessel. A Fisher Scientific Accumet Research AR15 pH meter was used to monitor the pH of the sample solutions during the titrations. The electrode was calibrated before each titration using commercially available standard solutions buffered to pH 4.0, 7.0, and 10.0. All samples were purged with argon prior to analysis and subsequently analyzed under an argon atmosphere at 25 °C to prevent carbonate contamination. All solution samples were prepared in solutions of 100 mM KCl in deionized Millipore water. The titrations investigating metal-ligand speciation were run with solutions that contained a 1:1 molar mixture of the ligand and $Fe^{II}(OTf)_2$. Carbonate-free solutions of 0.10 M KOH and 0.10 M HCl were prepared using argon-saturated deionized Millipore water. The titration data were analyzed and fit to speciation models using the Hyperquad2006 program.[22]

High-Pressure Liquid Chromatography (HPLC)

HPLC was performed with UV detection at 254 nm using an Agilent 1100 series apparatus and an Agilent Zorbax SB–C18 column (4.6 × 150 mm, 5 μm pore size). The following eluents were used: A) 99.9% water with 0.1% trifluoroacetic acid (TFA) and B) 99.9% MeCN with 0.1% TFA. The following method (Method 1) was used: Gradient 90% A and 10% B to 100% B over 20 min. Flow rate = 0.20 mL/min, injection volume = 25.0 μL, column temperature = 37.0 °C. Before each run, the HPLC instrument was flushed with eluent 100% A to 100% B over 16 min with a flow rate of 0.49 mL/min and an injection volume of 25.0 μL.

Magnetic Resonance Imaging (MRI)

All MRI data were collected at the Auburn University MRI Research Center on a Siemens Verio open-bore 3T MRI clinical scanner. A 15-channel knee coil was used to simultaneously image 12–15 samples. The imaging procedure was identical to those used for previous studies from our laboratory.[13-15,23-24] An inversion recovery sequence was used that featured a non-selective adiabatic inversion pulse followed by a slice-selective gradient recalled echo (GRE) readout after a delay period corresponding to the inversion time (TI).[25-26] The GRE was a saturation readout, such that only one line of k-space was acquired per repetition time (TR), in order to maximize both signal strength and the accuracy of the T_1 estimates. The specific imaging parameters were as follows: TR was set to 10 s, TI was varied from 10 to 2600 ms over 20 steps, the echo time (TE) was set to 2.75 ms, the flip angle equaled 90°, averages = 1, slice thickness = 10 mm, field of view = 64 × 64 mm, matrix = 64 × 64, resulting in a pixel size of 1.0 × 1.0 × 10.0 mm. All samples were run in 50 mM solutions of HEPES in water, buffered to pH 7.0 and kept at 22°C. The iron content was systematically varied from 0.10 to 1.00 mM. The inverses of the T_1 values from two separate batches of contrast agent were plotted versus the concentration of iron to obtain r_1 values.

MRI Data Analysis

Image analysis was performed using custom MATLAB programs (Mathworks, Natick, MA). The initial TI = 4.8 ms image was used as a baseline to determine circular region of interest (ROI) boundaries for each sample; from these, the mean pixel magnitudes for each ROI were calculated. For each of the 36 subsequent TI images, the same ROI boundaries were applied, and the mean pixel magnitude calculations were repeated. This gave consistent ROI spatial definitions and a corresponding time course of magnitudes for each of the samples over all the TI time points.

Each sample's complex phase was used to correct the magnitude polarity to produce a complete exponential T_1 inversion recovery curve. The Nelder-Mead simplex algorithm[27] was applied to each sample's exponential curve to estimate its corresponding T_1 value.

^{17}O NMR Water Exchange Measurements

The aquation numbers (q_{H2O}), rate constants, and activation parameters for the water exchange at Fe(II) and Fe(III) centers were determined from the temperature dependence of the ^{17}O-line broadening measured for aqueous solutions containing Fe(II) or Fe(III) complexes and for metal-free solutions buffered to pH 7.4 over the temperature range 274.2–343.2 K. The line widths at half height of the signal were determined by a deconvolution procedure on the real part of the Fourier-transformed spectra with a Lorentzian shape function in the data analysis module of Bruker Topspin 1.3 software. The measurements were performed with a commercial 5 mm Bruker broadband probe thermostated with a Bruker B-VT 3000 variable-temperature unit. Samples were prepared by adding a solution of solid dissolved in a minimal amount of MeCN (20% (v/v)) to an aqueous solution containing 60 mM 3-(N-morpholino) propane sulfonic acid (MOPS) buffered to pH 7.4. ^{17}O-labeled water (10%; D-Chem Ltd., Tel Aviv, Israel) was added to this solution resulting in a total enrichment of 1% ^{17}O in the studied samples. The resultant mixture contained 9.8 mM of the Fe(II) complex. The Fe(III) complex was obtained by the oxidation of 9.8 mM Fe(II) using 10 equiv. of H_2O_2 in 60 mM MOPS buffered to pH 7.4. The reaction was allowed to proceed for 15 min prior to data acquisition. The NMR data were fit to the Swift-Connick equation.[28] The q_{H2O} variable was set as a free parameter, and the B value was fixed. The number of exchanging water molecules was optimized at q_{H2O}=1.6.

Lipophilicity Measurements

The partition coefficients were obtained in *n*-butanol/water (log P_{BW}), in which the Fe(II) complex is more soluble, and then correlated to a corresponding *n*-octanol/water value by using a calibration curve prepared with well-known standards.[29] The partition between water and *n*-butanol was determined experimentally with the Fe(II) complex using a variation of the shake-flask method.[30] Distilled water and *n*-butanol were mixed vigorously for 24 h at 25°C, to promote solvent saturation in both phases, and the solvents were separated. Then, 0.1 mL of a solution of the Fe(II)-H_4qp4 complex in water saturated with *n*-butanol was shaken with 1 mL of *n*-butanol saturated with water in a plastic tube for 3 min using a Vortex-Genie. The biphasic mixture was centrifuged (3 min at 6000 rpm), and the layers were separated. The concentration of the iron complex in each layer was measured spectrophotometrically. If dilution was needed for the UV/vis measurements, the aqueous layer was diluted with water; whereas for the organic layer, water-saturated *n*-butanol was used instead. The spectrum baseline was chosen accordingly. The log P_{BW} was calculated using Equation (1):

$$\log P_{BW} = \log (C_{n\text{-BuOH}}/C_{H2O}) \quad (1)$$

The log P_{BW} values were converted to the more familiar log P_{OW} using Equation (2):

$$\log P_{OW} = 1.55 (\log P_{BW}) - 0.54 \quad (2)$$

Synthesis

(1-(2,5-dihydroxybenzyl)-8-(2,5-dihydroxybenzylalkoxide)-1,4,8,11-tetraazacyclotetradecane)iron(II) triflate ([$Fe^{II}(H_3qp4)$](OTf), 1)

H_4qp4 (500 mg, 1.12 mmol) and $Fe^{II}(OTf)_2$ (400 mg, 1.13 mmol) were dissolved in 5 mL of dry MeCN under N_2. The mixture was stirred at 60 °C for 48 h. The slow addition of CH_2Cl_2 deposited the product as a dark blue powder, which was collected via filtration (628 mg, 83%

yield). MS (Appendix B, Figure B1): calcd for $[Fe(H_2qp4)]^+$, *m/z* 498.1929; found, *m/z* 498.1888. Solid-state magnetic susceptibility (294 K): μ_{eff} = 4.8 μ_B. Solution-state magnetic susceptibility (CD_3CN, 298 K): μ_{eff} = 4.7 μ_B. Optical spectroscopy (MeCN, 294 K): 299 nm (ε =10800 M^{-1} cm^{-1}), 595 nm (ε = 2200 M^{-1} cm^{-1}). IR (KBr, cm^{-1}, Figure B2): 3378 (s), 3229 (s), 3070 (m), 2855 (w), 2323 (w), 1612 (w), 1512 (w), 1485 (s), 1469 (w), 1449 (m), 1364 (w), 1219 (s), 1151 (s), 1115 (w), 1079 (w), 1024 (s), 992 (w), 916 (w), 869 (m), 814 (s), 792 (w), 762 (m), 633 (s), 600 (w), 542 (w), 514 (m), 478 (w), 421 (w). ^1H NMR (500 MHz, CD_3CN, 298 K, Figure B3): δ 16.54, 6.75, 6.65, 5.0-2.0 (m), 1.13, 0.65, –2.20, –9.77, –14.55. Elemental analysis (powder) calcd. For $C_{25}H_{35}N_4O_7F_3S_1Fe \cdot 1.5H_2O \cdot 1CH_2Cl_2$: C, 42.70%; H, 5.30%; N, 7.38%. Found: C, 42.82%; H, 4.83%; N, 7.88 %. HPLC (Method 1): t_R= 7.50 (min).

(1-(2,5-dihydroxybenzyl)-8-(2,5-dihydroxybenzylalkoxide)-1,4,8,11-tetraazacyclotetradecane)iron(III) triflate ($[Fe^{III}(H_3qp4)](OTf)_2$, 3)

H_4qp4 (500 mg, 1.12 mmol) and $Fe^{III}(OTf)_3$ (637 mg, 1.13 mmol) were dissolved in 5 mL of dry MeCN under N_2. The mixture stirred at 60 °C for 48 h. Upon the slow addition of ether to the MeCN solution, the product deposited as a dark brown powder that could be isolated by filtration (780 mg, 83% yield). MS (ESI): calcd for $[Fe(H_2qp4)]^+$, *m/z* 498.1929; found, *m/z* 498.1921. Solid-state magnetic susceptibility (294 K): μ_{eff} = 5.7 μ_B. Optical spectroscopy (MeCN, 294 K): 299 nm (ε = 7900 M^{-1} cm^{-1}). IR (KBr, cm^{-1}): 3458 (s), 3302 (s), 3182 (s), 3098 (w), 2957 (w), 2890 (w), 2825 (m), 1655 (w), 1549 (w), 1520 (m), 1479 (w), 1448 (s), 1390 (w), 1342 (w), 1280 (w), 1247 (w), 1223 (w), 1192 (w), 1156 (s), 1131 (w), 1091 (m), 1052 (w), 1025 (s), 992 (w), 934 (w), 920 (w), 892 (w), 868 (w), 823 (m), 755 (m), 636 (m), 583 (w), 511 (w), 470 (w). Elemental analysis (powder) calcd for $C_{26}H_{35}N_4O_{10}F_6S_2Fe \cdot 0.5\ (C_2H_5)_2O$ (powder): C, 40.29 %; H, 4.83%; N, 6.71%. Found: C, 40.16 %; H, 4.91%; N, 7.05 %. HPLC (Method 1): t_R = 8.02 (min).

3.3 Results and Discussion

Synthesis and Characterization

We prepared [$Fe^{II}(H_3qp4)$](OTf) (**1**) by mixing the H_4qp4 ligand (Scheme 3.2) with an equimolar amount of $Fe^{II}(OTf)_2$ in MeCN. Adding CH_2Cl_2 deposits the product as a blue powder in high purity and yield (83%). We used an analogous reaction to prepare [$Mn^{II}(H_3qp4)$](OTf), which likewise was obtained in a sub-quantitative yield.[12] The free ligand has a strong affinity for protons, and we believe that residual H_4qp4 ligand deprotonates the metal-bound ligand to H_3qp4^- in both of these reactions.[12] Although **1** was not structurally characterized, its composition was confirmed by mass spectrometry and elemental analysis. The purity was further corroborated by HPLC (Figure B4). Solid-state magnetic susceptibility measurements ($\mu_{eff} = 4.8 \pm 0.1\ \mu_B$), solution-state magnetic susceptibility measurements ($\mu_{eff} = 4.7 \pm 0.3\ \mu_B$), NMR data (Figure B3), and the absence of an EPR signal indicate that the metal center is unambiguously high-spin Fe(II).

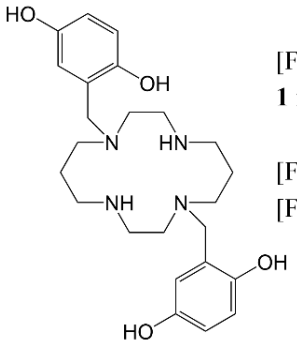

H_4qp4

[$Fe^{II}(H_3qp4)$](OTf) - **1**
1 forms [$Fe^{II}(H_3qp4)]^+$ and [$Fe^{II}(H_2qp4)$] at pH 7.00

[$Fe^{III}(H_2qp4)$](OTf) - **2**
[$Fe^{III}(H_3qp4)$]$(OTf)_2$ - **3**

Scheme 3.2 Structure of H_4qp4 and compositions of isolated and solution-state iron complexes described in this chapter. The H_4qp4 ligand coordinates to the iron as H_3qp4^- and H_2qp4^{2-}.

Stability and Speciation in Water

Complex **1**, like its Mn(II) analog, was found to be exceptionally stable in water (Table 3.1, Table B1). The aqueous behavior of **1** was studied between pH 2.5 and 9.0 and compared to

that of the free H_4qp4 ligand.[12] As the pH increases, two ionization events are observed, corresponding to pK_a values of 5.11 and 7.32; these are nearly identical to those observed for [Mn^{II}-(H_3qp4)](OTf). The ionization events for the free ligand centered at pH 3.50 and pH 7.70, conversely, are not observed, suggesting that the sample contains negligible amounts of free ligand. At pH 7.0, the UV/vis spectra of **1** and H_4qp4 differ markedly (Figure B5), with the former having a relatively intense band at 589 nm; this provides further support that the isolated **1** is an intact Fe(II) complex rather than a 1:1 mixture of $Fe^{II}(OTf)_2$ and unbound ligand. The 589 nm feature likely results from a charge transfer process with the Fe(II); the most intense band for [Mn^{II}(H_3qp4)](OTf) is at 388 nm and likely corresponds to an intraligand transition.[12] The two pK_a values for **1** are consistent with the deprotonation of phenols ligated to M(II) ions,[14,31-32] corroborating the oxidation state assignment from the magnetic susceptibility data. The UV/vis spectrum changes as the pH rises from 4.0 to 9.0; such shifts would be anticipated from the sequential deprotonation of the quinols (Figure B7). Complex **1,** therefore, exists as a mixture of [Fe^{II}(H_3qp4)]$^+$ and [Fe^{II}(H_2qp4)] between pH 7.0 and 7.4, where H_3qp4$^-$ and H_2qp4^{2-} are the singly and doubly deprotonated forms of the H_4qp4 ligand (Figure 3.1, Scheme 3.2).

Table 3.1 pFe, log K_{ML}, and pK_a Values Determined by Potentiometric Titration at 25 °C.

pK_{L1}[a]	3.50 (±0.05)	log K_{ML} ($Fe^{II}(H_2qp4)$)[c]	29.57
pK_{L2}[a]	7.70 (±0.05)	log K_{ML} $(Fe^{II}(H_3qp4))^{+}$ [c]	26.87
pK_{L3}[a]	8.80 (±0.05)	log K_{ML} $(Fe^{II}(H_4qp4))^{2+}$ [c]	23.18
pK_{L4}[a]	10.02 (±0.05)	pFe(pH 7.4)[d]	14.18
p$K_a(Fe^{II}(H_4qp4)^{2+})$[b]	5.11 (±0.05)		
p$K_a(Fe^{II}(H_3qp4)^{+})$[b]	7.32 (±0.05)		

[a]Ligand pK_a values: $K_{L1} = [H_5qp4^{+}][H^{+}]/[H_6qp4^{2+}]$;
$K_{L2} = [H_4qp4][H^{+}]/[H_5qp4^{+}]$;
$K_{L3} = [H_3qp4^{-}][H^{+}]/[H_4qp4]$;
$K_{L4} = [H_2qp4^{2-}][H^{+}]/[H_3qp4^{-}]$; all are from reference 12.

[b]Metal complex pK_a values: $K_a(Fe^{II}(H_4qp4)^{2+}) = [Fe^{II}(H_3qp4)^{+}][H^{+}]/[Fe^{II}(H_4qp4)^{2+}]$;
$K_a(Fe^{II}(H_3qp4)^{+}) = [Fe^{II}(H_2qp4)][H^{+}]/[Fe^{II}(H_3qp4)^{+}]$

[c]Metal complex K_{ML} values: $K_{ML}\,(Fe^{II}(H_2qp4)) = [Fe^{II}(H_2qp4)]/([Fe(II)][H_2qp4^{2-}])$;
$K_{ML}\,(Fe^{II}(H_3qp4))^{+} = [Fe^{II}(H_3qp4)^{+}]/([Fe(II)][H_3qp4^{-}])$;
$K_{ML}\,(Fe^{II}(H_4qp4))^{2+} = [Fe^{II}(H_4qp4)^{2+}]/([Fe(II)][H_4qp4])$

[d]$pFe = -\log[Fe(II)]_{free}$ calculated for [Fe(II)] = 1.0 mM, $[H_4qp4]$ = 1.0 mM, 298 K, pH 7.4.

The titration data are consistent with negligible metal ion dissociation from **1**, even under highly acidic conditions (Figures 3.1, B8). The log K_{ML} values for $[Fe^{II}(H_3qp4)]^{+}$ and $[Fe^{II}(H_2qp4)]$ are 26.87 and 29.57, respectively, with the Fe(II) complex with the dianionic H_2qp4^{2-} being more stable (Table 3.1). As anticipated from the Irving-Williams series,[33] both forms of the Fe(II) complex are more water-stable than their Mn(II) counterparts, which have log K_{ML} values of 18.22 and 20.85.[12] The magnitude of the enhanced stability, however, is surprising in that the K_{ML} values normally increase by 2–3 orders of magnitude for most ligands.[34] Transition metals with macrocyclic ligands, however, do not seem to follow Irving-Williams patterns as strictly, as assessed by the relative stabilities of Ni(II), Zn(II), and Cd(II) complexes with a variety of macrocycles.[35-36]

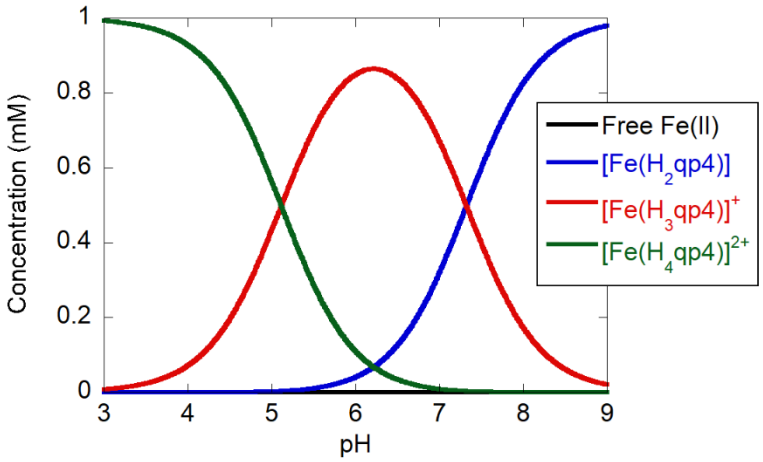

Figure 3.1 Predicted speciation as a function of pH for 1.0 mM **1** in an aqueous solution containing 100 mM KCl at 25 ºC.

Redox Stability

Cyclic voltammetry (CV) analysis of **1** in an aqueous solution containing 0.10 M phosphate buffered to pH 7.2 reveals two redox events (Figure B9). An irreversible feature centered at 90 mV *vs.* Ag/AgCl (ΔE=300 mV) is assigned to the oxidation and reduction of the quinols within the ligand since a feature with a nearly identical $E_{1/2}$ was observed for the Mn(II) analog.[12] We also observe a much more reversible redox event at -450 mV *vs.* Ag/AgCl (ΔE=60 mV). We propose that this corresponds to the Fe(III/II) redox couple. Although the CV data confirm our prediction that the Fe(II) in **1** is more susceptible to oxidation than the Mn(II) in $[Mn^{II}(H_3qp4)]^+$, **1** is not readily oxidized by air. Solutions of **1** in MeCN and HEPES-buffered water (pH 7.00) do not noticeably react with O_2 over 12 h as assessed by UV/vis; the intensities of the peaks change by less than 5% (Figures B10 and B11).

As with the Mn(II) analog,[12] prolonged (>1 week) exposure to air does eventually oxidize the metal, but not the ligand, in **1** to yield $[Fe^{III}(H_2qp4)](OTf)$ (**2**, Figure 3.2). The reaction with air, therefore, appears to be thermodynamically favorable but slow. The ferric product was crystallized from MeCN/ether mixtures. In **2**, the cation features a hexacoordinate metal center

bound to the full set of N_4O_2 donor atoms from the H_2qp4^{2-} ligand. The ligand is bound in a *trans*-III conformation,[37] with the N-donors from the macrocycle coordinating to the Fe(III) in a square planar fashion and the quinolates binding trans to each other. The structural data confirm that the ligand is not oxidized by O_2. The 1.89 Å Fe-O bonds are consistent with Fe(III)-O bonds to alkoxide ligands.[38] The C-O bond lengths of 1.35 Å (Fe-bound) and 1.38 Å (para to the Fe-bound O) are longer than those found in crystallographically characterized *para*-quinones.[12-14,39] With respect to the oxidation states of the metal ion and ligand and the conformation of the cyclam portion, **2** resembles $[Mn^{III}(H_2qp4)](OTf)$, which resulted from exposing $[Mn^{II}(H_3qp4)](OTf)$ to air for over a week.[12]

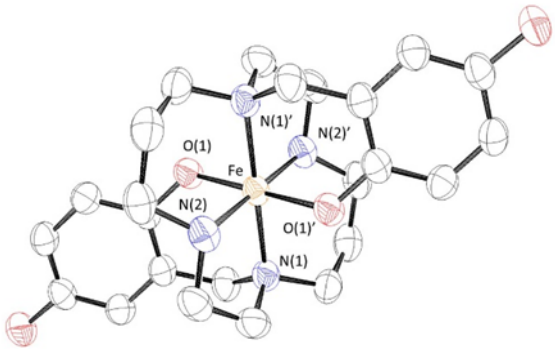

Figure 3.2 ORTEP representation of $[Fe^{III}(H_2qp4)]^+$ (**2**). All H atoms, solvent molecules, and counteranions have been omitted for clarity. All ellipsoids are drawn at 50% probability.

Reactivity with H_2O_2

Complex **1** reacts with H_2O_2 to yield Fe(III) species with oxidized ligands. Evidence for the oxidation of the quinols in the ligand to *para*-quinones is provided by UV/vis and IR (Figures B12 and B13). The loss of the feature at UV/vis 299 nm is consistent with the oxidation of quinols.[12-14] With previous quinol-containing ligands, the quinols do not get fully converted to the *para*-quinone upon oxidation by H_2O_2,[13,14] and it is likely that the H_4qp4 ligand in the oxidized products is a mixture of unreacted ligand, H_2qp4 (quinol/*para*-quinone) and qp4 (di-*para*-

quinone), as was found for the Mn(II) analog.[12] Unfortunately, we are unable to isolate individual oxidation products, and the presence of residual H_2O_2 precluded analysis of the oxidized reaction mixtures by HPLC due to the risk of damage to the instrument. With prior ligands, we quantitatively assessed the extent of ligand oxidation by exchanging Zn(II) for the Mn(II) after the addition of H_2O_2;[13,14] this yields diamagnetic Zn(II) compounds with the ligands that can be studied by ^{1}H NMR. With the H_4qp4 ligand and its oxidized products, Zn(II)-for-Fe(III) exchange does not readily occur, precluding this sort of analysis (*vida infra*).

The oxidation of the metal to Fe(III) is confirmed with EPR (Figure 3.3). At 77 K, the oxidized product displays signals consistent with both high-spin and low-spin Fe(III), suggesting that the products may include spin-crossover species. The reaction was also studied at room temperature (RT) using the Evans' method to measure solution-state magnetic susceptibilities.[20-21] After the reaction with H_2O_2, the μ_{eff} increases to 5.7 ± 0.3 μ_B, consistent with most of the metal in the oxidized product being high-spin Fe(III) at RT.

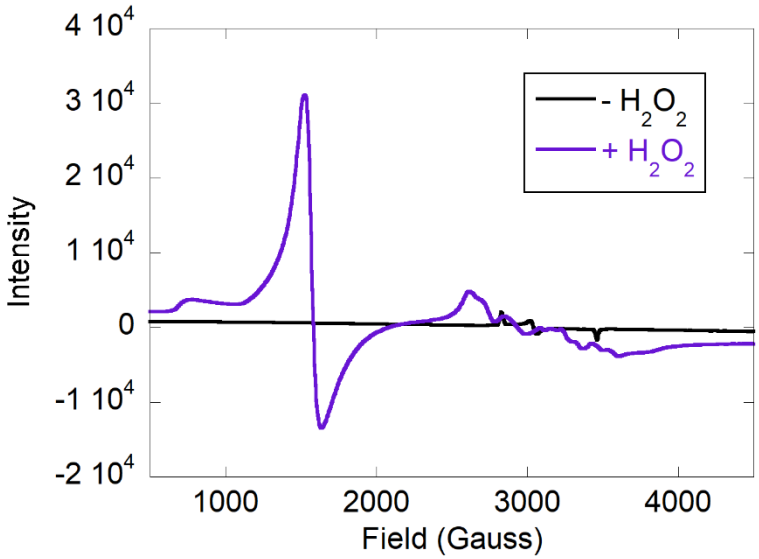

Figure 3.3 X-band EPR spectra depicting the reaction of 1.0 mM **1** with 10 mM H_2O_2 in 50 mM HEPES buffered to pH 7.0. The sample was frozen to 77 K 30 min after the addition of H_2O_2 prior to data acquisition. The signal at g = 4.3 is indicative of high-spin Fe(III), the smaller signals at g = 2.55, 2.27, and 1.99 are consistent with low-spin Fe(III) species.

The oxidation of **1** by H_2O_2 appears to be partly reversible in that the ligand can be reduced back to the diquinol form but the metal remains in the +3 oxidation state. When **1** is oxidized by 4 equiv. of H_2O_2 for 60 min, the subsequent reaction with 4 equiv. of either cysteine or dithionite yields a species with a *m/z* feature at 498.19, which is consistent with an Fe(III) complex with the reduced and doubly deprotonated form of the ligand (Figures B14 and B15). When 0.1 mM of the Fe(III) complex with the reduced ligand, $[Fe^{III}(H_3qp4)](OTf)_2$ (**3**), is allowed to react with 10 mM of L-cysteine in pH 7.4 HEPES buffer for 4 h, the 589 nm feature associated with ferrous **1** is not restored, leading us to conclude that the metal ion remains in the +3 oxidation state.

Magnetic Resonance Imaging

The MRI properties of **1** were assessed using methods that were previously employed in our studies of manganese-containing MRI contrast agents.[12-15,23] The relaxivity of **1** was measured before and after its reaction with excess H_2O_2 using a 3T MRI scanner (Figure 3.4). The r_1 for the pre-activated complex was calculated from the T_1 values of aqueous solutions containing 50 mM HEPES buffered to pH 7.00 and 0–1.0 mM **1**. T_1 measurements were also acquired for oxidized samples that contained 10 mM H_2O_2 in addition to the aforementioned reagents. The T_1 values were measured 30 min and 60 min after the solution samples were initially prepared.

The r_1 value of pre-activated **1** was found to be 0.22 (±0.09) mM^{-1} s^{-1}, which is similar to values measured for other Fe(II) complexes.[11] The relaxivity of pre-activated **1** was also measured at various pH values between 2 and 12 (Figure B16). As the solution is made more basic, the R_1 gradually decreases from 0.65 s^{-1} to 0.41 s^{-1}, with the iron-free water reference having a R_1 value of 0.36 s^{-1}. Between pH 6.5 and 8.0, which should encompass the range of physiologically relevant pH values that a sensor could encounter *in vivo*, the R_1 decreases by a mere 0.06 s^{-1}. Slight changes to the local pH should not significantly impact the relaxivity of **1**.

The quinol- and Mn(II)-containing H_2O_2 sensors previously reported by our laboratory display more drastic drops in their relaxivity upon basification.[12-14] We attribute the decrease in R_1 to the weakly metal-binding quinols getting deprotonated to much more strongly binding quinolates. Under acidic conditions, water molecules can displace the quinols, leading to higher aquation numbers and thereby higher relaxivities.[12-14] We confirmed that water exchange occurs on the Fe(II) metal center at pH 7.4 with ^{17}O NMR (Figure 3.5). The data are consistent with a $k_{ex}^{298} = 2.7 \times 10^6$ s^{-1}, $\Delta H^{\ddagger} = 54.5 \pm 3.2$ kJ mol^{-1}, $\Delta S^{\ddagger} = 61 \pm 11$ J mol^{-1} K^{-1}, and an aquation number (q) of 1.6. The highly positive $\Delta S^{\ddagger}$ is consistent with a dissociative mechanism for water exchange on the metal center.

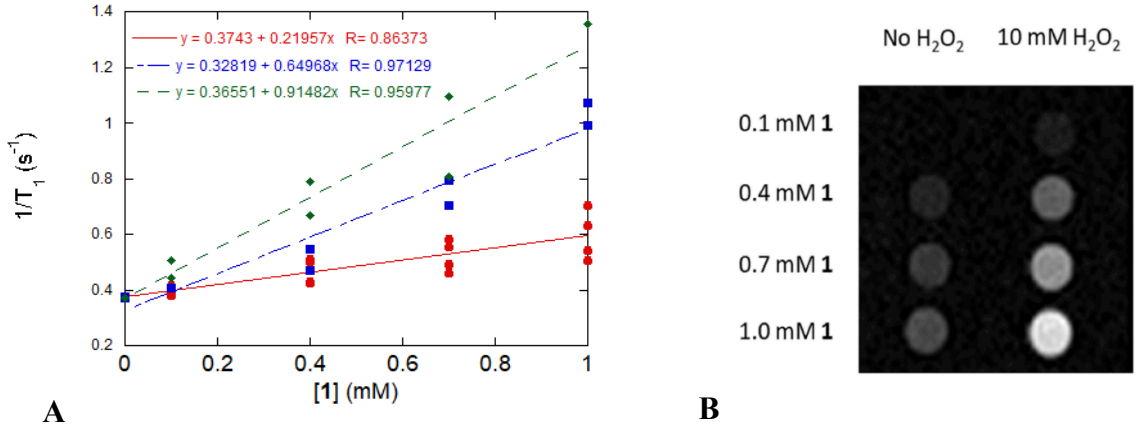

Figure 3.4 A) Plots of $1/T_1$ versus iron concentration for **1** in the presence (blue, green) and absence (red) of 10 mM H_2O_2. All samples were run in 298 K aqueous solutions containing 50 mM HEPES buffered to pH 7.00, using a 3T field provided by a clinical MRI scanner. All samples were prepared under air. The oxidized samples were prepared by directly adding H_2O_2 to solutions of **1** in aqueous solutions buffered to pH 7.00. T_1 measurements were taken 30 min (blue) and 60 min (green) after the reactions with H_2O_2 began. The data were fit to the indicated linear equations; the y-intercepts were within error of $1/T_1$ measurements associated with two control samples that contained no iron: pure water (0.35 s^{-1}) and 50 mM HEPES buffer (0.34 s^{-1}). B) Phantom images of solutions containing 0.1–1.0 mM **1** in the absence and presence of 10 mM H_2O_2. All solutions were given 60 min to equilibrate and imaged with time of inversion (TI) = 1750 ms.

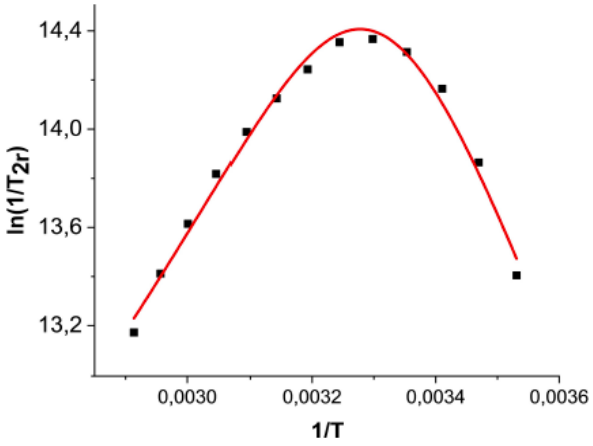

Figure 3.5 Water exchange at the Fe(II) center in **1** in an aqueous solution containing 0.06 M MOPS buffered to pH 7.4 followed by ^{17}O NMR. The NMR data were fit to the Swift-Connick equation.[28] The q_{H2O} variable was set as free parameter, and the B value was fixed. The number of exchanging water molecules was optimized at $q_{H2O} = 1.6$. This is the mean value for the two Fe(II) species existing in equilibrium at pH 7.4: $[Fe^{II}(H_2qp4)]$ and $[Fe^{II}(H_3qp4)]^+$.

Upon oxidation by H_2O_2, the r_1 increases over 4-fold to 0.91 (±0.26) mM^{-1} s^{-1}. Gale's Fe(II)-PyC3A complex, by comparison, exhibits a 10-fold increase in relaxivity at 1.4 T as the complex is oxidized to Fe(III), with even larger responses under stronger magnetic fields.[11] As with the Mn(II) complex with H_4qp4, the enhancement in r_1 occurs gradually when a large excess of H_2O_2 is added in a single portion.[12] The r_1 requires 60 min to reach its maximum value after 10 mM H_2O_2 is added. The maximum r_1 is in the middle of the range for Fe(III)-containing MRI contrast agents.[40] The relatively low value of r_1 for the activated sensor may suggest that the Fe(III) may lack an inner-sphere water. When we analyzed mixtures of **1** and H_2O_2 by ^{17}O NMR, we found that the iron did not alter the line-width of the water peak, confirming negligible water exchange on the NMR timescale for the oxidized product(s) (Figure B17).

Preparation and Characterization of a Ferric Oxidized Standard

Complex **2**, which features Fe(III) bound to the reduced form of the H_4qp4 ligand, was prepared through aerobic oxidation of **1** in trace quantities. The conjugate acid of **2**, $[Fe^{III}(H_3qp4)](OTf)_2$ (**3**), can also be prepared by directly reacting H_4qp4 with $Fe^{III}(OTf)_3$ in MeCN. Although it was not structurally characterized, **3** was characterized by elemental analysis, MS, IR, UV/vis, and EPR (Figures B18–B21). The UV/vis spectrum lacks the intense 589 nm band observed for **1**. The EPR displays an intense signal at $g = 4.3$, confirming a high-spin Fe(III) species. HPLC data confirm both the purity of the complex and the complexation of the ligand to the metal center (Figure B22). Only a single peak is observed in the trace, and its 8.02 min retention time differs from those of both **1** (7.50 min) and free H_4qp4 (2.32 min) under the same conditions.

We analyzed the speciation of Fe(III)/H_4qp4 mixtures between pH 3.0 and 8.0 using potentiometric pH titrations (Figure B23). As the pH increases, we observed two ionization events, consistent with pK_a values of 4.99 and 6.45 (Table B2). The UV/vis spectra do not change appreciably between pH 5.5 and 7.6, suggesting that the second ionization event does not correspond to the loss of the first proton from one of the quinol groups (Figure B20B) – this normally induces large changes to the UV/vis features (Figure B7). The first Fe(III)-quinol group likely deprotonates below pH 3.0, and we believe that the 4.99 pK_a value instead corresponds to the deprotonation of the second quinol: $[Fe^{III}(H_3qp4)]^{2+} \rightarrow [Fe^{III}(H_2qp4)]^{+} + H^{+}$. The second ionization event is more difficult to assign. It could correspond to the deprotonation of the non-metal-coordinating hydroxy group of one of the quinols. Alternatively, it could correspond to the deprotonation of Fe(III)-bound water to OH^{-}. Precipitate begins to be observed for **3** at approximately pH 8, further differentiating this titration from that of **1**. The log K_{ML} values for $[Fe^{III}(H_3qp4)]^{+}$ and $[Fe^{III}(H_2qp4)]$ are 33.80 and 38.84, respectively (Table B2), which are much

greater than the analogous values with Fe(II). Other iron complexes with macrocyclic ligands show similarly large gains in their stabilities upon exchanging Fe(II) for Fe(III).[41]

We assessed the stability of **3** in the presence of a competing metal ion. When we monitored the reaction between 10 mM **3** and 20 mM $Zn^{II}(ClO_4)_2$ by ^1H NMR, we only observed trace amounts of the Zn(II) complex with H_4qp4 at 48 h (Figure B25). Previously, we found that the products of the reaction between $[Mn^{II}(H_3qp4)](OTf)$ and H_2O_2 likewise did not exchange metal ions readily.[12]

The relaxivity of **3**, which will spontaneously deprotonate to **2** at pH 7.0, was assessed in order to determine how much metal oxidation by itself contributes to the H_2O_2 response of **1**. The measured r_1 of 0.87 mM^{-1} s^{-1} is within the error of the 0.91 mM^{-1} s^{-1} value (Figure B26), confirming that the relaxivity response of **1** to H_2O_2 results almost entirely from metal oxidation. This result also suggests that subsequently reducing the ligand in the oxidized form of the sensor will not reverse the r_1 response. This differs from the H_2O_2 response observed for $[Mn^{II}(H_3qp4)]^+$, which has been correlated to oxidation of the ligand to a less highly chelating form that opens new water coordination sites on the Mn(II) ion.[12] The smaller size of Fe(III) relative to both Fe(II) and Mn(II) should also favor lower coordination numbers and thereby lower values of q.[42]

Preliminary catalase activity

The Mn(II) complex with H_4qp4 likewise displayed a delayed response to H_2O_2.[12] Counterintuitively, adding a smaller concentration of H_2O_2 accelerated the oxidation of the Mn(II) complex to its higher-relaxivity form. Based on these observations, we previously proposed that the oxidation of the H_4qp4 complex proceeds through a transient higher-valent metal complex that can either oxidize the quinols through a relatively slow intramolecular reaction or react with a second equiv. of H_2O_2. The intramolecular reaction would become more prominent as the H_2O_2 is

depleted. With high concentrations of H_2O_2, conversely, the compound acts as a functional mimic of catalase.

When a lower amount of H_2O_2 was added to oxidize **1**, the quinol-derived features in the UV/vis vanished more quickly (Figure B27). With 0.60 mM H_2O_2, the complex oxidation appears to finish within 30 min, rather than 60 min. Since biologically relevant concentrations of H_2O_2 are believed to be sub micromolar,[43] the observed catalase activity would not be anticipated to compete with the oxidation reactions that lead to changes in r_1 *in vivo*. We further analyzed the iron-catalyzed decomposition of H_2O_2 and calculated an initial rate of $v_o/[\mathbf{1}]_T$ of 4.35×10^3 s^{-1} (Figure B28), which is slightly slower than the 6.6×10^3 s^{-1} value for the manganese analog.[12] The activity's dependence on the concentration of H_2O_2 can be fitted to the Michaelis-Menten equation. Our best fitting model is consistent with $k_{cat} = 2.73\ (\pm 0.10) \times 10^4$ s^{-1} and $k_{on} = 6.03\ (\pm 0.60) \times 10^5$ M^{-1} s^{-1} (Table B3). Further studies on the antioxidant properties of **1** are discussed in chapter 5.

Lipophilicity and Cytotoxicity

The lipophilicity of MRI contrast agents can impact how quickly they clear the body, with more lipophilic compounds possibly getting indefinitely trapped within cells.[44] We assessed the lipophilicity of **1** by first measuring the *n*-butanol/water partition coefficients and then correlating it to a *n*-octanol/water value using an established calibration curve.[29,30] The log P_{BW} value was calculated to be -0.00047 (Eq. (1)), which translates to a log P_{OW} value of -0.5407 (Eq. (2)). The results indicate that **1** is relatively hydrophilic and should not be cell-permeant.

We investigated the cytotoxicity of **1** using rat cardiac cells (H9c2). Although uncomplexed iron is highly toxic, we find that H9c2 cells can tolerate high doses of **1** (Figure 3.6). When the cells are incubated with **1** for 4 h, we do not observe any significant impact on their viability with concentrations up to 500 μM. This same concentration does kill approximately 25% of the cells at

24 h, but a freely circulating MRI contrast agent would be expected to clear the body well before this time. Over 24 h, the iron complex is slightly more toxic than its manganese analog. Both H_4qp4 complexes are less toxic than prior sensors reported by our laboratory, which begin to noticeably impact cell viability at 50 μM.[13-14]

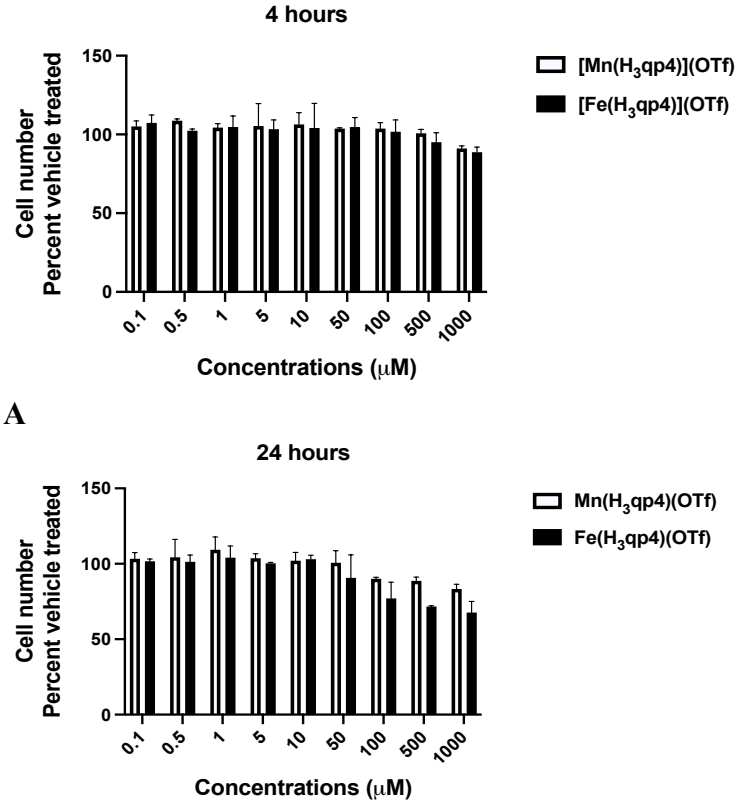

Figure 3.6 Cytotoxicity of [Fe^{II}(H_3qp4)](OTf) and [Mn^{II}(H_3qp4)](OTf) complexes toward H9c2 cells. H9c2 cells were obtained from the American Type Culture Collection (Manassas, VA, USA) and grown in Dulbecco's modified Eagle's medium (DMEM) supplemented with 10% fetal bovine serum at 37 °C with 95% humidity and 5% CO_2. Experiments were performed at 70−80% confluence. To determine the cytotoxic effects of these compounds, H9c2 cells were exposed to increasing concentrations of the iron or manganese compound (0.1−1000 μM) or their vehicles in DMEM for A) 4 h or B) 24 h. The cell number was assessed using the CyQUANT Cell Proliferation Assay Kit (Life Technologies Corporation, Carlsbad, CA) per manufacturer's instructions. Cell number was expressed as percentage of the vehicle-treated cells. Values are expressed as mean and standard deviation and represent three experiments performed in triplicate.

3.4 Conclusions

To conclude, we have found that substituting Fe(II) for Mn(II) in the H_4qp4 framework results in a highly water- and kinetically air-stable complex that exhibits a higher percentile increase in r_1 upon reaction with H_2O_2. Despite the similar aqueous speciation of the Fe(II) and Mn(II) compounds, the responses to H_2O_2 rely on fundamentally different mechanisms. Whereas the higher r_1 of the manganese sensor is connected to an increase in q enabled by oxidation of the organic component, that of the iron system appears to result almost entirely from changes to the characteristics of the oxidized metal center.

Appendix B

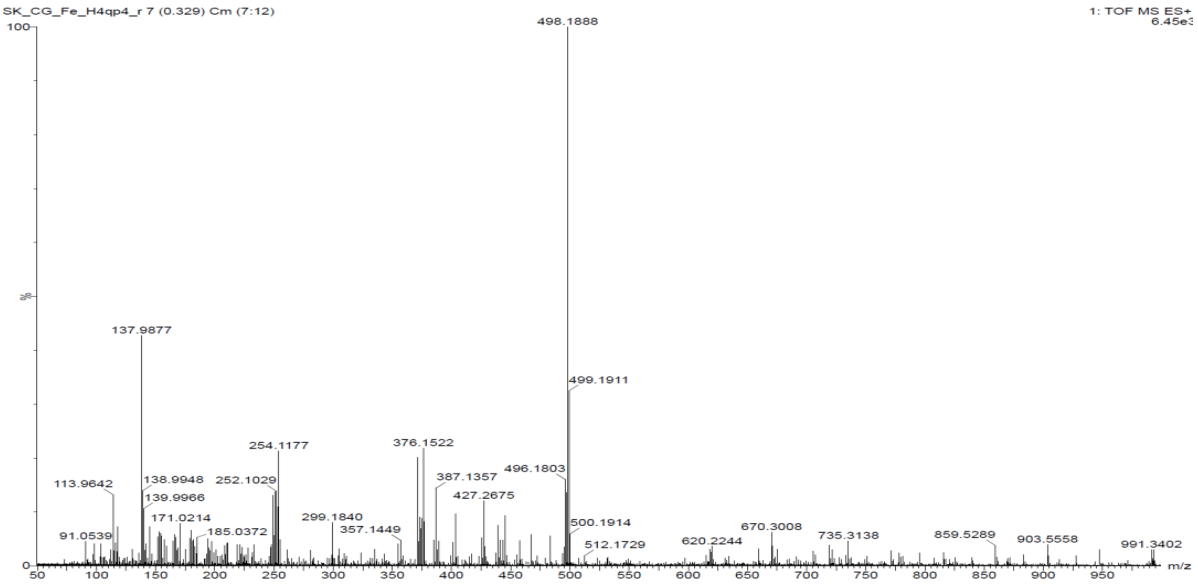

Figure B1. Mass spectrometry (ESI) of **1** in MeCN. The 498.1888 *m/z* feature is assigned to the iron complex with the doubly deprotonated H_4qp4 ligand: $[Fe(H_2qp4)]^+$ (calculated *m/z* = 498.1929).

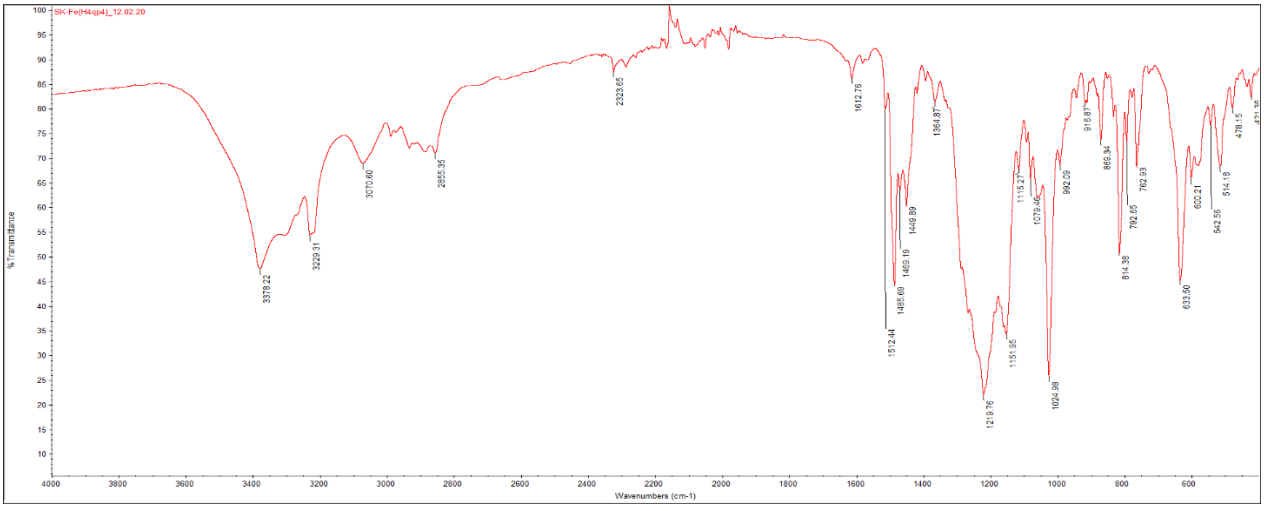

Figure B2. IR spectrum of **1** (KBr). The 3378cm^{-1} feature is assigned to the O-H stretches associated with the quinol groups of the H_4qp4 ligand.

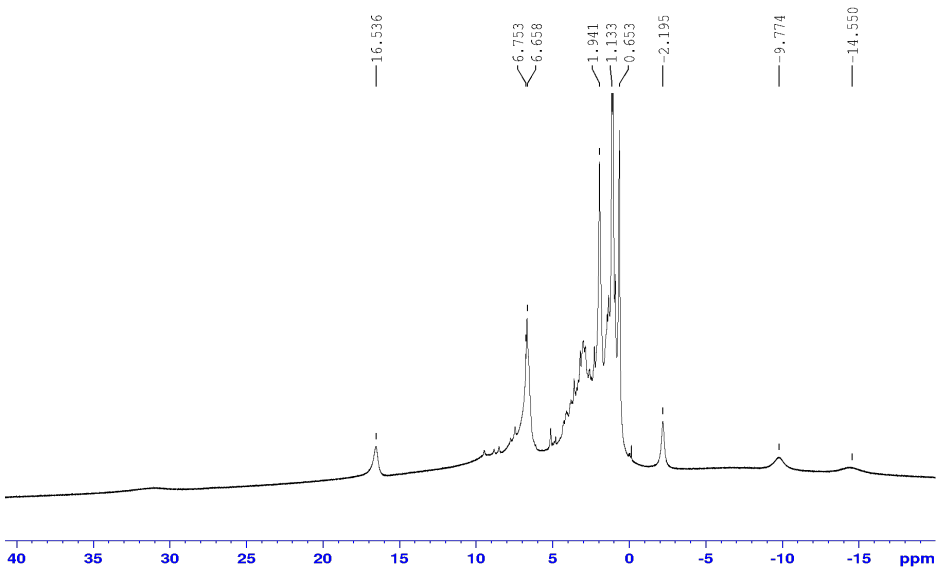

Figure B3. ^{1}H NMR spectrum of a 1 mM solution of **1** in CD_3CN (500 MHz). The peak at 1.94 ppm corresponds to MeCN.

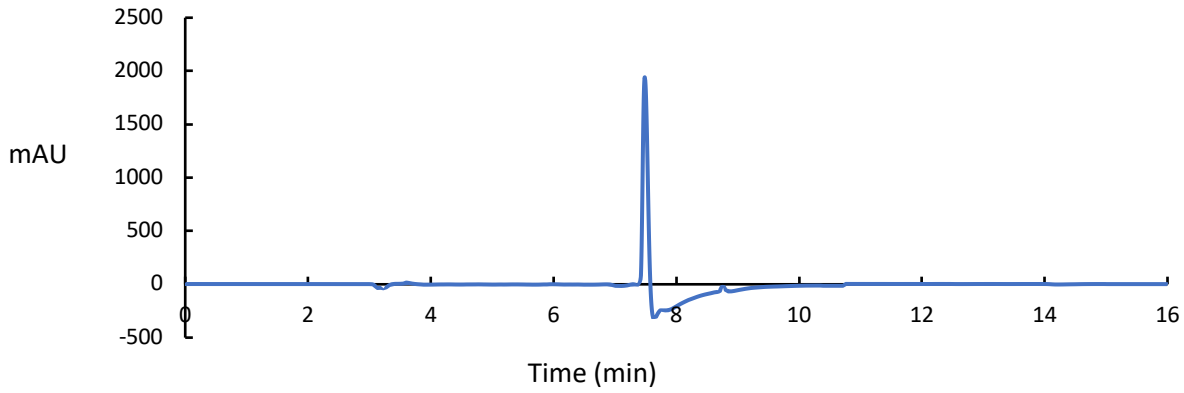

Figure B4. LC trace for **1** run under the method described in the Experimental Section. The only observed peak is at 7.50 min. The peak is distinct from that observed for the free H_4qp4 ligand which elutes at 2.32 min when run under the same conditions. The following method was used: Gradient 90% A and 10% B to 100% B over 20 min. Flow rate = 0.20 mL/min, injection volume = 25.0 µL, column temperature = 37.0 °C. Before each run, the HPLC instrument was flushed with eluent 100% A to 100% B over 16 min with a flow rate of 0.49 mL/min and an injection volume of 25.0 µL.

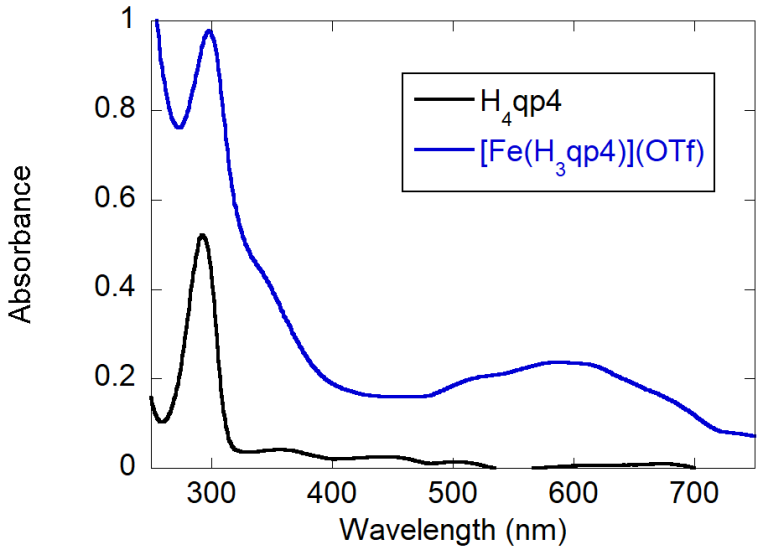

Figure B5. Comparative UV/vis spectra of 0.10 mM solutions of H_4qp4 and **1** in aqueous solutions containing 50 mM HEPES buffered to pH 7.0. Both spectra were obtained at 298 K under N_2 using a 1.0 cm pathlength cuvette.

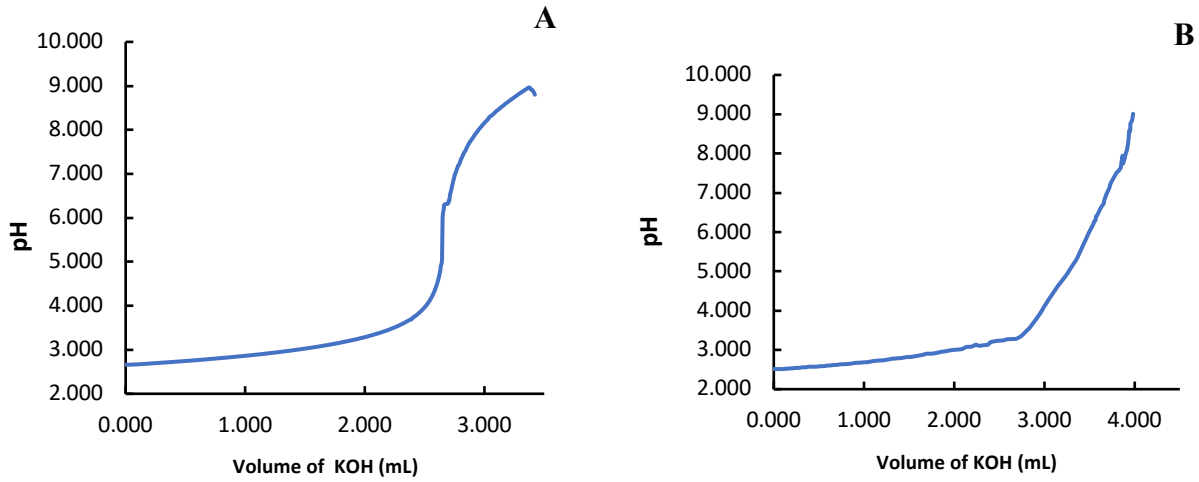

Figure B6. Potentiometric pH titration data for the addition of 0.08419 M KOH to acidic aqueous solutions containing 100 mM KCl and either A) 1.0 mM H_4qp4 or B) 1.0 mM **1**. Each titration was performed at 25 °C under an argon atmosphere.

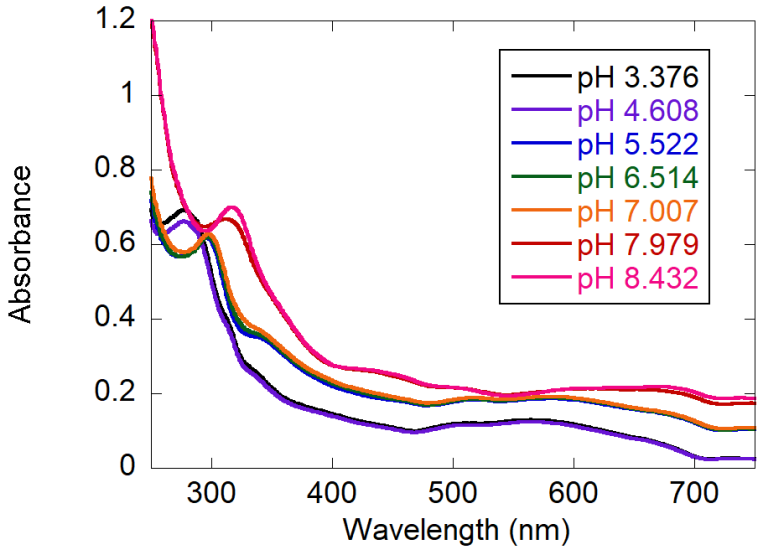

Figure B7. UV/vis spectra of a 0.05 mM solution of **1** in water adjusted to various pH values between 9 to 3 through the addition of either KOH or HCl. All spectra were obtained at 298 K under nitrogen using a 1.0 cm pathlength cuvette. The data are consistent with the deprotonation of the Fe(II)-bound quinols between pH 4.6 and 8.4.

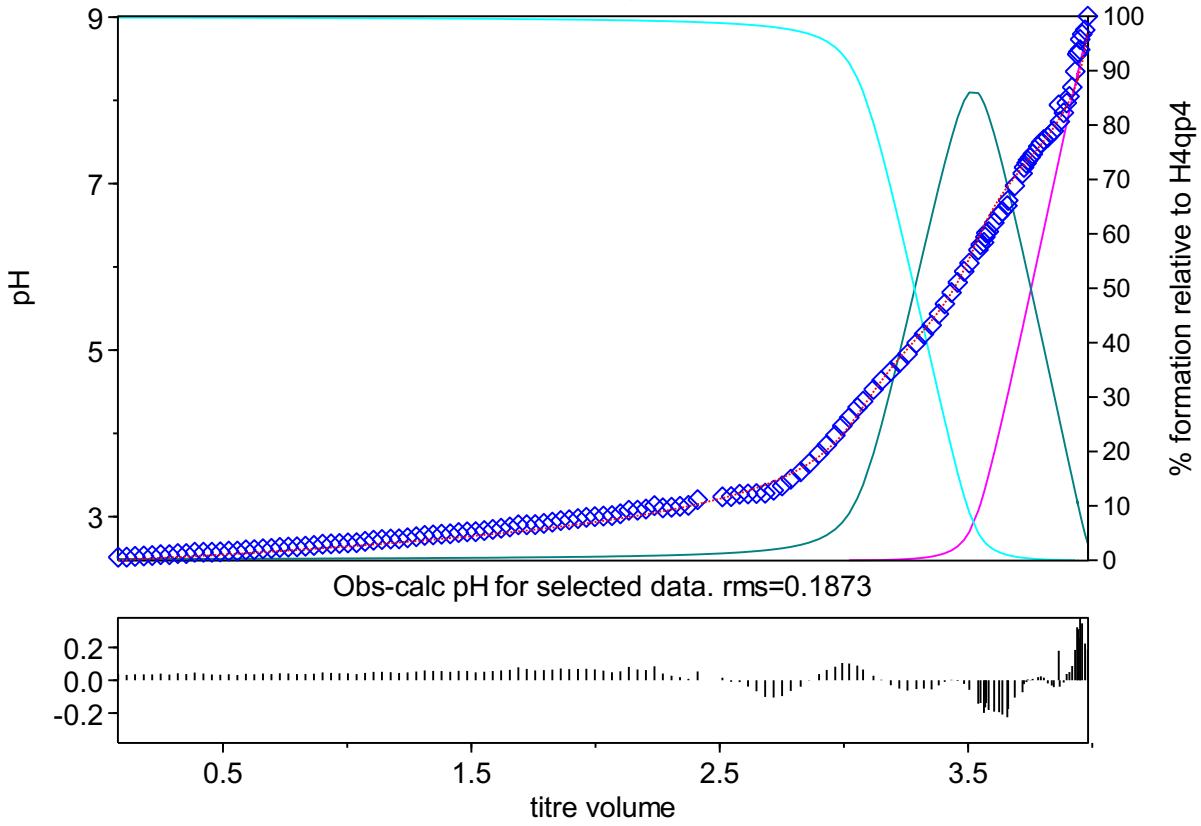

Figure B8. Hyperquad model (red line) overlaid on the experimental potentiometric pH titration data collected for **1** (blue). The curves represent the formation of various species including $[Fe^{II}(H_4qp4)]^{2+}$ (light blue), $[Fe^{II}(H_3qp4)]^{+}$ (green), and $[Fe^{II}(H_2qp4)]$ (pink). The deviations from the fit as a function of titre volume are provided below.

Table B1. Parameters for the Hyperquad model used in Figure **B8**.

Species	Fe(II)	H_4qp4	H^+	log(β)	Derived Values
$[\mathbf{H_2}qp4]^{2-}$	0	1	-2	12.48[a]	
$[\mathbf{H_3}qp4]^{1-}$	0	1	-1	22.504[a]	pK_{L4} = 10.02 (±0.05)[a]
$\mathbf{H_4}qp4$	0	1	0	31.3[a]	pK_{L3} = 8.80 (±0.05)[a]
$[\mathbf{H_5}qp4]^{1+}$	0	1	1	39.005[a]	pK_{L2} = 7.70 (±0.05)[a]
$[\mathbf{H_6}qp4]^{2+}$	0	1	2	42.506[a]	pK_{L1} = 3.50 (±0.05)[a]
Fe($\mathbf{H_2}$qp4)	1	1	-2	42.05[b]	log K_{ML} (Fe(H_2qp4)) = 29.57[c]
[Fe($\mathbf{H_3}$qp4)]$^{1+}$	1	1	-1	49.371[b]	pK_a(Fe(H_3qp4)$^+$) = 7.321[b] log K_{ML} (Fe(H_3qp4)$^+$) = 26.87[c]
[Fe($\mathbf{H_4}$qp4)]$^{2+}$	1	1	0	54.484[b]	pK_a(Fe(H_4qp4)$^{2+}$) = 5.113[b] log K_{ML} (Fe(H_4qp4)$^{2+}$) = 23.18[c]
pFe (pH 7.4) = 14.18[d]					

[a]Ligand log(β) and derived pK_a values from reference 12:

$K_{L1} = [H_5qp4^+][H^+]/[H_6qp4^{2+}]$, $pK_{L1} = \log\beta_{012} - \log\beta_{011}$

$K_{L2} = [H_4qp4][H^+]/[H_5qp4^+]$, $pK_{L2} = \log\beta_{011} - \log\beta_{010}$

$K_{L3} = [H_3qp4^-][H^+]/[H_4qp4]$, $pK_{L3} = \log\beta_{010} - \log\beta_{01(-1)}$

$K_{L4} = [H_2qp4^{2-}][H^+]/[H_3qp4^-]$, $pK_{L4} = \log\beta_{01(-1)} - \log\beta_{01(-2)}$

[b]Metal complex pK_a values:

$K_a(Fe(H_4qp4)^{2+}) = [Fe(H_3qp4)^+][H^+]/[Fe(H_4qp4)^{2+}]$ ~ *deprotonation of first quinol*

$pK_a(Fe(H_4qp4)^{2+}) = \log\beta_{110} - \log\beta_{11(-1)}$

$K_a(Fe(H_3qp4)^+) = [Fe(H_2qp4)][H^+]/[Fe(H_3qp4)^+]$ ~ *deprotonation of second quinol*

$pK_a(Fe(H_3qp4)^+) = \log\beta_{11(-1)} - \log\beta_{11(-2)}$

[c]Metal complex K_{ML} values:

K_{ML} (Fe(H_2qp4)) = [Fe(H_2qp4)]/([Fe(II)][H_2qp4^{2-}])

log K_{ML} (Fe(H_2qp4)) = $\log\beta_{11(-2)} - \log\beta_{01(-2)}$

K_{ML} (Fe(H_3qp4))$^+$ = [Fe(H_3qp4)$^+$]/([Fe(II)][H_3qp4^-])

log K_{ML} (Fe(H_3qp4))$^+$ = $\log\beta_{11(-1)} - \log\beta_{01(-1)}$

K_{ML} (Fe(H_4qp4))$^{2+}$ = [Fe(H_4qp4)$^{2+}$]/([Fe(II)][H_4qp4])

log K_{ML} (Fe(H_4qp4))$^{2+}$ = $\log\beta_{110} - \log\beta_{010}$

[d]pFe(pH 7.4) = -log([free Fe(II)]) at pH 7.4 and 298 K with 1.00 mM Fe(II) and 1.00 mM H_4qp4

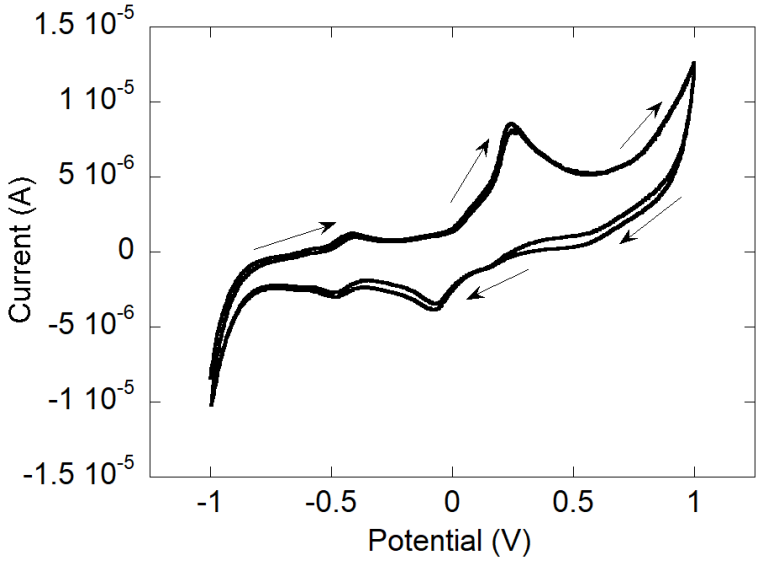

Figure B9. Cyclic voltammetry of 1.0 mM **1** in 0.10 M phosphate buffer (NaH_2PO_4/Na_2HPO_4, pH=7.2). The scan rate was 100 mV/s and began at -1.0 V. Two features are observed: a reversible feature with $E_{1/2}$ = -450 mV *vs.* Ag/AgCl (ΔE = 60 mV) and an irreversible feature with $E_{1/2}$ = 90 mV *vs.* Ag/AgCl (ΔE = 300 mV).

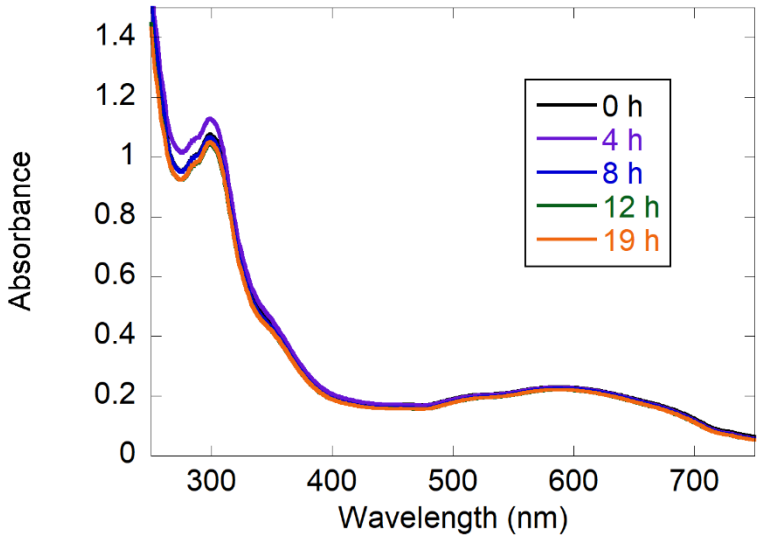

Figure B10. UV/vis spectra depicting the stability of a 0.10 mM solution of **1** in MeCN to air. The reaction monitored over 19 h. All spectra were obtained at 298 K using a 1.0 cm pathlength cuvette under air.

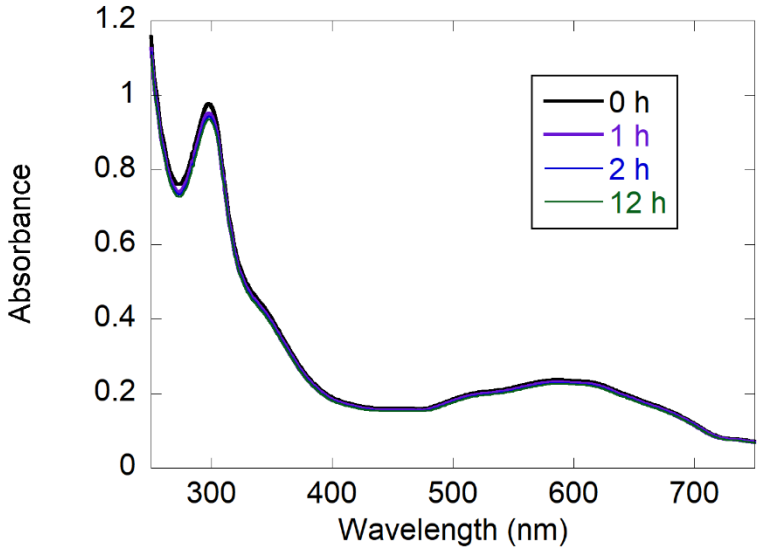

Figure B11. UV/vis spectra depicting the stability of a 0.10 mM solution of **1** in buffered water (50 mM HEPES, pH 7.0) to air. The reaction monitored over 12 h. All spectra were obtained at 298 K using a 1.0 cm pathlength cuvette under air.

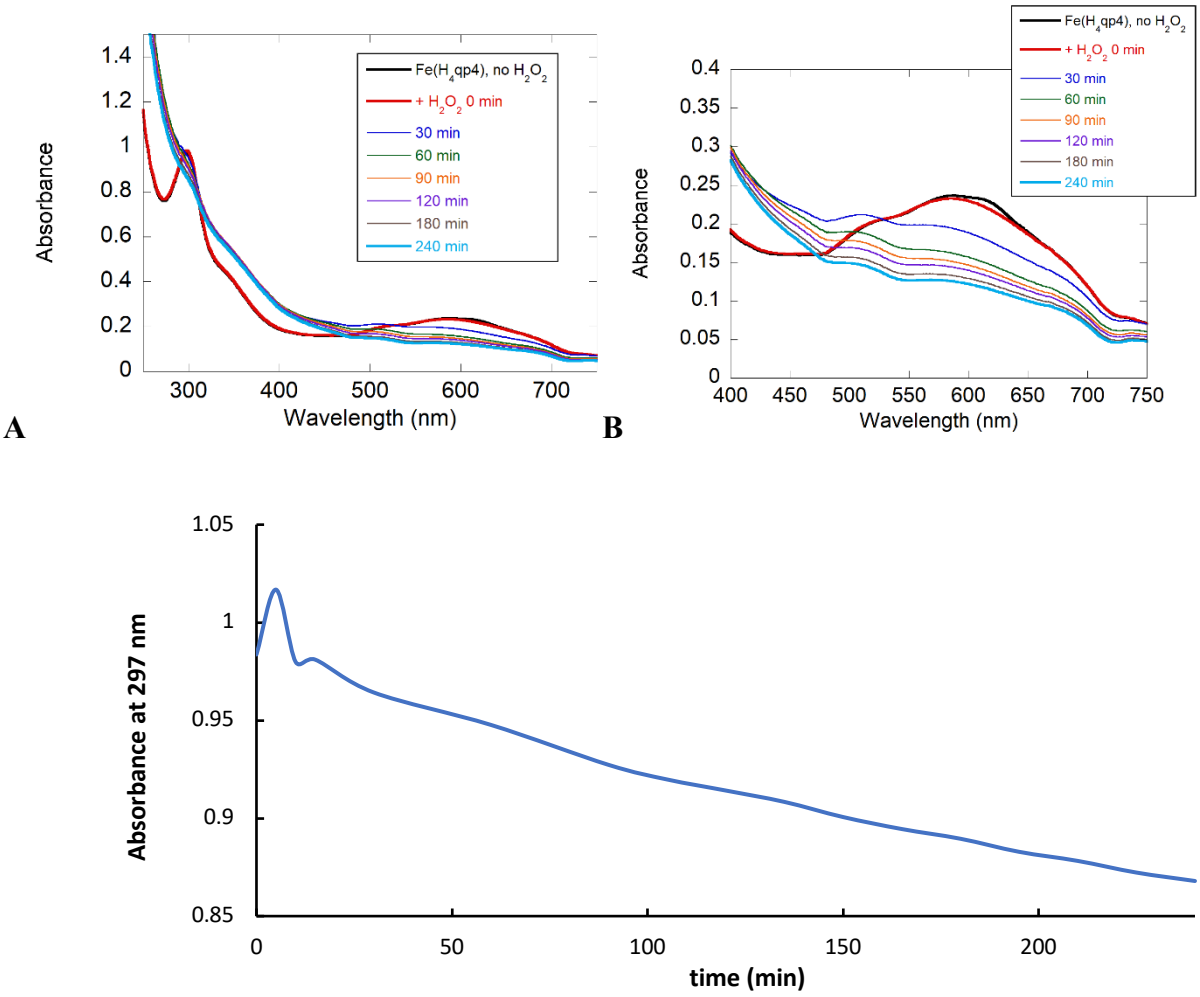

Figure B12. A) UV/vis spectra showing the reaction between 0.10 mM **1** and 10 mM H_2O_2 in 50 mM HEPES solution buffered to pH 7.00 under N_2 over 4 h. The absorbance initially increases slightly due to the unreacted H_2O_2. All spectra were obtained at 298 K using a 1.0 cm pathlength cuvette. B) Expansion of the 400-700 nm region. C) The change in the absorbance at 297 nm, which corresponds to the intraligand transition for the quinol portion of the H_4qp4 ligand, over this time. The data are consistent with the oxidation of the quinols.

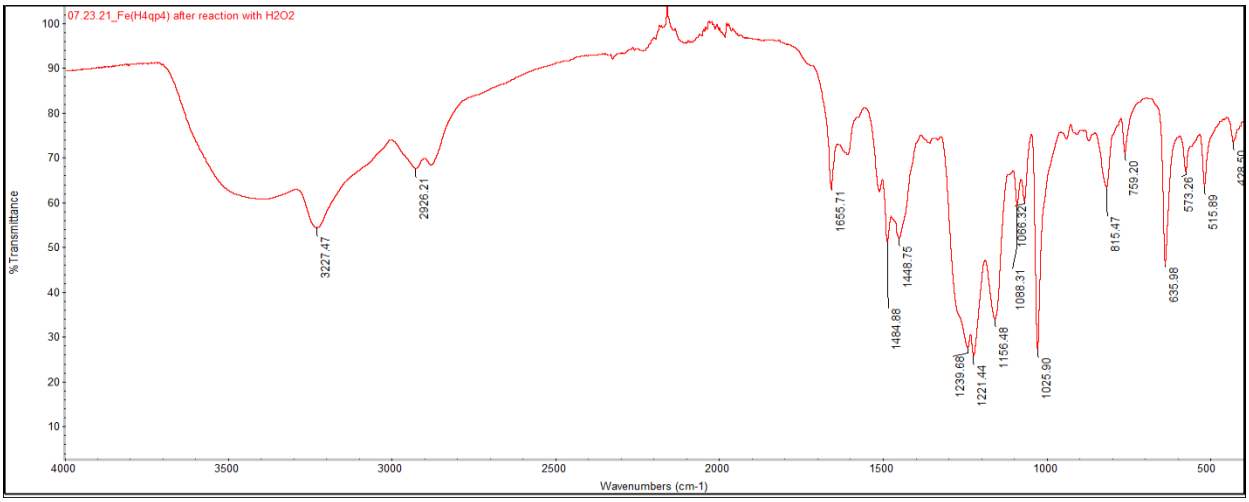

Figure B13. IR spectrum of the crude product from the reaction between 1.0 mM **1** and 10 mM H_2O_2 in 50 mM HEPES solution buffered to pH 7.0. After the reaction proceeded for 60 min, the solvents were removed, yielding the crude solid. The solid was mixed into a KBr pellet for IR analysis. The peak at 1655 cm^{-1} was not observed for **1** (Figure B2) and is assigned to the C=O stretches of the *para*-quinone subunits.

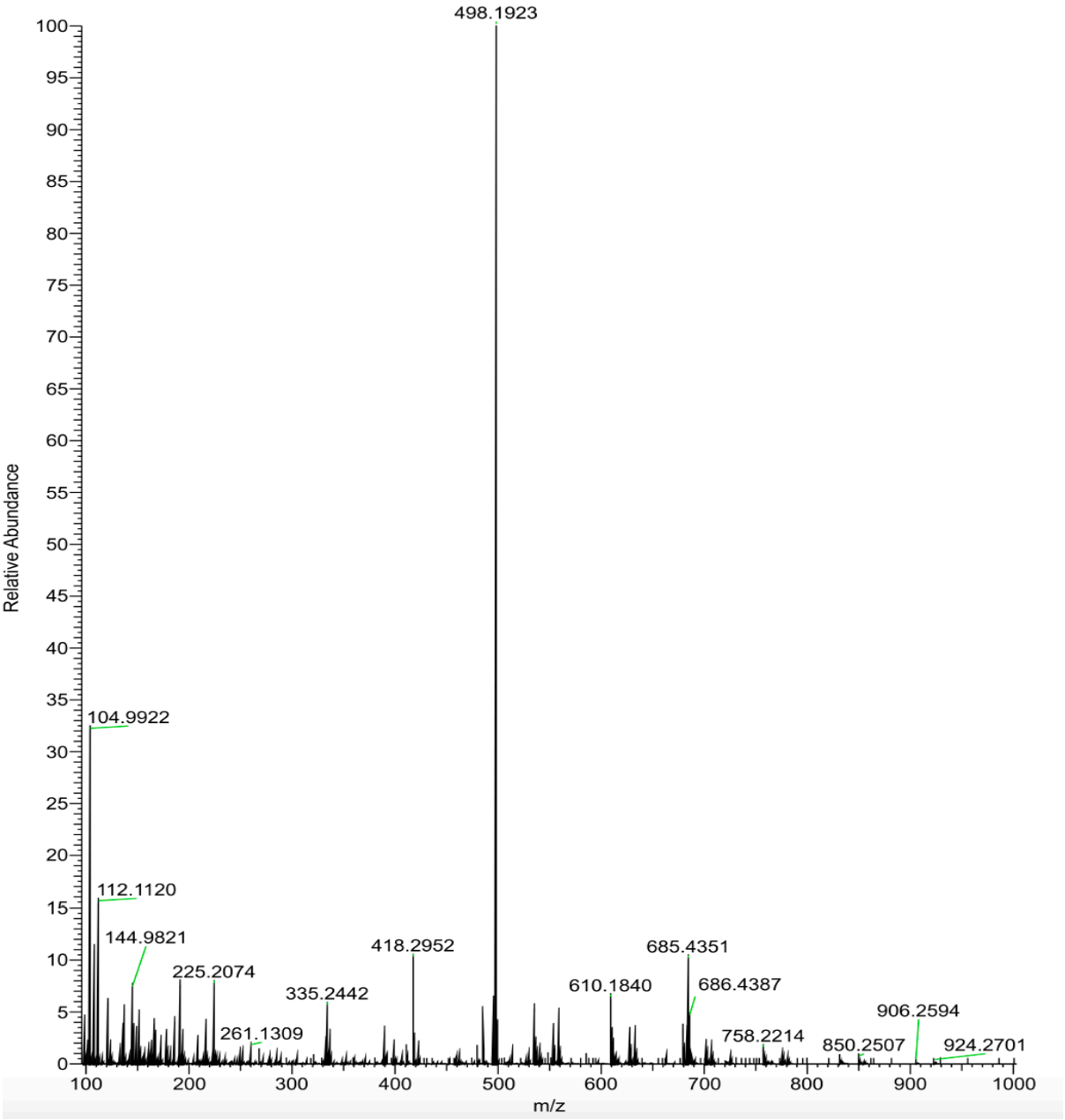

Figure B14. Mass spectrometry (ESI) of a sample of **1** that was oxidized by H_2O_2 and subsequently reduced by cysteine. Complex **1** first reacted with 4 equiv. of H_2O_2 for 60 min at RT in MeOH. The solvent and excess H_2O_2 was removed, and the crude was allowed to react with 4 equiv. cysteine for an additional 60 min. The excess cysteine was removed via filtration prior to analysis. The 498.1923 *m/z* feature is assigned to $[Fe^{III}(H_2qp4)]^+$ (calculated *m/z* = 498.1929).

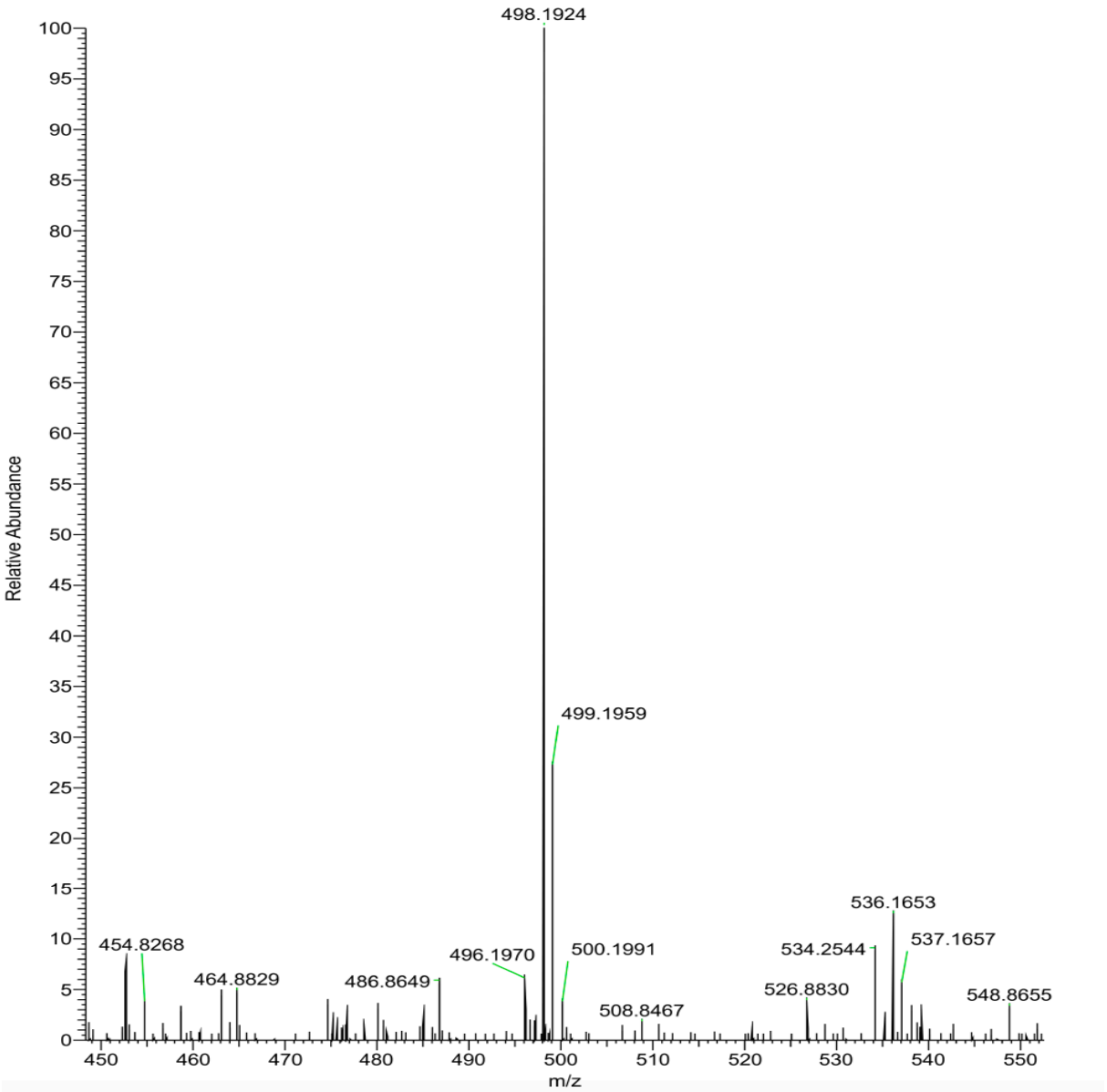

Figure B15. Mass spectrometry (ESI) of a sample of **1** that was sequentially oxidized by H_2O_2 and reduced by sodium dithionite. Complex **1** first reacted with 4 equiv. of H_2O_2 for 60 min at RT in MeOH. The solvent and excess H_2O_2 was removed, and the crude was allowed to react with 4 equiv. sodium dithionite of for an additional 60 min. The excess sodium dithionite was removed via filtration prior to analysis. The 498.1924 *m/z* feature is assigned to $[Fe^{III}(H_2qp4])^+$ (calculated *m/z* = 498.1929).

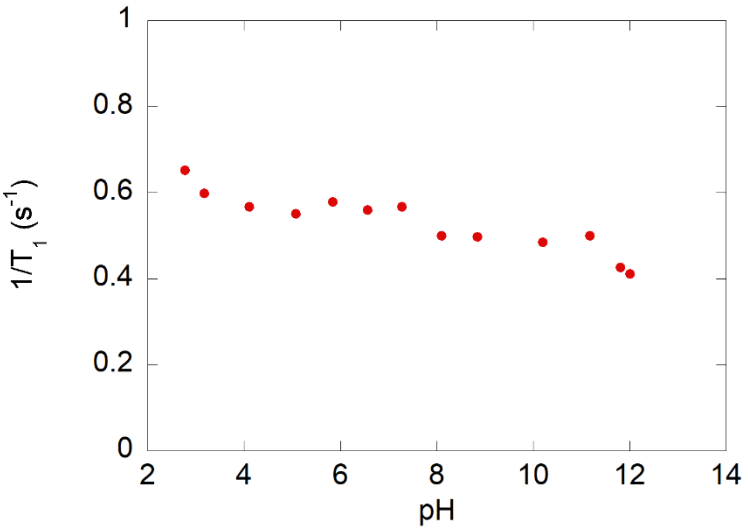

Figure B16. Plot of R_1 ($1/T_1$) versus pH for a 0.50 mM solution of **1** in unbuffered water. The pH was controlled via the addition of HCl and KOH. All samples were analyzed at 298 K using a 3T field provided by a clinical MRI scanner. The R_1 for the iron-free water reference was 0.36 s^{-1}.

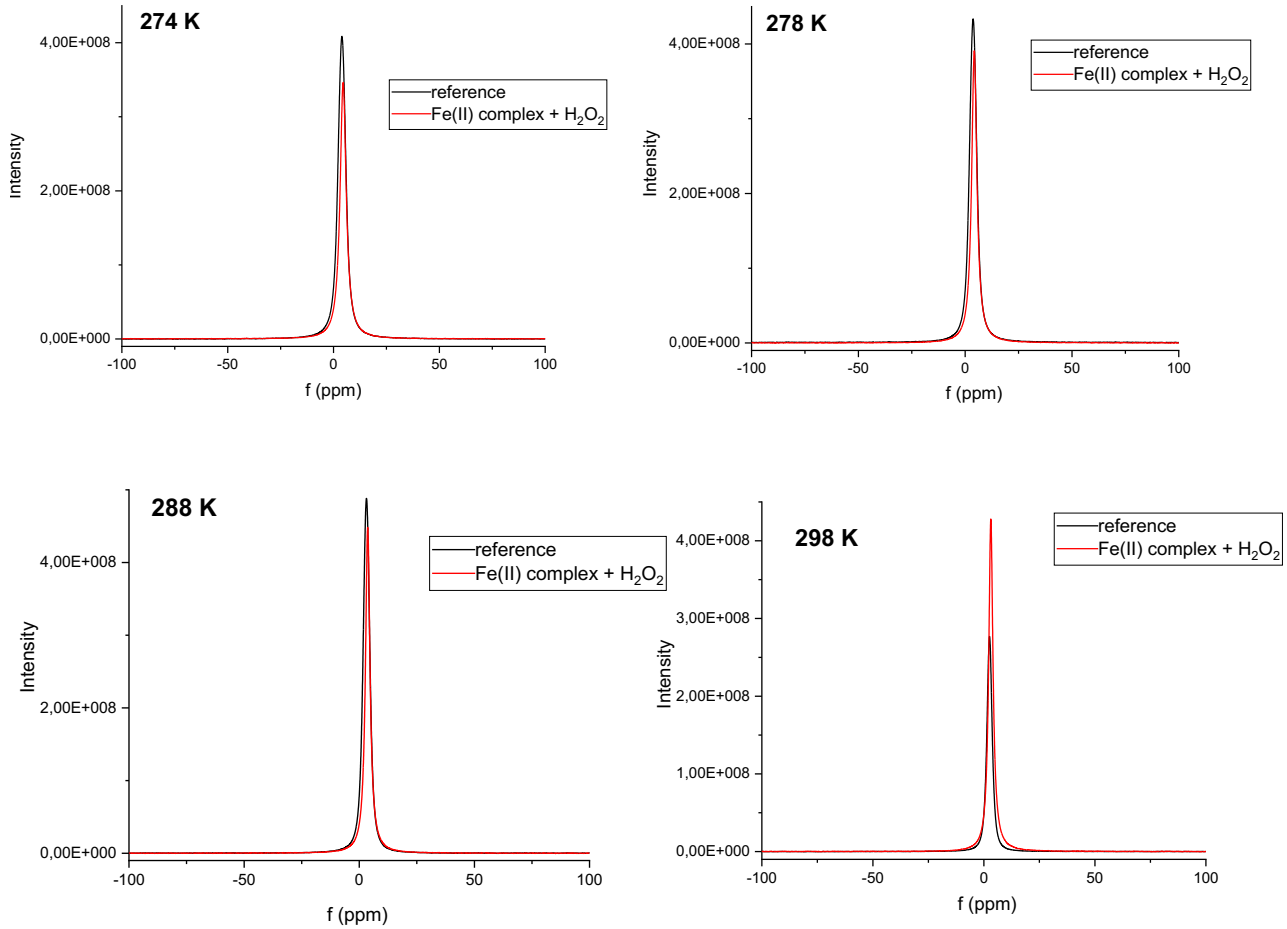

Figure B17. ^{17}O NMR signals of the bulk solvent in the absence (black line, reference) and presence of a 1:10 mixture of **1** and H_2O_2 at various temperatures. Experimental conditions: $[\mathbf{1}]_o$ = 9.8 mM in 0.06 M MOPS buffered to pH 7.4, 20 % (v/v) MeCN, 1% ^{17}O enrichment. The nearly identical line-widths suggest that water molecules do not exchange rapidly on the Fe(III) metal centers in the oxidized products.

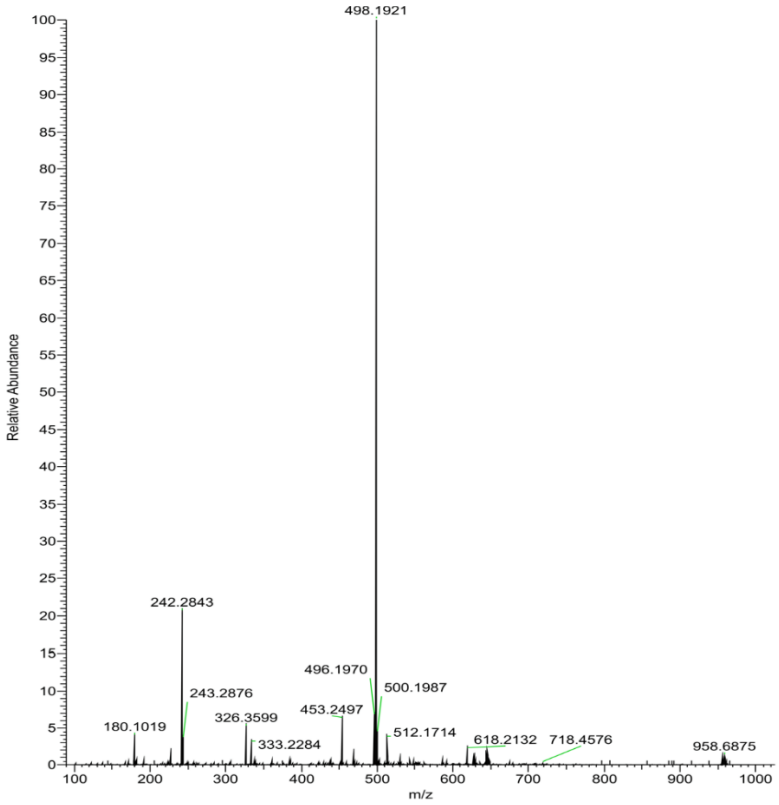

Figure B18. Mass spectrometry (ESI) of **3** in MeCN. The 498.1921 *m/z* feature is assigned to the doubly deprotonated Fe(III) complex $[Fe(H_2qp4)]^+$ (calculated *m/z* = 498.1929).

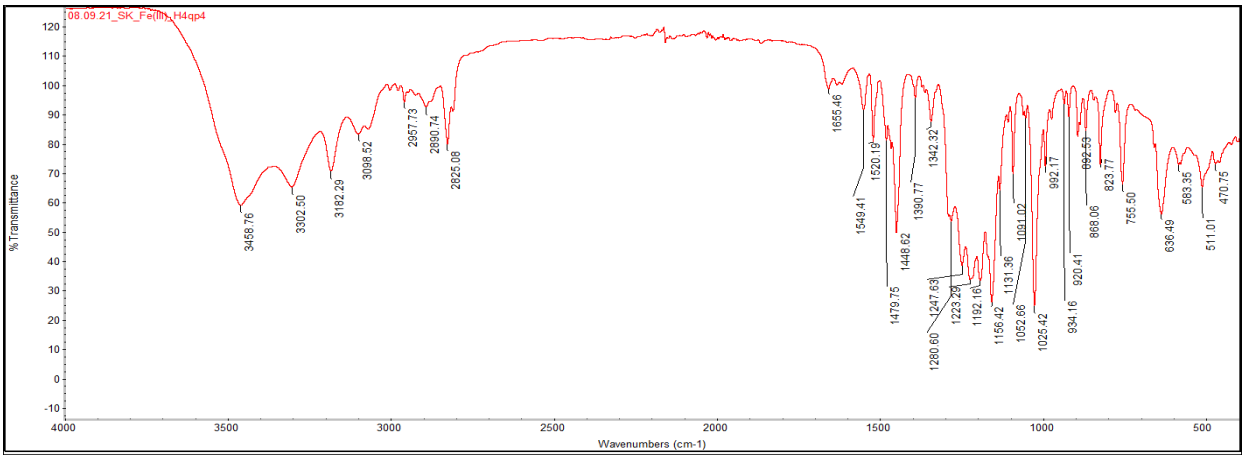

Figure B19. IR spectrum of $[Fe^{III}(H_3qp4)](OTf)_2$ (**3**). The 3458 cm^{-1} feature is assigned to the O-H stretches associated with the quinol groups of the H_4qp4 ligand.

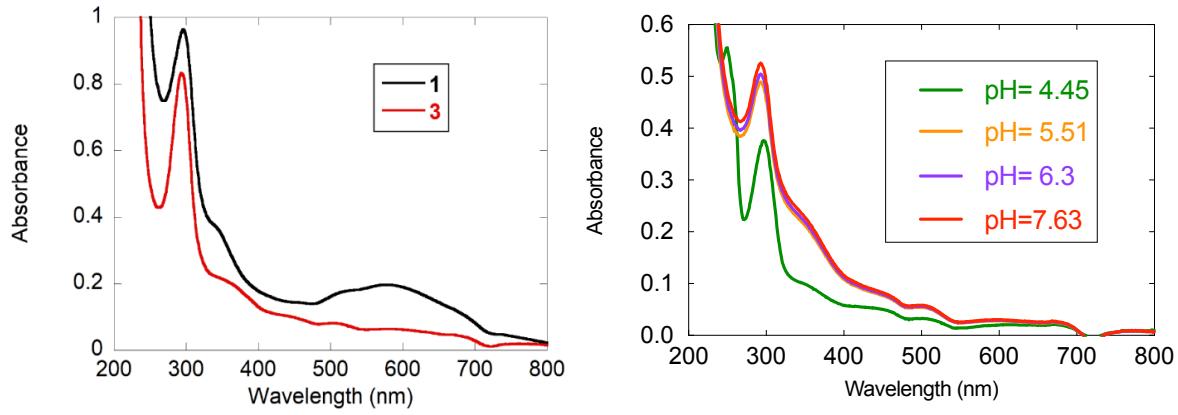

A **B**

Figure B20. A) UV/vis spectrum of a 0.10 mM solution of **3** in an aqueous solution containing 50 mM HEPES buffered to pH 7.0. This spectrum was obtained at 298 K using a 1.0 cm pathlength cuvette under air. The spectrum of **1** obtained under the same conditions is provided as a reference. B) Spectrophotometric pH titration of 0.05 mM solution of **3** at 298 K with a 1.0 cm pathlength cuvette.

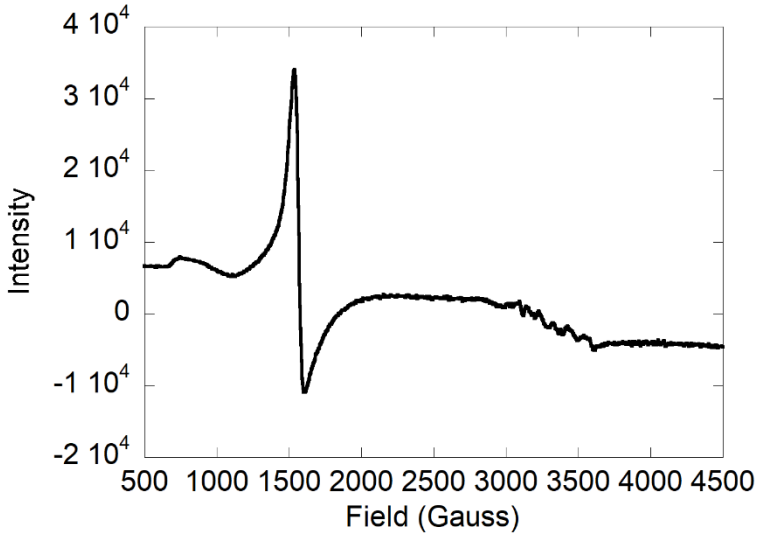

Figure B21. X-band EPR spectrum for a 1.0 mM solution of **3** in an aqueous solution containing 50 mM HEPES buffered to pH 7.0. The sample was frozen to 77 K prior to data collection.

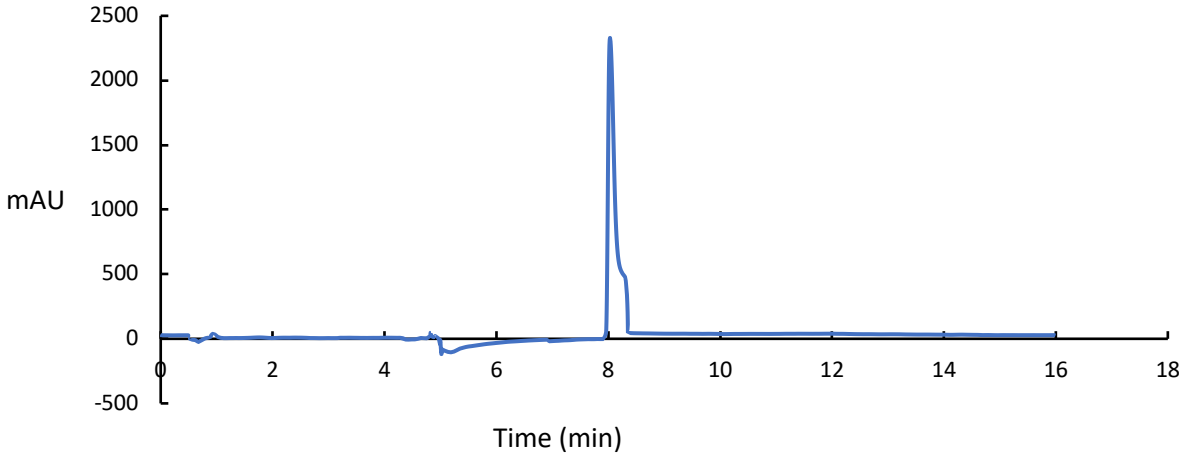

Figure B22. LC trace for **3** run under the method described in the Experimental Section. The only observed peak is at 8.02 min. The peak is distinct from that observed for the free H_4qp4 ligand which elutes at 2.32 min when run under the same conditions. The following method was used: Gradient 90% A and 10% B to 100% B over 20 min. Flow rate = 0.20 mL/min, injection volume = 25.0 µL, column temperature = 37.0 °C. Before each run, the HPLC instrument was flushed with eluent 100% A to 100% B over 16 min with a flow rate of 0.49 mL/min and an injection volume of 25.0 µL.

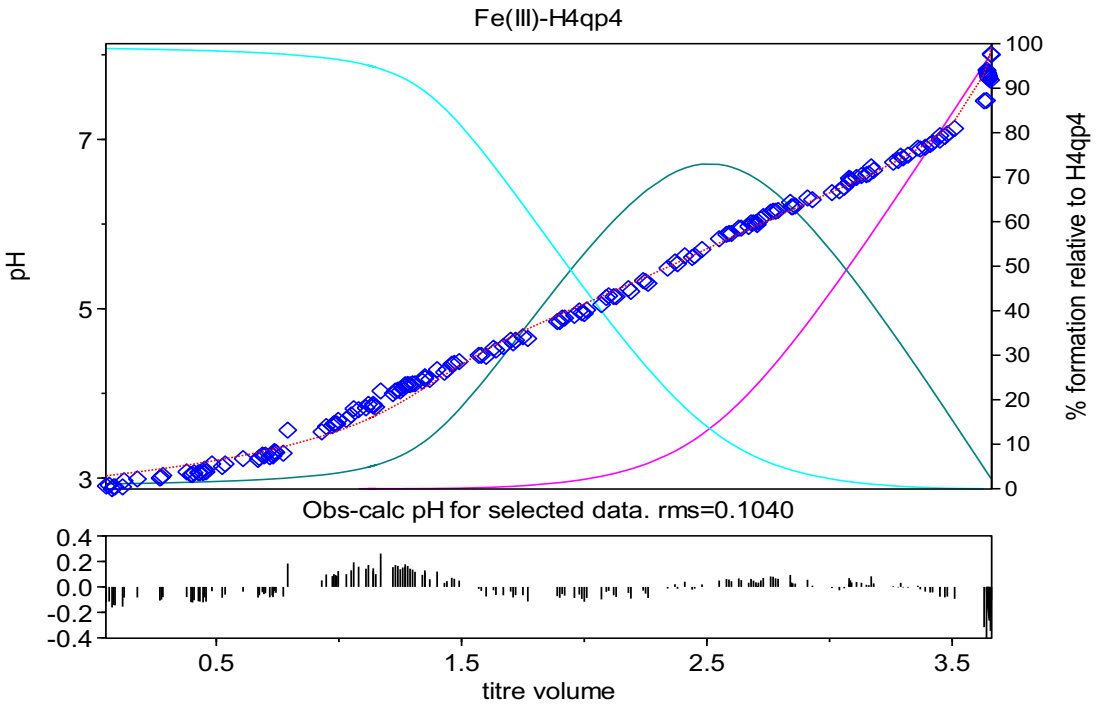

Figure B23. Hyperquad model (red line) overlaid on the experimental potentiometric pH titration data collected for **3** (blue). The curves represent the formation of various species including $[Fe^{III}(H_4qp4)]^{2+}$ (light blue), $[Fe^{III}(H_3qp4)]^{+}$ (green), and $[Fe^{III}(H_2qp4)]$ (pink). The deviations from the fit as a function of titre volume are provided below. Precipitate began to form at pH 8.0, halting the collection of data.

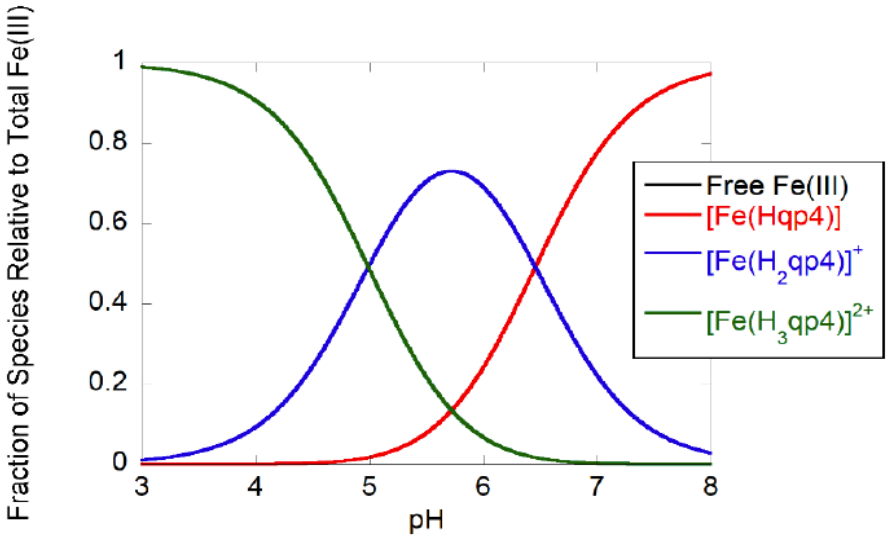

Figure B24. Predicted speciation as a function of pH for 1.0 mM **3** in an aqueous solution containing 100 mM KCl at 25 ºC.

Table B2. Parameters for the Hyperquad model used in Figure **B23.**

Species	Fe(III)	H_4qp4	H^+	log(β)	Derived Values
$[\mathbf{H_2}qp4]^{2-}$	0	1	-2	12.48[a]	
$[\mathbf{H_3}qp4]^{1-}$	0	1	-1	22.504[a]	pK_{L4} = 10.02 (±0.05)[a]
$\mathbf{H_4}qp4$	0	1	0	31.3[a]	pK_{L3} = 8.80 (±0.05)[a]
$[\mathbf{H_5}qp4]^{1+}$	0	1	1	39.005[a]	pK_{L2} = 7.70 (±0.05)[a]
$[\mathbf{H_6}qp4]^{2+}$	0	1	2	42.506[a]	pK_{L1} = 3.50 (±0.05)[a]
[Fe(**H**qp4)]	1	1	-3	44.8611[b]	
$[Fe(\mathbf{H_2}qp4)]^+$	1	1	-2	51.3183[b]	$pK_a(Fe(H_2qp4)^+)$ = 6.457[b] log K_{ML} $(Fe(H_2qp4)^+)$ = 38.8383[c]
$[Fe(\mathbf{H_3}qp4)]^{2+}$	1	1	-1	56.308[b]	$pK_a(Fe(H_3qp4)^{2+})$ = 4.990[b] log K_{ML} $(Fe(H_3qp4)^{2+})$ = 33.804[c]

[a]Ligand log(β) and derived pK_a values from reference 12:

$K_{L1} = [H_5qp4^+][H^+]/[H_6qp4^{2+}]$, $pK_{L1} = \log\beta_{012} - \log\beta_{011}$

$K_{L2} = [H_4qp4][H^+]/[H_5qp4^+]$, $pK_{L2} = \log\beta_{011} - \log\beta_{010}$

$K_{L3} = [H_3qp4^-][H^+]/[H_4qp4]$, $pK_{L3} = \log\beta_{010} - \log\beta_{01(-1)}$

$K_{L4} = [H_2qp4^{2-}][H^+]/[H_3qp4^-]$, $pK_{L4} = \log\beta_{01(-1)} - \log\beta_{01(-2)}$

[b]Metal complex pK_a values:

$K_a(Fe(H_3qp4)^{3+}) = [Fe(H_2qp4)^{2+}][H^+]/[Fe(H_3qp4)^{3+}]$ ~ *deprotonation of Second quinol*

$pK_a(Fe(H_3qp4)^{3+}) = \log\beta_{11(-1)} - \log\beta_{11(-2)}$

$K_a(Fe(H_2qp4)^+) = [Fe(Hqp4)^+][H^+]/[Fe(H_2qp4)^{2+}]$ ~ subsequent deprotonation

$pK_a(Fe(H_2qp4)^{2+}) = \log\beta_{11(-2)} - \log\beta_{11(-3)}$

[c]Metal complex K_{ML} values:

$K_{ML}\,(Fe(H_2qp4)^+) = [Fe(H_2qp4)^+]/([Fe(III)][H_2qp4^{2-}])$

log K_{ML} $(Fe(H_2qp4)^+) = \log\beta_{11(-2)} - \log\beta_{01(-2)}$

$K_{ML}\,(Fe(H_3qp4)^{2+}) = [Fe(H_3qp4)^{2+}]/([Fe(III)][H_3qp4^-])$

log K_{ML} $(Fe(H_3qp4))^+ = \log\beta_{11(-1)} - \log\beta_{01(-1)}$

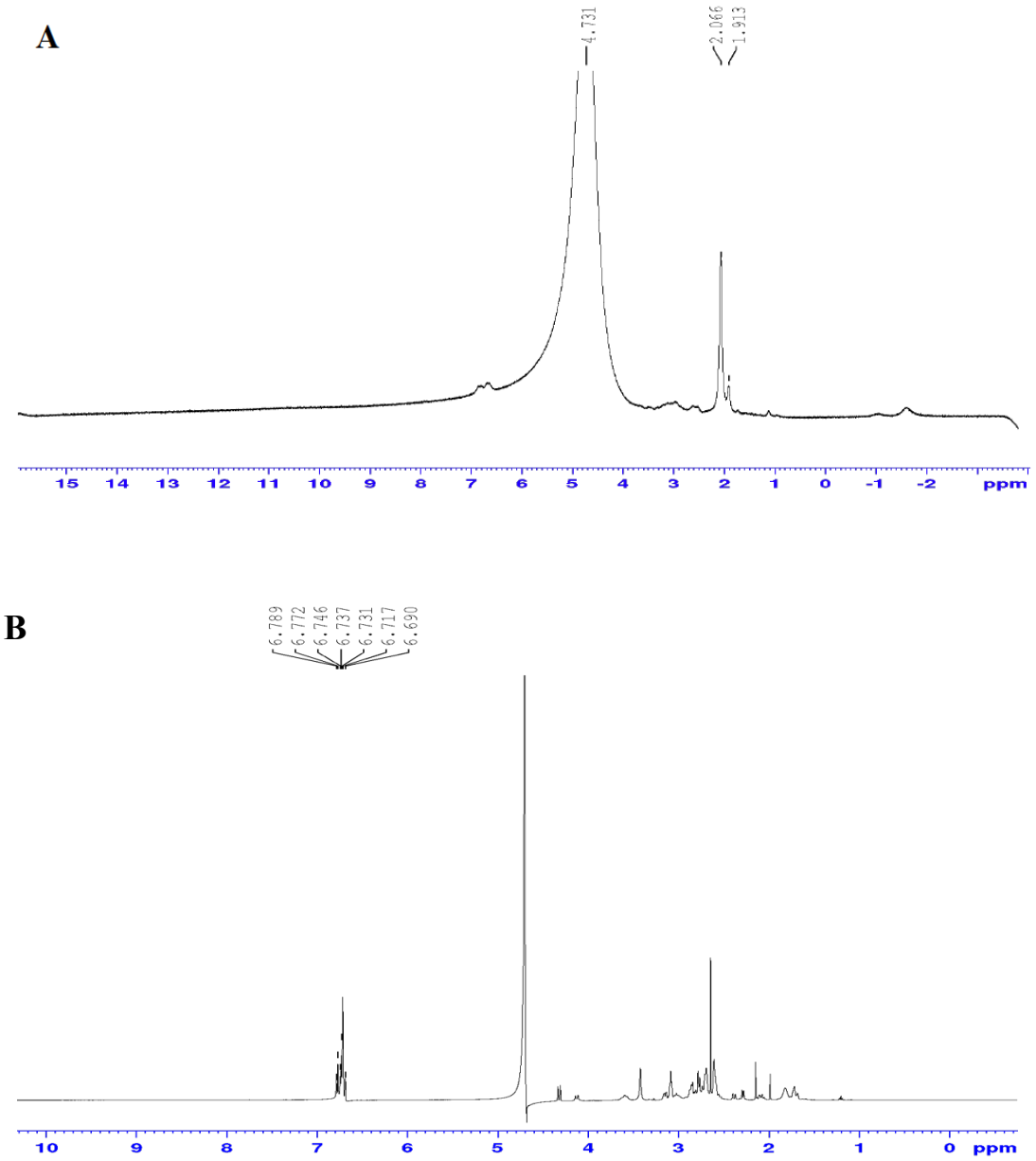

Figure B25. A) Reaction between 20 mM $Zn(ClO_4)_2$ and 10 mM **3** in D_2O. The reaction equilibrated at 295 K for 48 h prior to data acquisition. B) ^1H NMR spectrum of the product of the reaction between 10 mM $Zn(ClO_4)_2$ and 10 mM metal-free H_4qp4 in D_2O.

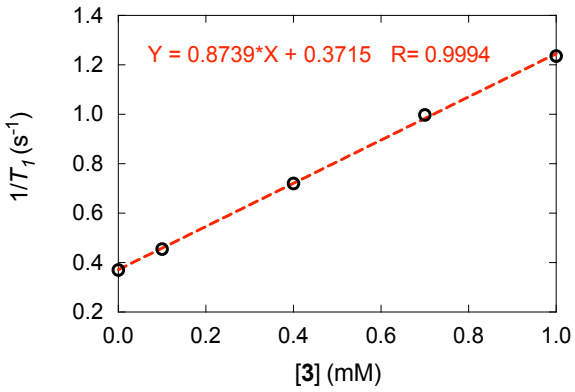

Figure B26. Plot of $1/T_1$ versus iron concentration for **3** in 298 K aqueous solutions containing 50 mM HEPES buffered to pH 7.00 using a 3T field provided by a clinical MRI scanner. All samples were prepared under air. The data were fit to the provided linear equation. The calculated r_1 for **3** under these conditions is 0.87 mM^{-1} s^{-1}.

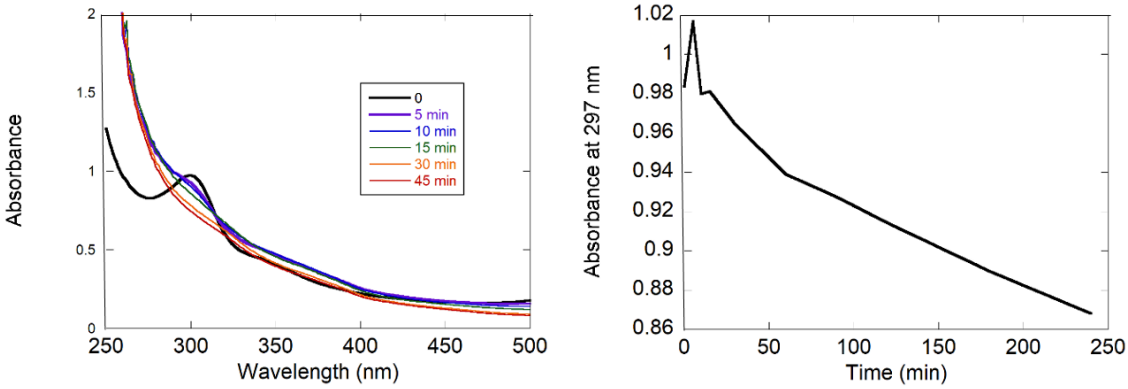

A **B**

Figure B27. A) UV/vis spectra for the reaction between 0.10 mM **1** and 0.60 mM H_2O_2 in an aqueous solution containing 50 mM HEPES buffered to pH 7.0. The Fe(II) complex oxidizes much more quickly than in Figure B12. B) Plot of the absorbance at 297 nm as a function of time.

Start Time: 0 s; End Time: 3.707 s; Catalase Activity During Monitored Time: 1.021

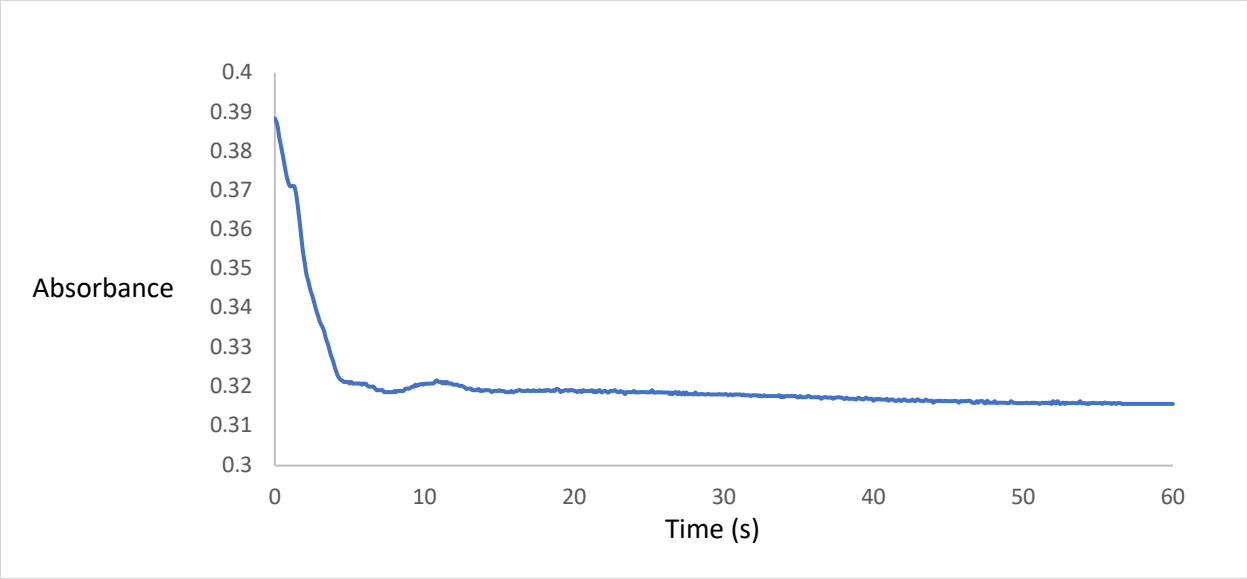

Start Time: 0 s; End Time: 2.977 s; Catalase Activity During Monitored Time: 1.029

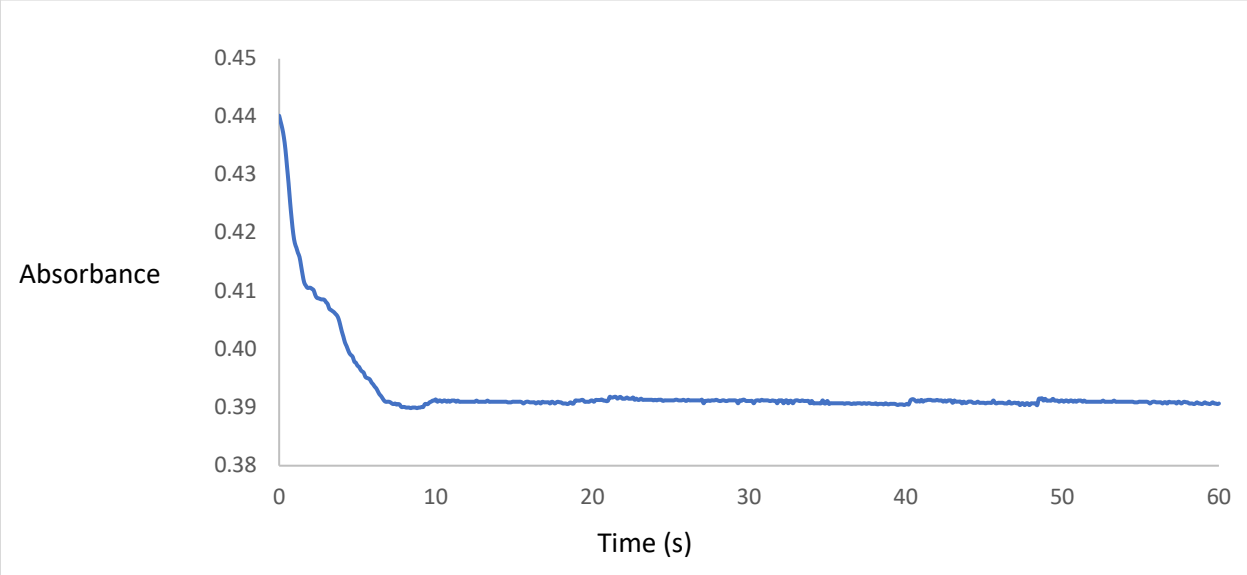

Figure B28. Representative kinetic traces for the reaction between 100 nM **1** and 10 mM H_2O_2 in 200 mM phosphate solution buffered to pH 7.0. The absorbance at 240 nm was monitored over time. Activity values were calculated using the UV-1601PC Kinetics program and converted to an initial rate ($v_o/[\mathbf{1}]_T$) using the following equation:

$v_o/[\mathbf{1}]_T$ = (activity)/[60 s × 0.1 μM × 0.0000394 μM^{-1} cm^{-1} × 1.0 cm]

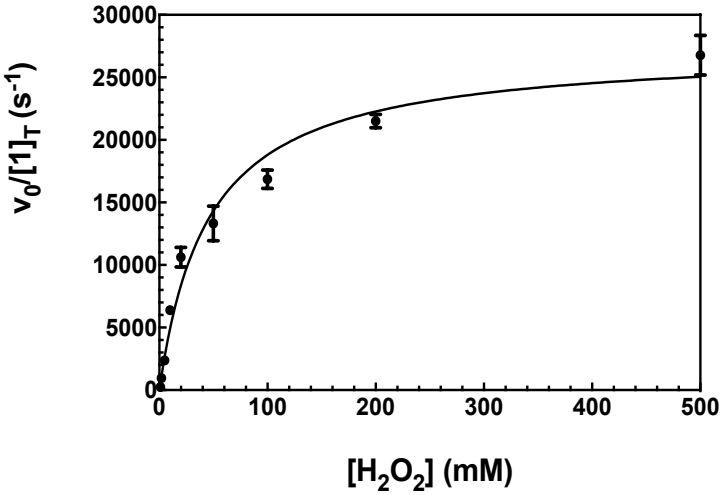

Figure B29. Activity of **1** with increasing concentrations of H_2O_2. All reactions were performed in 200 mM phosphate buffered to pH 7.0 at 25 °C with a 100 nM concentration of 1. The reaction was run five times per H_2O_2 concentration.

Table B3. Fit of the data from Figure **B29** to the Michaelis-Menten equation. Our best fit provides $k_{cat} = 2.73 \times 10^4$ s^{-1} and $k_{on} = 6.03 \times 10^5$ M^{-1} s^{-1}.

Rearranged Michaelis Menten	
Best-fit values	
Kcat	27319
Kon	602.8
Std. Error	
Kcat	1039
Kon	59.89
95% CI (asymptotic)	
Kcat	25223 to 29415
Kon	482.1 to 723.6
Goodness of Fit	
Degrees of Freedom	43
R squared	0.9461
Sum of Squares	197941948
Sy.x	2146
Number of points	

References

1. Laforge, M.; Elbim, C.; Frère, C.; Hémadi, M.; Massaad, C.; Nuss, P.; Benoliel, J. -J.; Becker, C. *Nat. Rev. Immunol.* **2020**, 20, 515-516.

2. Chang, M.C.; Pralle, A.; Isacoff, E.Y.; Chang, C. J.; *J. Am. Chem. Soc.* **2004**, 126, 15392-15393.

3. Ekanger, L. A.; Ali, M. M.; Allen, M. J. *Chem. Commun.* **2014**, 50, 14835-14838.

4. Lippert, A. R.; Van de Bittner, G. C.; Chang, C. J. *Acc. Chem. Res.* **2011**, 44, 793-804.

5. Lou, Z.; Li, P.; Han, K. *Acc. Chem. Res.* **2015,** 48, 1358-1368.

6. Miller, E. W.; Albers, A. E.; Pralle, A.; Isacoff, E. Y.; Chang, C. J. *J. Am. Chem. Soc*. **2005**, 127, 16652-16659.

7. Song, B.; Wu, Y.; Yu, M.; Zhao, P.; Zhou, C.; Kiefer, G. E.; Sherry, A. D. *Dalton Trans.* **2013**, 42, 8066-8069.

8. Srikun, D.; Miller, E. W.; Domaille, D. W.; Chang, C. J. *J. Am. Chem. Soc.* **2008**, 130, 4596-4597.

9. Tsitovich, P. B.; Burns, P. J.; McKay, A. M.; Morrow, J. R. *J. Inorg. Biochem*. **2014**, 133, 143-154.

10. Loving, G. S.; Mukherjee, S.; Caravan, P. *J. Am. Chem. Soc.* **2013**, 135, 4620-4623.

11. Wang, H.; Jordan, V. C.; Ramsay, I. A.; Sojoodi, M.; Fuchs, B. C.; Tanabe, K. K.; P.; Caravan, Gale, E. M. *J. Am. Chem. Soc.* **2019**, 141, 5916-5925.

12. Karbalaei, S.; Knecht, E.; Franke, Zahl, A.; Saunders, A. C.; Pokkuluri, P. R.; Beyers, R. J.; Ivanovi´c-Burmazovi´c, I.; Goldsmith, C. R. *Inorg. Chem.* **2021**, 60, 8368-8379.

13. Yu, M.; Ambrose, S. L.; Whaley, Z. L.; Fan, S.; Gorden, J. D.; Beyers, R. J.; Schwartz, D. D.; Goldsmith, C. R. *J. Am. Chem. Soc*. **2014**, 136, 12836-12839.

14. Yu, M.; Ward, M. B.; Franke, A.; Ambrose, S. L.; Whaley, Z. L.; Bradford, T. M.; Gorden, J. D.; Beyers, R. J.; Cattley, R. C.; Ivanovi´c-Burmazovi´c, I.; Schwartz, D. D.; Goldsmith, C. R.; *Inorg. Chem.* **2017**, 56, 2812-2826.

15. Yu, M.; Beyers, R. J.; Gorden, J. D.; Cross, J. N.; Goldsmith, C. R. *Inorg. Chem.* **2012**, 51, 9153-9155.

16. Cotton, F. A.; Wilkinson, G. *in Advanced Inorganic Chemistry*, 5 ed., John Wiley & Sons, New York, **1988**.

17. Hoener, B. -a.; Engelstad, B. L.; Ramos, E. C.; Macapinlac, H. A.; Price, D. C.; Johnson, T. R.; White, D. L. *J. Magn. Reson.* **1991**, 1, 357-362.

18. Schwert, D. D.; Davies, J. A.; Richardson, N. *Top. Curr. Chem.* **2002**, 221, 165-199.

19. Bain, G. A.; Berry, J. F. *J. Chem. Educ.* **2008**, 85, 532-536.

20. Evans, D. F. *J. Chem. Soc.* **1959**, 2003-2005.

21. Sur, S. K. *J. Magn. Reson.* **1989**, 82, 169-173.

22. Gans, P.; Sabatini, A.; Vacca, A. *Talanta* **1996**, 43, 1739-1753.

23. Zhang, Q.; Gorden, J. D.; Beyers, R. J.; Goldsmith, C. R. *Inorg. Chem.* **2011**, 50, 9365-9373.

24. Hutchinson, T. E.; Bashir, A.; Yu, M.; Beyers, R. J.; Goldsmith, C. R. *Inorg. Chim. Acta* **2019,** 496, 119045.

25. Bernstein, M. A.; King, K. F.; Zhou, X. J. *in Handbook of MRI Pulse Sequences*, Elsevier Academic Press, Amsterdam, **2004**.

26. Haacke, E. M.; Brown, R. W.; Thompson, M. R.; Venkatesan, R. *in Magnetic Resonance Imaging: Physical Principles and Sequence Design*, John Wiley & Sons, New York, NY, 1999.

27. Nelder, J. A.; Mead, R. *Comput. J.* **1965**, 7, 308-313.

28. Swift, T. J.; Connick, R. E *J. Chem. Phys.* **1962**, 37, 307-320.

29. Ran, Y.; He, Y.; Yang, G.; Johnson, J. L. H.; Yalkowsky, S. H. *Chemosphere* 2002, 48, 487-509.

30. Engelmann, F. M.; Rocha, S. V. O.; Toma, H. E.; Araki, K.; Baptista, M. S. *Int. J. Pharm.* **2007**, 329, 12-18.

31. Gale, E. M.; Mukherjee, S.; Liu, C.; Loving, G. S.; Caravan, P. *Inorg. Chem.* **2014**, 53, 10748-10761.

32. Sahoo, S. C.; Dubey, M.; Alam, M. A.; Ray, M. *Inorg. Chim. Acta* **2010**, 363, 3055-3060.

33. Irving, H.; Williams, R. J. P. *J. Chem. Soc.* **1953**, 3192-3210.

34. Martell, A. E. *in Critical Stability Constants*, Plenum Press, New York, NY, **1974**.

35. Antunes, P.; Campello, P. M.; Delgado, R.; Drew, M. G. B.; Félix, V.; Santos, I. *Dalton Trans.* **2003**, 1852-1860.

36. Davies, P. J.; Taylor, M. R.; Wainwright, K. P.; Harriott, P.; Duckworth, P. A. *Inorg. Chim. Acta* **1996**, 246, 1-6.

37. Liang, X.; Weish.upl, M.; Parkinson, J. A.; Parsons, S.; McGregor, P. A.; Sadler, P. J. *Chem. Eur. J.* **2003**, 9, 4709-4717.

38. Goldsmith, C. R.; Jonas, R. T.; Stack, T. D. P. *J. Am. Chem. Soc.* **2002,** 124, 83-96.

39. Chan, T. -L.; Mak, T. C. W.; *J. Chem. Soc. Perkin Trans. 2* **1983**, 777-781.

40. Snyder, E. M.; Asik, D.; Abozeid, S. M.; Burgio, A.; Bateman, G.; Turowski, S. G.; Spernyak, J. A.; Morrow, J. R. *Angew. Chem. Int. Ed.* **2020**, 59, 2414–2419; *Angew. Chem.* 2020, 132, 2435-2440.

41. Martell, A. E.; Motekaitis, R. J.; Chen, D.; Hancock, R. D.; McManus, D. *Can. J. Chem.* **1996**, 74, 1872-1879.

42. Casanova, D.; Alemany, P.; Bofill, J. M.; Alvarez, S. *Chem. Eur. J.* **2003**, 9, 1281-1295.

43. Giorgio, M.; Trinei, M.; Migliaccio, E.; Pelicci, P. G.; *Nat. Rev. Mol. Cell Biol.* **2007**, 8, 722-728.

44. Carney, C. E.; MacRenaris, K. W.; Meade, T. J. *J. Biol. Inorg. Chem.* **2015**, 20, 971-977.

Chapter 4

An Fe(II) Complex Acts as a Bimodal Sensor for Hydrogen Peroxide with ^{1}H and ^{19}F Magnetic Resonance Imaging Responses*

* This chapter is a version of a manuscript under preparation by the following authors: Sana Karbalaei, Alicja Franke, P. Raj Pokkuluri, Ronald J. Beyers, Ivana Ivanović-Burmazović, and Christian R. Goldsmith.

4.1 Introduction

Various oxidatively reactive small molecules are classified as reactive oxygen species (ROS), including H_2O_2, O_2^-, and $^{\cdot}OH$. Normal cellular metabolism generates ROS, which controls several physiological processes; however, if their concentrations are not properly regulated, they can induce oxidative stress that can in turn result in various health disorders, such as cancer, neurodegenerative disease, and cardiovascular disease.[1–4] Given the potential roles of ROS in disease, extensive effort has been directed towards developing probes that could detect these species in physiological environments.[5–11] A particularly attractive spectroscopic mode for these sensors is magnetic resonance imaging (MRI), which uses widely available clinical instrumentation to non-invasively visualize soft tissues within the body without the use of ionizing radiation.

We have recently synthesized a series of redox-responsive ^{1}H MRI contrast agents consisting of Mn(II) and Fe(II) complexes with linear and macrocyclic quinol-containing ligands (Scheme 4.1). Upon reaction with H_2O_2, these convert to species with higher T_1-weighted relaxivities (r_1) associated with changes in either the number of water molecules attached to the metal center or the oxidation state of the metal.[12–15] For the Mn(II) complexes, the quinols oxidize to *para*-quinones during the reaction with H_2O_2; this weakens the abilities of these groups to coordinate to the metal center and facilitates their displacement by water molecules, which in turn increases r_1.[12–14] The manganese remains in the highly paramagnetic +2 oxidation state. This contrasts with the Fe(II)-containing $[Fe^{II}(H_3qp4)]^{1+}$, which oxidizes to an Fe(III) species with a r_1 over four times that of the starting Fe(II) species.[15]

Although these ^{1}H-based MRI contrast agents show large percentile changes to their r_1 values upon oxidation, it is difficult to determine whether an observed enhancement in contrast

results from the activation of the probe or its accumulation in an area of interest. These situations can be differentiated by using a dual-mode probe that provides distinct signals for its activated and pre-activated forms. Previously, ^{1}H MRI contrast agents have been modified to have additional outputs that can be visualized through techniques such as positron emission tomography (PET) and chemical exchange saturation transfer (CEST) modes of MRI.[16–20] ^{19}F MRI is an attractive second mode since it shares most of the instrumentation associated with ^{1}H MRI. Additionally, the background signal in ^{19}F MRI is negligible since there is not much fluorine within the body, and most of this biological fluorine is ensconced in matrices that prevent these atoms from having long enough transverse relaxation times (T_2) to give rise to a strong signal. The large chemical shift range (>300 ppm) for ^{19}F nuclei enables ^{19}F MRI to easily differentiate F atoms in different chemical environments, facilitating the development of ratiometric-responsive ^{19}F MRI probes.[21] Although the ^{19}F MRI signal tends to be weak, it can be enhanced by nearby paramagnetic metal ions,[22–25] and this technique has already been applied to some redox-responsive sensors.[26–28]

Here, we incorporate fluorine atoms into a macrocyclic quinol-containing ligand to yield F_2H_4qp4 and find that its Fe(II) complex can ratiometrically detect H_2O_2 through ^{19}F and ^{1}H MRI. Before oxidation, the sensor has a strong ^{19}F MRI signal but does not substantially impact T_1-weighted ^{1}H MRI contrast. The reaction with H_2O_2 oxidizes the metal to Fe(III), eliminating the former ^{19}F MRI signal while activating the ^{1}H MRI response.

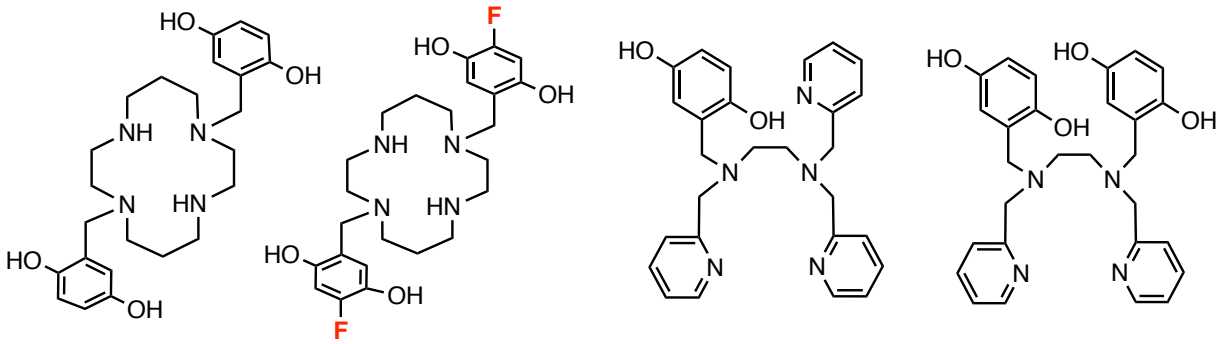

H_4qp4 **F_2H_4qp4** **H_2qp1** **H_4qp2**

[$Fe^{II}(F_2H_3qp4)$](OTf) (**1**)
[$Mn^{II}(H_3qp4)$](OTf)
[$Fe^{II}(H_3qp4)$](OTf) (**2**)
[$Mn^{II}(H_2qp1)(MeCN)$]$(OTf)_2$
[$Mn^{II}(H_4qp2)Br_2$]

Scheme 4.1 Structures of quinol-containing polydentate ligands and formulae for their coordination complexes

4.2 Experimental Section

Materials

All chemicals and solvents were purchased from Sigma-Aldrich and used as received unless otherwise noted. All deuterated solvents were bought from Cambridge Isotopes. Diethyl ether (ether) and methanol (MeOH) were bought from Fisher. Methylene chloride (CH_2Cl_2) was purchased from Mallinckrodt Baker.

Instrumentation

All ^1H and ^{13}C NMR spectra were recorded on a 500 MHz AV Bruker NMR spectrometer. All reported NMR resonance peak frequencies were referenced to internal standards. A Varian Cary 50 spectrophotometer was used to collect optical data, which were then processed using software from the WinUV Analysis Suite. Electron paramagnetic resonance (EPR) spectra were

collected using a Bruker EMX-6/1 X-band EPR spectrometer operated in the perpendicular mode and subsequently analyzed with the program EasySpin. All EPR samples were run as frozen solutions in quartz tubes. We used a Johnson Matthey magnetic susceptibility balance (model MK I#7967) to measure the magnetic moments of solid samples of the metal complexes and estimated the diamagnetic component of the susceptibility using Pascal's constants.[29] Solution-state magnetic moments were obtained using the Evans' method.[30,31] Cyclic voltammetry (CV) was performed under N_2 at 294 K with an Epsilon electrochemistry workstation (Bioanalytical System, Inc.). The working, auxiliary, and reference electrodes were gold, platinum wire, and silver/silver(I) chloride, respectively. High-resolution mass spectrometry (HR-MS) data were collected at the Mass Spectrometer Center at Auburn University on a Bruker Microflex LT MALDI-TOF mass spectrometer via direct probe analysis operated in the positive ion mode. Solid samples of the Fe(II) complex were dried, stored under N_2, and sent to Atlantic Microlabs (Norcross, GA) for elemental analysis.

X-Ray Crystallography

Crystallographic data for 2,5-dimethoxy-4-fluorobenzaldehyde and 2,5-dihydroxy-4-fluorobenzaldehyde compounds were collected using a Bruker D8 VENTURE κ-geometry diffractometer system equipped with an Incoatec IμS 3.0 microfocus sealed tube and a multilayer mirror monochromator (Mo Kα, λ = 0.71073 Å). Diffraction data were integrated with the Bruker SAINT software package using a narrow-frame algorithm. Data were corrected for absorption effects using the Multi-Scan method (SADABS). The structure was solved and refined using the Bruker SHELXTL Software Package.

Potentiometric Titrations

The aqueous speciations of F_2H_4qp4 and its Fe(II) complex were assessed using a METROHM 765 Dosimat with a jacketed, airtight glass titration vessel. A Fisher Scientific Accumet Research AR15 pH meter was used to monitor the pH of the sample solutions during the titrations. The electrode was calibrated before each titration using commercially available standard solutions buffered to pH 4.0, 7.0, and 10.0. All samples were purged with argon prior to analysis and subsequently analyzed under an argon atmosphere at 25 °C to prevent carbonate contamination. All solution samples were prepared in solutions of 100 mM KCl in deionized Millipore water. The titrations investigating metal-ligand speciation were run with solutions that contained a 1:1 molar mixture of the ligand and $Fe^{II}(OTf)_2$. Carbonate-free solutions of 0.10 M KOH and 0.10 M HCl were prepared using argon-saturated deionized Millipore water. The titration data were analyzed and fitted to speciation models using the Hyperquad2006 program.[32]

High-Pressure Liquid Chromatography (HPLC)

HPLC was performed with UV detection at 254 nm using an Agilent 1100 series apparatus and an Agilent Zorbax SB-C18 column (4.6 × 150 mm, 5 μm pore size). The following eluents were used: A) 99.9 % water with 0.1% trifluoroacetic acid (TFA) and B) 99.9% MeCN with 0.1% TFA. The following method (Method 1)was used: Gradient 90% A and 10% B to 100% B over 20 min. Flow rate = 0.20 mL/min, injection volume = 25.0 μL, column temperature = 37.0 °C. Before each run, the HPLC instrument was flushed with eluent 100 % A to 100% B over 16 min with a flow rate of 0.49 mL/min and an injection volume of 25.0 μL.

Magnetic Resonance Imaging (MRI)

All MRI data were collected at the Auburn University MRI Research Center on a Siemens 3T Verio human-bore clinical MRI and Siemens 7T Magnetom human-bore research MRI

scanners. For the 3T work, a 15-channel knee coil was used to simultaneously image 12-15 samples. The imaging procedure was identical to those used for similar studies from our laboratory.[11–15,33,34] An inversion recovery (IR) sequence was used that featured a non-selective adiabatic inversion pulse followed by a slice-selective gradient recalled echo (GRE) readout after a delay period corresponding to the inversion time (TI).[35,36] The GRE was a saturation readout, with only one line of *k*-space acquired per repetition time (TR) to maximize both signal strength and the accuracy of the T_1 estimates. The applied 3T imaging parameters included: TR = 10 s, 20 TI times ranging from 10 to 2600 ms, GRE echo time (TE) = 2.75 ms, GRE flip angle = 90°, averages = 1, slice thickness = 10 mm, the field of view = 64 × 64 mm, matrix = 64 × 64, resulting in a pixel size of 1.0 × 1.0 × 10.0 mm. All samples were run in 50 mM solutions of HEPES in water, buffered to pH 7.0, and kept at 22 °C. The iron content was systematically varied from 0.10 to 1.00 mM. The inverses of the T_1 values from two separate batches of contrast agents were plotted versus the concentration of Fe(II) to obtain r_1 values.

For the 7T work, we developed a 7T ^{19}F (279.6 MHz) Transmit/Receive coil with interface/preamplifier optimized for ^{19}F and pretested/validated its operation on sodium fluoride solution ($NaF+H_2O$) phantoms. We applied a $^{1}H/^{19}F$ frequency-selectable, Inversion Recovery Look-Locker (IRLL) sequence that employed a non-selective adiabatic inversion RF pulse followed by multiple GRE-FLASH readouts of one *k*-space line temporally repeated on a preplanned inversion time (TI) schedule. We also applied ^{19}F T_1-weighted FLASH imaging at flip angles 10° and 30° to demonstrate ^{19}F T_1-weighted contrast. For 7T scanning, six Fe(II)-F_2H_4qp4 phantoms were prepared with 10.00, 15.00, and 20.00 mM concentrations, and each concentration was prepared with or without 10.00 mM hydrogen peroxide (H_2O_2) – activated versus non-activated, respectively.

Specific for 7T ^{1}H: TR = 10 sec; 20 TI times ranging from 10 to 2600 ms; GRE flip-angle = 3°; Manual Tx Vref = 50 V; Averages = 4.

Specific for 7T ^{19}F: TR = 10 sec; 10 TI times ranging from 10 to 2000 ms; Manual Tx Vref = 50 V; GRE flip-angle = 5°; Averages = 9.

MRI Data Analysis

For both 3T ^{1}H and 7T ^{19}F measurements, image analysis was performed using custom MATLAB programs (Mathworks, Natick, MA). The initial smallest TI image was used as a baseline to determine circular region of interest (ROI) boundaries for each sample; from these, the mean pixel magnitudes for each ROI were calculated. For each of the subsequent TI images, the same ROI boundaries were applied, and the mean pixel magnitude calculations were repeated. This gave consistent ROI spatial definitions and a corresponding time course of magnitudes for each of the samples over all the TI time points. Each sample's complex phase was used to correct the magnitude polarity to produce a complete exponential T_1 inversion recovery curve. The Nelder-Mead simplex algorithm[37] was applied to each sample's ^{1}H or ^{19}F inversion-recovery exponential curve to estimate its corresponding ^{1}H or ^{19}F T_1 value.

Synthesis

2,5-Dimethoxy-4-fluorobenzaldehyde

A solution of 2,5-dimethoxyfluorobenzene (2.67 g, 17.1 mmol) was dissolved in 20 mL of dichloromethane and cooled in an ice bath. Once the temperature reached 0 °C, 34.2 mL (34.2 mmol) of $SnCl_4$, 1.0 M soln. in dichloromethane, was added under vigorous stirring, followed by the dropwise addition of dichloromethyl methyl ether (1.6 mL, 17.4 mmol). The reaction mixture was allowed to warm to room temperature during 30 min with continued stirring and then was poured into a mixture of 50 g of ice and 4 mL of concentrated HC1. The green solution was stirred

for 1.5 h, the CH_2C1_2 layer was separated and washed with 2 × 50 mL of 10% HC1, 10% NaOH, and saturated brine. Then, the CH_2C1_2 layer was dried over anhydrous Na_2SO_4, the solvent was rotavapped, and the residue was recrystallized by slow evaporation from a saturated solution of the crude product in EtOH to yield 2.78 g (88.3%) white crystals of 2,5-dimethoxy-4-fluorobenzaldehyde suitable for single X-ray diffraction. ^{1}H NMR (500 MHz, DMSO-*d6*) δ 10.27 (s, 1H), 7.39 (d, *J* = 9.9 Hz, 1H), 7.29 (d, *J* = 13.2 Hz, 1H), 3.89 (s, 3H), 3.85 (s, 3H). ^{19}F NMR (471 MHz, CD_3OD) δ -121.71 (q, *J* = 9.42 Hz). ^{13}C NMR (126 MHz, CD_3CN) δ 188.45, 158.97, 158.39, 158.32, 156.94, 142.87, 121.72, 112.51, 112.47, 103.02, 102.84, 57.35, 57.11.

2,5-Dihydroxy-4-fluorobenzaldehyde

2,5-Dimethoxy-4-fluorobenzaldehyde (2 g, 10.9 mmol) was dissolved in 10 mL of dichloromethane under nitrogen atmosphere. Boron tribromide, 1.0 M soln. in dichloromethane (~ 22 mL, 21.72 mmol) was added dropwise into the reaction flask. After 24 hours stirring, the reaction was quenched with 40 mL of 0.5 M HCl. The crude product was extracted with 2 × 100 mL portions of ethyl acetate. The organic fraction was dried with anhydrous MgSO4 and the solvent was removed under reduced pressure, and the residue was purified by silica gel chromatography (10:3 CH_2Cl_2/MeOH eluent, product R_f = 0.35) (1.60 g, 93.9%). Crystals suitable for single crystal X-ray diffraction were grown by slow evaporation from a saturated solution of the product in ethyl acetate. ^{1}H NMR (500 MHz, DMSO-*d6*) δ 10.48 (s, 1H), 10.14 (s, 1H), 9.66 (s, 1H), 7.20 (d, *J* = 10.2 Hz, 1H), 6.78 (d, *J* = 12.3 Hz, 1H). ^{19}F NMR (471 MHz, CD_3OD) δ -123.24 (q, *J* = 9.4). ^{13}C NMR (126 MHz, CD_3CN) δ 197.20, 196.98, 196.76, 159.10, 157.25, 157.15, 157.09, 138.93, 138.81, 122.02, 121.97, 105.93, 105.75.

1,8-Bis(2,5-dihydroxy-4-fluorobenzyl)-1,4,8,11-tetraazacyclotetradecane (F_2H_4qp4)

1,4,8,11-tetraazacyclotetradecane (cyclam) (1.00 g, 4.99 mmol) and 2,5-dihydroxy-4-fluorobenzaldehyde (1.54 g, 9.91 mmol) were combined in 10 mL of dry MeOH. The mixture was heated at reflux for 4 h under N_2. The reaction mixture was then cooled to 0 °C with an ice bath. Once the temperature reached 0 °C, 3 mL of additional dry MeOH and trifluoroacetic acid (1.55 mL, 19.82 mmol) was added to the MeOH solution at 0 °C, followed by sodium cyanoborohydride (934 mg, 14.86 mmol). The resultant solution was heated at reflux for 6 h under N_2 at which point the solvent was removed to yield the crude product. The crude product was purified by repeated precipitation from MeOH/ether to yield the product as a pale-yellow solid that was washed with cold acetone (1.03 g, 43% yield). Typical yields range from 40 to 45%. MS (ESI): calcd for $[M-3H]^+$, *m/z* 477.2307; found, *m/z* 477.2309, calcd for $[M+H]^+$, *m/z* 481.2620 ; found, *m/z* 481.2613. ^{1}H NMR (500 MHz, CD_3OD, *d4*) δ 6.88 (d, *J* = 9.9 Hz, 2H), 6.52 (d, *J* = 12.6 Hz, 3H), 6.45 (d, *J* = 9.5 Hz, 1H), 6.39 (d, *J* = 13.1 Hz, 2H), 4.59 (s, 3H), 4.56 (s, 4H), 3.38 (s, 1H), 3.37 (s, 2H), 2.98 (t, *J* = 5.1 Hz, 3H), 2.89 (s, 3H), 1.86 (t, *J* = 5.5 Hz, 2H), 1.31 (s, 4H).^{19}F NMR (471 MHz, CD_3OD) δ -138.29 (t, *J* = 9.4 Hz), -139.51(t, *J* = 11.1 Hz). ^{13}C NMR (126 MHz, CD_3OD) δ 163.24, 162.97, 152.91, 149.02, 124.67, 119.41, 118.39, 118.36, 117.07, 104.28, 104.11, 62.74, 60.36, 50.45, 49.46, 49.28, 49.11, 47.69, 26.42. IR (cm^{-1}): 3263 (s), 2960 (m), 2858 (s), 2337 (m), 2184 (w), 1679 (s), 1605 (w), 1502 (w), 1437 (s), 1203 (m), 1121 (s), 928 (m), 865 (w), 842 (w), 800 (m), 723 (s), 517 (w).

(1,8-Bis(2,5-dihydroxy-4-fluorobenzyl)-1,4,8,11tetraazacyclotetradecane)Iron(II) triflate ([$Fe^{II}(F_2H_3qp4)$](OTf), 1)

F_2H_4qp4 (500 mg, 1.12 mmol) and $Fe^{II}(OTf)_2$ (400 mg, 1.13 mmol) were dissolved in 5 mL of dry MeCN under N_2. The mixture was stirred at 60 °C for 24 h. Then, the solvent was removed under reduced pressure. The obtained solid was dissolved in MeOH and the slow addition of CH_2Cl_2 deposited the product as a red powder, which was collected via filtration (595 mg, 80% yield). MS (ESI): calcd for $[Fe(F_2H_2qp4)]^+$, *m/z* 530.1625; found, *m/z* 530.1624. Solid-state magnetic susceptibility (294 K): $\mu_{eff} = 4.8\ \mu_B$. Solution-state magnetic susceptibility (CD_3CN, 298 K): $\mu_{eff} = 4.7\ \mu_B$. Optical spectroscopy (HEPES buffer, pH= 7.0, 294 K): 343 nm ($\varepsilon = 8667\ M^{-1}\ cm^{-1}$). IR (KBr, cm^{-1}): 3486 (s), 1601 (s), 1255 (s), 1230 (s), 1169 (s), 1033 (s), 765 (w), 629 (m). ^1H NMR (500 MHz, $CDCl_3$, *d*): δ 12.06, 9.08, 8.38, 7.16, 6.43. Elemental analysis (powder) calcd for $C_{25}H_{33}N_4O_7F_5S_1Fe \cdot 0.5$ MeOH: C, 43.72%; H, 5.03%; N, 7.99%. Found: C, 43.76%; H, 4.96%; N, 7.48%.

4.3 Results and Discussion

Synthesis and Characterization

The F_2H_4qp4 ligand is synthesized in three steps from 2,5-dimethoxyfluorobenzene (Scheme 4.2). The initial step, in which we install a formyl group (-CH=O) *para* to the fluorine, is synthetically precedented.[38] The formylated product is purified through crystallization from EtOH and then dealkylated with boron tribromide to yield 2,5-dihydroxy-4-fluorobenzaldehyde. The aldehyde is purified through column chromatography and subsequent crystallization from ethyl acetate (Figure C8). In the final step, we react cyclam and two equiv. of 2,5-dihydroxy-4-fluorobenzaldehyde to yield F_2H_4qp4; the synthetic protocol is almost completely identical to that used to prepare the non-fluorinated H_4qp4.[14] The major difference is that we use sodium

cyanoborohydride as the reducing agent instead of $NaBH_4$-Al_2O_3 due to the product's sensitivity to basic conditions. Repeated precipitation from MeOH/ether yields the product as a pale-yellow solid (43% yield). We investigated column chromatography as an alternative means of purification, but this greatly lowered the overall yield to less than 10%. The identity and purity of the F_2H_4qp4 ligand were established by NMR, HR-MS, and UV/vis. We obtained crystals from the slow evaporation of a saturated solution of F_2H_4qp4 in MeOH, but these were not suitable for single-crystal X-ray diffraction.

Reacting the ligand and an equimolar amount of $Fe^{II}(OTf)_2$ in dry MeCN at 60 °C for 24 h under N_2 yields $[Fe^{II}(F_2H_3qp4)](OTf)$ (**1**) as a red powder in 80% yield. As with other complexation reactions involving macrocyclic ligands, the efficient insertion of Fe(II) into F_2H_4qp4 requires higher temperatures and longer times.[39,40] NMR, MS, and UV/vis spectroscopic measurements, HPLC, and elemental analysis confirmed the purity and composition of **1**. The absence of an EPR signal and the μ_{eff} = 4.7 μ_B from magnetic susceptibility measurements are consistent with the metal ion being high-spin Fe(II). The isolated complex contains $F_2H_3qp4^-$ rather than F_2H_4qp4; the H_4qp4 ligand likewise deprotonates upon coordination of Mn(II) and Fe(II).[14,15]

Stability and Speciation in Water

We evaluated the aqueous behavior and speciation of the free F_2H_4qp4 ligand from pH 2.5 to 11.0. The best-fitting model to the potentiometric pH titration data displays four ionization events corresponding to pK_a values of 2.85, 6.2, 8.44, and 10.0 (Figures 4.1A and C17, Tables 4.1 and C1). The three pK_a values below 10 were lower than the 3.5, 7.7, and 8.8 values corresponding to analogous ionization events observed for H_4qp4.[14] The pK_a value of 8.44 likely corresponds to the deprotonation of the first quinol, and our model suggests that the ligand is mostly neutral F_2H_4qp4 around pH 7 (Figure 4.1A).

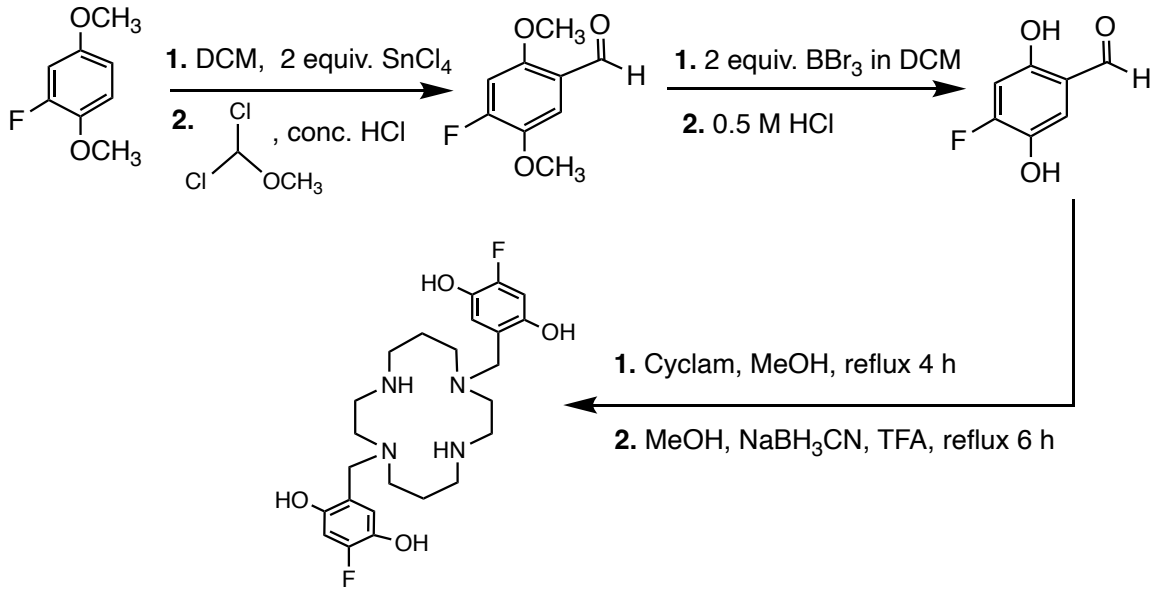

Scheme 4.2 Synthesis of F_2H_4qp4.

The aqueous stability and speciation of **1** were evaluated from pH 2.5 to 9.0 (Figures 4.1B and C18, Tables 4.1 and C1). Our best-fitting model indicates two ionization events with pK_a values of 4.31 and 6.11. We assign these to the sequential deprotonations of the two Fe(II)-bound quinol groups. Spectrophotometric pH titration data support these assignments (Figure C19). At pH 2.9, we observe a band consistent with a neutral quinol at 268 nm, and this shifts to a 345 nm value that is more consistent with a quinolate at pH 7.2. The energy of the absorption band stops shifting above pH 7.2, consistent with the quinols having fully deprotonated. Similar pH-dependent shifts in UV/vis bands were observed for other Mn(II) and Fe(II) quinol-containing complexes characterized by our laboratory and Gale et al.[12–15,41] The pK_a values of 4.31 and 6.11 measured for **1** indicate that it is more acidic than **2** (5.11, 7.32) and [Mn^{II}(H_3qp4)](OTf) (5.09, 7.39), as would be anticipated from the installation of electron-withdrawing fluorines onto the quinols.

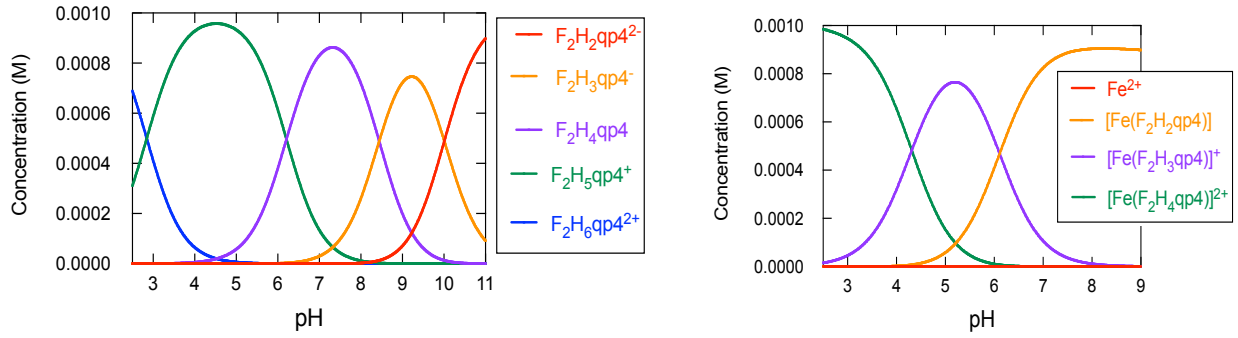

A **B**

Figure 4.1 Predicted speciation as a function of pH for A) 1.0 mM F_2H_4qp4 and B) 1.0 mM **1** in an aqueous solution containing 100 mM KCl at 25 ºC.

Table 4.1 pFe, log K_{ML}, and pK_a Values Determined by Potentiometric Titration at 25 °C**.**

pK_{L1}[a]	2.85 (±0.05)	log K_{ML} ($Fe^{II}(F_2H_2qp4)$)[c]	28.20
pK_{L2}[a]	6.21 (±0.05)	log K_{ML} ($Fe^{II}(F_2H_3qp4)$)$^+$ [c]	24.30
pK_{L3}[a]	8.44 (±0.05)	log K_{ML} ($Fe^{II}(F_2H_4qp4)$)$^{2+}$ [c]	20.17
pK_{L4}[a]	10.01 (±0.05)	pFe(pH 7.4)[d]	13.76
pK_a($Fe^{II}(F_2H_4qp4)^{2+}$)[b]	4.31 (±0.05)		
pK_a($Fe^{II}(F_2H_3qp4)^+$)[b]	6.11 (±0.05)		

[a]Ligand pK_a values: $K_{L1} = [F_2H_5qp4^+][H^+]/[F_2H_6qp4^{2+}]$;
$K_{L2} = [F_2H_4qp4][H^+]/[F_2H_5qp4^+]$;
$K_{L3} = [F_2H_3qp4^-][H^+]/[F_2H_4qp4]$;
$K_{L4} = [F_2H_2qp4^{2-}][H^+]/[F_2H_3qp4^-]$

[b]Metal complex pK_a values: $K_a(Fe^{II}(F_2H_4qp4)^{2+}) = [Fe^{II}(F_2H_3qp4)^+][H^+]/[Fe^{II}(F_2H_4qp4)^{2+}]$;
$K_a(Fe^{II}(F_2H_3qp4)^+) = [Fe^{II}(F_2H_2qp4)][H^+]/[Fe^{II}(F_2H_3qp4)^+]$

[c]Metal complex K_{ML} values: K_{ML} ($Fe^{II}(F_2H_2qp4)$) $= [Fe^{II}(F_2H_2qp4)]/([Fe(II)][F_2H_2qp4^{2-}])$;
K_{ML} ($Fe^{II}(F_2H_3qp4)$)$^+ = [Fe^{II}(F_2H_3qp4)^+]/([Fe(II)][F_2H_3qp4^-])$;
K_{ML} ($Fe^{II}(F_2H_4qp4)$)$^{2+} = [Fe^{II}(F_2H_4qp4)^{2+}]/([Fe(II)][F_2H_4qp4])$

[d]pFe = $-\log[Fe(II)]_{free}$ calculated for [Fe(II)] = 1.0 mM, $[F_2H_4qp4]$ = 1.0 mM, 298 K, pH 7.4.

As with the H_4qp4 complexes with Mn(II) and Fe(II), the macrocycle of the F_2H_4qp4 ligand renders its Fe(II) complex exceptionally stable in water (Figure 4.1B). At pH 7.4 and 1.0 mM concentrations of ligand and Fe(II), pFe is calculated to be 13.76, which is more stable than $[Mn^{II}(H_3qp4)](OTf)$ (pMn = 9.81)[14] but slightly less stable than **2** (pFe = 14.18) under the same

conditions.[15] The installation of fluorines onto the ligand weakens the binding affinity, as was seen for Fe(III) complexes with 3-hydroxypyridin-4-one derivatives,[42] but the water-stability of **1** still compares favorably to those of other reported iron-containing MRI contrast agents.[43] The aqueous stability of **1** is confirmed through HPLC. The HPLC trace of **1** shows a single peak with a retention time of 6.57 min (Figure C21), which is distinct from the 3.83 min for the peak observed for metal-free F_2H_4qp4 (Figure C20).

*Redox Properties of **1** and F_2H_4qp4*

Both **1** and the metal-free F_2H_4qp4 ligand were characterized by cyclic voltammetry (CV) in aqueous solutions containing 0.10 M phosphate solution buffered to pH 7.2. For **1**, we observe a reversible feature with $E_{1/2}$ = -200 mV *vs.* Ag/AgCl (ΔE = 81 mV) and assign it to the Fe(III/II) redox couple (Figure C24). The reduction potential is noticeably more positive than the -450 mV *vs.* Ag/AgCl value for the analogous redox event seen for $[Fe^{II}(H_3qp4)](OTf)$, demonstrating that the electron-withdrawing fluorines are stabilizing the Fe(II) form.[15]

In addition to the metal-centered redox, we detect an irreversible feature at 340 mV *vs.* Ag/AgCl (ΔE = 337 mV) for **1**. When we analyze the metal-free F_2H_4qp4 under the same conditions, we observe a redox feature with an $E_{1/2}$ of 337 mV *vs.* Ag/AgCl (ΔE = 402 mV) that is identical within error to that seen for **1** (Figure C23). Consequently, we assign this redox event to the oxidation and reduction of the quinols within the ligand. The installation of the fluorines greatly shifts the reduction potential of the quinols to more positive values; in complexes with non-fluorinated quinols, the $E_{1/2}$ is normally about 60-195 mV *vs.* Ag/AgCl.[12–15,44,45]

*Reactivity of **1** with H_2O_2*

The reaction between H_2O_2 and **1** oxidizes both the metal and the ligand, resulting in Fe(III) species with oxidized ligands. UV/vis and IR confirm the oxidation of the quinols to *para*-

quinones (Figures 4.2A and C22). The appearance of an IR band at 1651 cm^{-1} is consistent with the formation of the *para*-quinone C=O bonds. The UV/vis data for the reaction between **1** and 10 mM H_2O_2 in 50 mM HEPES buffered to pH 7.00 shows that the intensity of the quinolate band at 345 nm decreases substantially by 5 min. Similar observations have been made for other metal-quinol complexes reported by our groups.[12–15,45]

Electron paramagnetic resonance spectroscopy (EPR) data suggest that the reaction between **1** and H_2O_2 in 50 mM HEPES buffered to pH 7.0 also oxidizes the metal center to Fe(III). Before the reaction, we observe a weak signal with features at g = 2.55, 2.27, and 1.99 indicative of low-spin Fe(III) metal center (Figure 4.2B). 60 min after the beginning of the reaction with 10 mM H_2O_2, a much more intense signal appears at g = 4.3, indicating the formation of a high-spin Fe(III) species. We also monitored the reaction between **1** and 10 mM H_2O_2 in RT CD_3CN with solution-state magnetic susceptibility.[30] Over 60 min, the μ_{eff} value increases from 4.7 μ_B to 5.8 μ_B, consistent with the oxidation of high-spin Fe(II) to high-spin Fe(III). The data suggest that the low-spin Fe(III) species observed by EPR is only present in trace quantities before and after the reaction with H_2O_2. We also evaluated the ^{19}F NMR response of **1** to H_2O_2 (Figure 4.2C). Prior to the reaction, the ^{19}F NMR spectrum of **1** displays a sharp peak at -137 ppm. 60 min after the beginning of the reaction with H_2O_2, the signal weakens and broadens, as would be anticipated from the conversion of a high-spin Fe(II) complex to a high-spin Fe(III) species.

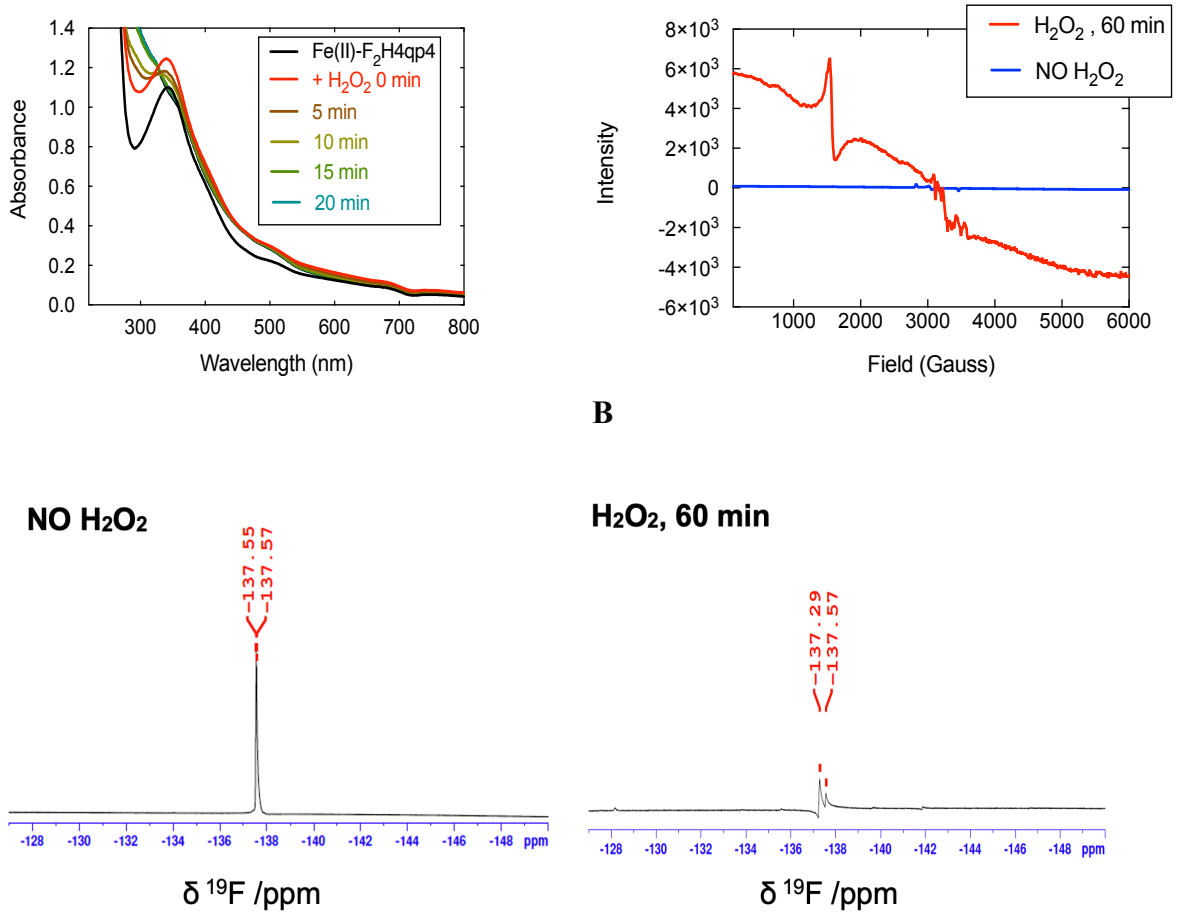

Figure 4.2 A) UV/vis spectra showing the reaction between 0.13 mM **1** and 10 mM H_2O_2 in 50 mM HEPES solution buffered to pH 7.00. The absorbance initially increases slightly due to the unreacted H_2O_2. All spectra were obtained at 298 K using a 1.0 cm pathlength cuvette. B) X-band EPR spectra depicting the reaction of 1.0 mM **1** with 10 mM H_2O_2 in 50 mM HEPES buffered to pH 7.0. The sample was frozen to 77 K 60 min after the addition of H_2O_2. The signal at $g = 4.3$ is indicative of high-spin Fe(III), the smaller signals at $g = 2.55$, 2.27, and 1.99 are consistent with low-spin Fe(III) species. C) ^{19}F NMR spectra of 0.1 mM **1** in 50 mM HEPES buffer (pH=7.0) containing 10% CD_3OD before addition of H_2O_2 and after 60 min reaction with 10 equiv. of H_2O_2.

^{1}H and ^{19}F Magnetic Resonance Imaging with **1**

We initially investigated the MRI properties of **1** using a 3T MRI scanner and the same protocols used for prior manganese- and iron-containing MRI contrast agents from our laboratory to study the ^{1}H MRI response to H_2O_2 (Figure 4.3).[11–15] T_1 values were measured for 0-1.0 mM solutions of **1** in 50 mM HEPES buffered to pH 7.00 with and without 10 mM H_2O_2. The

large excesses of H_2O_2 are not likely to be biologically relevant but do ensure that **1** is oxidized to as full an extent as possible. This enables comparisons to MRI contrast agent sensors that were previously reported by our laboratories.[11–15] T_1 values were measured 30 min and 60 min after the addition of H_2O_2 to aqueous solutions of **1**, and the r_1 values were directly determined by plotting $1/T_1$ versus iron concentration.

In the absence of H_2O_2, r_1 equals 0.414 mM^{-1} s^{-1}. Upon reaction with excess H_2O_2, r_1 increases to 0.554 mM^{-1} s^{-1} at 30 min and 1.54 mM^{-1} s^{-1} at 60 min. Although the percentile increase in r_1 (270%) is lower than that observed for **2**,[15] the absolute value is larger and in the middle of the range for Fe(III)-containing MRI contrast agents.[43] As with **2**, the increase in r_1 can be largely attributed to the oxidation of the metal center to Fe(III), which is slightly more paramagnetic and has a slower spin relaxation time that is more suitable for T_1-weighted MRI.

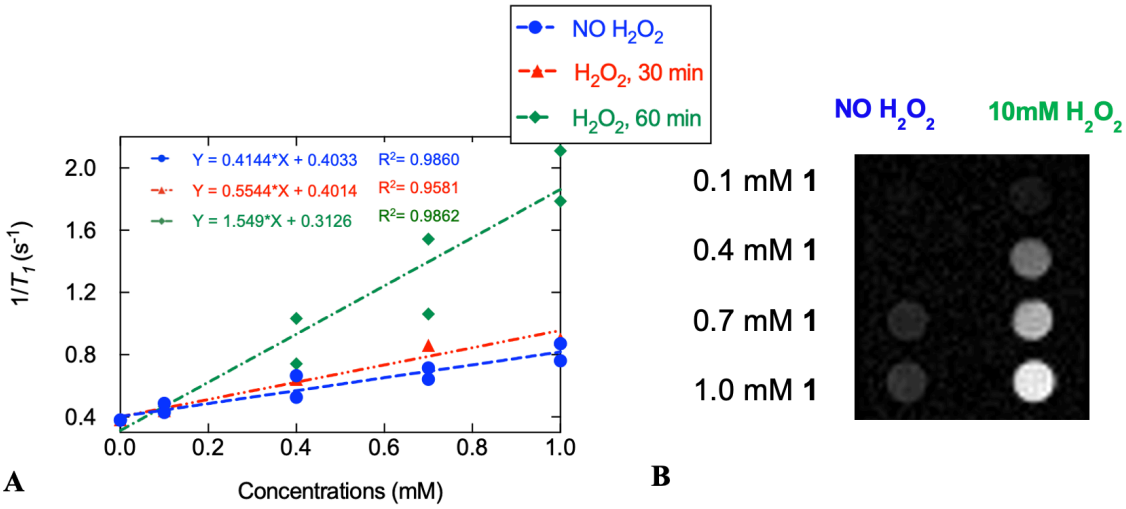

Figure 4.3 A) Plots of $1/T_1$ versus iron concentration for **1** in the presence (red, green) and absence (blue) of 10 mM H_2O_2. All samples were run in 298 K aqueous solutions containing 50 mM HEPES buffered to pH 7.00, using a 3T field provided by a clinical MRI scanner. All samples were prepared under air. The oxidized samples were prepared by directly adding H_2O_2 to solutions of **1** in aqueous solutions buffered to pH 7.00. T_1 measurements were taken 30 min (red) and 60 min (green) after the reactions with H_2O_2 began. The data were fit to the indicated linear equations; the y-intercepts were within the error of $1/T_1$ measurements associated with two control samples that contained no iron: pure water (0.378 s^{-1}) and 50 mM HEPES buffer (0.382 s^{-1}). B) Phantom images of solutions containing 0.1–1.0 mM **1** in the absence and presence of 10 mM H_2O_2. All solutions were given 60 min to equilibrate and imaged with the time of inversion (TI)= 1750 ms.

To improve the signal-to-noise ratio, we instead used a 7T scanner for ^{19}F MRI measurements. With 0-1.0 mM concentrations of **1**, we were not able to detect a sufficiently strong ^{19}F signal and eventually settled on a standard concentration of 10.0 mM. At this concentration and field, the signal-to-noise ratio (SNR) of the ^{19}F image of **1** dropped 5-fold upon reaction with H_2O_2 (Figures 4.4A and 4.4B), suggesting that the formation of high-spin Fe(III) broadens and weakens the ^{19}F signal (Figures 4.2C and 4.4A). Chen et al. employed a similar strategy to develop a sensor relying on a manganese(II)/(III) couple with the key difference being that the more oxidized metal ion displays the stronger ^{19}F MRI signal and lesser ^{1}H MRI relaxivity.[28]

SNR was calculated for solutions of 10.0, 15.0, and 20.0 mM **1** before and after adding 10.0 mM H_2O_2 using a 7T field. As shown in Figure 4.4B, SNR is improved by raising the concentration of **1**, and it decreases for each concentration after 60 min reaction with H_2O_2.

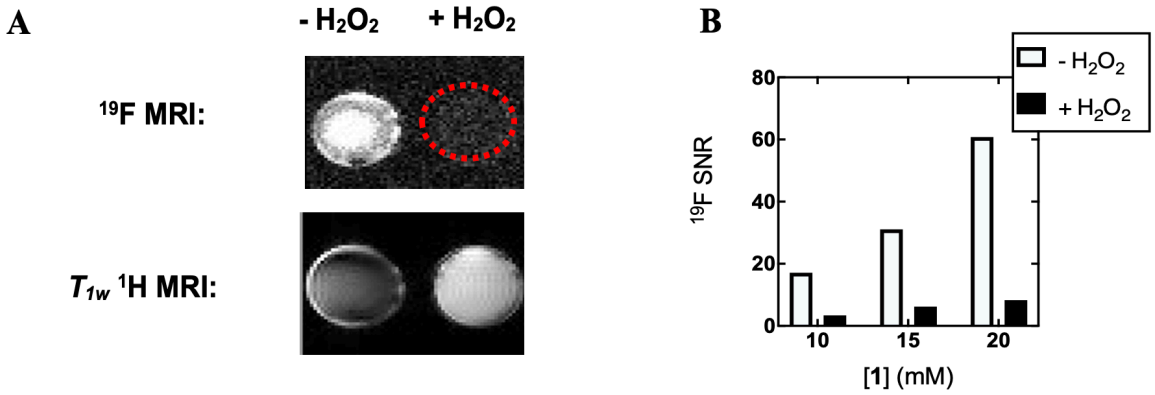

Figure 4.4 A) ^{19}F and T_1-weighted ^{1}H MRI phantom images of 10.0 mM **1** before and after reaction with 10.0 mM H_2O_2 in HEPES buffered to pH=7.00 using a 7T field provided by a clinical MRI scanner, B) A histogram of signal-to-noise ratios (SNRs) corresponding to ^{19}F MRI phantom images of 10.0, 15.0, 20.0 mM of **1** in aqueous solutions containing HEPES buffered to pH=7.00 using a 7T field provided by a clinical MRI scanner.

4.4 Conclusions

A water-stable Fe(II) complex with a fluorinated quinol-containing ligand displays a strong ^{19}F MRI signal that vanishes and is replaced by a strong ^{1}H MRI signal upon reaction with H_2O_2. The ^{1}H T_1-weighted relaxivity increases approximately three-fold upon oxidation, which is comparable to that of a previously reported non-fluorinated analog. The iron complex thereby acts as a bimodal sensor for H_2O_2 that can ratiometrically detect this ROS through ^{19}F and T_1-weighted ^{1}H MRI data (Scheme 4.3).

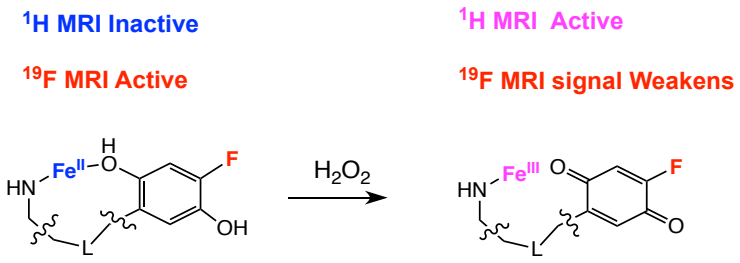

Scheme 4.3 A bimodal sensor with ^{1}H T_1-weighted and ^{19}F MRI responses to H_2O_2.

Appendix C

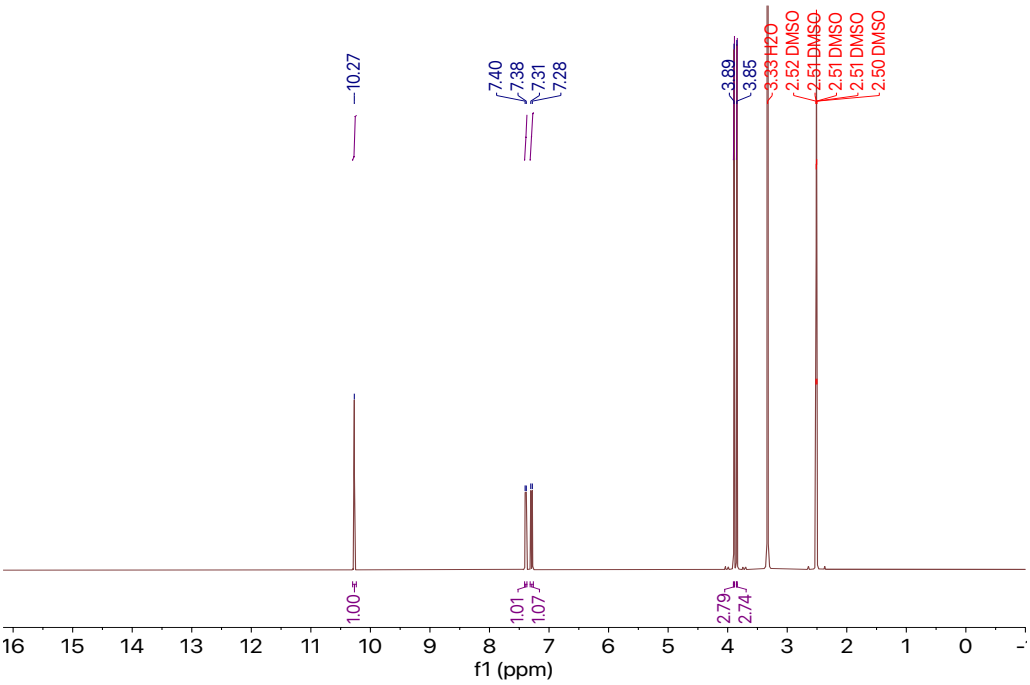

Figure C1. [1]H NMR spectrum of 2,5-dimethoxy-4-fluorobenzaldehyde in DMSO-*d6*.

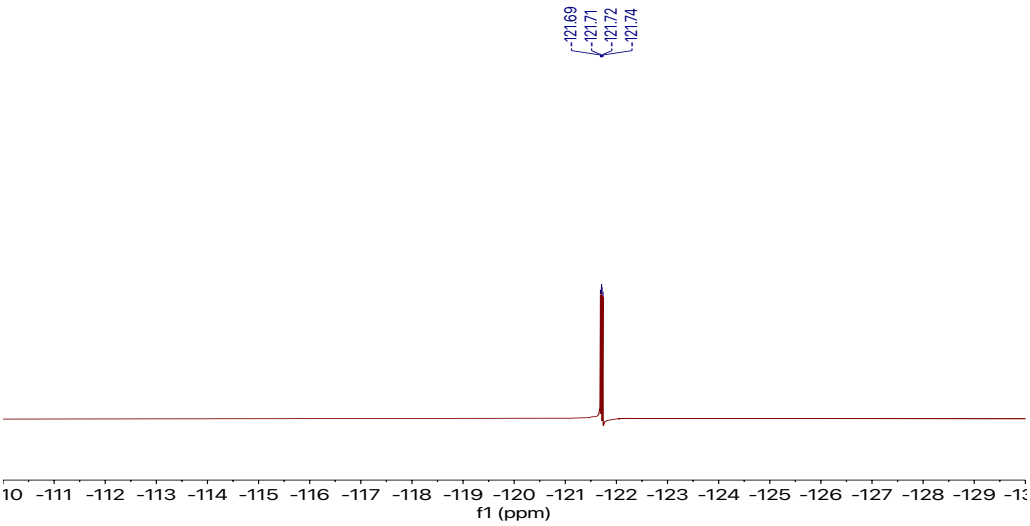

Figure C2. [19]F NMR spectrum of 2,5-dimethoxy-4-fluorobenzaldehyde in CD_3OD.

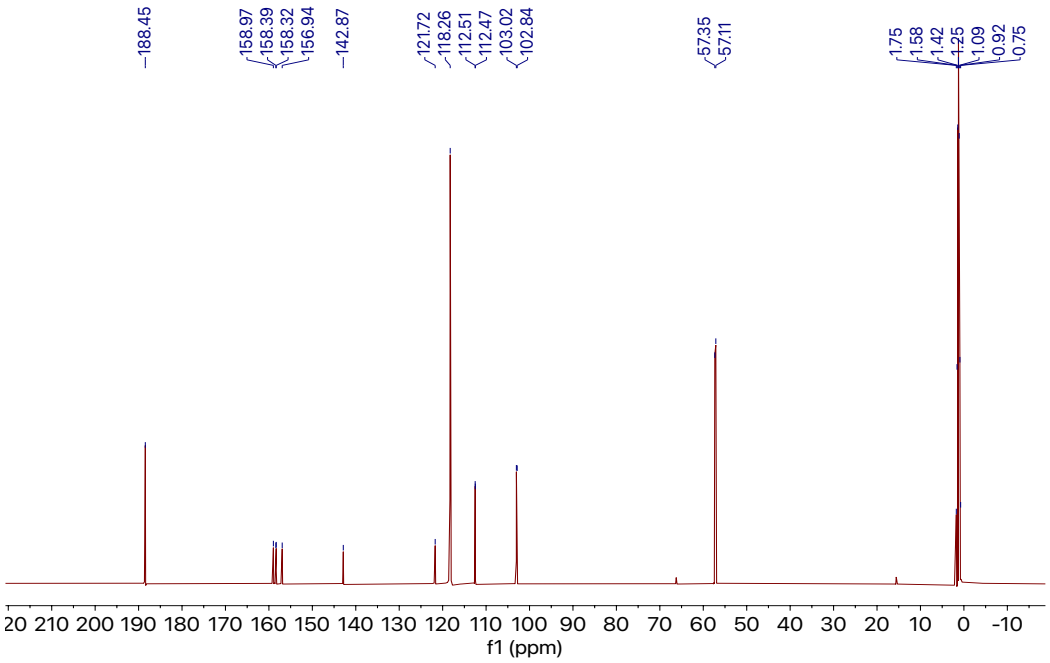

Figure C3. ^{13}C NMR spectrum of 2,5-dimethoxy-4-fluorobenzaldehyde in CD_3CN. Solvent peaks from MeCN (118.26, 1.75- 0.75) are present**.**

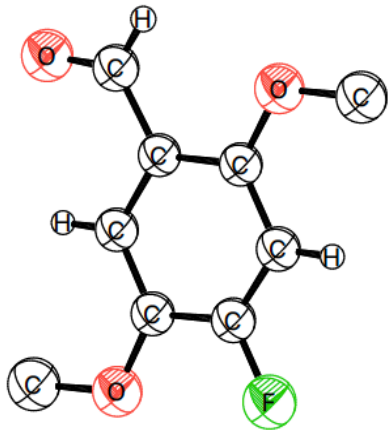

Figure C4. ORTEP representation of 2,5-dimethoxy-4-fluorobenzaldehyde. The hydrogen atoms from the methoxy groups and the solvent molecules have been removed for clarity.

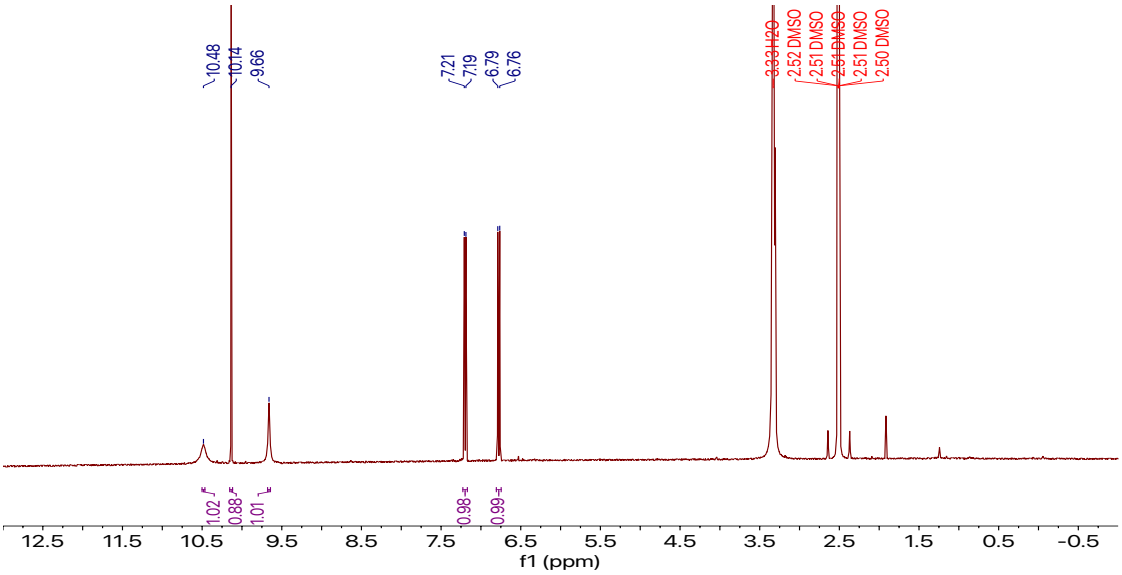

Figure C5. ^{1}H NMR spectrum of 2,5-dihydroxy-4-fluorobenzaldehyde in DMSO-*d6*.

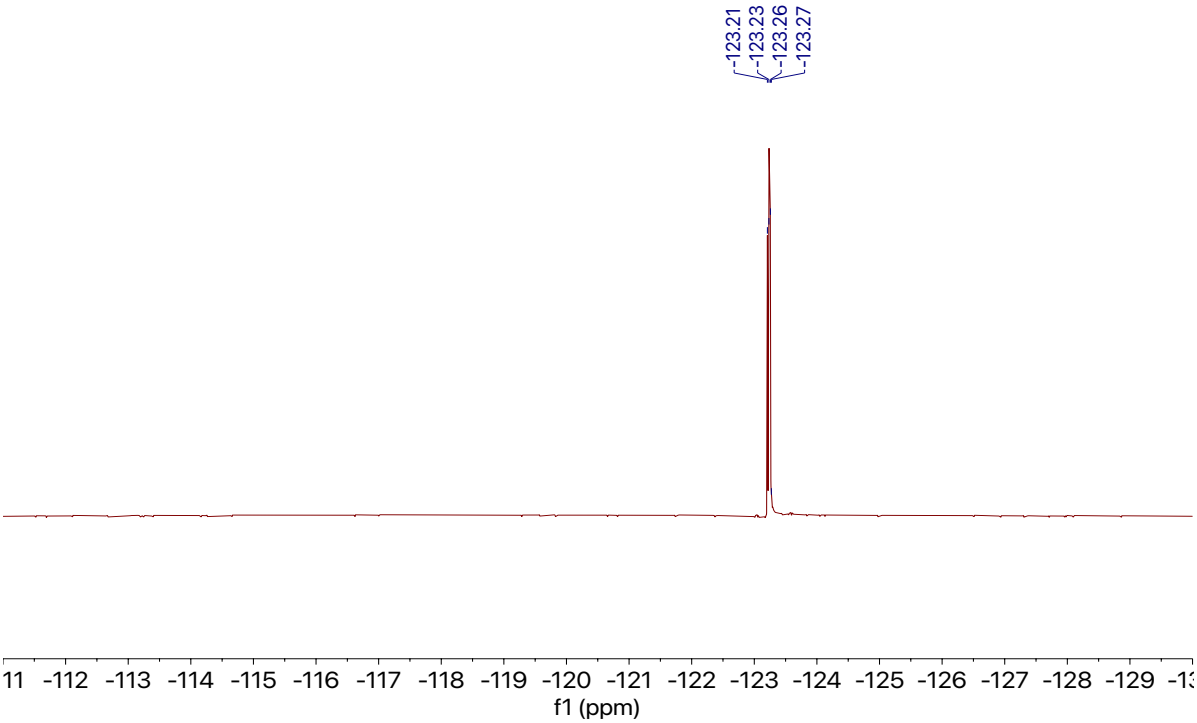

Figure C6. ^{19}F NMR spectrum of 2,5-dihydroxy-4-fluorobenzaldehyde in CD_3OD.

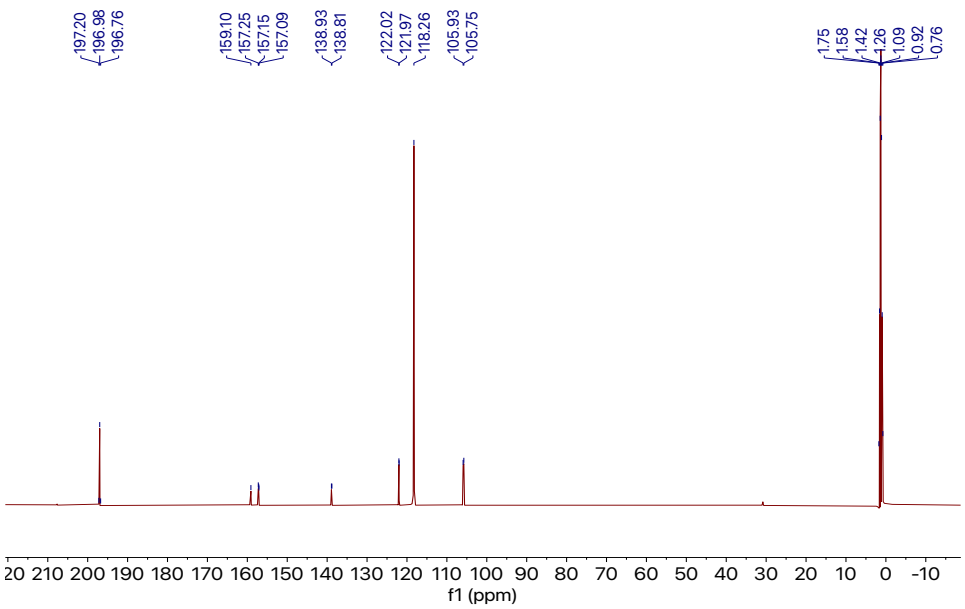

Figure C7. ^{13}C NMR spectrum of 2,5-dihydroxy-4-fluorobenzaldehyde in CD_3CN. Solvent peaks from MeCN (118.26, 1.75- 0.75) are present.

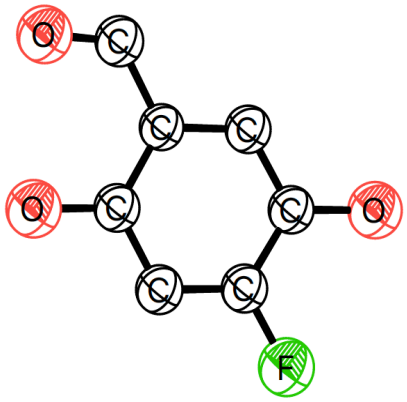

Figure C8. ORTEP representation of 2,5-dihydroxy-4-fluorobenzaldehyde. All hydrogen atoms and solvent molecules have been removed for clarity.

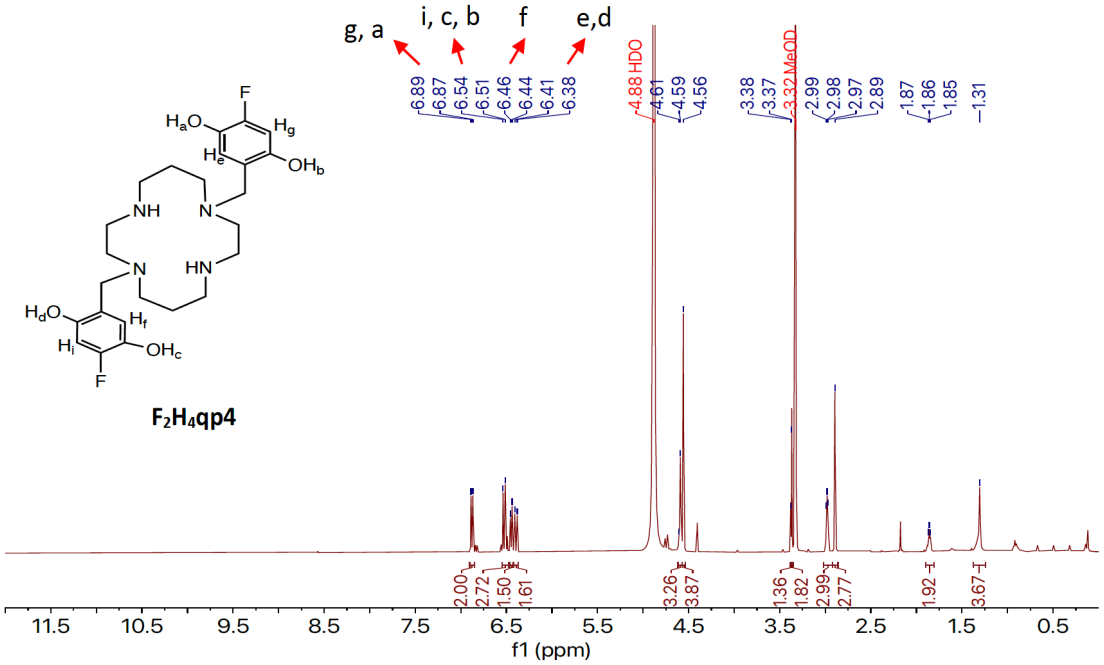

Figure C9. ^{1}H NMR spectrum of F_2H_4qp4 in CD_3OD.

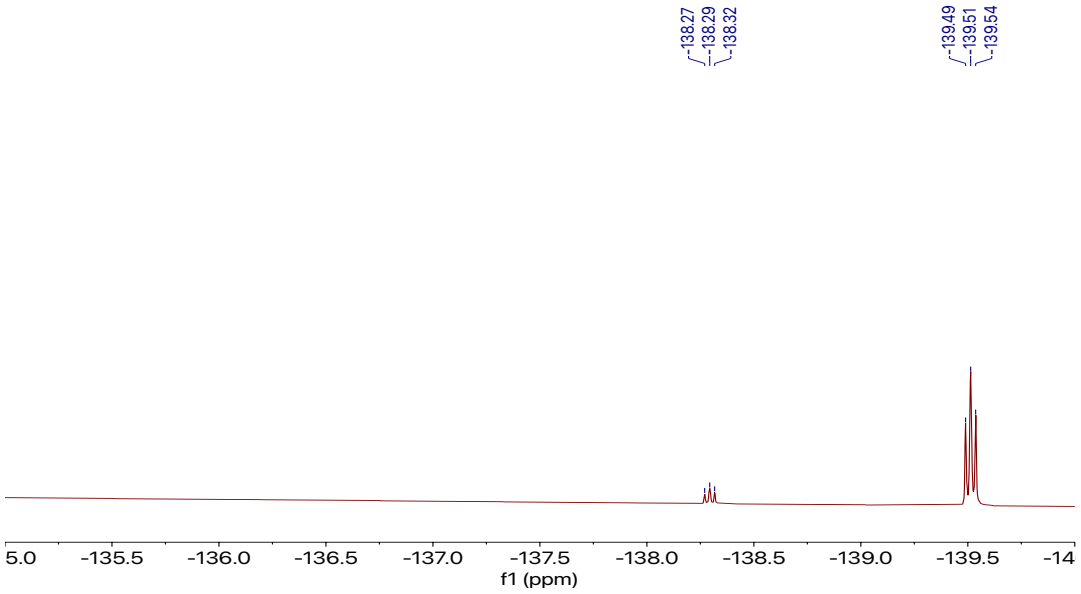

Figure C10. ^{19}F NMR spectrum of F_2H_4qp4 in CD_3OD.

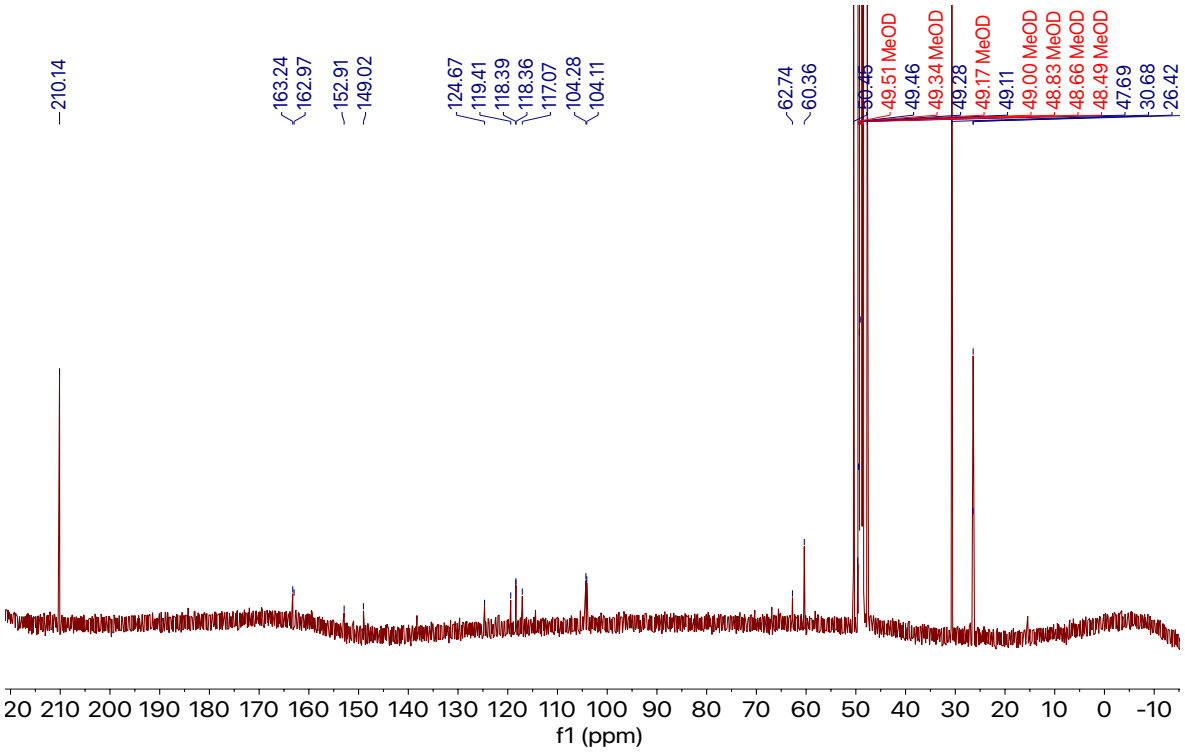

Figure C11. ^{13}C NMR spectrum of F_2H_4qp4 in CD_3OD. Solvent peaks from acetone (30.68, 210.14) are present.

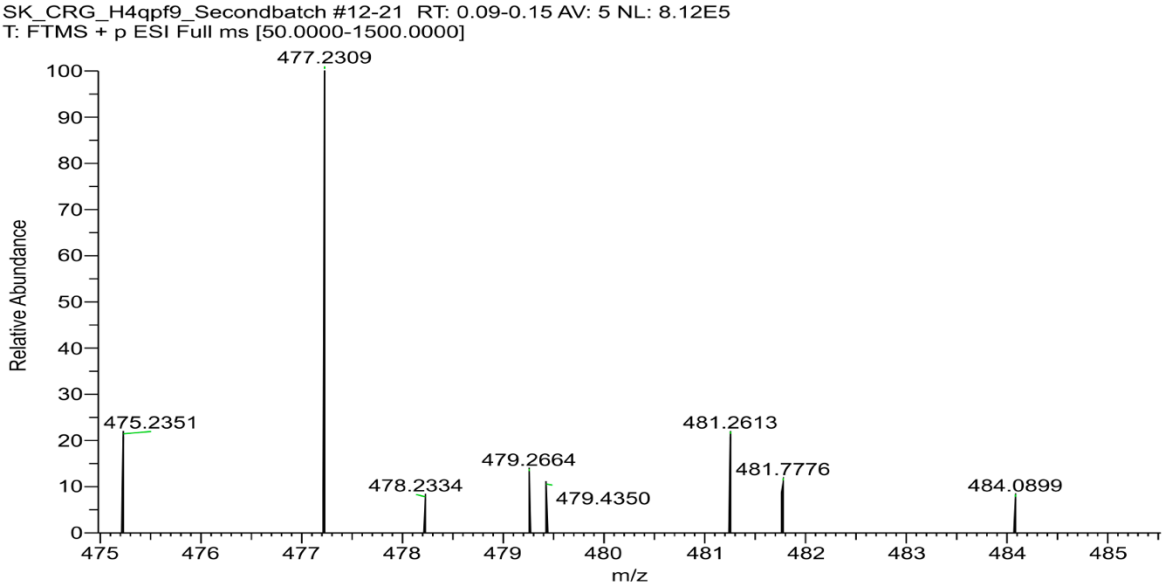

Figure C12. MS (ESI+) of F_2H_4qp4 in MeOH. The 477.2309 *m/z* feature is assigned to the triply deprotonated ligand $(F_2Hqp4)^+$ (calculated *m/z* = 477.2307). The 481.2613 *m/z* feature is assigned to the mono protonated ligand $(F_2H_5qp4)^+$ (calculated m/z = 481.2627).

Figure C13. IR spectrum of F_2H_4qp4. The 3262 cm^{-1} feature is assigned to the O-H stretches associated with the quinol groups of the F_2H_4qp4 ligand.

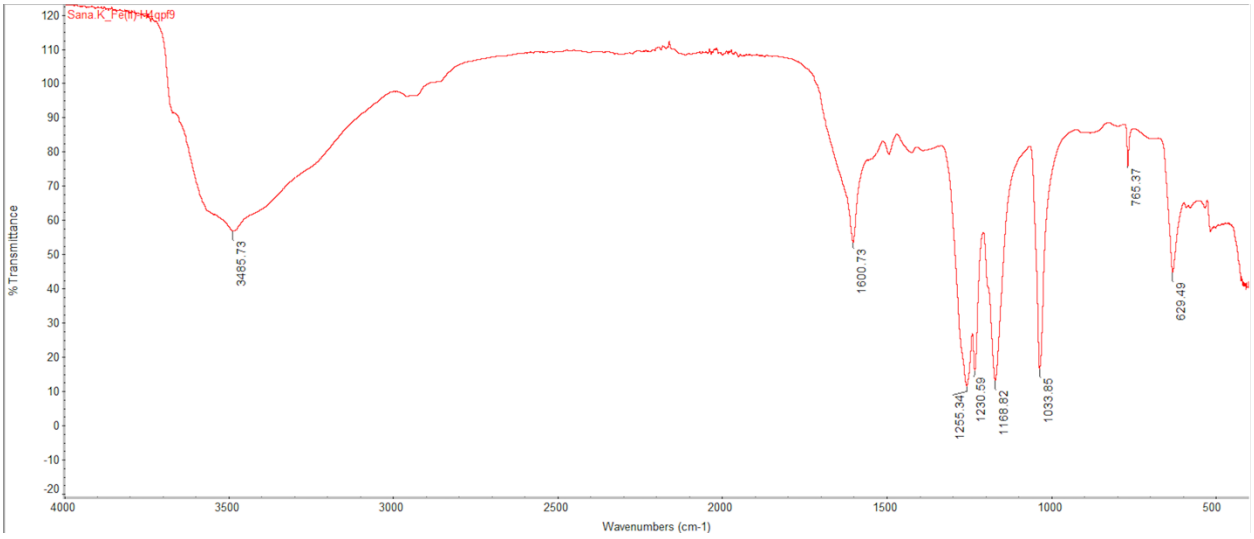

Figure C14. IR spectrum of $[Fe^{II}(F_2H_3qp4)](OTf)$ (**1**). The 3485 cm^{-1} feature is assigned to the O-H stretches associated with the quinol groups of the F_2H_4qp4 ligand.

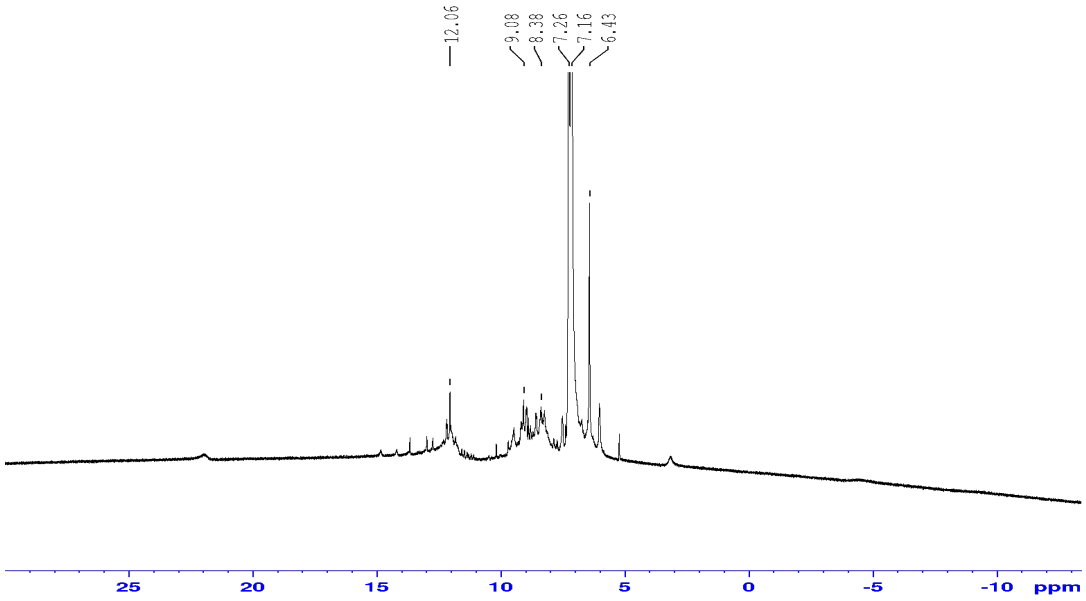

Figure C15. ^{1}H NMR spectrum of a 1 mM solution of [Fe^{II}(F_2H_3qp4)](OTf) (**1**) in $CDCl_3$ (500 MHz). The peak at 7.26 ppm corresponds to chloroform..

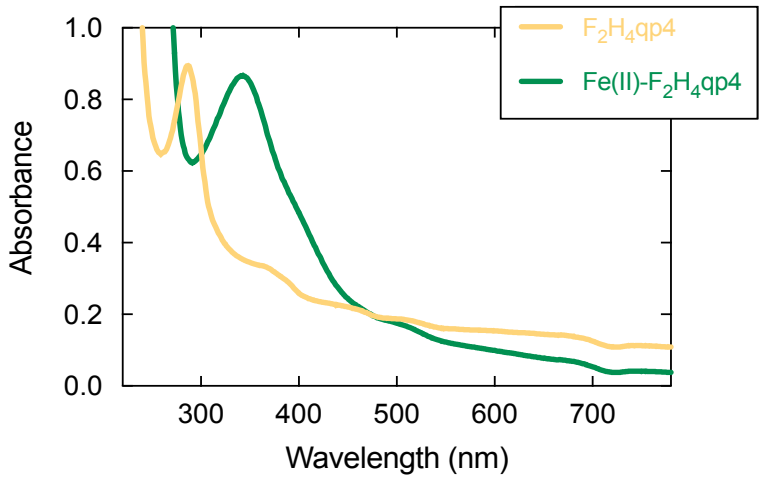

Figure C16. UV/vis spectra of 0.10 mM solutions of F_2H_4qp4 and [Fe^{II}(F_2H_3qp4)](OTf) (**1**) in aqueous solutions containing 50 mM HEPES buffered to pH 7.00

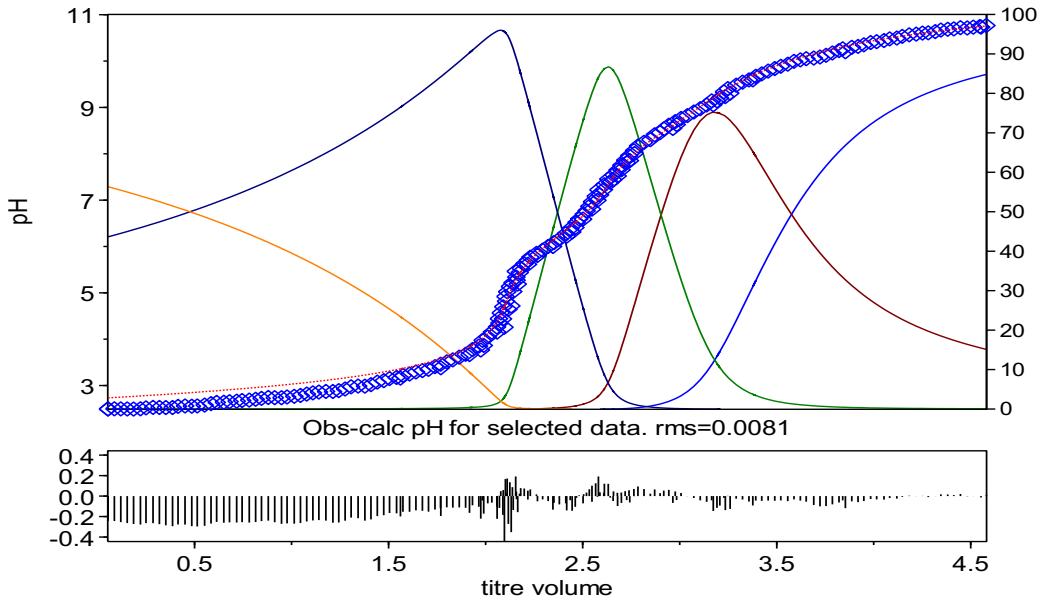

Figure C17. Hyperquad model (red line) overlaid on the experimental data from the potentiometric titration of F_2H_4qp4 (blue). The data above pH 11 have been excluded from the calculations since precipitation was observed above this value. The parameters for the Hyperquad model are provided on Table C1. The residuals for the fit are provided below. The curves represent the formation of various species including $F_2H_2qp4^{-2}$ (blue), $F_2H_3qp4^{-}$ (brown), F_2H_4qp4 (pine green), $F_2H_5qp4^{+}$ (indigo), and $F_2H_6qp4^{2+}$ (orange).

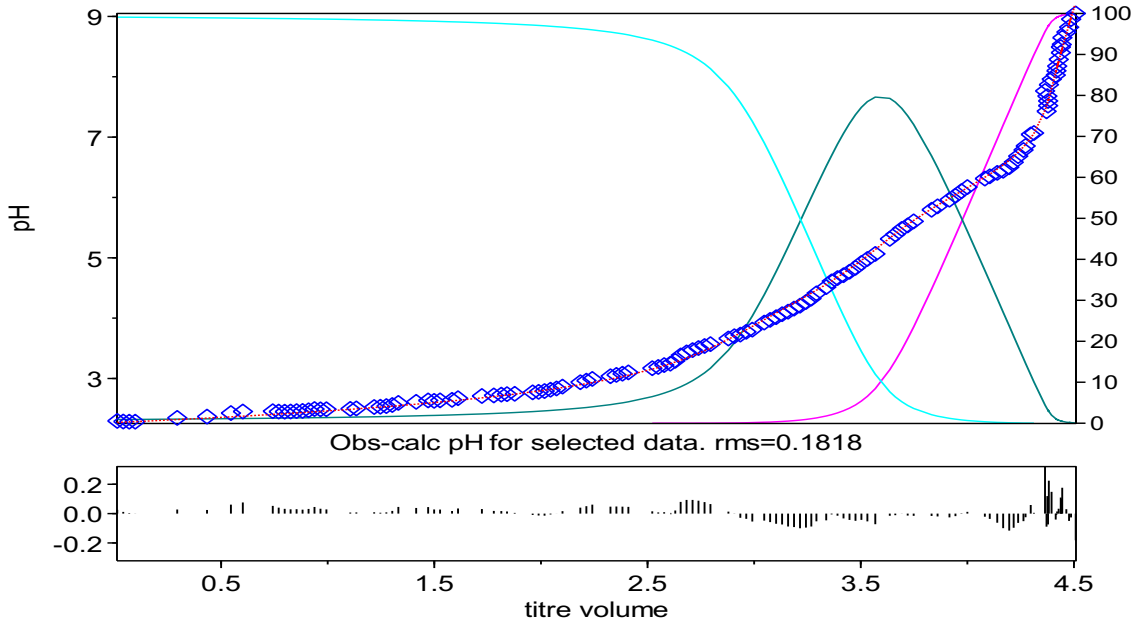

Figure C18. Hyperquad model (red line) overlaid on the experimental data from the potentiometric titration of 1.0 mM **1** (blue). The data above pH 9 have been excluded from the calculations since precipitation was observed above this value. The parameters for the Hyperquad model are provided on Table C1. The residuals for the fit are provided below. The curves represent the formation of various species including $[Fe^{II}(F_2H_2qp4)]$ (pink), $[Fe^{II}(F_2H_3qp4)]^{+}$ (green), and $[Fe^{II}(F_2H_4qp4)]^{2+}$ (light blue).

Table C1. Parameters for the Hyperquad model used in Figures **C17** and **C18**.

Species	**Fe(II)**	**F_2H_4qp4**	**H^+**	**log(β)**	**Derived Values**
$F_2\mathbf{H_2}qp4^{2-}$	0	1	-2	13.2	
$F_2\mathbf{H_3}qp4^{-}$	0	1	-1	23.209	pK_{L4} = 10.009 (±0.05)[a]
$F_2\mathbf{H_4}qp4$	0	1	0	31.651	pK_{L3} = 8.442 (±0.05)[a]
$F_2\mathbf{H_5}qp4^{+}$	0	1	1	37.86	pK_{L2} = 6.209 (±0.05)[a]
$F_2\mathbf{H_6}qp4^{2+}$	0	1	2	40.706	pK_{L1} = 2.846 (±0.05)[a]
[Fe($F_2\mathbf{H_2}$qp4)]	1	1	-2	41.40	log K_{eq} (Fe(F_2H_2qp4)) = 28.20[c]
[Fe($F_2\mathbf{H_3}$qp4)]$^+$	1	1	-1	47.511	pK_a(Fe(F_2H_3qp4)$^+$) = 6.11 (±0.05)[b] log K_{eq} (Fe(F_2H_3qp4))$^+$ = 24.302[c]
[Fe($F_2\mathbf{H_4}$qp4)]$^{2+}$	1	1	0	51.824	pK_a(Fe(F_2H_4qp4)$^{2+}$) = 4.313 (±0.05)[b] log K_{eq} (Fe(F_2H_4qp4))$^{2+}$ = 20.173[c]
pFe (pH 7.4) = 13.76[d]					

[a]Ligand pK_a values:

K_{L1} = [F_2H_5qp4$^+$][H^+]/[F_2H_6qp4^{2+}], pK_{L1} = logβ_{012} – logβ_{011}
K_{L2} = [F_2H_4qp4][H^+]/[F_2H_5qp4$^+$], pK_{L2} = logβ_{011} – logβ_{010}
K_{L3} = [F_2H_3qp4$^-$][H^+]/[F_2H_4qp4], pK_{L3} = logβ_{010} – log$\beta_{01(-1)}$
K_{L4} = [F_2H_2qp4^{2-}][H^+]/[F_2H_3qp4$^-$], pK_{L4} = log$\beta_{01(-1)}$ – log$\beta_{01(-2)}$

[b]Metal complex pK_a values:

K_a(Fe(F_2H_4qp4)$^{2+}$) = [Fe(F_2H_3qp4)$^+$][H^+]/[Fe(F_2H_4qp4)$^{2+}$] {deprotonation of first quinol}
pK_a(Fe(F_2H_4qp4)$^{2+}$) = logβ_{110} – log$\beta_{11(-1)}$
K_a(Fe(F_2H_3qp4)$^+$) = [Fe(F_2H_2qp4)][H^+]/[Fe(F_2H_3qp4)$^+$] {deprotonation of second quinol}
pK_a(Fe(F_2H_3qp4)$^+$) = log$\beta_{11(-1)}$ – log$\beta_{11(-2)}$

[c]Metal complex K_{eq} values:

K_{eq} (Fe(F_2H_2qp4)) = [Fe(F_2H_2qp4)]/([Fe(II)][F_2H_2qp4^{2-}])
log K_{eq} (Fe(F_2H_2qp4)) = log$\beta_{11(-2)}$ – log$\beta_{01(-2)}$
K_{eq} (Fe(F_2H_3qp4))$^+$ = [Fe(F_2H_3qp4)$^+$]/([Fe(II)][F_2H_3qp4$^-$])
log K_{eq} (Fe(F_2H_3qp4))$^+$ = log$\beta_{11(-1)}$ – log$\beta_{01(-1)}$
K_{eq} (Fe(F_2H_4qp4))$^{2+}$ = [Fe(F_2H_4qp4)$^{2+}$]/([Fe(II)][F_2H_4qp4])
log K_{eq} (Fe(F_2H_4qp4))$^{2+}$ = logβ_{110} – logβ_{010}

[d]pFe(pH 7.4) = -log([free Fe(II)]) at pH 7.4 and 298 K with 1.00 mM Fe(II) and 1.00 mM F_2H_4qp4

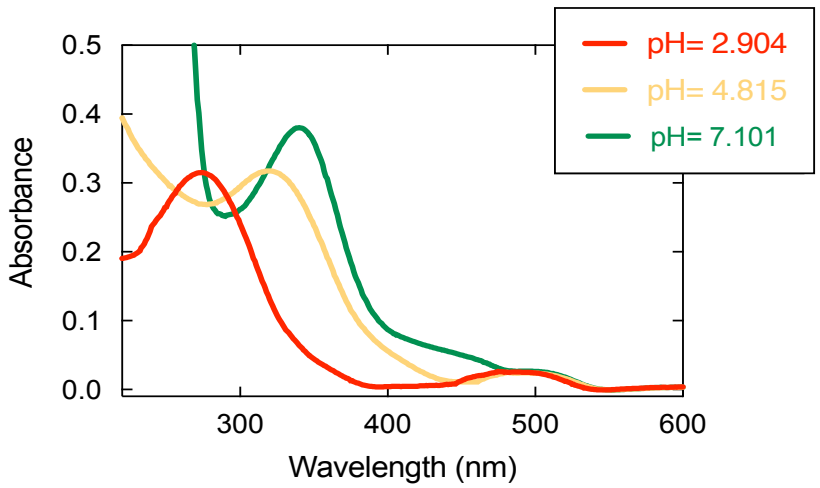

Figure C19. UV/vis spectra of a 0.05 mM solution of **1** in water adjusted to various pH values between 2 and 7 through the addition of either KOH or HCl. All spectra were obtained at 298 K under air using a 1.0 cm pathlength cuvette.

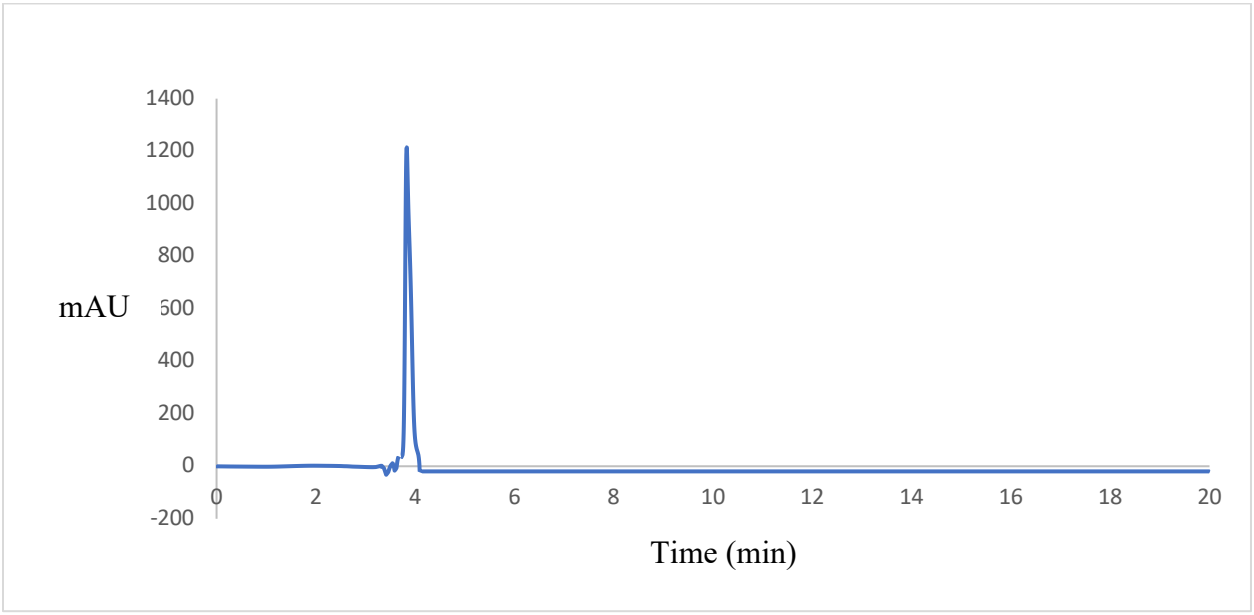

Figure C20. LC trace for the free F_2H_4qp4 ligand run under Method **1**. The ligand elutes at 3.83 min**.**

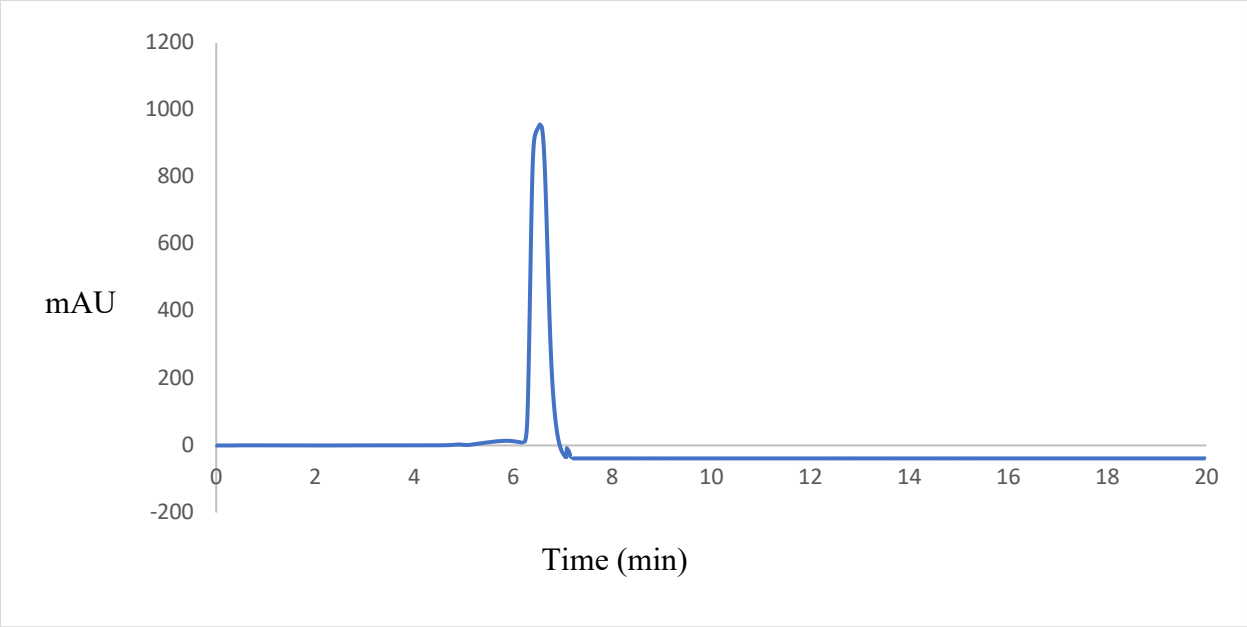

Figure C21. LC trace for **1** run under Method **1**. The Fe(II) complex elutes at 6.57 min.

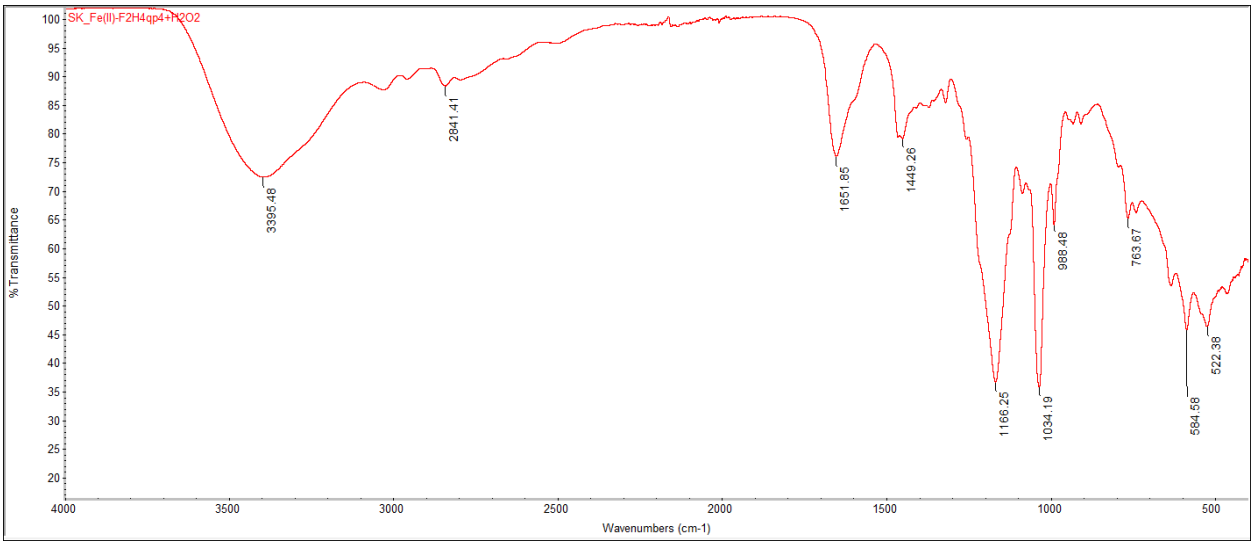

Figure C22. IR spectrum of the crude product from the reaction between 1.0 mM **1** and 10 mM H_2O_2 in 50 mM HEPES solution buffered to pH 7.0. After the reaction proceeded for 60 min, the solvents were removed, yielding the crude solid. The peak at 1651 cm^{-1} was not observed for **1** (Figure C14) and is assigned to the C=O stretches of the *para*-quinone subunits formed upon the partial oxidation of the F_2H_4qp4 ligand.

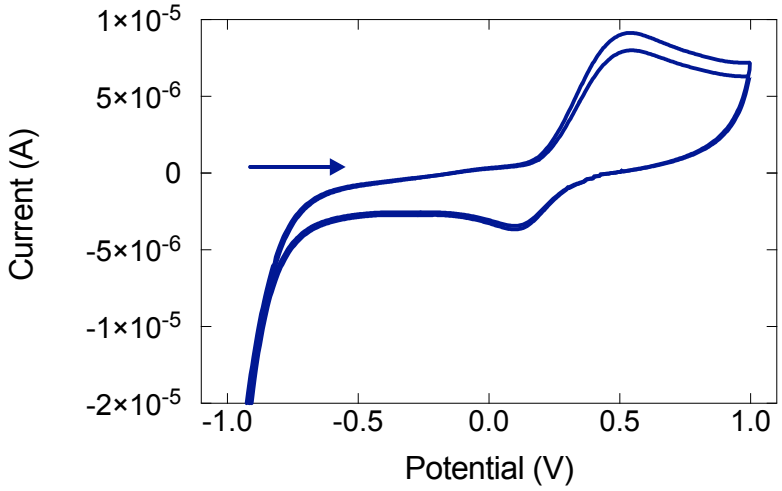

Figure C23. Cyclic voltammetry of 1.0 mM F_2H_4qp4 in 0.10 M phosphate buffer (NaH_2PO_4/Na_2HPO_4, pH = 7.2). The scan rate was 100 mV/s. The black arrow indicates the origin and initial direction of the scan. For the redox event: $E_{1/2}$ = 337 mV *vs.* Ag/AgCl, ΔE = 402 mV.

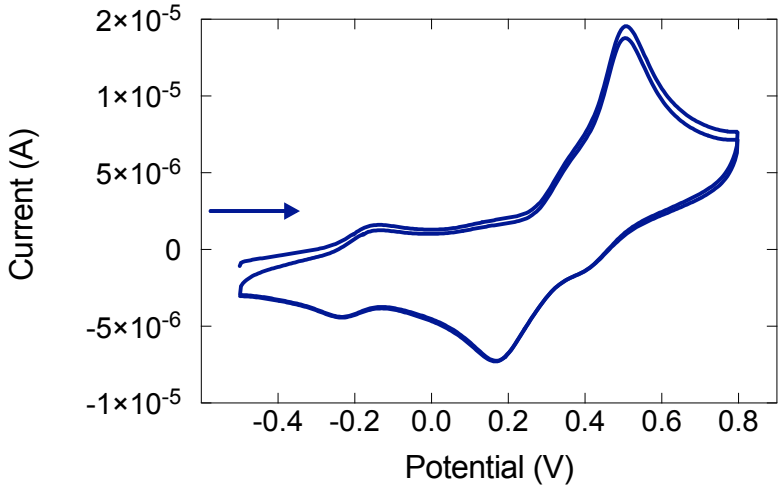

Figure C24.A. Cyclic voltammetry of 1.0 mM [Fe^{II}(F_2H_3qp4)](OTf) (**1**) in 0.10 M phosphate buffer (NaH_2PO_4/Na_2HPO_4, pH = 7.2). The scan rate was 100 mV/s and began at -0.5 V. The black arrow indicates the origin and initial direction of the scan. Two features are observed: a reversible feature with $E_{1/2}$ = -199.5 mV *vs.* Ag/AgCl (ΔE = 81 mV) and an irreversible feature with $E_{1/2}$ = 340.5 mV *vs.* Ag/AgCl (ΔE = 337 mV).

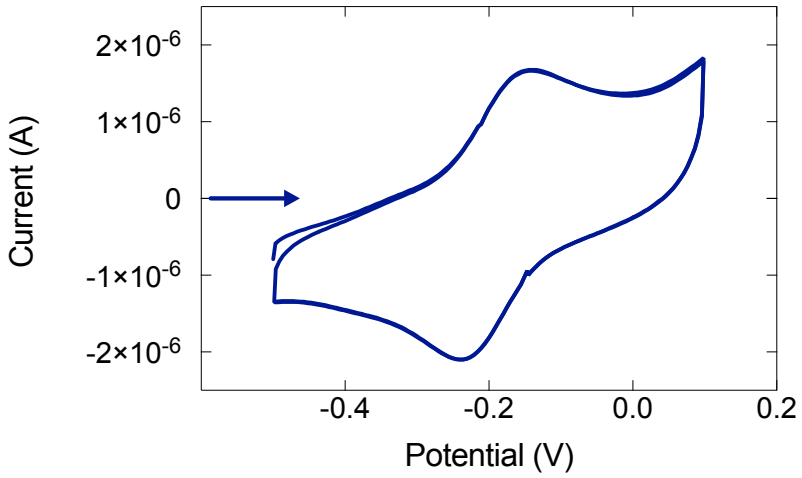

Figure C24.B. Cyclic voltammetry of 1.0 mM $[Fe^{II}(F_2H_3qp4)](OTf)$ (**1**) in 0.10 M phosphate buffer (NaH_2PO_4/Na_2HPO_4, pH = 7.2). The scan rate was 100 mV/s and began at -0.5 V (Expansion of -0.5 V to +0.1 V). The black arrow indicates the origin and initial direction of the scan.

Table C2. Selected crystallographic data for 2,5-dimethoxy-4-fluorobenzaldehyde and 2,5-dihydroxy-4-fluorobenzaldehyde

Parameter	2,5-Dimethoxy-4-fluorobenzaldehyde	2,5-Dihydroxy-4-fluorobenzaldehyde
Formula	$C_9H_9FO_3$	$C_7H_5FO_3$
MW	184.16 g/mol	156.11 g/mol
Crystal system	Monoclinic	Triclinic
Space group	*C 1 2/c 1*	*P -1*
a (Å)	18.7223(13)	7.6681(5)
b (Å)	11.2619(7)	8.3643(6)
c (Å)	8.6284(7)	11.4816(8)
α (°)	90	76.068(2)
β (°)	109.598(3)	77.790(2)
γ (°)	90	64.382(2)
V (Å^3)	1713.9(2)	639.61(8)
Z	8	4
Crystal color	Colorless	Colorless
T (K)	306	110
Reflns collected	23277	46412
Unique reflns	2133	6236
R1 (F, I > 2σ(I))[a]	0.0409	0.0344
wR2 (F^2, all data)[a]	0.1278	0.1086

[a] $R1 = \Sigma \big| |F_o| - |F_c| \big| / \Sigma |F_o|$; $wR2 = [\Sigma w(F_o^2-F_c^2)^2/\Sigma w(F_o^2)^2]^{1/2}$.

References

1. Gupta, S. C.; Hevia, D.; Patchva, S.; Park, B.; Koh, W.; Aggarwal, B. B. *Antioxid. Redox Signal.* **2012**, 16, 1295-1322.

2. Nogueira, V.; Hay, N. *Clin. Cancer Res.* **2013**, 19, 4309-4314.

3. Barnham, K. J.; Masters, C. L.; Bush, A. I. *Nat. Rev. Drug Discov.* **2004**, 3, 205-214.

4. Finkel, T.; Holbrook, N. J. *Nature* **2000**, 408, 239-247.

5. Lou, Z.; Li, P.; Han, K. *Acc. Chem. Res.* **2015**, 48, 1358-1368.

6. Chang, M. C. Y.; Pralle, A.; Isacoff, E. Y.; Chang, C. J. *J. Am. Chem. Soc.* **2004**, 126, 15392-15393.

7. Lippert, A. R.; Van de Bittner, G. C.; Chang, C. J. *Acc. Chem. Re.s* **2011**, 44, 793-804.

8. Carroll, V.; Michel, B. W.; Blecha, J.; VanBrocklin, H.; Keshari, K.; Wilson, D.; Chang, C. J. *J. Am. Chem. Soc.* **2014**, 136, 14742-14745.

9. Hou, C.; Hsieh, C.-J.; Li, S.; Lee, H.; Graham, T. J.; Xu, K.; Weng, C.-C.; Doot, R. K.; Chu, W.; Chakraborty, S. K.; Dugan, L. L.; Mintun, M. A.; Mach, R. H. *ACS Chem. Neurosci.* **2018**, 9, 578-586.

10. Loving, G. S.; Mukherjee, S.; Caravan, P. *J. Am. Chem. Soc.* **2013**, 135, 4620-4623.

11. Yu, M.; Beyers, R. J.; Gorden, J. D.; Cross, J. N.; Goldsmith, C. R. *Inorg. Chem.* **2012**, 51, 2725-2727.

12. Yu, M.; Ambrose, S. L.; Whaley, Z. L.; Fan, S.; Gorden, J. D.; Beyers, R. J.; Schwartz, D. D.; Goldsmith, C. R. *J. Am. Chem. Soc.* **2014**, 136, 12836-12839.

13. Yu, M.; Ward, M. B.; Franke, A.; Ambrose, S. L.; Whaley, Z. L.; Bradford, T. M.; Gorden, J. D.; Beyers, R. J.; Cattley, R. C.; Ivanović-Burmazović, I.; Schwartz, D. D.; Goldsmith, C. R. *Inorg. Chem.* **2017**, 56, 2812-2826.

14. Karbalaei, S.; Knecht, E.; Franke, A.; Zahl, A.; Saunders, A. C.; Pokkuluri, P. R.; Beyers, R. J.; Ivanović-Burmazović, I.; Goldsmith, C. R. *Inorg. Chem.* **2021**, 60, 8368-8379.

15. Karbalaei, S.; Franke, A.; Jordan, A.; Rose, C.; Pokkuluri, P. R.; Beyers, R. J.; Zahl, A.; Ivanović-Burmazović, I.; Goldsmith, C. R. *Chem. Eur. J.* **2022**, 28.

16. Ni, D.; Ehlerding, E. B.; Cai, W. *Angew. Chem. Int. Ed. Engl.* **2019**, 58, 2570-579.

17. Brunnquell, C. L.; Hernandez, R.; Graves, S. A.; Smit-Oistad, I.; Nickles, R. J.; Cai, W.; Meyerand, M. E.; Suzuki, M. *Contrast Media Mol. Imaging* **2016**, 11, 371-380.

18. Ekanger, L. A.; Polin, L. A.; Shen, Y.; Haacke, E. M.; Martin, P. D.; Allen, M. J. *Angew. Chem. Int. Ed.* **2015**, 54, 14398-14401.

19. Ekanger, L. A.; Ali, M. M.; Allen, M. J. *Chem. Commun.* **2014**, 50, 14835-14838.

20. Srivastava, K.; Ferrauto, G.; Young, V. G.; Aime, S.; Pierre, V. C. *Inorg. Chem.* **2017**, 56, 12206-12213.

21. Peterson, K. L.; Srivastava, K.; Pierre, V. C. *Front. Chem.* **2018**, 6, 160.

22. Neubauer, A. M.; Myerson, J.; Caruthers, S. D.; Hockett, F. D.; Winter, P. M.; Chen, J.; Gaffney, P. J.; Robertson, J. D.; Lanza, G. M.; Wickline, S. A. *Magn. Reson. Med.* **2008**, 60, 1066-1072.

23. Wang, C.; Adams, S. R.; Xu, H.; Zhu, W.; Ahrens, E. T. *ACS Appl. Bio. Mater.* **2019**, 2, 3836-3842.

24. Kislukhin, A. A.; Xu, H.; Adams, S. R.; Narsinh, K. H.; Tsien, R. Y.; Ahrens, E. T. *Nat. Mater.* **2016**, 15, 662-668.

25. Mizukami, S.; Takikawa, R.; Sugihara, F.; Hori, Y.; Tochio, H.; Wälchli, M.; Shirakawa, M.; Kikuchi, K. *J. Am. Chem. Soc.* **2008**, 130, 794-795.

26. Yu, M.; Xie, D.; Phan, K. P.; Enriquez, J. S.; Luci, J. J.; Que, E. L. *Chem. Commun.* **2016**, 52, 13885-13888.

27. Yu, M.; Bouley, B. S.; Xie, D.; Enriquez, J. S.; Que, E. L. *J. Am. Chem. Soc.* **2018**, 140, 10546–10552.

28. Chen, H.; Tang, X.; Gong, X.; Chen, D.; Li, A.; Sun, C.; Lin, H.; Gao, J. *Chem. Commun.* **2020**, 56, 4106-4109.

29. Bain, G. A.; Berry, J. F. *J. Chem. Educ.* **2008**, 85, 532-536.

30. Evans, D. F. *J. Chem. Soc.* **1959**, 2003-2005.

31. Sur, S. K. *J. Mag. Reson. (1969)* **1989**, 82, 169-173.

32. Gans, P.; Sabatini, A.; Vacca, A. Investigation of Equilibria in Solution. *Talanta* **1996**, 43, 1739-1753.

33. Hutchinson, T. E.; Bashir, A.; Yu, M.; Beyers, R. J.; Goldsmith, C. R. *Inorganica Chim. Acta* **2019**, 49*6*, 119045.

34. Zhang, Q.; Gorden, J. D.; Beyers, R. J.; Goldsmith, C. R. *Inorg. Chem.* **2011**, 50, 9365-9373.

35. Bernstein, M. A.; King, K. F.; Zhou, X. J. *Handbook of MRI Pulse Sequences*. Elsevier Academic Press: Amsterdam, **2004**.

36. Brown, R. W.; Cheng, Y.-C. N.; Haacke, E. M.; Thompson, M. R.; Venkatesan, R. *Magnetic Resonance Imaging: Physical Principles and Sequence Design*, Second edition.; John Wiley & Sons, Inc: Hoboken, New Jersey, **2014**.

37. Nelder, J. A.; Mead, R. A Simplex Method for Function Minimization. *The Comput. J.* **1965**, 7, 308-313.

38. Glennon, R. A.; Young, R.; Benington, F.; Morin, R. D. B *J. Med. Chem.* **1982**, 25, 1163-1168.

39. Wang, S.; Westmoreland, T. D. *Inorg. Chem.* **2009**, 48, 719-727.

40. Major, J. L.; Parigi, G.; Luchinat, C.; Meade, T. J. *Proc. Natl. Acad. Sci. U.S.A.* **2007**, 104, 13881-13886.

41. Gale, E. M.; Mukherjee, S.; Liu, C.; Loving, G. S.; Caravan, P. *Inorg. Chem.* **2014**, 53, 10748-10761.

42. Ma, Y.; Roy, S.; Kong, X.; Chen, Y.; Liu, D.; Hider, R. C. *J. Med. Chem.* **2012**, 55, 2185-2195.

43. Snyder, E. M.; Asik, D.; Abozeid, S. M.; Burgio, A.; Bateman, G.; Turowski, S. G.; Spernyak, J. A.; Morrow, J. R. *Angew. Chem. Int. Ed.* **2020**, 59, 2414-2419.

44. Ward, M. B.; Scheitler, A.; Yu, M.; Senft, L.; Zillmann, A. S.; Gorden, J. D.; Schwartz, D. D.; Ivanović-Burmazović, I.; Goldsmith, C. R. *Nature Chem.* **2018**, 10, 1207-1212.

45. Moore, J. L.; Oppelt, J.; Senft, L.; Franke, A.; Scheitler, A.; Dukes, M. W.; Alix, H. B.; Saunders, A. C.; Karbalaei, S.; Schwartz, D. D.; Ivanović-Burmazović, I.; Goldsmith, C. R. *Inorg. Chem.* **2022**, 61, 19983-19997.

Chapter 5

A Macrocyclic Quinol-Containing Ligand Enables High Catalase Mimicry even with a Redox-Inactive Metal at the Expense of the Ability to Mimic Superoxide Dismutase[*]

[*] This chapter is a version of a submitted manuscript by the following authors: Sana Karbalaei, Alicja Franke, Julian Oppelt, Tarfi Aziz, Aubree Jordan, P. Raj Pokkuluri, Dean D. Schwartz, Ivana Ivanović-Burmazović, and Christian R. Goldsmith.

5.1 Introduction

High concentrations of reactive oxygen species (ROS), such as hydrogen peroxide (H_2O_2) and superoxide ($O_2^{\cdot-}$) are capable of damaging biomolecules, and the accumulation of these species has been linked to a wide array of health conditions.[1-5] In response, the body produces a variety of antioxidants to manage ROS concentrations. These include superoxide dismutases (SODs), which catalyze the conversion of $O_2^{\cdot-}$ to O_2 and H_2O_2, and catalases, which promote the dismutation of H_2O_2 to O_2 and H_2O. The high activities of these enzymes have motivated us and other researchers to develop small molecules capable of replicating this catalysis. Such compounds could potentially be used to bolster the body's defenses against ROS and treat health conditions associated with oxidative stress.

In previous work from our laboratories, we found that linear polydentate ligands with 1,4-hydroquinone (quinol) groups could be used as the organic components in a variety of SOD mimics (Scheme 5.1).[6-10] A manganese complex with H_2qp1 displayed activity that was comparable to those of the most effective SOD mimetics reported to date: manganese complexes with pentaazamacrocycle and cationic porphyrin ligands.[11-14] The redox activity of the quinol group enables it to act as the redox partner for $O_2^{\cdot-}$ and can allow SOD mimicry even without a redox-active metal. The Zn(II) complexes with H_2qp1 and H_4qp2 are likewise functional SOD mimics, with the latter ligand resulting in higher activity.[9-10]

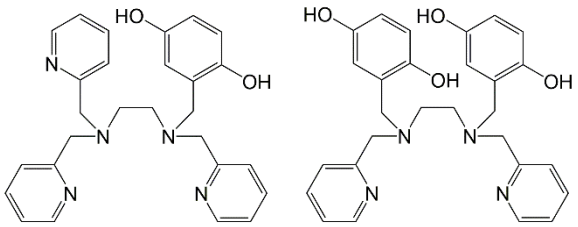

H_2qp1 **H_4qp2**

Scheme 5.1 Linear polydentate quinol-containing ligands from prior work.[6-10]

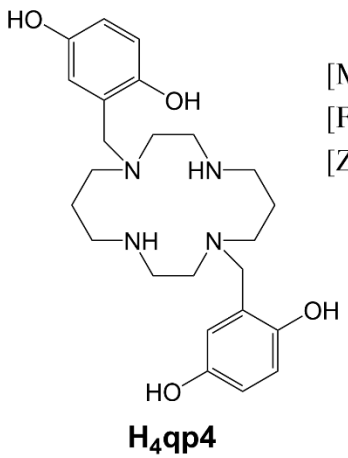

$[Mn^{II}(H_3qp4)](OTf)$ - **1**
$[Fe^{II}(H_3qp4)](OTf)$ - **2**
$[Zn^{II}(H_3qp4)](OTf)$ - **3**

Scheme 5.2 Structure of H_4qp4 ligand and formulations of the discussed coordination complexes.

More recent work has focused on the macrocyclic ligand 1,8-bis(2,5-dihydroxybenzyl)-1,4,8,11-tetraazacyclotetradecane (H_4qp4, Scheme 5.2).[15-16] Our initial interest in this molecule was as a component in highly water-stable magnetic resonance imaging (MRI) contrast agent sensors for H_2O_2. When the quinols are oxidized to *para*-quinones, water molecules displace these groups, increasing the T_1-weighted relaxivity (r_1) of its Mn(II) complex, $[Mn^{II}(H_3qp4)](OTf)$ (**1**).[15] Although quinol oxidation and an accompanying enhancement in r_1 also occur when the Fe(II) complex, $[Fe^{II}(H_3qp4)](OTf)$ (**2**), reacts with H_2O_2, it is instead metal oxidation that is responsible for the increase in relaxivity.[16] For both **1** and **2**, we found that the oxidation of the quinols and the accompanying activation of the sensor occur more slowly in higher concentrations of H_2O_2.[15-16] This led us to speculate that the initial reactions with H_2O_2 may be generating a higher-valent metal species that can either react intramolecularly to oxidize the ligand or intermolecularly with a second equiv. of H_2O_2. The intermolecular activity depletes H_2O_2, thereby mimicking catalase. The intramolecular reaction was proposed to be inherently slower, only proceeding to a noticeable extent after the $[H_2O_2]$ decreases enough to make the intermolecular reaction less competitive.

In this chapter, we thoroughly investigate the abilities of the Mn(II) and Fe(II) complexes with H_4qp4 to mimic both SOD and catalase. We also prepare and evaluate the antioxidant

properties of a Zn(II) complex with H_4qp4: [Zn^{II}(H_3qp4)](OTf) (**3**). We find that although the SOD activities are severely attenuated relative to those of complexes with linear quinol-containing ligands, all three H_4qp4 complexes act as highly potent catalase mimics, with activities that greatly exceed those exhibited by most other reported small molecule mimics of these enzymes.[17-27] The Zn(II) complex is further notable in that it represents the first instance, to the best of our knowledge, where a coordination complex with a redox-inactive metal ion successfully catalyzed the degradation of H_2O_2.

5.2 Experimental Section

Materials

All chemicals and solvents were purchased from Sigma-Aldrich and used without further purification unless otherwise noted. All deuterated solvents were bought from Cambridge Isotopes. Diethyl ether (ether) and methanol (MeOH) were bought from Fisher. Methylene chloride (CH_2Cl_2) was purchased from Mallinckrodt Baker. 1,8-Bis(2,5-dihydroxybenzyl)-1,4,8,11-tetraazacyclotetradecane (H_4qp4), [Mn^{II}(H_3qp4)](OTf), and [Fe^{II}(H_3qp4)](OTf) were synthesized and purified as previously described.[15-16]

Instrumentation

All nuclear magnetic resonance (NMR) data were collected on a 500 MHz AV Bruker NMR spectrometer. All NMR resonance peak frequencies were referenced to internal standards. UV/Vis were collected on a Varian Cary 50 spectrophotometer and analyzed using software from the WinUV Analysis Suite. High-resolution mass spectrometry (HR-MS) data were obtained at the Mass Spectrometer Center at Auburn University on a Bruker Microflex LT MALDI-TOF mass spectrometer via direct probe analysis operated in the positive ion mode. Infrared spectroscopy (IR) data were obtained with a Shimadzu IR Prestige-21 FT-IR spectrophotometer. Cyclic

voltammetry (CV) was performed under N_2 at 294 K using an Epsilon electrochemistry workstation (Bioanalytical System, Inc.), a gold working electrode, a platinum wire auxiliary electrode, and a silver/silver(I) chloride reference electrode. All elemental analyses (C, H, N) were performed by Atlantic Microlabs (Norcross, GA); samples were dried under vacuum and placed under a N_2 atmosphere prior to shipment.

X-Ray Crystallography

Crystallographic data for $[Zn^{II}(H_3qp4)](OTf)$ (**3**) were collected using a Bruker D8 VENTURE κ-geometry diffractometer system equipped with a Incoatec IμS 3.0 microfocus sealed tube and a multilayer mirror monochromator (Mo Kα, λ = 0.71073 Å). Diffraction data were integrated with the Bruker SAINT software package using a narrow-frame algorithm. Data were corrected for absorption effects using the Multi-Scan method (SADABS). The structure was solved and refined using the Bruker SHELXTL Software Package. Selected crystallographic data is presented in Appendix D.

Antioxidant Assays

The ability of coordination complexes to catalyze the degradation of $O_2^{\cdot-}$ was initially screened using the hypoxanthine/xanthine oxidase/lucigenin assay.[28-29] The reaction between hypoxanthine and xanthine oxidase generates $O_2^{\cdot-}$, which can then subsequently react either with lucigenin to provide a luminescent response or an antioxidant. The extent to which various concentrations of an antioxidant eliminate the lucigenin response provides a quantitative measure of its activity. These assays were performed with 1 mL of saline solutions buffered with 50 mM phosphate to pH 7.2. The solutions also contained 50 μM hypoxanthine, 0.005 U/mL xanthine oxidase (Calbiochem), 5 μM dark adapted lucigenin, and the tested antioxidant in concentrations ranging from 0.1 nM to 10 μM. Reactions were carried out at room temperature (RT) and were

initiated by the addition of xanthine oxidase to the hypoxanthine-containing solution. The copper/zinc superoxide dismutase isolated from bovine erythrocytes (0.001−100 U/mL, Calbiochem) was used as a positive control. Luminescence was measured using a TD-20/20 (Turner Designs) luminometer and expressed as relative light units (RLU). Luminescence was measured for four 10 s integrations after an initial delay of 3 s. The four RLU values were averaged, and each concentration was expressed as a percent of that produced in the presence of the vehicle. Each measurement within an individual run was performed in triplicate, and each assay was repeated three times.

Kinetic Assessment of Catalase and Peroxidase Activity

The ability of antioxidants to catalyze H_2O_2 degradation was initially evaluated by monitoring the decrease in the absorbance of H_2O_2 at 240 nm (ε_{240} = 39.4 M^{-1} cm^{-1})[30] over time. These measurements were performed in 200 mM phosphate solutions buffered to pH 7.0 that contained 100 nM of the tested compound and 1-500 mM H_2O_2 at RT. The changes in the UV/vis data were followed using a Shimadzu UV-1601 spectrophotometer (Columbia, MD). Under the described conditions, we observed a single hyperbolic phase and could fit the data to a standard Michaelis–Menten equation to obtain apparent k_{cat} and k_{on} values (Eq. 1).

$$\frac{v_o}{[\mathbf{1}]_T} = \frac{k_{cat}[H_2O_2]}{k_{cat}/k_{on}+[H_2O_2]} = \frac{k_{cat}[H_2O_2]}{K_M+[H_2O_2]} \quad (1)$$

The catalase activity was more stringently assessed by polarigraphically following O_2 production using a Clark-type O_2 sensitive electrode (Hansatech Pentney, Norfolk, England). We first calibrated the system using a N_2 saturated solution to establish a zero O_2 level within the reaction chamber prior to experimental measurements. The initial series of reactions contained 1 nM of the tested antioxidant and were carried out at RT in solutions containing 50 mM tris(hydroxymethyl)aminomethane (Tris) buffered to pH 7.2. The buffer and solution containing

the coordination complex were initially mixed in the reaction chamber for 20 s to establish a baseline, after which H_2O_2 was injected to initiate the evolution of O_2.[31] Subsequently, we measured the initial rates of reactions between 10 mM H_2O_2 and 1.0-100 nM of the catalysts to calculate k_2 rate constants.

Peroxidase activity can also contribute to the degradation of H_2O_2, representing a means for H_2O_2 to get consumed without generating O_2. This potential reactivity was evaluated by monitoring the abilities of the antioxidants to promote the reaction between H_2O_2 and 2,2'-azinobis(3-ethylbenzothiazoline-6-sulfonate) (ABTS); this reaction generates the radical cation $ABTS^{\bullet+}$ (ε_{417} = 34.7 mM^{-1} cm^{-1}).[32] All reactions were run in RT 50 mM acetate solution buffered to pH 5.0, with reaction concentrations of 10 mM ABTS, 0.1 mM coordination complex, and 1-500 mM H_2O_2. Another series of reactions were run in RT 50 mM acetate solution buffered to pH 5.0, with reaction concentrations of 10 mM H_2O_2, 0.1 mM coordination complex, and 1-100 mM ABTS. The conversion of ABTS to its radical cation was followed using a Shimadzu UV-1601 spectrophotometer (Columbia, MD). To present the compound's activity in terms of the initial rate, more specifically, $v_o/[M]_T$ in units of s^{-1}, the following equation is used for the calculation of initial rates:

$$\frac{v_o}{[M]_T} = \frac{\Delta \text{ Abs (at 417 nm for 60 s)}}{60\ s \times 100\ \mu M \times 0.0347\ \mu M^{-1} cm^{-1} \times 1\ cm} \quad (2)$$

Where 100 is the final concentration of the compound in μM, and 0.0347 $\mu M^{-1}cm^{-1}$ is the molar absorptivity of $ABTS^{\bullet+}$ at 417 nm.

Syntheses

(1-(2,5-dihydroxybenzyl)-8-(2,5-dihydroxybenzylalkoxide)-1,4,8,11-tetraazacyclotetradecane)zinc(II) triflate ([$Zn^{II}(H_3qp4)$](OTf), 3)

H_4qp4 (500 mg, 1.12 mmol) and $Zn^{II}(OTf)_2$ (415 mg, 1.12 mmol) were dissolved in 5 mL of dry MeCN and then stirred at 60 °C for 24 h. The slow addition of ether to the MeCN solution deposited the product as a colorless powder that could be isolated by filtration (703 mg, 88% yield). Crystals suitable for single crystal X-ray diffraction were grown by layer diffusion of ether to a saturated solution of the crude product in MeOH. Optical spectroscopy (H_2O, 294 K): 299 nm (ε = 7000 M^{-1} cm^{-1}). IR (cm^{-1}): 3403 (s), 3260 (s), 3055 (s), 2988 (w), 2887 (w), 2724 (m), 1607 (w), 1508 (s), 1432 (w), 1375 (m), 1300 (m), 1247 (w), 1217 (w), 1196 (w), 1147 (w), 1115 (w), 1101 (m), 1077 (m), 1061 (s), 1021 (s), 1004 (w), 961 (m), 939 (w), 914 (m), 894 (m), 869 (w), 830 (m), 781 (m), 759 (m), 630 (s), 567 (w). ^{1}H NMR (500 MHz, CD_3OD, 298 K): δ 6.64-6.75 (m, 6H), 4.57 (s, 3H), 2.70 (d, *J* = 25 Hz, 6), 2.28 (s, 2H), 2.03 (s, 2H), 1.34-1.35 (m, 4H). ^{13}C NMR (125 MHz, CD_3OD, 298 K): δ 151.83, 149.78, 149.00, 122.99, 120.48, 119.96, 119.84, 119.45, 117.92, 117.69, 117.56, 117.16, 116.99, 58.54, 54.84, 54.54, 53.80, 53.67, 53.05, 51.91, 51.79, 50.99, 25.82, 25.78, 24.23. MS (ESI): calcd for $[Zn(H_3qp4)]^+$, *m/z* 507.1944; found, *m/z* 507.1941. Elemental analysis (powder) calcd for $C_{25}H_{35}N_4O_7F_3S_1Zn\cdot0.5(C_2H_5)_2O\cdot0.5MeCN$ (powder): C, 46.99%; H, 5.84%; N, 8.81%. Found: C, 46.52%; H, 5.99%; N, 8.81%.

5.3 Results

Synthesis and Structural Characterization of [$Zn^{II}(H_3qp4)$](OTf)

Mn(II) and Fe(II) complexes with H_4qp4 were previously reported.[15-16] The isolated compounds, [$Mn^{II}(H_3qp4)$](OTf) (**1**) and [$Fe^{II}(H_3qp4)$](OTf) (**2**), feature the singly deprotonated ligand H_3qp4^-; we believe that the residual non-complexed ligand deprotonates the metal-bound

H_4qp4. The complexation of Zn(II) to H_4qp4 similarly yields a H_3qp4$^-$ complex: [Zn^{II}(H_3qp4)](OTf) (**3**). As with **1** and **2**, the synthesis of **3** required us to heat the mixture of ligand and metal salt for a prolonged period of time (24 h) to maximize complexation of the metal ion. Complex **3** was characterized by NMR, IR, MS, and UV/vis (Figures D1-5).

The redox capabilities of **3** were initially assessed using cyclic voltammetry (CV, Figure D6). In phosphate solution buffered to pH 7.2, we observed one irreversible redox event with $E_{1/2}$ = 110 mV *vs.* Ag/AgCl (ΔE = 260 mV). This resembles the irreversible CV features seen for both **1** and **2**. The redox event for the Mn(II) complex has an $E_{1/2}$ at 110 mV *vs.* Ag/AgCl (ΔE = 260 mV);[15] whereas, that for the Fe(II) compound has an $E_{1/2}$ at 90 mV *vs.* Ag/AgCl (ΔE = 300 mV).

We crystallized **3** from MeOH/ether and structurally characterized the complex through single crystal X-ray diffraction (Figure 5.1, Table D1). The H_3qp3$^-$ ligand coordinates to the Zn(II) through five out of its six possible donor atoms, with the neutral quinol not directly binding to the metal center. The coordination geometry of the N_4O donors around the Zn(II) is best described as a distorted trigonal bipyramidal, with a τ_5 value of 0.70.[33] The pendent quinol may hydrogen bond to the outer-sphere triflate; the distance between O(3) and O(6) is 2.72 Å.

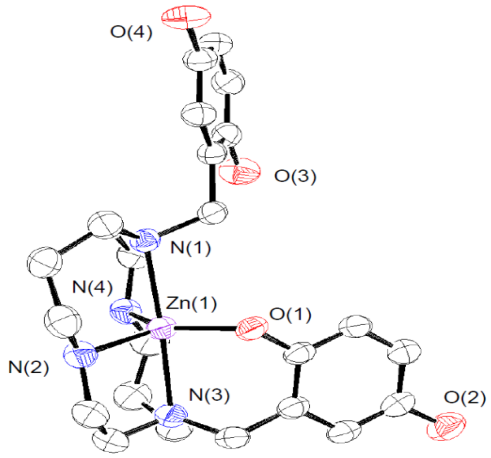

Figure 5.1 ORTEP representation of the structure of [Zn^{II}(H_3qp4)]$^+$. The triflate counteranion and all H atoms are omitted for clarity. All ellipsoids are drawn at 50% probability. Full crystallographic data are provided in Appendix D.

Aqueous Solution Characterization of [Zn^{II}(H_3qp4)](OTf)

We investigated the stability and speciation of **3** in water using potentiometric pH titrations (Figure D7). As the pH of a 1:1 mixture of $Zn^{II}(OTf)_2$ and H_4qp4 was increased from 2.5 to 10, we observed two ionization events consistent with pK_a values of 6.16 and 9.71 (Table D2). We assign these to the deprotonation of the quinols. Although the first value is consistent with other M(II)-quinol pK_a values that we have measured,[6, 8-9, 15] the second value is much higher and more consistent with a metal-free quinol or phenol. The solid-state structure featuring a pentacoordinate metal center (Figure 5.1) may therefore be retained in water. Despite the one fewer chelating group, the Zn(II)-H_3qp4 complex appears to be extremely stable against metal ion dissociation, with a log K_{ML} = 41.1; this value is higher than the analogous values for **1** and **2**.[15-16]

Superoxide Dismutase Mimicry

Compounds **1**, **2**, and **3** were initially screened using the hypoxanthine/xanthine oxidase/lucigenin assay (Figure 5.2).[28-29] By this measure, both **1** and **2** initially appeared to be capable of catalyzing superoxide dismutation. The Mn(II) complex **1** is most active, with an IC_{50} value of 15 nM. The Fe(II) complex **2** also has above-baseline activity, with an IC_{50} value of 21 nM. These IC_{50} values are similar to those measured for $[Mn^{II}(H_2qp1)(MeCN)]^{2+}$ (**4**) and $[Mn^{II}(H_4qp2)Br_2]$ (**5**, Scheme 5.1),[6] which were subsequently confirmed to be functional SOD mimics via analysis of the direct reactions between the manganese compounds and KO_2.[8] Compound **3** is essentially inactive, with an IC_{50} of 515 nM.

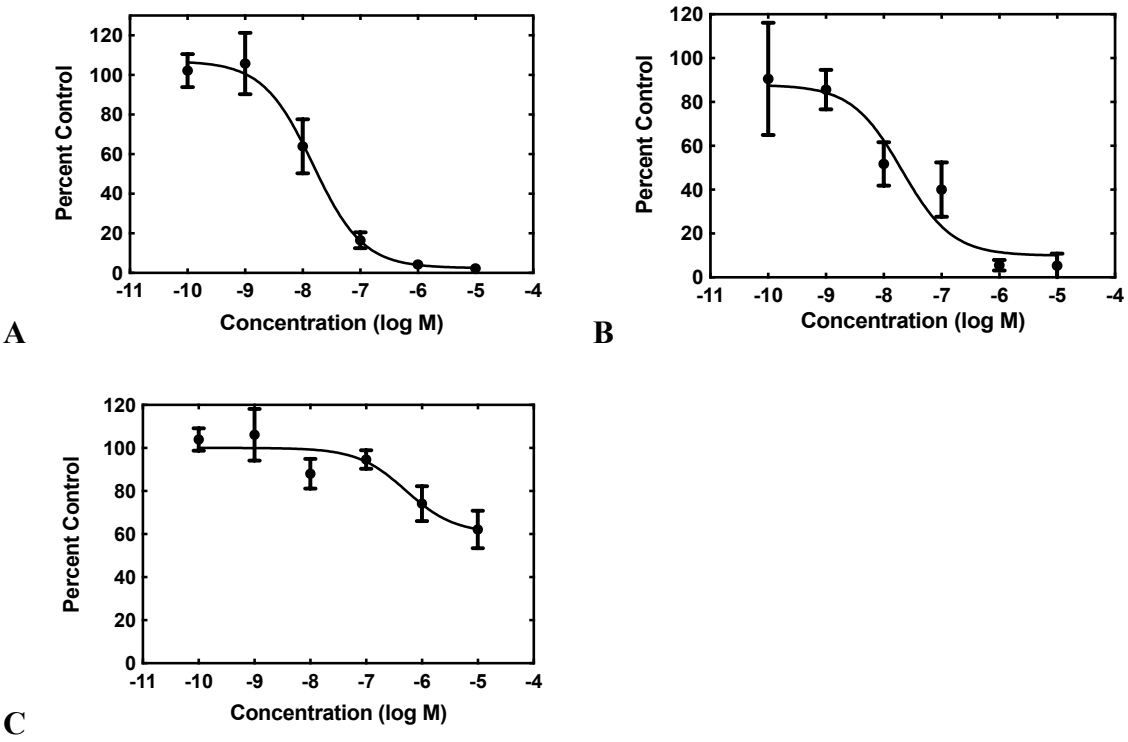

Figure 5.2 Superoxide scavenging effects of A) **1**, B) **2**, and C) **3**. $O_2^{\cdot-}$ was generated from the reaction between hypoxanthine and xanthine oxidase reaction and detected using the chemiluminescent probe lucigenin. All reactions were carried out in pH 7.2 phosphate buffered saline (PBS) (50 mM phosphate). Data for the various concentrations of the three coordination complexes are expressed as percentages of luminescence in the presence of vehicle.

The aforementioned assay is somewhat notorious for providing misleading results due to possible side reactions between its components.[34-39] In the case of **4** and **5**, the assay predicted similar activities, but later stopped-flow kinetics analysis of the direct reactions between the Mn(II) compounds and KO_2 indicated that the H_2qp1 complex was much more active than the H_4qp2 complex in HEPES solutions.[8] Complexes **1**, **2**, and **3** were studied in 60 mM MOPS buffered to pH 7.4 and 7.8 and 50 mM phosphate buffered to pH 7.4 (Table 5.1). The stopped-flow kinetics data indicate that **1** is significantly less active than either **4** or **5** in either a sulfonate-containing buffer or phosphate (Figure D8). As with **4** and most other manganese-containing SOD mimics,[8, 35, 40] complex **1** is less catalytically active in phosphate buffer. The iron and zinc complexes, **2** and

3, have no noticeable impact on the rate of decomposition of $O_2^{\cdot -}$ when analyzed by stopped-flow kinetics.

Table 5.1 Catalytic rate constants, k_{cat} (M^{-1} s^{-1}), measured by stopped-flow kinetics for the direct reactions of **1**, **2**, and **3** with superoxide.

Buffer, pH	**1**	**2**	**3**	**4** [a]	**5** [a]
60 mM MOPS/HEPES, 7.4	6.0×10^6	N.A.	N.A.	9.7×10^7	1.2×10^7
60 mM MOPS, 7.8	4.5×10^6	N.A.	N.A.	N.D.	N.D.
50 mM Phosphate, 7.4	2.9×10^6	N.A.	N.A.	8.0×10^6	1.0×10^7

[a] Data from reference 8; the first-row data for **4** and **5** were collected in HEPES, rather than MOPS.

Catalase Activity

Previously, **1** and **2** had been found to react with excess H_2O_2 in a manner consistent with catalase activity.[15-16] We further investigated this potential catalysis by monitoring the reactions of these two compounds, **3**, and metal-free H_4qp4 with H_2O_2 using oxygraphy and UV/vis. The metal-free H_4qp4 ligand was unable to catalyze the degradation of H_2O_2. Each coordination complex, conversely, catalyzes the decomposition of H_2O_2. In all three cases, the reactivity is consistent with Michaelis-Menten kinetics with clear saturation behavior observed at high concentrations of H_2O_2 (Figure 5.3). Oxygraphic measurements confirm that O_2 is being evolved; these data were fitted to the re-arranged Michaelis-Menten equation, which has parameters k_{cat} and k_{cat}/K_M (Table 5.2, Table D3). The iron complex **2** appears to be slightly more active than the other two, but the individual rate constants do not vary much within this series. Although the reactions involving **2** have the highest k_{cat}, **1** has the highest catalytic efficiency, as indicated by its k_{cat}/K_M.

Table 5.2 Michaelis-Menten rate constants, k_2 rate constants, and turnover numbers (TON) calculated from oxygraphic data.

Complex	k_{cat} (s^{-1})	k_{cat}/K_M (M^{-1} s^{-1})	K_M (M)	k_2 (M^{-1} s^{-1})	TON
1 (Mn)	2.9×10^3	3.5×10^5	8.3×10^{-3}	1.3×10^3	100
2 (Fe)	3.7×10^3	2.0×10^5	1.9×10^{-2}	1.7×10^3	150
3 (Zn)	2.6×10^3	1.0×10^5	2.6×10^{-2}	1.1×10^3	70

Full details regarding the models used to fit the data for the three compounds are provided in Table D3 in Appendix D.

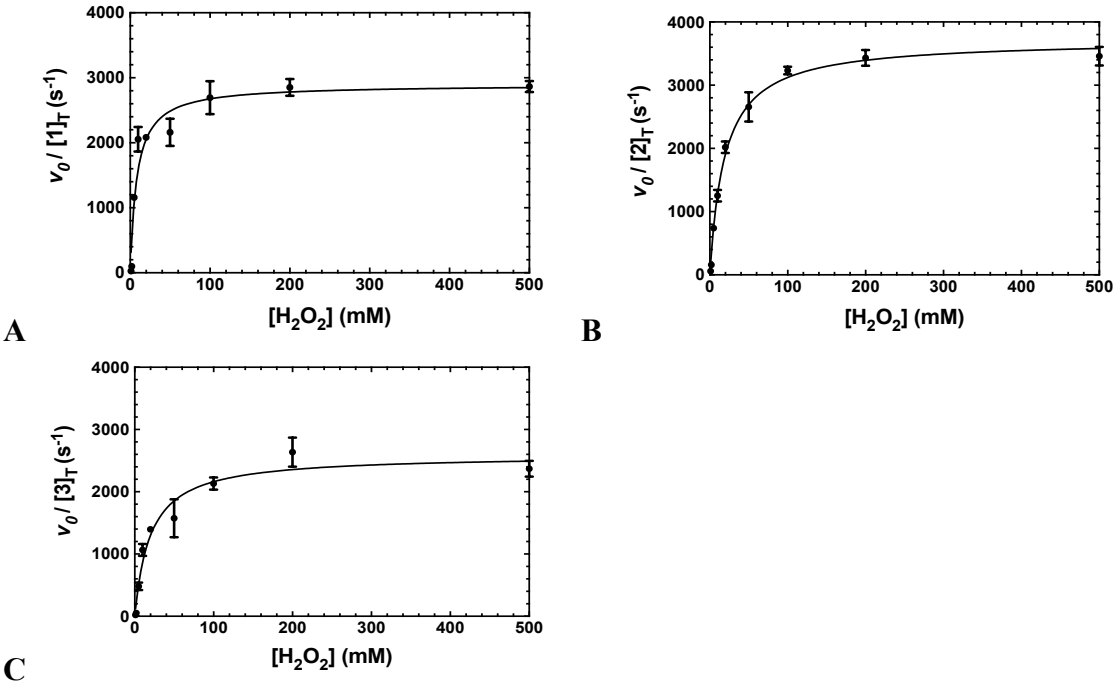

Figure 5.3 Plots of v_o/[**M**] *vs.* the concentration of H_2O_2, where [**M**] is the concentration of the tested H_4qp4 complex. The v_o corresponds to the formation of O_2, which was measured through oxygraphy. All reactions were performed in 25 °C 50 mM Tris buffered to pH 7.2. 1 nM of each coordination complex was present as a catalyst. Each shown data point is the average of at least five independent runs. A) Data for **1**. B) Data for **2**. C) Data for **3**. Further details regarding the models used to fit the data can be found in Table D3.

Second-order rate constants (k_2) were calculated by measuring the initial rates of O_2 production via oxygraphy with catalyst concentrations ranging from 1.0 to 100 nM (Figure 5.4). The k_2 values are much lower than the k_{cat}/K_M values obtained from the Michaelis-Menten models but more accurately represent the activities of the catalysts.[22] We also measured turnover numbers (TON) by quantifying the total O_2 made over time (Figure D9). This parameter depends on both the robustness and activity of the catalyst and is arguably the most accurate measure of how practical a catalase mimic is. As assessed by both the initial rates analysis and the overall O_2 production, **2** clearly outperforms its manganese and zinc analogs.

The activity was qualitatively confirmed with parallel experiments that monitored the disappearance of H_2O_2 (Figure D10, Table D4). The rate constants from these experiments are much less reliable than those calculated from O_2 production since all three complexes absorb strongly at the monitored 240 nm wavelength, and this technique generally tends to overestimate the activities of catalase mimics.[22] Nonetheless, the activities of the complexes follow the same general order, with **2** and **3** being the most and least effective catalase mimics, respectively.

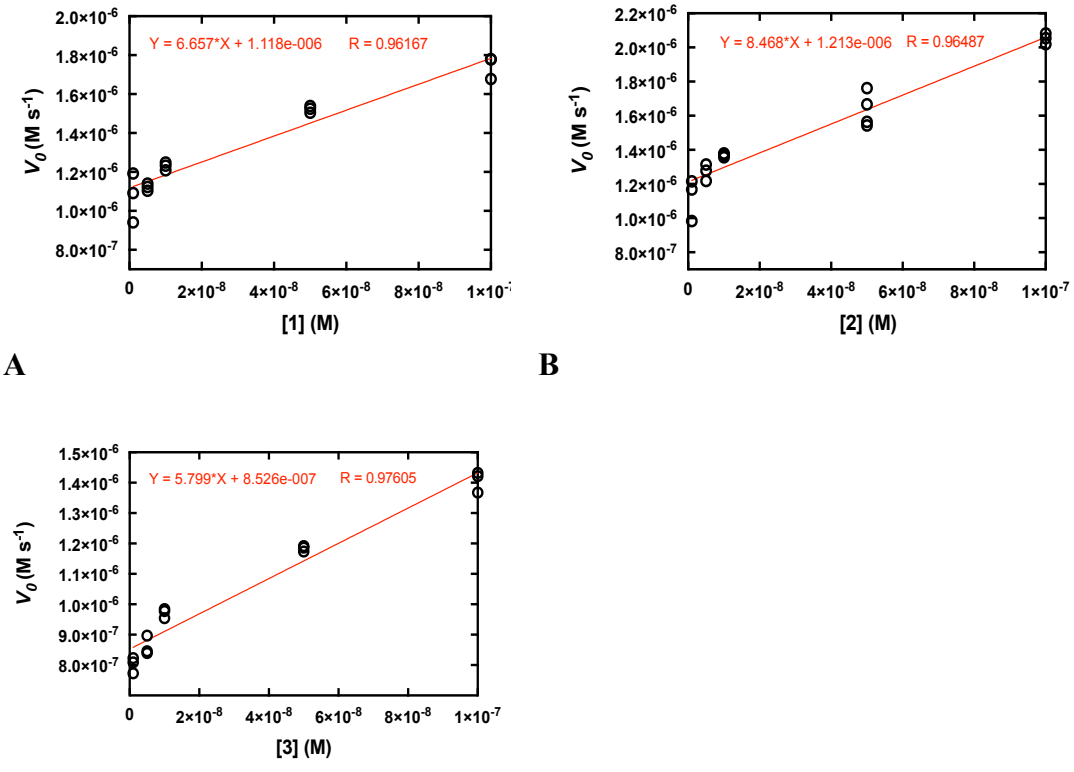

Figure 5.4 Determination of k_2 from plots of the initial rates (v_0) *vs.* concentration of catalyst. All reactions were run at 25 °C in 50 mM Tris buffered to pH 7.2. The initial concentration of H_2O_2 was 10.0 mM for all reactions. The reaction was run at least three times at each catalyst concentration. The k_2 values on Table 5.2 were calculated by dividing the slopes by the concentration of H_2O_2 (0.010 M) and multiplying by 2 to account for the reaction stoichiometry (2 equiv. of H_2O_2 consumed per equiv. of O_2 made). A) Data for **1**. B) Data for **2**. C) Data for **3**.

Peroxidase Activity

The three H_4qp4 complexes were also assessed as peroxidase mimics using an established protocol that assesses the ability of a compound to catalyze the reaction between H_2O_2 and 2,2'-azinobis(3-ethylbenzothiazoline-6-sulfonate) (ABTS).[32] Both **1** and **2** appear to catalyze the reaction, as evidenced by the formation of $ABTS^{\bullet+}$. The activity shows no dependence on the concentration of H_2O_2, suggesting that the activation of the bound H_2O_2, rather than H_2O_2 binding, is rate-determining (Figure D11.). The initial rates scale with $[ABTS]_o$. Using these data, we calculated third-order rate constants of 0.41 ± 0.02 M^{-2} s^{-1} and 33.8 ± 1.2 M^{-2} s^{-1}, respectively for **1** and **2**. At 10 mM H_2O_2, peroxidase activity is negligible compared to catalase activity (Figure D11).

Mechanistic Studies

Previous UV/vis and EPR analyses of the reactions between **1** and **2** and H_2O_2 indicated that the quinol portions of the ligands slowly oxidize to *para*-quinones and that the Fe(II) in **2** eventually oxidizes to Fe(III).[15-16]

We further analyzed the reactions between H_2O_2 and the three H_4qp4 complexes by EPR, with an emphasis on collecting data at an earlier time point that would coincide with higher catalase activity. EPR analysis suggests that a small amount of the Mn(II) and Fe(II) in **1** and **2** has been oxidized 30 s after the reactions begin (Figure D12). With **3**, we observe a weak signal with $g = 2$. The intensity of the signal is barely above the noise level, and it is ambiguous whether this can be attributed to a species on the main catalytic cycle.

UV/vis analysis suggests that the quinols are oxidized during the reaction between **3** and H_2O_2 (Figure 5.5). With an initial concentration of 0.6 mM H_2O_2, the 299 nm band attributable to the quinols almost completely vanishes by 15 min. The rate of quinol oxidation is approximately

as fast as that observed for **1**, which likewise lacks obfuscating charge transfer bands, under the same conditions.[15] With an initial concentration of 10 mM H_2O_2, however, the quinols in **3** oxidize much more quickly than those in **1** under the same conditions. The quinols in **3** appear to be almost entirely consumed by 30 min; whereas, ligand oxidation does not occur to a noticeable extent for **1** by 30 min. The results suggest that the redox-active ligand is more heavily involved in H_2O_2 degradation for **3** than **1**.

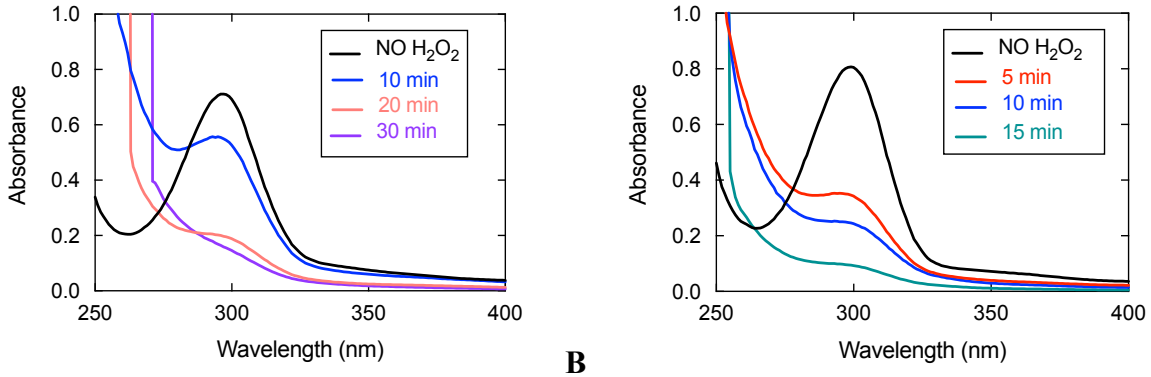

Figure 5.5 UV/vis spectra of reactions between **3** and H_2O_2. A) Data for the reaction between 0.1 mM **3** and 10 mM H_2O_2. B) Data for the reaction between 0.1 mM **3** and 0.60 mM H_2O_2. All data were taken in 50 mM HEPES buffered to pH 7.00 at 298 K with a 1.0 cm pathlength cuvette.

MS studies of reactions between 10 mM H_2O_2 and the H_4qp4 complexes in MeCN further suggest that ligand-derived redox is more prevalent for **3** than it is for the two H_4qp4 complexes with redox-active metals. The data for **1** and **2** at 30 s look identical to those in solutions that lack H_2O_2;[15-16] the major *m/z* peaks are consistent with $[Mn^{III}(H_2qp4)]^+$ and $[Fe^{III}(H_2qp4)]^+$, respectively (Figures D13 and D14). Without H_2O_2, the Mn(II) and Fe(II) appear to oxidize spontaneously under ionizing conditions. The data are inconsistent with M(II) or M(III) complexes with oxidized forms of the ligand, leading us to conclude that the ligand exists as the doubly deprotonated H_2qp4^{2-} rather than the monoquinol/mono-*para*-quinone H_2qp4. When we react **3** and 10 mM H_2O_2, however, we observe a much different set of *m/z* peaks that are consistent with ligand oxidation (Figure D15). Specifically, we detect a *m/z* peak at 505.1790 at 30 s that is consistent

with a Zn(II) complex with the monoquinolate/mono-*para*-quinone form of the ligand (calculated *m/z* = 505.1794). Further, we observe peaks that are consistent with the addition of one oxygen atom to the mono-*para*-quinone complex ($[Zn(Hqp4+O)]^+$) with *m/z* = 521.1736 (calculated *m/z* = 521.1743) and with the addition of two oxygen atoms to the diquinol complex ($[Zn(H_3qp4+2O)]^+$) with *m/z* = 539.1395 (calculated *m/z* = 539.1848). After 60 s, oxygenate products appear to become more prominent (Figure D17).

5.4 Discussion

The manganese and iron complexes with 1,8-bis(2,5-dihydroxybenzyl)-1,4,8,11-tetraazacyclotetradecane (H_4qp4) were previously found to act as T_1-weighted MRI contrast agent sensors for H_2O_2.[15-16] The responses, which rely either wholly or partly on the oxidation of the quinolic portions of the ligand, were found to both display an induction period and be noticeably slower with larger excesses of H_2O_2. This initially counter-intuitive observation led us to speculate that both $[Mn^{II}(H_3qp4)](OTf)$ (**1**) and $[Fe^{II}(H_3qp4)](OTf)$ (**2**) were proceeding through higher-valent metal species that could either self-oxidize to the activated sensor or catalyze the decomposition of the excess H_2O_2.

Given that other quinol-containing ligands had been found to allow the redox-inactive metal ion Zn(II) to catalyze the dismutation of superoxide,[9] we also prepared and tested the reactivity of a Zn(II) complex with H_4qp4, $[Zn^{II}(H_3qp4)](OTf)$ (**3**). The synthesis of the Zn(II) complex was identical in most aspects to those used to prepare both **1** and **2**, and as with these syntheses, a complex with a singly deprotonated ligand (H_3qp4^-) was the isolated product.[15-16] Unlike the manganese and iron systems, we were able to obtain a crystal structure for the complex with the divalent metal. The H_3qp4^- ligand does not fully coordinate to the metal center (Figure 5.1), which may suggest that the Zn(II) is too small to be fully accommodated by the ligand pocket.

Only one of the quinols is coordinated in the crystal structure, and it appears that it remains unassociated with the metal center in aqueous solution since the second measured pK_a of 9.71 is only slightly lower than the value of ~10 expected for a non-coordinated quinol. Nonetheless, the Zn(II) complex is highly stable in water like **1** and **2**; the analogous log K_{ML} values for Mn(II) and Fe(II) are 18.22 and 26.87, respectively.[15-16]

Given that manganese and zinc complexes with other quinol-containing ligands were found to act as functional mimics of superoxide dismutase (SOD),[8-10] we assessed the abilities of the three complexes to catalyze the degradation of $O_2^{\cdot-}$. We initially screened **1**, **2**, and **3** using the xanthine oxidase/hypoxanthine/lucigenin assay (Figure 5.2).[28-29] Although the assay suggests that **1** and **2** are potent antioxidants, subsequent stopped-flow analysis of the direct reactions between KO_2 and the complexes found that only the manganese complex **1** had a noticeable effect on $O_2^{\cdot-}$ decomposition. The activity of **1** was generally inferior to those displayed by two manganese complexes that were previously reported by our lab groups: $[Mn^{II}(H_2qp1)(MeCN)](OTf)_2$ (**4**) and $[Mn^{II}(H_4qp2)Br_2]$ (**5**, Scheme 5.1).[8] As with most other manganese-containing SOD mimics, **1** is most effective as a catalyst in pH 7.4 solutions with sulfonate-based buffers (HEPES/MOPS) and becomes less active as the solution becomes more basic or when the buffer component is switched to phosphate.[35,41-47] The phosphate inhibition suggests that phosphate is competing with superoxide for coordination sites on the metal center, which would be consistent with an inner-sphere mechanism for superoxide dismutation.[35]

Although **3** does not seem to be an effective SOD mimic, the compound does react with KO_2, as assessed by EPR and UV/vis analysis (Figures D18 and D19). The EPR data show a weak signal at $g = 2$ at 30 s that completely disappears within 15 min. We do not believe that the EPR feature corresponds to residual $O_2^{\cdot-}$ since the oxidant should be consumed below the limit of EPR

detection within 1 s, even without a catalyst.[9] The energy of the signal and its short lifetime are consistent with organic radicals similar to what we observed for previous Zn(II)-quinoxyl radical species.[9-10] A Zn(II)-semiquinone species observed with the H_4qp2 ligand, for instance, persists to detectable levels for over 45 min.[10] The Zn(II)-H_4qp2 complex is an effective SOD mimic but reacts very slowly with H_2O_2, consistent with a lack of catalase activity. The UV/vis data indicate that the complex is initially deprotonated by KO_2, which is a base as well as an oxidant, and then slowly oxidized to Zn(II)-*para*-quinone species over 90 s. Although **3** does react with $O_2^{\cdot -}$, this activity is not enough to noticeably accelerate superoxide degradation beyond the rate observed for the uncatalyzed reaction.

The catalase activities of **1**, **2**, and **3** were assessed polarigraphically, using a Clark-type O_2 sensitive electrode to follow O_2 production (Figure 5.3). This technique is a more reliable measure of catalase activity than using UV/vis to follow H_2O_2 depletion. We find that all three complexes are highly catalytically active. The activity of the Zn(II) complex is further notable in that all previously characterized systems capable of such catalysis contain a redox-active metal ion. Catalase enzymes use either dinuclear manganese or heme in their active sites. Most previously characterized small molecule functional mimics of catalase contain manganese or iron.[17-23, 26-27] The activation of quinolic ligands by redox-inactive metal ions towards the degradation of reactive oxygen species is therefore not strictly limited to $O_2^{\cdot -}$. Given the magnitudes of these constants, care must be taken to ensure that these are calculated properly.[19, 25] Inspection of the plots from Figure 5.3 shows that the rates per M of catalyst do indeed plateau at the k_{cat} values. We measured second-order rate constants by assessing the initial rates of O_2 production (Figure 5.4) and determined overall turnover numbers (TON) by monitoring the

reactions until completion. Of the three complexes, the iron-containing **2** is the most active, followed by **1**, then **3**.

The catalysts are highly active and their k_2 values might be exceeded only by an Fe(III) complex with a fluorinated corrole prepared by Mahammed and Gross.[27] The reactivity between this compound and H_2O_2 follows second-order kinetics with a k_2 = 4300 M^{-1} s^{-1} in 37 °C pH 7.4 phosphate buffer. The Fe(III)-corrole has a tendency to condense into less active binuclear Fe(III) species; this process can be hindered by adding imidazole to the solution, increasing the k_2 to 6400 M^{-1} s^{-1}. Comparisons between Mahammed and Gross's results and ours, however, are obfuscated by the higher temperature at which they studied their catalase activity and by the fact that they had to follow the kinetics by UV/vis rather than oxygraphy. The TON of the H_4qp4 complexes range from 70 (**3**) to 150 (**2**). These compare extremely well to TON values reported for other catalase mimics; in a recent review of catalase mimics, the best listed TON was 12.54.[22] Mahammed and Gross did not report a TON for their Fe(III)-corrole complex, but the overall O_2 production appears to be severely limited by the formation of the binuclear ferric side-product, even when imidazole is present to hinder that reaction.[27]

The high stability of the H_4qp4 complexes in aqueous solutions enables them to act as effective catalysts in water. The activities of non-porphyrinic manganese-containing catalase mimics, conversely, are instead determined in MeCN.[17-23] The abilities of the H_4qp4 complexes to function in water make them more suitable for potential applications in the clinical treatment of oxidative stress.

We also analyzed the capabilities of the complexes to act as peroxidase mimics using 2,2'-azinobis(3-ethylbenzothiazoline-6-sulfonate) (ABTS) as the substrate. We found that **1** and **2**, but not **3**, can catalyze the oxidation of ABTS to $ABTS^{\bullet+}$ by H_2O_2. Enzymes that can perform both

catalase and peroxidase activity have been proposed to go through a common intermediate, and the same could conceivably hold for **1** and **2**. The reactivity of **3**, however, is less straightforward, but it appears that whatever intermediates are generated from the reaction between the Zn(II) complex and H_2O_2 cannot be directed towards other substrates. With **1** and **2**, the peroxidase activity is much slower than the catalase activity. This reaction selectivity is an attractive quality for a catalase mimic since competing *in vivo* peroxidase activity could potentially oxidize essential biomolecules.

The relative lack of peroxidase activity that protects the three H_4qp4 complexes from oxidative ligand degradation may partly explain the high catalase activity. Iron porphyrin and corrole mimics of catalase, conversely, commonly undergo oxidative degradation,[26] and the efficient catalase mimicry exhibited by Mahammad and Gross's complex has been attributed to its ability to resist such decomposition.[27] As mentioned above, the three H_4qp4 complexes are also all highly water-stable, and metal ion dissociation from the ligand is negligible even under highly acidic conditions.[15-16] This represents a substantial advantage over most manganese-containing catalase mimics. With these compounds, the aqueous stabilities have not been established, and the catalysis is studied in organic solvents instead of water.[21, 23-25]

That **1**, **2**, and **3** catalyze H_2O_2 dismutation at similar rates led us to initially hypothesize that the three catalysts mainly rely on a common mechanistic cycle that does not feature redox at the metal center. EPR analysis of the reactions between H_2O_2 and **1** and **2** at 30 s, however, reveals that the metals in these complexes do noticeably oxidize, with Mn(II) and Fe(III) signals diminishing and intensifying, respectively. Our prior analysis of the reactions between H_2O_2 and **1** and **2** suggested that the quinols in the H_4qp4 ligand do not start to convert to *para*-quinones until most of the H_2O_2 has been depleted.[15-16]

UV/vis and MS analysis of the reactions between **3** and H_2O_2, conversely, demonstrate that one of the quinols oxidizes to a *para*-quinone early in the reaction (Figure 5.5, Figure D15). Additionally, we observe a *m/z* feature at 539.1396; the mass and charge are consistent with a Zn(II)-OOH complex with the mono-*para*-quinone form of the H_4qp4 ligand, H_2qp4. We do not observe any MS data consistent with a diquinone (qp4) species. Based on these results, we tentatively propose that the H_2O_2 dismutation for **3** proceeds through the cycle shown in Scheme 5.3. H_2O_2 reacts with $[Zn(H_3qp4)]^+$ to yield a M(II)-OOH species (**B**), with subsequent intramolecular oxidation of one of the quinols to a *para*-quinone (**C**). A second equiv. of H_2O_2 then coordinates the metal center as HOO^-, generating $[Zn^{II}(H_2qp4)(OOH)]^+$ (**D**), which we may be detecting by MS. The *para*-quinone can then oxidize this second equiv. of H_2O_2. Since **D** appears to accumulate, this may be the rate-limiting step in the catalase activity. A previous report found that acids could catalyze the reduction of *para*-quinone to quinol,[48] and the Zn(II) in **3** may do likewise in its capacity as a Lewis acid. The Zn(II) could either coordinate water and facilitate the delivery of protons to the *para*-quinone, or it could promote the reduction portion of the proton-coupled electron transfer (PCET) by coordinating the *para*-quinone.

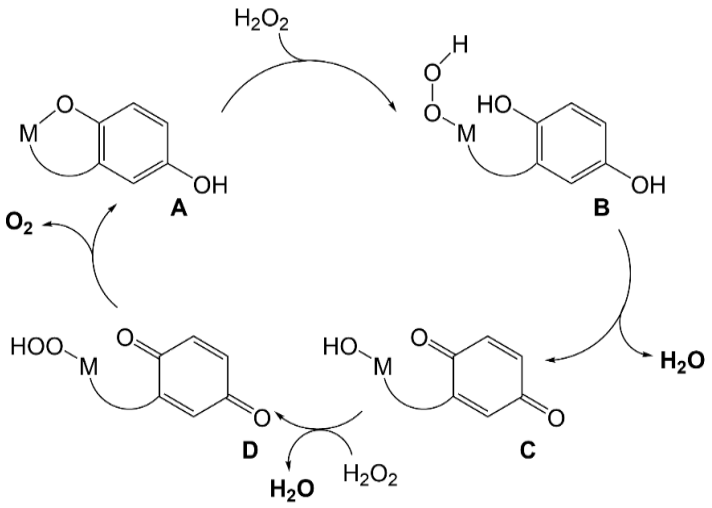

Scheme 5.3 Proposed mechanism for catalase activity that avoids metal-centered redox.

Redox-inactive metal ions, such as Al(III) and Ga(III), are capable of activating H_2O_2; in this chemistry, hydroxyl and hydroperoxyl radicals are released upon the coordination of multiple equiv. of the oxidant to the metal center.[49-51] Given the observed Michaelis-Menten kinetics and lack of a second-order dependence of the rate on [H_2O_2], we do not believe that the simultaneous coordination of two equiv. of H_2O_2 is required for catalase activity to proceed. Further, the inability of **3** to oxidize external substrates such as ABTS is inconsistent with the release of highly oxidizing hydroxyl and hydroperoxyl radicals.

Since extensive ligand oxidation is not observed in the early stages of catalase activity, we propose that **1** and **2** mostly catalyze H_2O_2 dismutation through a fundamentally different mechanism (Scheme 5.4). The initial step corresponding to the coordination of H_2O_2 to the divalent metal ion remains the same, but once **B** is generated, the O-O bond breaks heterolytically to yield a M(IV) species (**C'**). This species is stabilized by two factors: the presence of the anionic quinolate and the ability of the quinolate to donate an electron to the metal center to yield an isoelectronic M(III)-ligand radical. Species **C'** can either react with a second equiv. of H_2O_2, removing two net hydrogen atoms to yield O_2 and a M(II)-OH_2 species (**D'**), or it can further oxidize the ligand to a *para*-quinone species (**E**). Although **E** is shown as a hydroxyl complex in Scheme 5.4, the OH group is basic enough to abstract a proton from the buffered medium, yielding the aquated species observed in our prior report on **1**.[15] The Fe(II) in **2** eventually is oxidized to Fe(III),[16] and this may occur through a side reaction between Fe(II) species and 0.5 equiv. H_2O_2.

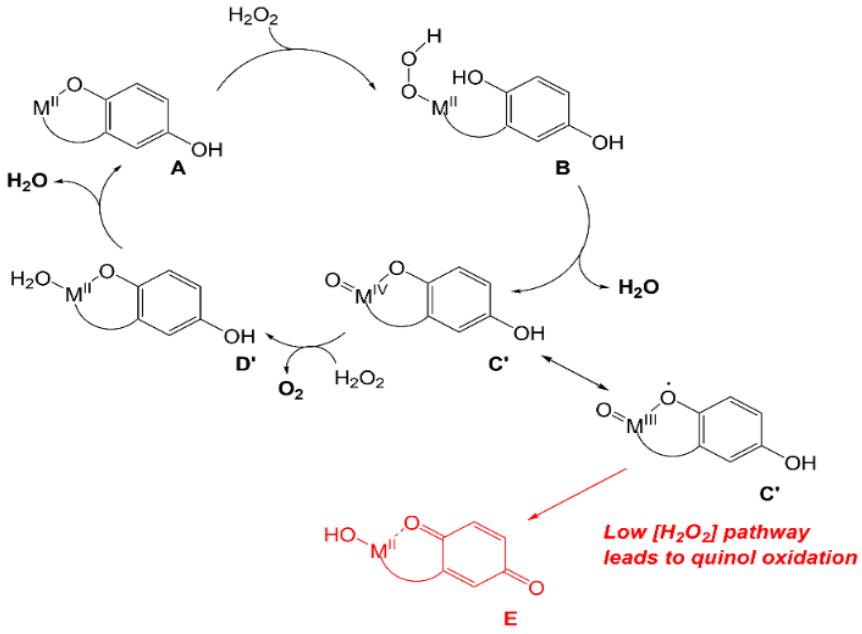

Scheme 5.4 Proposed mechanism for catalase activity with metal-centered redox.

5.5 Conclusions

We find that quinol-containing ligands can substantially enhance the ability of metal ions to catalyze the dismutation of H_2O_2. The described complexes with the macrocyclic ligand H_4qp4 are arguably the most active small molecule catalase mimics reported to date. Notably, the redox-inactive Zn(II) activates ligand-centered redox catalysis. Despite the similar rate constants for catalase activity, the Zn(II) complex appears to react with H_2O_2 through a fundamentally different mechanism than the complexes with manganese and iron; the complexes with the redox-active metals do not rely as heavily on ligand-centered redox processes. Although similar ligands have been used in highly efficient small molecule mimics of superoxide dismutases, the H_4qp4 ligand does not enable metals to rapidly dismutate superoxide. Only the manganese complex displays such activity, and even this compares poorly to those of manganese complexes with other polydentate quinol-containing ligands. As such, there appear to be subtle factors that direct antioxidant behavior towards specific reactive oxygen species.

Appendix D

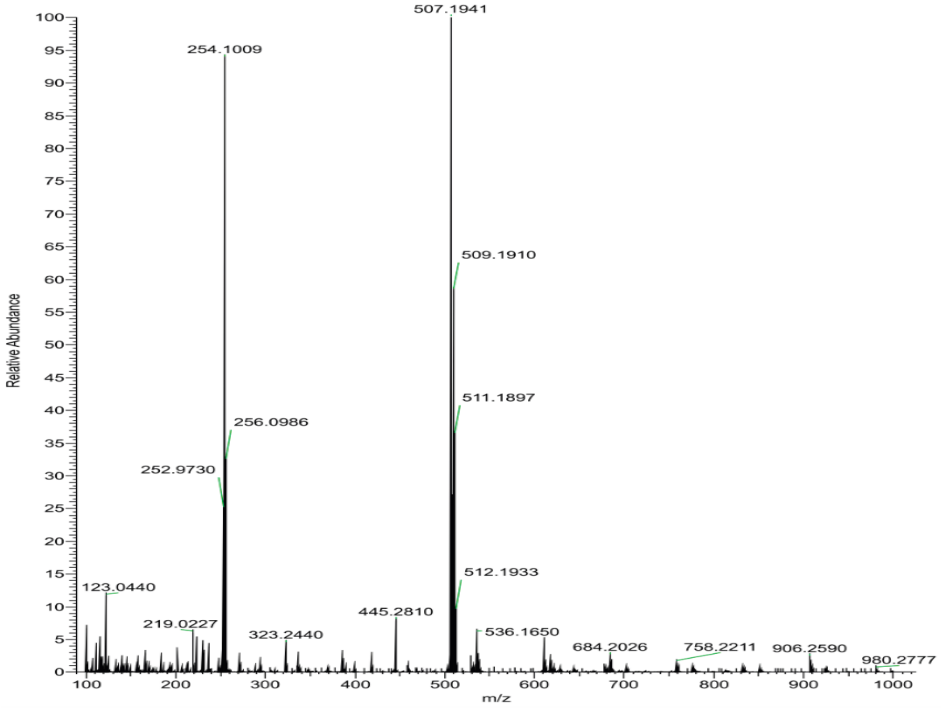

Figure D1. Mass spectrometry (ESI) of **3** in MeOH. The 507.1941 *m/z* feature is assigned to the Zn(II) complex with the singly deprotonated H_4qp4 ligand: $[Zn(H_3qp4)]^+$ (calculated *m/z* = 507.1944).

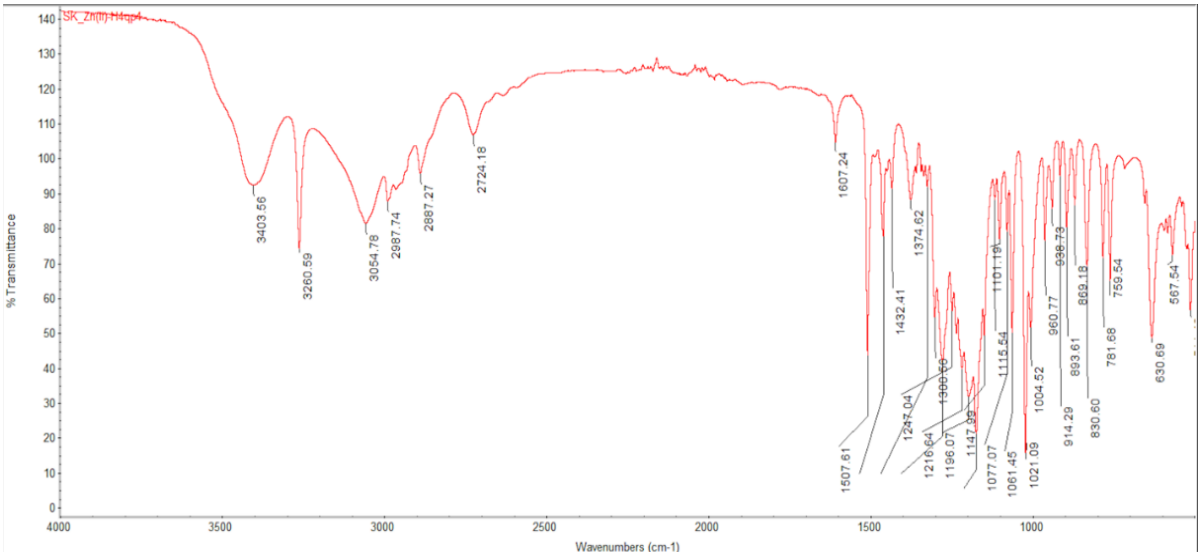

Figure D2. IR spectrum of **3**. The 3404 cm^{-1} feature is assigned to the O-H stretches associated with the quinol groups of the H_3qp4^- ligand.

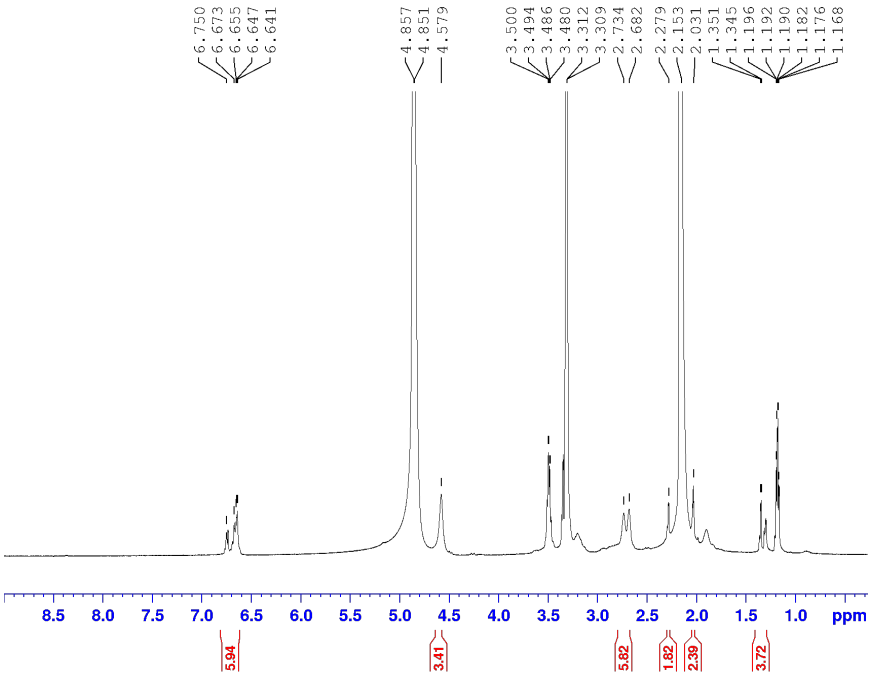

Figure D3. [1]H NMR spectrum of a crystalline sample of **3** dissolved in CD_3OD (500 MHz, 298 K). Solvent peaks from diethyl ether (1.16-1.19, 3.48-3.50), acetone (2.15), MeOH (3.31), and water (4.85) are present.

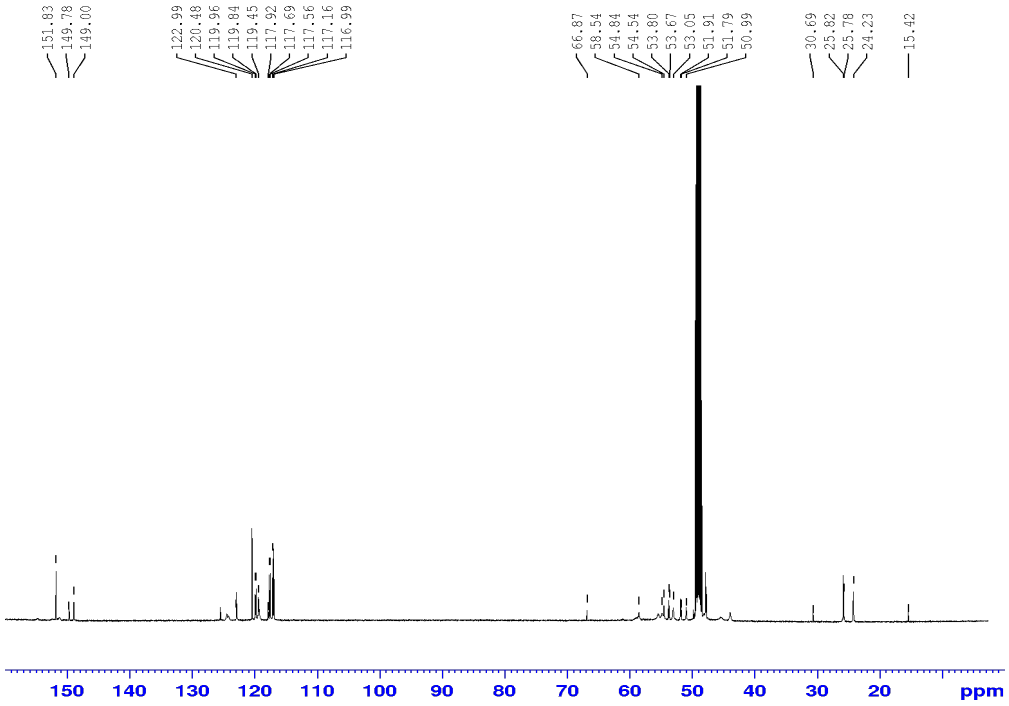

Figure D4. [13]C NMR spectrum of crystalline **3** in CD_3OD (125 MHz, 298 K). Solvent peaks from diethyl ether (15.42, 66.87 ppm), acetone (30.69) and MeOH (49) are present.

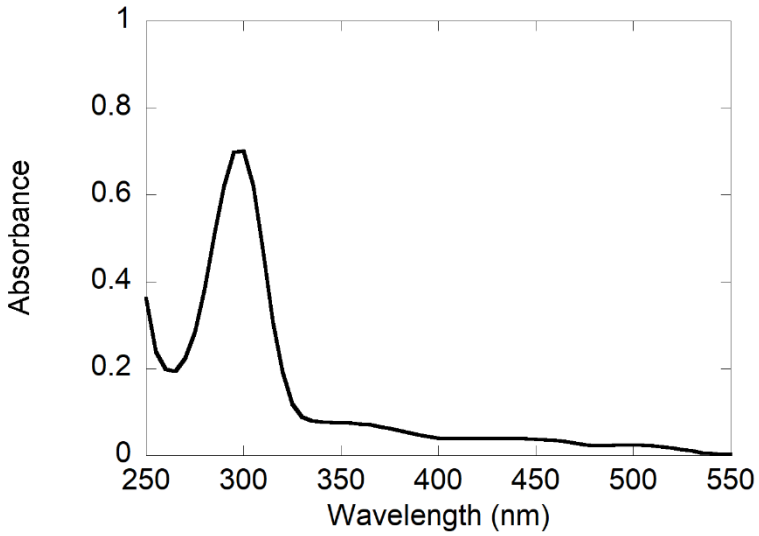

Figure D5. UV/vis data for a 0.10 mM solution of **3** in 294 K water. The major band at 299 nm (ε = 7000 M^{-1} cm^{-1}) is attributed to an intraligand transition associated with the quinol.

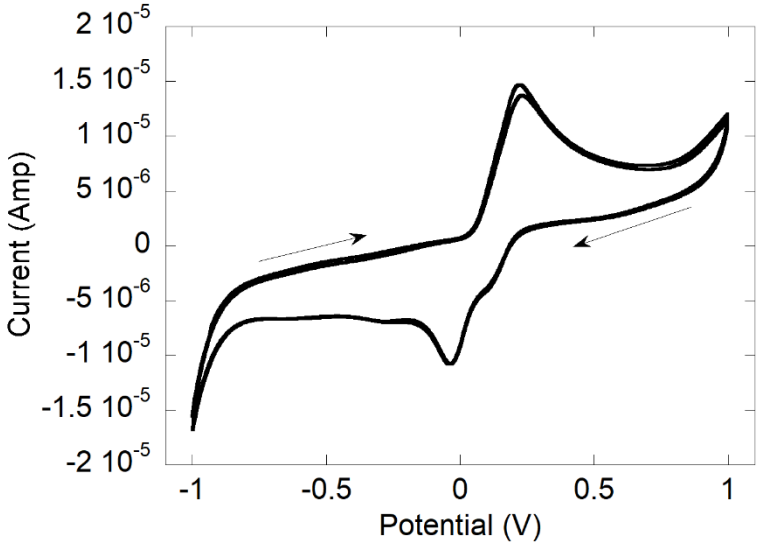

Figure D6. Cyclic voltammogram of 1.0 mM **3** in aqueous phosphate solution buffered to pH 7.2. An irreversible feature is observed with $E_{1/2}$ = 110 mV *vs.* Ag/AgCl (ΔE = 260 mV).

Table D1. Selected crystallographic data for $[Zn^{II}(H_3qp4)](OTf)$ (**3**)

Parameter	$[Zn^{II}(H_3qp4)](OTf)$
Formula	$C_{25}H_{35}F_3N_4O_7SZn$
MW	658.00
Crystal system	Monoclinic
Space group	P 1 21/c 1
a (Å)	9.4279(5)
b (Å)	14.3589(7)
c (Å)	21.7932(9)
α (°)	90
β (°)	100.919(2)
γ (°)	90
V (Å^3)	2896.8(2)
Z	4
Crystal color	Colorless
T (K)	306(2)
Reflns collected	74846
Unique reflns	5940
R1 (F, I > 2σ(I))[a]	0.0318
wR2 (F^2, all data)[a]	0.0915

[a] $R1 = \Sigma \left| \left| F_o \right| - \left| F_c \right| \right| / \Sigma \left| F_o \right|$; $wR2 = [\Sigma w(F_o^2 - F_c^2)^2 / \Sigma w(F_o^2)^2]^{1/2}$.

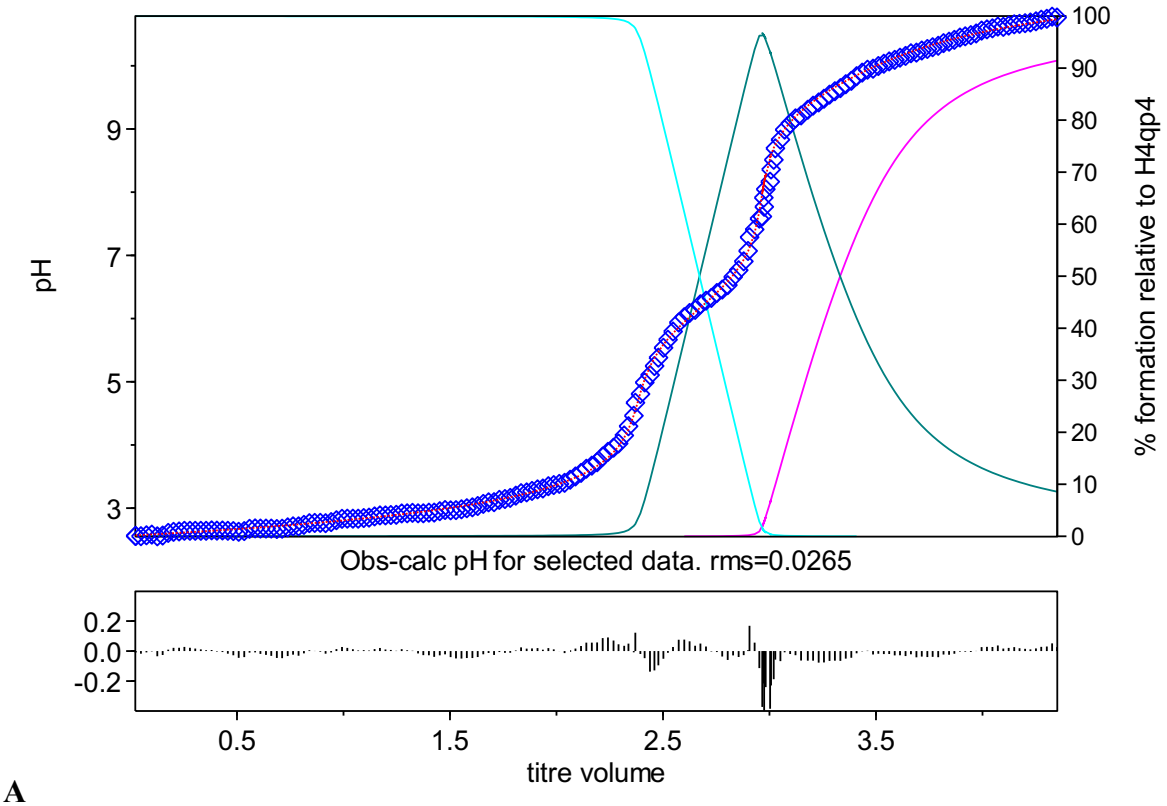

A

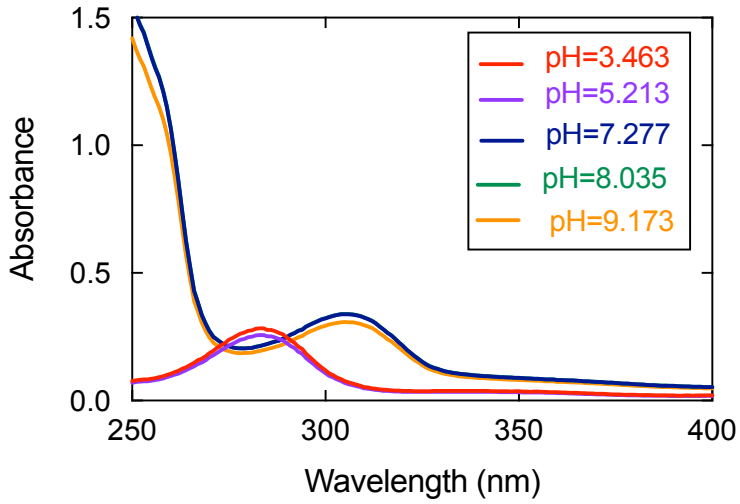

B

Figure D7. A) Hyperquad model (red line) overlaid on the experimental potentiometric pH titration data collected for **3** (blue). The curves represent the formation of various species including $[Zn^{II}(H_4qp4)]^{2+}$ (light blue), $[Zn^{II}(H_3qp4)]^{+}$ (green), and $[Zn^{II}(H_2qp4)]$ (pink). The deviations from the fit as a function of titre volume are provided below. B) Spectrophotometric pH titration of a 0.05 mM solution of **3** in water adjusted to various pH values between 3 and 10 through the addition of either KOH or HCl. All spectra were obtained at 298 K using a 1.0 cm pathlength cuvette. The data are consistent with a metal-bound quinol deprotonating to a quinolate between pH 5.2 and 7.3.

Table D2. Parameters for the Hyperquad model for the potentiometric pH titration data.

Species	Zn(II)	H_4qp4	H^+	log(β)	Derived Values
$[\mathbf{H_2}qp4]^{2-}$	0	1	-2	12.48[a]	
$[\mathbf{H_3}qp4]^{1-}$	0	1	-1	22.504[a]	pK_{L4} = 10.02 (±0.05)[a]
$\mathbf{H_4}qp4$	0	1	0	31.3[a]	pK_{L3} = 8.80 (±0.05)[a]
$[\mathbf{H_5}qp4]^{1+}$	0	1	1	39.005[a]	pK_{L2} = 7.70 (±0.05)[a]
$[\mathbf{H_6}qp4]^{2+}$	0	1	2	42.506[a]	pK_{L1} = 3.50 (±0.05)[a]
$[Zn(\mathbf{H_2}qp4)]$	1	1	-2	53.891[b]	log K_{ML} ($Zn(H_2qp4)$) = 41.411[c]
$[Zn(\mathbf{H_3}qp4)]^{1+}$	1	1	-1	63.601[b]	$pK_a(Zn(H_3qp4)^+)$ = 9.71[b] log K_{ML} $(Zn(H_3qp4))^+$= 41.097[c]
$[Zn(\mathbf{H_4}qp4)]^{2+}$	1	1	0	69.764[b]	$pK_a(Zn(H_4qp4)^{2+})$ = 6.163[b] log K_{ML} $(Zn(H_4qp4))^{2+}$= 38.464[c]
pZn (pH 7.4) = 37.01[d]					

[a]Ligand log(β) and derived pK_a values from reference 15:

$K_{L1} = [H_5qp4^+][H^+]/[H_6qp4^{2+}]$, $pK_{L1} = \log\beta_{012} - \log\beta_{011}$

$K_{L2} = [H_4qp4][H^+]/[H_5qp4^+]$, $pK_{L2} = \log\beta_{011} - \log\beta_{010}$

$K_{L3} = [H_3qp4^-][H^+]/[H_4qp4]$, $pK_{L3} = \log\beta_{010} - \log\beta_{01(-1)}$

$K_{L4} = [H_2qp4^{2-}][H^+]/[H_3qp4^-]$, $pK_{L4} = \log\beta_{01(-1)} - \log\beta_{01(-2)}$

[b]Metal complex pK_a values:

$K_a(Zn(H_4qp4)^{2+}) = [Zn(H_3qp4)^+][H^+]/[Zn(H_4qp4)^{2+}]$ ~ *deprotonation of first quinol*

$pK_a(Zn(H_4qp4)^{2+}) = \log\beta_{110} - \log\beta_{11(-1)}$

$K_a(Zn(H_3qp4)^+) = [Zn(H_2qp4)][H^+]/[Zn(H_3qp4)^+]$ ~ *deprotonation of second quinol*

$pK_a(Zn(H_3qp4)^+) = \log\beta_{11(-1)} - \log\beta_{11(-2)}$

[c]Metal complex K_{ML} values:

K_{ML} $(Zn(H_2qp4)) = [Zn(H_2qp4)]/([Zn(II)][H_2qp4^{2-}])$

log K_{ML} $(Zn(H_2qp4)) = \log\beta_{11(-2)} - \log\beta_{01(-2)}$

K_{ML} $(Zn(H_3qp4))^+ = [Zn(H_3qp4)^+]/([Zn(II)][H_3qp4^-])$

log K_{ML} $(Zn(H_3qp4))^+ = \log\beta_{11(-1)} - \log\beta_{01(-1)}$

K_{ML} $(Zn(H_4qp4))^{2+} = [Zn(H_4qp4)^{2+}]/([Zn(II)][H_4qp4])$

log K_{ML} $(Zn(H_4qp4))^{2+} = \log\beta_{110} - \log\beta_{010}$

[d]pZn(pH 7.4) = -log([free Zn(II)]) at pH 7.4 and 298 K with 1.00 mM Zn(II) and 1.00 mM H_4qp4

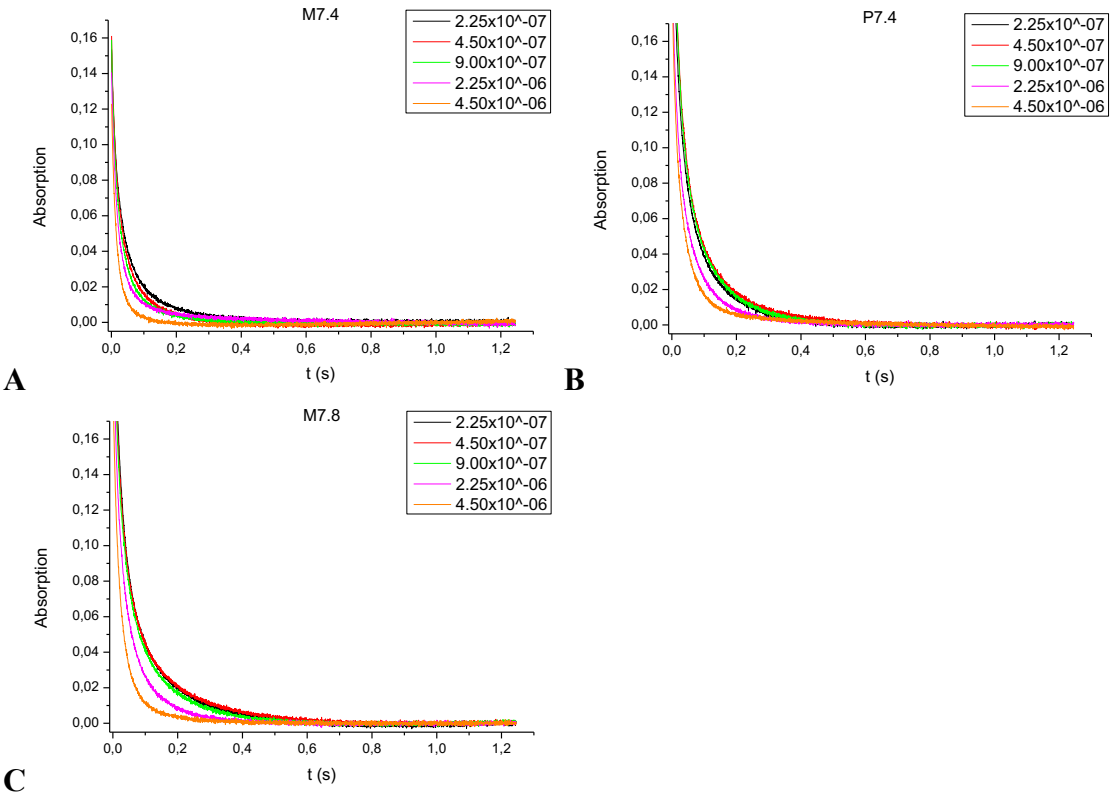

Figure D8. Kinetic traces of superoxide decomposition at 250 nm by **1** in three different aqueous solutions. First-order decay is observed in all instances. The legends provide the k_{obs} measured for each trace. A) 60 mM MOPS buffer, pH 7.4, ionic strength of 111 mM. $k_{cat} = 5.96 \times 10^6$ M^{-1} s^{-1}. B) 50 mM phosphate buffer, pH 7.4, ionic strength of 111 mM. $k_{cat} = 2.94 \times 10^6$ M^{-1} s^{-1}. C) 60 mM MOPS buffer, pH 7.8, ionic strength of 111 mM. $k_{cat} = 4.54 \times 10^6$ M^{-1} s^{-1}.

Table D3. Parameters for the Michaelis-Menten models that were fitted to the oxygraphy data displayed in Figure 5.3.

Parameters	**1**	**2**	**3**
k_{cat}	2896 (±108)	3717 (±88)	2590 (±120)
k_{on}	352.3 (±52.7)	195.3 (±15.4)	130.4 (±20.1)
k_{cat} (95% Confidence Interval)	2677 - 3114	3540 - 3983	2348 - 2833
k_{on} (95% Confidence Interval)	246.0 – 458.5	164.3 – 226.4	90.0 – 170.9
Goodness of Fit			
Degrees of Freedom	43	43	43
R^2	0.8737	0.9650	0.8788
Sum of Squares	6592970	2760470	5073854
Sy.x [a]	391.6	253.4	343.5

[a]Sy.x is defined as the standard deviation of the residuals associated with the model.

$$Sy.x = \sqrt{\frac{\sum(residual^2)}{n-K}}$$

In this equation, n – K = the Degrees of Freedom, and $\Sigma(\text{residual}^2)$ = Sum of Squares.

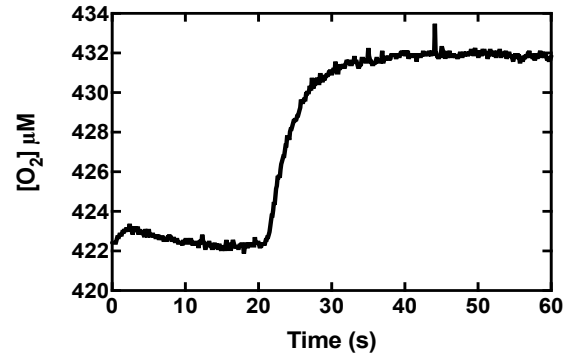

A

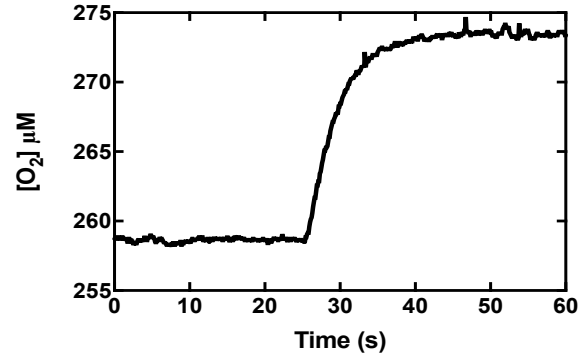

B

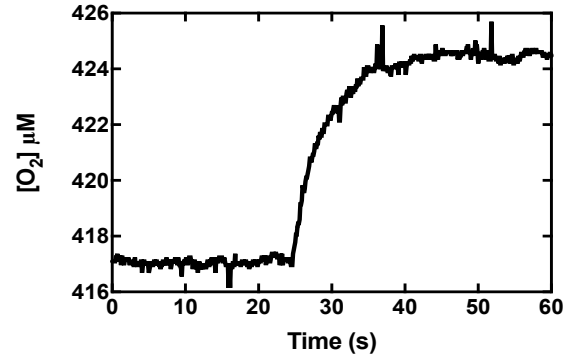

C

Figure D9. Kinetic traces of oxygen production upon reaction between 0.1 µM of each H_4qp4 catalyst and 10.0 mM H_2O_2 in 50 mM Tris buffered to pH 7.2 and 0.1 M EDTA to scavenge adventitious metal ions. A) Data for 1. TON = 100. B) Data for 2. TON = 150. C) Data for 3. TON = 70.

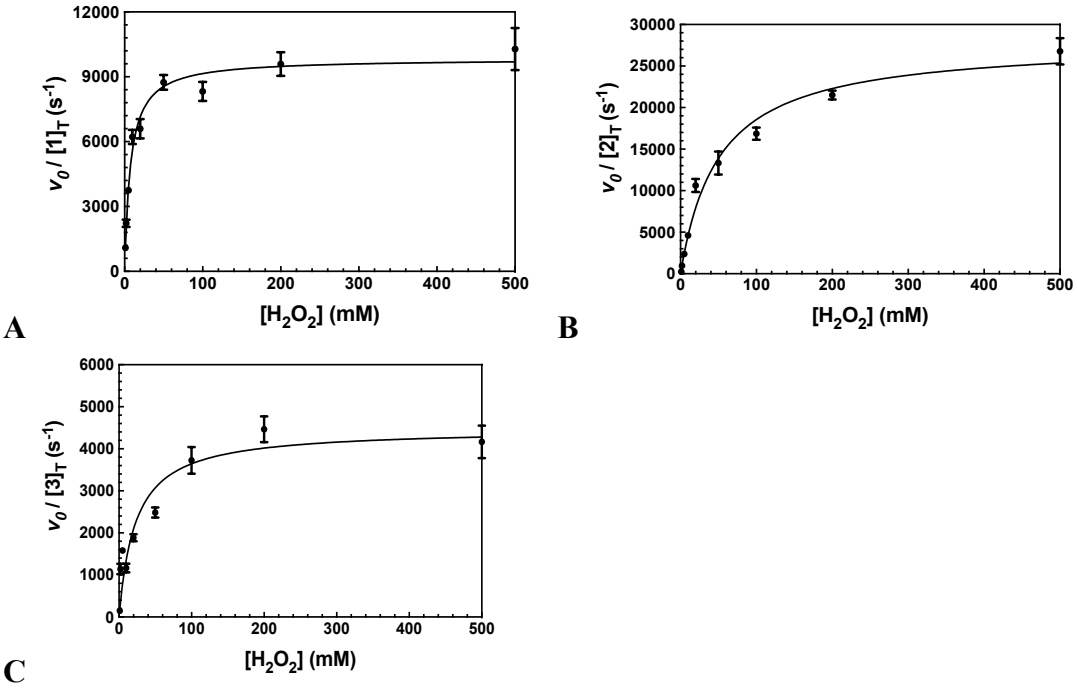

Figure D10. Plots of v_o/[**M**] *vs.* the concentration of H_2O_2, where [**M**] is the concentration of the tested H_4qp4 complex. The v_o corresponds to the decomposition of H_2O_2, which was measured through UV/vis. All reactions were performed in 25 °C 200 mM phosphate buffered to pH 7.0. 100 nM of each coordination complex was present as a catalyst. Five data points were taken for each shown data point. A) Data for **1**. $k_{cat} = 9.8 \times 10^3$ s^{-1}, $k_{on} = 1.3 \times 10^6$ M^{-1} s^{-1}. B) Data for **2**. $k_{cat} = 2.8 \times 10^4$ s^{-1}, $k_{on} = 5.5 \times 10^5$ M^{-1} s^{-1}. C) Data for **3**. $k_{cat} = 4.5 \times 10^3$ s^{-1}, $k_{on} = 2.0 \times 10^5$ M^{-1} s^{-1}.

Table D4. Parameters for the Michaelis-Menten models that were fitted to the UV/vis data displayed in **Figure D10**.

Parameters	**1**	**2**	**3**
k_{cat}	9838 (±285)	27909 (±1060)	4474 (±232)
k_{on}	1306 (±154)	553 (±53)	196 (±33)
k_{cat} (95% Confidence Interval)	9264 - 10412	25773 - 30044	4005 - 4943
k_{on} (95% Confidence Interval)	996 - 1615	447 – 660	130 - 262
Goodness of Fit			
Degrees of Freedom	43	43	43
R^2	0.9005	0.9508	0.8252
Sum of Squares	47117198	185718722	17267586
Sy.x [a]	1047	2078	634

[a]Sy.x is defined as the standard deviation of the residuals associated with the model.

$$Sy.x = \sqrt{\frac{\sum(residual^2)}{n-K}}$$

In this equation, n – K = the Degrees of Freedom, and $\Sigma(residual^2)$ = Sum of Squares.

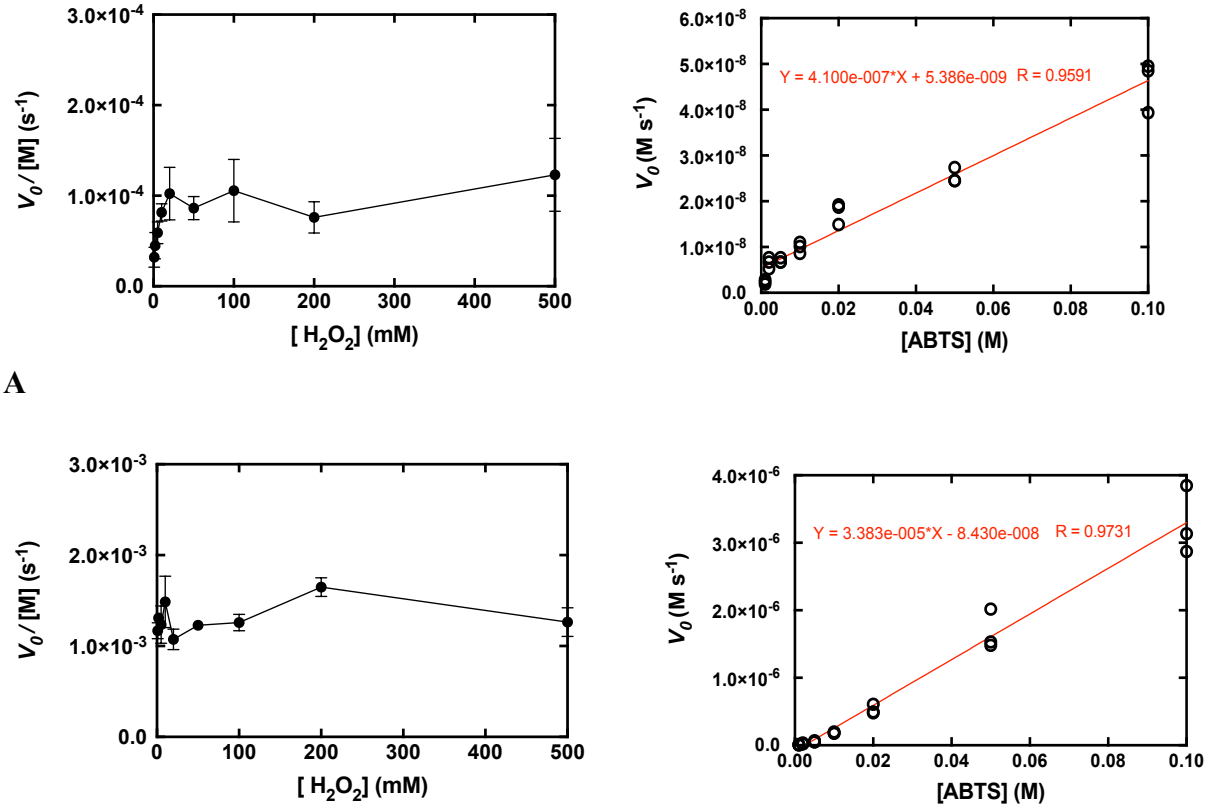

Figure D11. Plots of v_o/[**M**] *vs*. the concentration of H_2O_2, where [**M**] is the concentration of the tested complex of A) **1**, B) **2**. The v_o corresponds to the formation of $ABTS^{\cdot+}$, which was measured through UV/vis. All reactions were run in RT 50 mM acetate solution buffered to pH 5.0, with reaction concentrations of 10 mM ABTS, 0.1 mM of the tested compound, and 1-500 mM H_2O_2. Three data points were taken for each concentration of H_2O_2.
Determination of k_3 from plots of the initial rates (v_o) vs. concentration of ABTS for A) **1**, B) **2**. All reactions were run in RT 50 mM acetate solution buffered to pH 5.0, with reaction concentrations of 10 mM H_2O_2, 0.1 mM of the tested compound, and 1-100 mM ABTS.

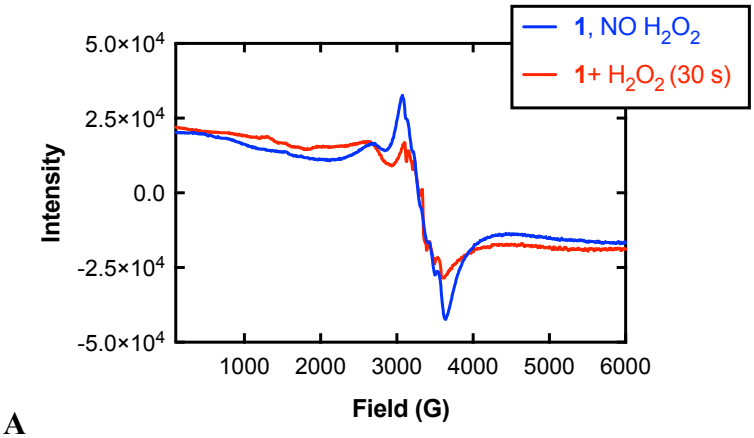

A

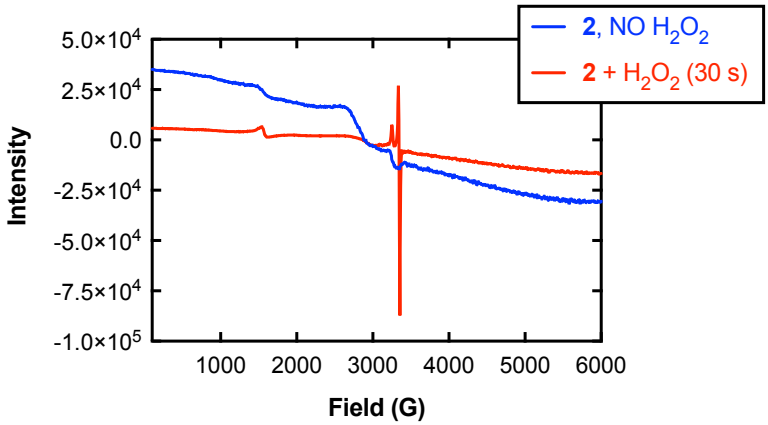

B

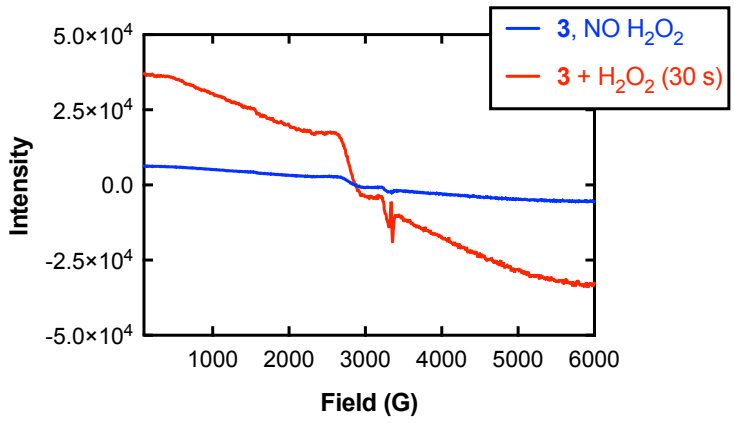

C

Figure D12. X-band EPR spectra of 1.0 mM solutions of **1**, **2**, and **3** in MeCN in the absence and presence of 10 mM H_2O_2. The reactions between each metal complex and H_2O_2 proceeded for 30 s before the samples were frozen and analyzed at 77 K.

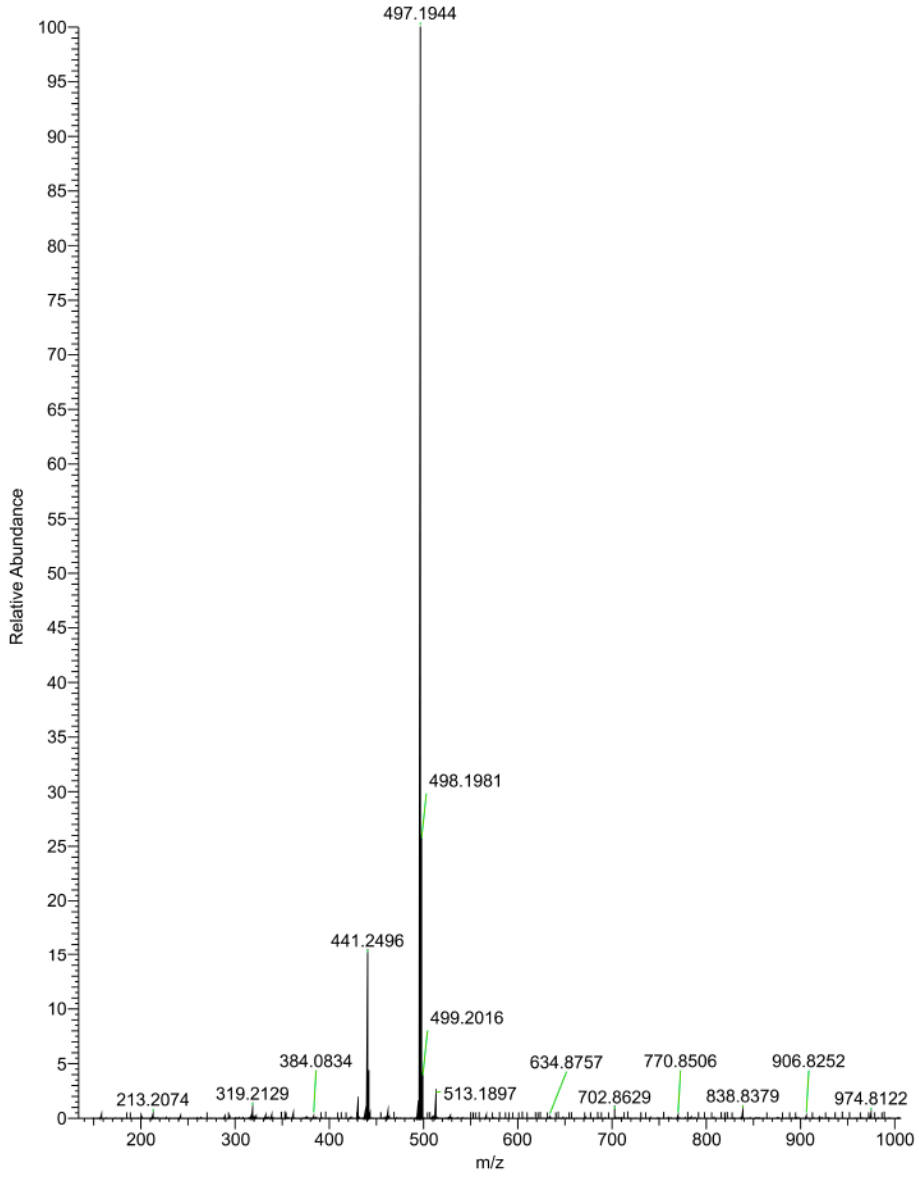

Figure D13. Mass spectrometry (ESI) of the reaction between 10 mM H_2O_2 and **1** in MeCN at RT. The sample was analyzed 30 s after the beginning of the reaction. The 497.1944 *m/z* feature is assigned to the Mn(III) complex with the doubly protonated H_4qp4 ligand, H_2qp4^{2-}: $[Mn(H_2qp4)]^+$ (calculated *m/z* = 497.1955).

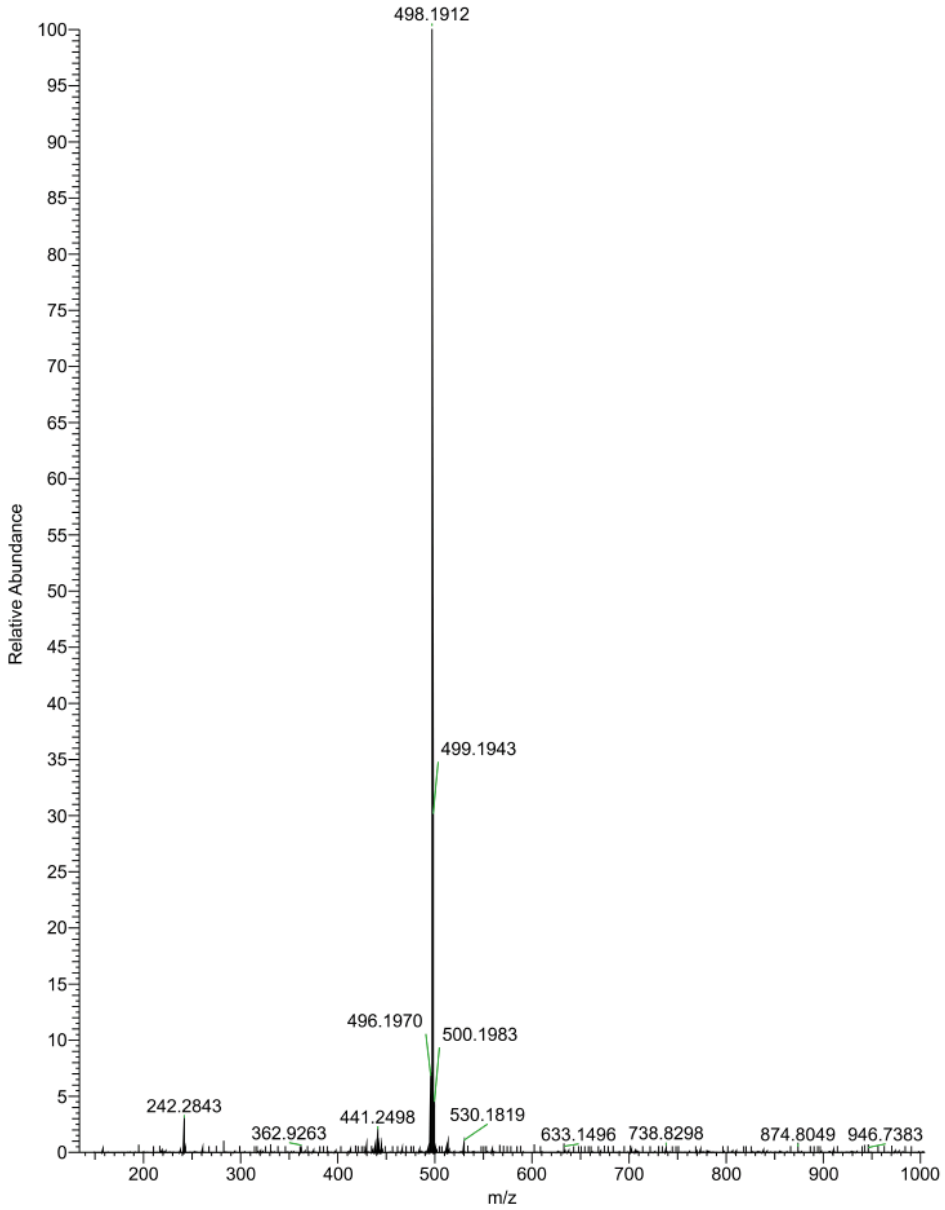

Figure D14. Mass spectrometry (ESI) of the reaction between 10 mM H_2O_2 and **2** in MeCN at RT. The sample was analyzed 30 s after the beginning of the reaction. The 498.1912 *m/z* feature is assigned to the Fe(III) complex with the doubly protonated form of the H_4qp4 ligand, H_2qp4^{2-}: [Fe(H_2qp4)]$^+$ (calculated *m/z* = 498.1929).

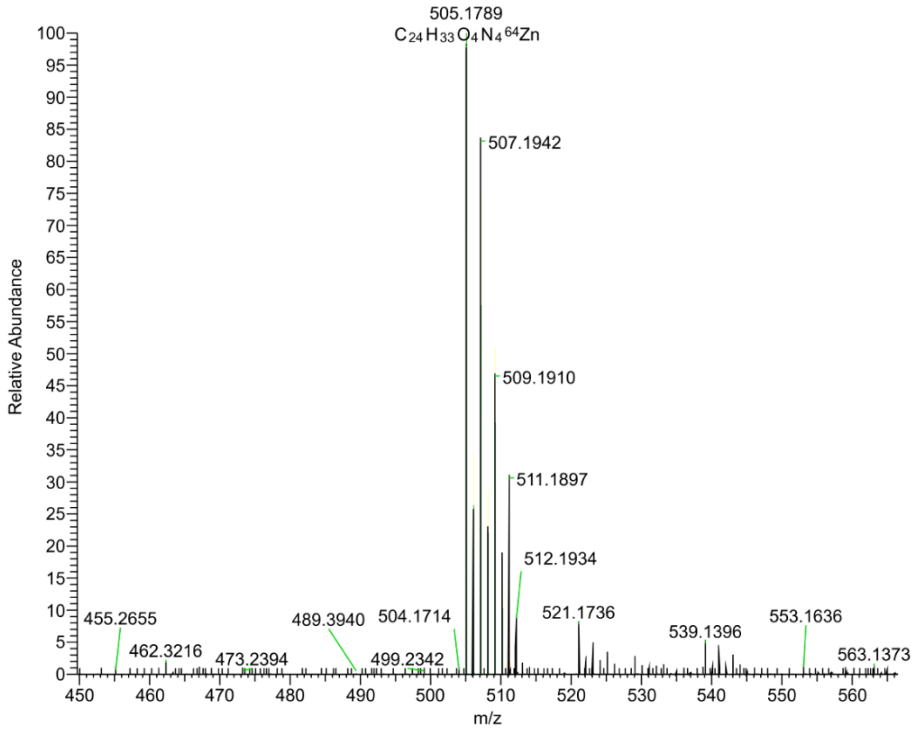

Figure D15. Mass spectrometry (ESI) of the reaction between 10 mM H_2O_2 and **3** in MeCN at RT. The sample was analyzed 30 s after the beginning of the reaction. The 505.1789 *m/z* feature is assigned to the Zn(II) complex with the singly deprotonated form of the monoquinolate/mono-*para*-quinone H_2qp4 ligand: $[Zn(Hqp4)]^+$ (calculated *m/z* = 505.1794). The 507.1942 *m/z* feature is assigned to the Zn(II) with the singly deprotonated form of the diquinol H_4qp4 ligand: $[Zn(H_3qp4)]^+$ (calculated *m/z* = 507.1951).

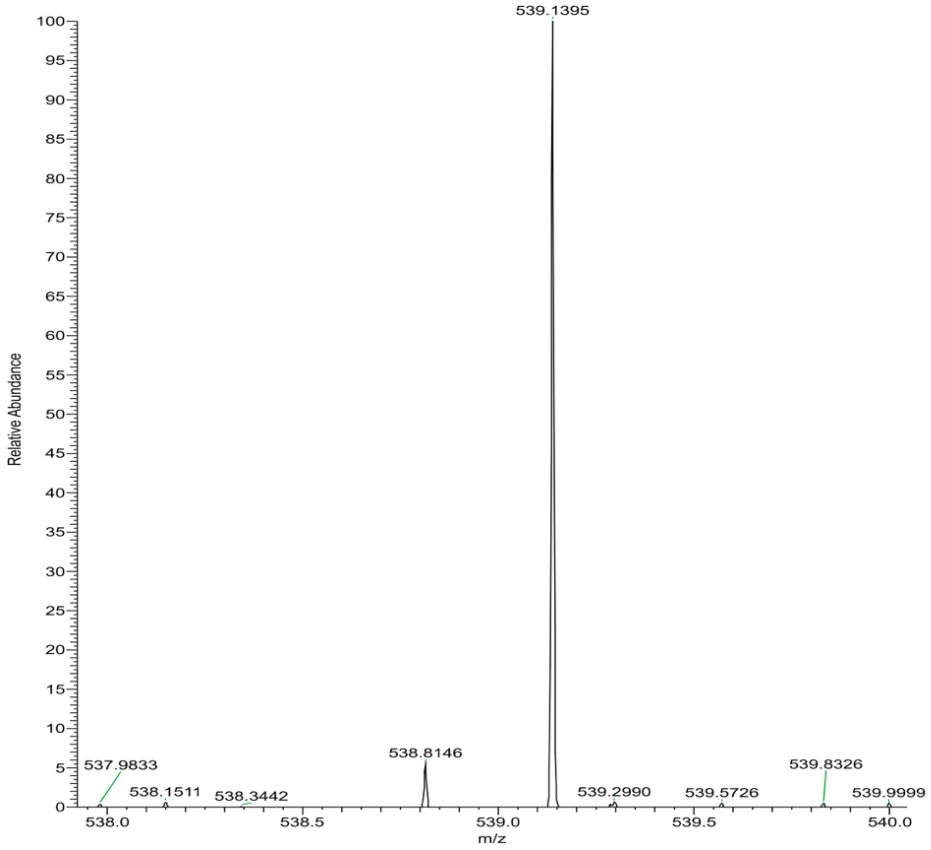

Figure D16. Expansion of the data in **Figure D15**, showing the new feature with *m/z* = 539.1395, which is consistent with the addition of two O atoms to $[Zn(H_3qp4)]^+$. The *m/z* may be consistent with $[Zn(H_2qp4)(OOH)]^+$, where H_2qp4 is the monoquinol/mono-*para*-quinone form of the ligand (calculated *m/z* = 539.1848).

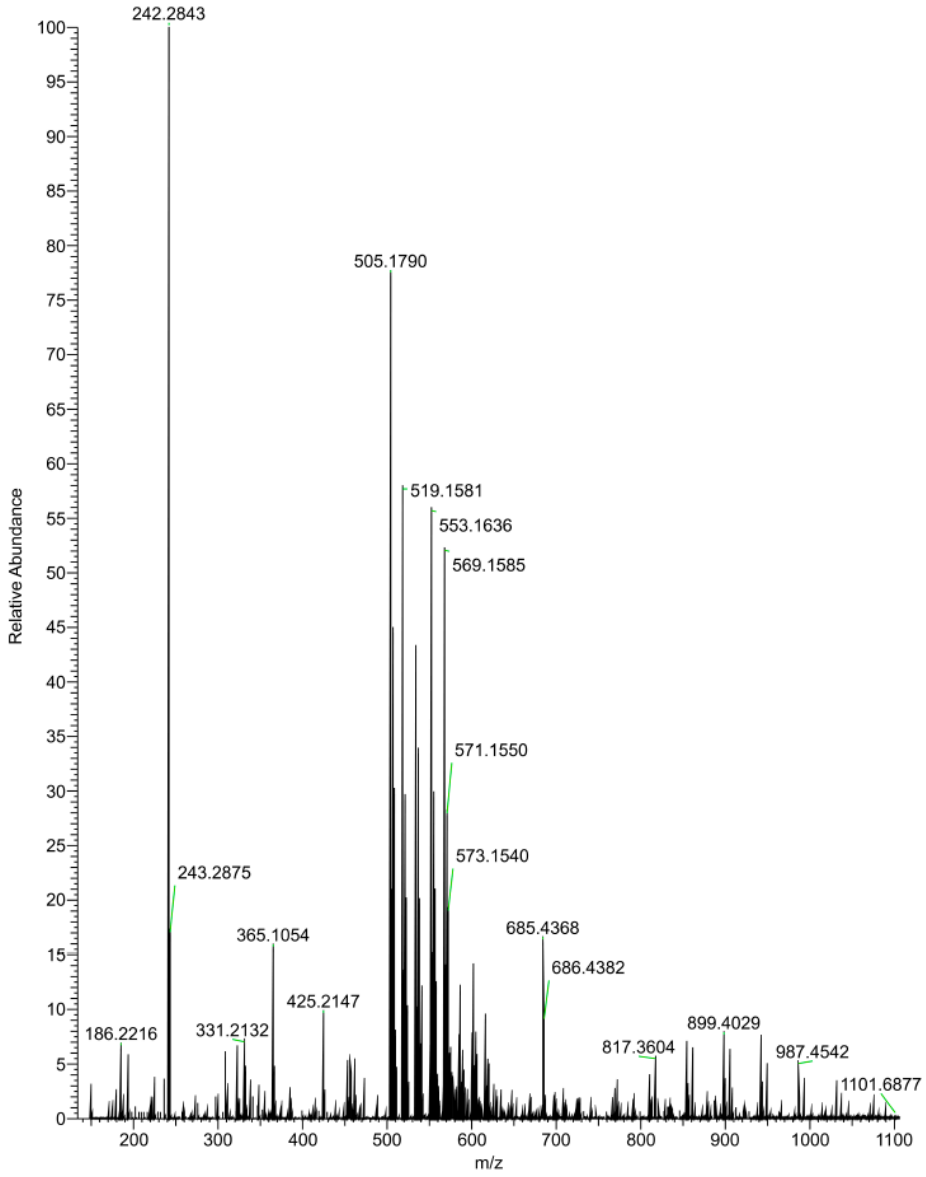

Figure D17. Mass spectrometry (ESI) of the reaction between 10 mM H_2O_2 and **3** in MeCN at RT. The data were acquired 60 s after the beginning of the reaction. Oxygenated products become more prominent.

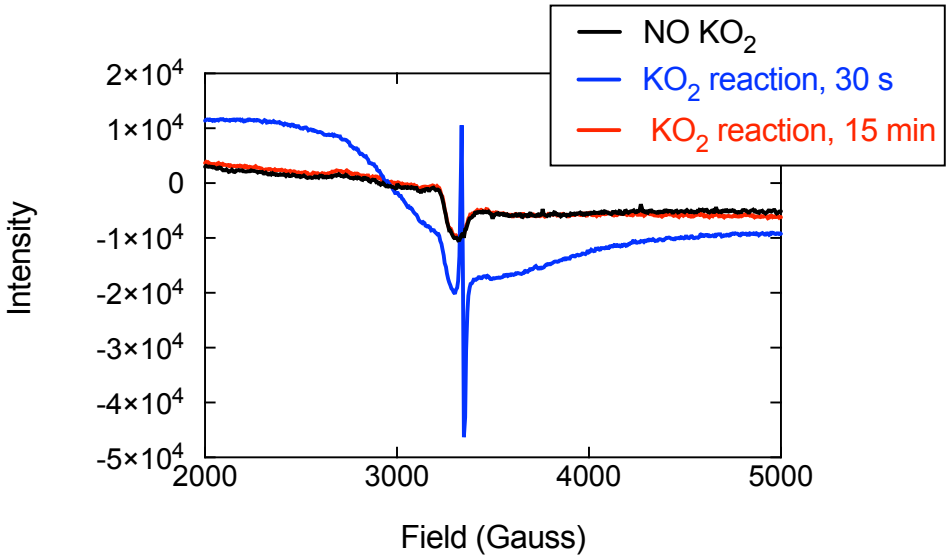

Figure D18. X-band EPR data for the reaction between 1 mM **3** and 20 equiv. KO_2 in 50 mM HEPES buffered to pH 7.0. The data were acquired at 77 K.

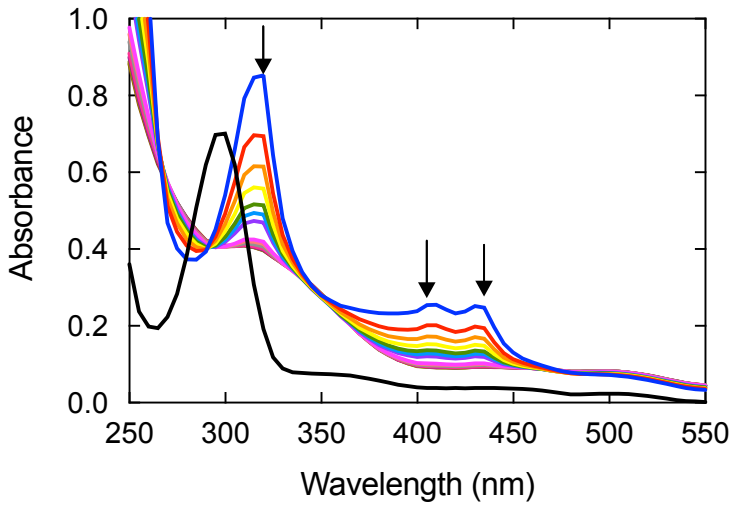

Figure D19. UV/vis data for the reaction between 0.1 mM **3** and 20 equiv. KO_2 in water. The black spectrum shows 3 prior to the addition of KO_2. The blue spectrum was obtained 20 s after KO_2 addition, with subsequent spectra taken every 15 s.

References

1. Lushchak, V. I. *Chem. Biol. Interact* **2014,** 224, 164-175.

2. Batinic-Haberle, I.; Spasojevic, I. *J. Porphyr. Phthalocya.* **2019,** *23* (11n12), 1326-1335.

3. Mosley, R. L.; Benner, E. J.; Kadiu, I.; Thomas, M.; Boska, M. D.; Hasan, K.; Laurie, C.; Gendelman, H. E. *Clin. Neurosci. Res.* **2006,** 6, 261-281.

4. Fearon, I. M.; Faux, S. P. *J. Mol. Cell. Cardiol.* **2009,** 47, 372-381.

5. Roberts, C. K.; Sindhu, K. K. *Life Sci.* **2009,** 84, 705-712.

6. Yu, M.; Ward, M. B.; Franke, A.; Ambrose, S. L.; Whaley, Z. L.; Bradford, T. M.; Gorden, J. D.; Beyers, R. J.; Cattley, R. C.; Ivanović-Burmazović, I.; Schwartz, D. D.; Goldsmith, C. R. *Inorg. Chem.* **2017,** 56, 2812-2826.

7. Yu, M.; Ambrose, S. L.; Whaley, Z. L.; Fan, S.; Gorden, J. D.; Beyers, R. J.; Schwartz, D. D.; Goldsmith, C. R. *J. Am. Chem. Soc.* **2014,** 136, 12836-12839.

8. Senft, L.; Moore, J. L.; Franke, A.; Fisher, K. R.; Scheitler, A.; Zahl, A.; Puchta, R.; Fehn, D.; Ison, S.; Sader, S.; Ivanović-Burmazović, I.; Goldsmith, C. R. *Chem. Sci.* **2021,** 12, 10483-10500.

9. Ward, M. B.; Scheitler, A.; Yu, M.; Senft, L.; Zillmann, A. S.; Gorden, J. D.; Schwartz, D. D.; Ivanović-Burmazović, I.; Goldsmith, C. R. *Nat. Chem.* **2018,** 10, 1207-1212.

10. Moore, J. L.; Oppelt, J.; Senft, L.; Franke, A.; Scheitler, A.; Dukes, M. W.; Alix, H. B.; Saunders, A. C.; Karbalaei, S.; Schwartz, D. D.; Ivanović-Burmazović, I.; Goldsmith, C. R. *Inorg. Chem.* **2022,** 61, 19983-19997.

11. Tovmasyan, A.; Carballal, S.; Ghazaryan, R.; Melikyan, L.; Weitner, T.; Maia, C. G. C.; Reboucas, J. S.; Radi, R.; Spasojevic, I.; Benov, L.; Batinic-Haberle, I. *Inorg. Chem.* **2014,** 53, 11467-11483.

12. Batinic-Haberle, I.; Reboucas, J. S.; Spasojevic, I. *Antioxid. Redox Signal.* **2010,** *13*, 877-918.

13. Aston, K.; Rath, N.; Naik, A.; Slomczynska, U.; Schall, O. F.; Riley, D. P. *Inorg. Chem.* **2001,** 40, 1779-1789.

14. Salvemini, D.; Wang, Z.-Q.; Zweier, J. L.; Samouilov, A.; Macarthur, H.; Misko, T. P.; Currie, M. G.; Cuzzocrea, S.; Sikorski, J. A.; Riley, D. P. *Science* **1999,** 286, 304-306.

15. Karbalaei, S.; Knecht, E.; Franke, A.; Zahl, A.; Saunders, A. C.; Pokkuluri, P. R.; Beyers, R. J.; Ivanović-Burmazović, I.; Goldsmith, C. R. *Inorg. Chem.* **2021,** 60, 8368-8379.

16. Karbalaei, S.; Franke, A.; Jordan, A.; Rose, C.; Pokkuluri, P. R.; Beyers, R. J.; Zahl, A.; Ivanović-Burmazović, I.; Goldsmith, C. R. *Chem. Eur. J.* **2022,** 28, e202201179.

17. Vincent, A.; Thauvin, M.; Quévrain, E.; Mathieu, E.; Layani, S.; Seksik, P.; Batinic-Haberle, I.; Vriz, S.; Policar, C.; Delsuc, N. *J. Inorg. Biochem.* **2021,** 219, 111431.

18. Ledesma, G. N.; Eury, H.; Anxolabéhère-Mallart, E.; Hureau, C.; Signorella, S. R. *J. Inorg. Biochem.* **2015,** 146, 69-76.

19. Signorella, S.; Rompel, A.; Buldt-Karentzopoulos, K.; Krebs, B.; Pecoraro, V. L.; Tuchagues, J.-P. *Inorg. Chem.* **2007,** 46, 10864-10868.

20. Delroisse, M.; Rabion, A.; Chardac, F.; Tétard, D.; Verlhac, J.-B.; Fraisse, L.; Séris, J.-L. *J. Chem. Soc., Chem. Commun.* **1995**, 949-950.

21. Gelasco, A.; Bensiek, S.; Pecoraro, V. L. *Inorg. Chem.* **1998,** 37, 3301-3309.

22. Tovmasyan, A.; Maia, C. G. C.; Weitner, T.; Carballal, S.; Sampaio, R. S.; Lieb, D.; Ghazaryan, R.; Ivanovic-Burmazovic, I.; Ferrer-Sueta, G.; Radi, R.; Reboucas, J. S.; Spasojevic, I.; Benov, L.; Batinic-Haberle, I. *Free Rad. Biol. Med.* **2015,** 86, 308-321.

23. Wu, A. J.; Penner-Hahn, J. E.; Pecoraro, V. L. *Chem. Rev.* **2004,** 104, 903-938.

24. Larson, E. J.; Pecoraro, V. L. *J. Am. Chem. Soc.* **1991,** 113, 3810-3818.

25. Triller, M. U.; Hsieh, W.-Y.; Pecoraro, V. L.; Rompel, A.; Krebs, B. *Inorg. Chem.* **2002,** 41, 5544-5554.

26. Haber, A.; Gross, Z. *Chem. Commun.* **2015,** 51, 5812-5827.

27. Mahammed, A.; Gross, Z. *Chem. Commun.* **2010,** 46, 7040-7042.

28. McCord, J. M.; Fridovich, I. *J. Biol. Chem.* **1969,** 244, 6049-6055.

29. Iranzo, O. *Bioorg. Chem.* **2011,** 39, 73-87.

30. Nelson, D. P.; Kiesow, L. A. *Anal. Biochem.* **1972,** 49, 474-8.

31. Ndontsa, E. N.; Moore, R. L.; Goodwin, D. C. *Arch. Biochem. Biophys.* **2012,** 525, 215-222.

32. Scott, S. L.; Chen, W. J.; Bakac, A.; Espenson, J. H. *J. Phys. Chem.* **1993,** 97, 6710-6714.

33. Addison, A. W.; Rao, T. N.; Reedijk, J.; van Rijn, J.; Verschoor, G. C. *J. Chem. Soc., Dalton Trans.* **1984,** (7), 1349-1356.

34. Riley, D. P. *Chem. Rev.* **1999,** 99, 2573-2588.

35. Friedel, F. C.; Lieb, D.; Ivanović-Burmazović, I. *J. Inorg. Biochem.* **2012,** 109, 26-32.

36. Fridovich, I. *J. Biol. Chem.* **1997,** 272, 18515-18517.

37. Liochev, S. I. *Chem. Res. Toxicol.* **2013,** 26, 1312-1319.

38. Riley, D. P.; Rivers, W. J.; Weiss, R. H. *Anal. Biochem.* **1991,** 196, 344-349.

39. Liochev, S. I.; Fridovich, I. *Arch. Biochem. Biophys.* **1997,** 337, 115-120.

40. Kenkel, I.; Franke, A.; Dürr, M.; Zahl, A.; Dücker-Benfer, C.; Langer, J.; Filipović, M. R.; Yu, M.; Puchta, R.; Fiedler, S. R.; Shores, M. P.; Goldsmith, C. R.; Ivanović-Burmazović, I. *J. Am. Chem. Soc.* **2017,** 139, 1472-1484.

41. Lieb, D.; Friedel, F. C.; Yawer, M.; Zahl, A.; Khusniyarov, M. M.; Heinemann, F. W.; Ivanović-Burmazović, I. *Inorg. Chem.* **2013,** 52, 222-236.

42. Ivanović-Burmazović, I. *Adv. Inorg. Chem.* **2008,** 60, 59-100.

43. Weekley, C. M.; Kenkel, I.; Lippert, R.; Wei, S.; Lieb, D.; Cranwell, T.; Wedding, J. L.; Zillmann, A. S.; Rohr, R.; Filipovic, M. R.; Ivanović-Burmazović, I.; Harris, H. H., *Inorg. Chem.* **2017,** 56, 6076-6093.

44. Riley, D. P.; Weiss, R. H. *J. Am. Chem. Soc.* **1994,** 116, 387-388.

45. Riley, D. P.; Schall, O. F. *Adv. Inorg. Chem.* **2006,** 59, 233-263.

46. Riley, D. P.; Henke, S. L.; Lennon, P. J.; Weiss, R. H.; Neumann, W. L.; Rivers, W. J.; Aston, K. W.; Sample, K. R.; Rahman, H.; Ling, C.-S.; Shieh, J.-J.; Busch, D. H. *Inorg. Chem.* **1996,** 35, 5213-5231.

47. Riley, D. P.; Lennon, P. J.; Neumann, W. L.; Weiss, R. H. *J. Am. Chem. Soc.* **1997,** 119, 6522-6528.

48. Minisci, F.; Citterio, A.; Vismara, E.; Fontana, F.; De Bernardinis, S.; Correale, M. *J. Org. Chem.* **1989,** 54, 728-731.

49. Novikov, A. S.; Kuznetsov, M. L.; Pombeiro, A. J. L.; Bokach, N. A.; Shul'pin, G. B. *ACS Catal.* **2013,** 3, 1195-1208.

50. Kuznetsov, M. L.; Kozlov, Y. N.; Mandelli, D.; Pombeiro, A. J. L.; Shul'pin, G. B. *Inorg. Chem.* **2011,** 50, 3996-4005.

51. Novikov, A. S.; Kuznetsov, M. L.; Rocha, B. G. M.; Pombeiro, A. J. L.; Shul'pin, G. B. *Catal. Sci. Technol.* **2016,** 6, 1343-1356.